INTERNATIONAL DOCTORAL
SCHOOL OF THE USC

Bruno
Delgado González

PhD Thesis

Dynamic Covalent Boronate Chemistry for Bioactive Polymeric Materials

Santiago de Compostela, 2024

Doctoral Programme in Chemical Science and Technology

ESCOLA DE DOUTORAMENTO
INTERNACIONAL DA USC

TESIS DOCTORAL

DYNAMIC COVALENT BORONATE CHEMISTRY FOR BIOACTIVE POLYMERIC MATERIALS

Bruno Delgado González

Director: Eduardo Fernández Megía

PROGRAMA DE DOCTORADO EN CIENCIA Y TECNOLOGÍA QUÍMICA

SANTIAGO DE COMPOSTELA

USC
UNIVERSIDADE
DE SANTIAGO
DE COMPOSTELA

Acknowledgements

Existe una verdad universal que todos debemos enfrentar tarde o temprano: al final todo se acaba. Por mucho que haya anhelado que llegara este día, los finales siempre son amargos: el viaje de vuelta, el último capítulo de un libro, la última partida. Sin embargo, los finales son inevitables. Llega septiembre, se termina la película, decimos adiós. La presentación de esta tesis representa uno de esos momentos, es tiempo de dejar atrás un mundo conocido, de concluir una aventura que empezó hace 10 años al entrar por primera vez en la Facultad de Química, en la cual espero defender este trabajo.

Quiero agradecer a la Xunta de Galicia por haberme otorgado una beca predoctoral. Asimismo, a Eduardo, mi director de tesis. Aunque siempre hay dos caras de una moneda, tu ayuda ha sido esencial para poder crecer tanto en lo profesional como en lo personal a lo largo de estos años. Tu pasión por la ciencia, y esa búsqueda incansable de la perfección que te define, hacen que valga la pena seguir acudiendo al laboratorio para continuar aprendiendo. A mis compañeros de tesis. A Roi, Samuel, y Juan, por acogerme, por tener paciencia infinita, por enseñarme que el trabajo bien hecho, el esfuerzo sin recompensa inmediata, y el trabajar sin mirar el reloj por algo que te gusta, merece la pena. A Celia, Alba y Lucas, vuestros ánimos, consejos, y sobre todo las risas de estos años han sido una vacuna contra cualquier contratiempo. A Pupilo y Natalia, por enseñarme que una mirada asesina puede esconder un tesoro. A Carla y Pol, por vuestra paciencia. También a mis compañeros de Eindhoven, en especial Alex, Fran, y Diego. A lo largo de estos años os habéis convertido en una segunda familia. No podría estar más agradecido de haberos tenido como compañeros y, sobre todo, de teneros como amigos.

Pero, en especial, hay personas que siempre han estado y seguirán estando presentes pase lo que pase, son tierra firme, una brújula a la cual recurrir cuando nada parece ir bien, y los primeros confidentes con quienes compartir una alegría. Papá, mamá, cualquier logro conseguido es gracias a vosotros. Sois un ejemplo de superación constante, de esfuerzo, de bondad, de comprensión, de humildad. Gracias por estar siempre con nosotros. Carlota, tenerte como hermana es la mayor suerte que he tenido. Haces que cualquier meta parezca pequeña, por muy cuesta arriba que se haga el camino. Anny, tu has sido una luz permanente en este camino. Gracias por quererme y animarme a cada paso, por ser inspiración constante. Te quiero. A mis tíos y mis abuelos, en especial quien no puede estar, y sin cuyo ejemplo nada de esto hubiese ocurrido. Sois mi familia, no miento si digo que todo lo mencionado se os aplica a vosotros, gracias por estar ahí. A mi pequeña, pero cada vez más grande, segunda casa en Barcelona. Poder veros es siempre una muestra de cariño y de aire fresco.

Me queda un grupo de personas muy especial a quien dar las gracias, mis amigos. Hace años que se han ido cerrando etapas, tomando nuevos caminos, y siempre habéis estado ahí, siendo la causa por la que coger vacaciones, la excusa para hacer un nuevo viaje, o para probar algo nuevo. Soy como soy en gran medida gracias a todos vosotros, no cambiéis.

Pienso que la presencia de referentes constituye una motivación fundamental tanto dentro del ámbito científico como fuera de él. Por ello, no podría concluir estos agradecimientos sin expresar mi gratitud hacia aquellas personas a quienes he admirado desde la distancia. En particular, a un buen amigo por animarme a emprender esta aventura.

Por último, deseo expresar mi más profundo agradecimiento a todo el CiQUS, en especial a mis compañeros del P3L6 y del P2L3, por el inestimable apoyo y la valiosa ayuda brindada durante estos años.

USC
UNIVERSIDADE DE COMPOSTELA

List of Contents

Acknowledgements I
List of Contents II
Summary V
Resumo XI
List of Abbreviations XVII
1. INTRODUCTION 1
1.1 DRUG DELIVERY 3
1.1.1 Origin of Drug Delivery 3
1.1.2 Engeeniring Drug Delivery Systems 4
1.1.2.1 Surface Properties 4
1.1.2.2 Targetting 5
1.1.2.3 Physico-chemical Properties of DDS 6
1.1.3 Polymers in Drug Delivery 7
1.1.4 Smart Polymers for DDS 10
1.2 GENE DELIVERY 12
1.2.1 Origin and Current Status of Gene Delivery 12
1.2.2 Biological Barriers 13
1.2.2.1 Carrier and Cargo Degradation 13
1.2.2.2 Cytotoxicity 14
1.2.2.3 Cellular Internalization 14
1.2.2.4 Endosomal Escape 15
1.2.2.5 Diffusion to Nuclei 15
1.2.3 Polycation Architecture Mediates Polyplex Activity 16
1.3 COMPLEX COACERVATES AS ARTIFICIAL CELL MODELS 19
1.3.1 Bottom-up Synthetic Biology 19
1.3.2 The Importance of Macromolecular Crowding 20
1.3.3 Complex Coacervates: Origin, Characteristics, and Applications 21
1.4 DYNAMIC COVALENT CHEMISTRY 27
1.4.1 DCvC Reactions 27
1.4.1.1 Disulfide Exchange 27
1.4.1.2 Formation of Oximes and Hydrazones 27
1.4.1.3 Formation of Boronate Esters 28
1.4.2 Applications of DCvC 29
1.4.2.1 DCvC for Drug Delivery 29
1.4.2.2 DCvC for Delivery of Biopharmaceuticals 31
1.4.2.3 DCvC for the Construction of Artificial Cells 34
2. OBJECTIVES 35
3. MATERIALS AND METHODS 36

USC UNIVERSIDADE DE SANTIAGO DE COMPOSTELA

3.1 EXPERIMENTAL DATA FOR A HIERARCHICAL ASSEMBLY OF *IN SITU* PREPARED BORONATE-ESTER DENDRIMERS REGULATES THE SIZE OF DOXORUBICIN POLYMER THERAPEUTICS 36
3.1.1 Materials 36
3.1.2 Instrumentation 36
3.1.3 Micelles Preparation 37
3.1.3.1 CAT Micelles 37
3.1.3.2 DOX Micelles 37
3.1.4 Dynamic Light Scattering (DLS), Size, and Stability of Micelles 39
3.1.4.1 CAT-Micelles 40
3.1.4.2 DOX Micelles 44
3.1.5 Characterization Assays 48
3.1.6 Cell Studies 49
3.2 EXPERIMENTAL DATA FOR DYNAMIC BORONATE CHEMISTRY ACCELERATES THE SCREENING OF POLYMERIC GENE DELIVERY VEHICLES *VIA IN SITU* COMPLEXATION OF NUCLEIC ACIDS 51
3.2.1 Materials 51
3.2.2 Instrumentation 51
3.2.3 Synthesis and Characterization of New Compounds 53
3.2.4 pEGFP-N1 Production 76
3.2.5 Polyplex Preparation and Dynamic Light Scattering Measurements 77
3.2.6 Cell Studies 90
3.2.7 *In vitro* Assays 96
3.3 EXPERIMENTAL DATA FOR DYNAMIC COVALENT BORONATE CHEMISTRY FOR THE *IN SITU* PREPARATION, STABILIZATION, AND ACTIVITY OPTIMIZATION OF COACERVATE ARTIFICIAL CELLS 97
3.3.1 Materials 97
3.3.2 Instrumentation 97
3.3.3 Preparation Of Fluorescently Labeled Compounds 97
3.3.4 Coacervate Preparation 98
3.3.5 Characterization of Coacervates 100
3.3.6 Enzymatic Cascade Reaction 101
3.3.7 Studies on Doped Coacervates 103
4. RESULTS AND DISCUSSION 106
4.1 A HIERARCHICAL ASSEMBLY OF *IN SITU* PREPARED BORONATE-ESTER DENDRIMERS REGULATES THE SIZE OF DOXORUBICIN POLYMER THERAPEUTICS 106
4.1.1 Research Background 106
4.1.2 The PEGylation Degree Determines the Size of Boronate Based Micelles 107
4.1.3 A Model of Spherical Micelles Describes the Hierarchical Assembly 110
4.1.4 The PEGylation Degree Regulates the Size of a Doxorubicin Polymer Therapeutic 112

USC UNIVERSIDADE DE SANTIAGO DE COMPOSTELA

4.1.5 DOX Micelles as Size-Tailored DDS 115
4.2 DYNAMIC BORONATE CHEMISTRY ACCELERATES THE SCREENING OF POLYMERIC GENE DELIVERY VEHICLES *VIA IN SITU* COMPLEXATION OF NUCLEIC ACIDS 119
4.2.1 Research Background 119
4.2.2 A Highly Adaptable Gene Delivery Platform Based on Cationic Polyboronate Vectors 120
4.2.3 Dynamic Covalent Libraries for Screening Polymeric Vectors 121
4.2.4 Endocytosis-Endosomal Escape Dilemma of Cationic Polyboronates 124
4.2.5 Optimizing Polymeric Vectors by Dynamic Covalent Libraries 125
4.2.6 Protection Imparted by Cationic Polyboronate Vectors to pDNA 127
4.3 DYNAMIC COVALENT BORONATE CHEMISTRY FOR THE *IN SITU* PREPARATION, STABILIZATION, AND ACTIVITY OPTIMIZATION OF COACERVATE ARTIFICIAL CELLS 129
4.3.1 Research Background 129
4.3.2 Formation of CCs Induced by the *In Situ* Phase Separation of Dynamic Zwitterionic Polyboronates 129
4.3.3 DCvC for the Stabilization of Polyboronate Coacervates 130
4.3.4 Life-Like Activity of Stabilized Polyboronate Coacervates: Protein Encapsulation and Chemical Communication 132
4.3.5 Optimizing Polyboronate Coacervates by the Introduction of Dopants 133
5. CONCLUSIONS 135
6. REFERENCES 136
7. APPENDICES 151
7.1 LIST OF FIGURES 151
7.2 LIST OF TABLES 156
7.3 LIST OF PUBLICATIONS 157
7.4 RIGHTS AND PERMISSIONS 158

USC
UNIVERSIDADE DE SANTIAGO DE COMPOSTELA

Summary

Polymeric scaffolds have played fundamental roles since the origin of life and represent a unique tool for the future of our society. Regarding the functions of polymers in a biological context, they are responsible of many natural processes, such as the transmission of genetic information, or the storage of energy within catabolic substrates. Moreover, during the last decades they have also been involved in the design of novel biomaterials. Their exquisite structural tunability have inspired scientists to investigate how chemical modifications along the polymeric backbones can alter the performance of the derived materials. Giving the importance of structure-activity relations in the discovery of functional drug delivery systems (DDS), as well as in the comprehension of the rules that govern biological activities, they can be considered as an attractive research target with crucial implications on the future of the field. However, the scope of such research is often limited by the need to introduce a large number of structural modifications.

In this context Dynamic Covalent Chemistry (DCvC) emerges as a unique tool to design sophisticated biomaterials that can be formed, adjusted, and disrupted under controlled conditions. DCvC refers to chemical transformations carried out reversibly under equilibrium control. Considered as a link between conventional static systems and supramolecular assemblies, DCvC effectively surpasses the inherent limitations of the former, while allowing the preparation of more robust conjugates than the latter. Among the different functionalities exploited in DCvC, boronic acids (BAs) represent a remarkable exponent. BAs are synthetic organic compounds with a trivalent boron atom bonded to an aryl or alkyl chain and two hydroxyl groups. The relevance of BAs in DCvC relies on their ability to form esters with 1,2- and 1,3- diols. The equilibrium processes leading to the formation of boronate esters are highly dependent on the pK_a of BA and diol, as well as the pH of the medium, which dictates the hybridization state of the BA (sp^2 or sp^3). Thus, since arylboronic acids are commonly used in the biomedical field, several modifications have been introduced at its aromatic ring and substituents to adjust their pK_a and improve the efficacy of the ester formation at physiological pH. Particularly, Wulff-type BAs add an *ortho*-aminomethyl group adjacent to the boron atom, facilitating boronate ester formation through a B−N dative bond in aprotic media. This induces a hybridization change in the boron center that lowers the pK_a and allows the formation of more stable boronate esters. Conversely, in protic media this effect is originated by a solvent insertion into the boron atom. This results in the formation of a boronate anion capable of interacting with the adjacent nitrogen group to create a zwitterionic species, thereby lowering the pK_a. Consequently, this facilitates the formation of stable esters at physiological pH, which can be hydrolyzed under acidic conditions.

The present Ph.D. dissertation aims to address the challenges that hinder the discovery of advanced polymeric materials by exploiting the unique properties of DCvC. To this end, the chemical versatility imparted by BAs will be combined with the unique properties of dendritic scaffolds. First described by Vötgle, Newkome, and Tomalia, dendrimers are tree-like, monodisperse and synthetic macromolecules characterized for having a globular architecture. They are composed of branched repeating units emerging radially from a central core. The precise control over molecular weight, shape, and terminal groups achieved during their synthesis allows them to be specifically tuned for the target application. Additionally, dendrimers can also serve as building blocks for the construction of different copolymers and supramolecular aggregates. For instance, in the last decades, linear-dendritic block copolymers have been prepared and found wide application in the biomedical field, particularly for the

USC DE COMPOSTELA

design of drug delivery systems (DDS) when incorporating linear poly(ethyleneglycol) (PEG) chains. Along this thesis a PEG_{5k}-dendritic block copolymer (PEG[G3]-BA) and its nonPEGylated analog (3[G2]-BA), both from the GATG family and functionalized with 27 peripheral BAs, were employed as structural scaffolds. O*rtho*-aminomethylphenyl-BAs were selected because of their convenient pK_a *ca.* 6.5. Since the optimal pH for boronate ester formation is generally above the pK_a, these would allow the formation of stable boronate bonds at physiological pH, while facilitating their controlled disruption in the presence of acidic media. The addition of different catechol-derived subunits allows the obtention of dynamic polyboronates, which properties are dictated by the nature of the mentioned subunits. This versatile technology represents the cornerstone of the thesis, which was focused on analyzing its implications in drug delivery, gene therapy, and the fabrication of artificial cells.

DDS for cancer treatment attempt to surmount the limitations of standard free administration of antineoplastic drugs by improving the delivery of the compounds into the affected tissue. However, the chemotherapy efficacy of any DDS depends on the optimal selection of the carrier. Attempting to answer the increasing demand of DDS able to interact with the tumoral environment, and considering the unique properties of DCvC for controlling such interaction, our group has developed an advanced carrier based on a PEG-GATG copolymer functionalized with peripheral Wulff-type BAs able to act as chemical handles. This system allows the entrapment of 1,2-diol containing drugs under physiological conditions, while facilitating controlled drug release below the pK_a of the BAs. The *in situ* conjugation of drugs onto the dendritic surface alters the hydrophilic-hydrophobic balance of the copolymer, resulting in its self-aggregation.

Regarding the efficacy of DDS, structural parameters have an important contribution. DDS size has been identified as a fundamental parameter to consider regarding pharmacokinetics and tumour retention. However, a precise control over DDS size remains elusive by current chemical methodologies. In this context, our group has recently demonstrated how the hierarchical assembly of dendrimers can be programmed to engineer size-controlled polyion complex (PIC) micelles (from 40 nm up to nearly 2 μm). This study introduces a method to tune the size of PIC micelles employing a PEG-dendritic copolymer/dendrimer pair and an oppositely charged polyamino acid. Control over the size is achieved through the adjustment of micelle PEGylation. Along the study, a model based on spherical micelles was adopted to describe such an organized process and to explain the observed variation of size with % PEG. Its validation through static light scattering (SLS) measurements confirmed that the proposed model can perfectly disclose how the number of particles, the total surface area of particles, and the PEG density per particle change with % PEG along the micelle series. The first section of this thesis aims to integrate the advanced design of the previous copolymer with the size control achieved for PIC, to develop a more sophisticated DDS. This conjugation emerges not only as a powerful method to prepare smart DDS with tailored sizes, but also as an extrapolation of the already described hierarchical assembly process, which is aimed to surpass the electrostatic nature of PIC micelles.

Inspired by the principles that rule the formation of micelles, the above-described method was founded on reducing PEGylation while maintaining a constant amount of charged units. Such reduction promoted the obtention of larger micelles, which accommodate a reduced number of PEG chains at the corona, while incorporating increasing amount of components within the core. To transfer this concept towards *in situ* hydrophobized dendrimers, a degree of PEGylation (% PEG) was defined as the percentage between PEG[G3]-BA and 3[G2]-BA.

USC
UNIVERSIDADE DE COMPOSTELA

Among commercially available diols, catechol (CAT) was selected as model due to its high-water solubility and its known ability to form strong associations with BAs in aqueous solutions. Micelles with variable % PEG from PEG[G3]-BA/3[G2]-BA and CAT were prepared by adding a mixture of dendritic components over a CAT solution. The *in situ* attachment of CAT units along the surface of the dendrimers drives their self-assembly into micelles, which size is dictated by the employed % PEG. The size of the resulting structures was analysed by dynamic light scattering (DLS) measurements, which revealed hydrodynamic radii (*R*) increasing gradually from 16 to 535 nm on reducing the % PEG from 100 to 0.15%. Interestingly, further reductions of % PEG below these values caused micelle aggregation, highlighting the crucial role of the PEG chains at the corona, which not only serve as templates for micelle formation but also are essential for colloidal stability. Physical characterization, by scanning-transmission electronic microscopy (STEM) and laser scanning confocal microscopy (LSCM), of CAT micelles prepared at different % PEG corroborated the trends observed by DLS and the predicted assembly of PEG chains along the surface of the micelles. Interestingly, the obtained values fit well with the previously designed model, confirming its successful translation to amphiphilic micelles.

DDS derived from these particles were obtained by using doxorubicin (DOX) not only as therapeutic cargo, but also as an active participant in the self-assembly process. The dual conjugation of DOX, *via* its 2-keto-1,3-diol functionality, and CAT, onto the outer layer of the dendrimers facilitated the previously described self-assembly into nanometric micelles, with high encapsulation efficiency (EE) and drug loading (DL). The morphology and time dependent stability of these micelles were analyzed by DLS. Interestingly, experimental data for these micelles also fitted the size variation model developed for PIC. Further experiments were conducted to evaluate the performance of DOX micelles as DDS. This was addressed by analyzing their *in vitro* delivery performance in terms of cellular uptake and cytotoxicity in F-98 cells, a glioma model cell line derived from rats. Results revealed no differences along the tested % PEG.

As a conclusion from this part of the thesis, following a systematic workflow a novel technology for obtaining size tunable DDS was developed. The successful translation of the size regulation imparted by the hierarchical assembly of PEG chains to polyboronate micelles allowed the preparation of pH-responsive and DOX-loaded DDS with different sizes and % PEG. The present study sheds light on how these last parameters affect the pH-triggered release, intracellular trafficking, and cytotoxicity of the prepared micelles.

Gene therapy provides new therapeutic opportunities beyond the reach of traditional treatments. Despite the progress in the use of viral vectors, their high cost, complex manufacturing, and severe side effects have encouraged the development of nonviral alternatives. These are mainly based on cationic polymers, peptides, and lipids that interact electrostatically with nucleic acids (NAs), that, although representing safer and more cost-effective alternatives, are less efficient in overcoming cellular barriers. This is where the exquisite structural tunability of polymers might excel. Recent advances in synthetic methodologies allow researchers to impart desired functions to polymeric gene carriers. However, since material properties need to be engineered for each NA, the identification of polymers that can replace viral vectors in clinical gene therapy has proven elusive. The need to fine-tune several structural parameters represents a bottleneck of current screening processes, which has only been partially dampened by the advent of combinatorial approaches. Therefore, there is an urgent demand for technologies to speed up

USC UNIVERSIDADE DE SANTIAGO DE COMPOSTELA

the optimization of polymeric vectors by the simultaneous adjustment of multiple variables. DCvC represents a promising pillar for such innovative technologies.

Along the second part of this thesis, a highly adaptable gene delivery platform using a polymeric BA that is activated in the presence of pDNA by the addition of cationic catechols is described. The fast and strong boronate ester bonding affords cationic dynamic polyboronates able to complex pDNA *in situ* to afford polyplexes that, without further manipulation, efficiently transfect cells. The robustness of the strategy entitles the simultaneous screening of several structural parameters: (i) % PEG, the ratio between PEG[G3]-BA and 3[G2]-BA. (ii) The N/P ratio of ionizable nitrogen atoms in the polymer (equal to BA groups) to negatively charged phosphate groups in the NAs. (iii) The ratio between added cationic catechols and BA groups (CBA ratio). (iv) The polycation chemical composition among a selection of catechols functionalized with primary (A) and tertiary (T) amines, guanidine (G), ethylenediamine (D), and imidazole (I) groups. Finally (v), the incorporation of catechols with hydrophobic moieties such as, a medium-chain fatty acid (octanoic acid, O), a fluorocarbon chain (perfluorobutanoic acid, P), and cholesterol (C). Polyplexes were produced by dynamic covalent libraries and evaluated for their size and polydispersity index (PDI), pDNA complexation (pEGFP-N1), and transfection efficiency *in vitro*.

A first combinatorial library was designed to get general trends about the effect of % PEG, the N/P ratio, and the nature of the cationic group (G, A, D, and mixtures thereof) on the polyplex performance. DLS data showed a mean diameter of *ca.* 125-150 nm for the G-polyplexes, independently of % PEG. Conversely, a size increase inversely proportional to % PEG was revealed for A- and D-polyplexes (up to 220 and 260 nm, respectively), probably associated with a lower pDNA complexing ability. Despite differences in size, a complete pDNA complexation was revealed for all polyplexes. Regarding transfection efficiencies, while some of the G-polyplexes outperformed LP 2000, none of the A- or D-polyplexes produced any transfection, confirming a much lower delivery efficiency. Similarly, the incorporation of catechols A and, particularly, D into the G-polyplexes drastically reduced transfection efficiency. Among the G-polyplexes, increased transfections were observed for the higher N/P ratios and lower % PEG. Doping one of the best performing G-polyplexes with either alternative T and I cationic catechols or catechols O, P, and C to enhance the hydrophobic interactions with pDNA did not afford improved transfections. The influence of % PEG could not be unequivocally associated with an impaired endocytosis or endosomal escape since PEGylation is known to dramatically damage both steps. This endocytosis vs endosomal escape issue was addressed by analyzing in detail the cell internalization of selected polyplexes using a fluorescently labeled plasmid. The quantitative cellular uptake alongside with an undistinguishable intracellular distribution observed for all-tested formulations lead to the association of the observed lack of transfection with an endosomal escape issue. Aimed by further optimizing G-polyplexes, a second combinatorial library was planned focused on analyzing even lower % PEG, and on evaluating the role of the CBA ratio. Interestingly, results pointed that the CBA ratio modulates the transfection within each tested N/P. Highest transfections were observed at CBA 10 for N/P 5, CBA 5 and 10 for N/P 10, and CBA 5 for N/P 15. So, a balance between both parameters is revealed, with higher CBA ratios increasing the transfection at low N/P ratios but compromising cell viability at higher N/P, especially for N/P 15. From this study, two optimized polyplexes were selected for further transfection studies. Finally, further experiments were conducted to corroborate the NA protection imparted by these vectors, as well as their hemocompatibility.

USC
UNIVERSIDADE
DE SANTIAGO
DE COMPOSTELA

In synthesis of the second part of this thesis, a highly adaptable gene delivery platform was designed based on the activation of dendritic scaffolds in the presence of pDNA by the addition of cationic catechols. The resulting cationic polyboronates can complex pDNA *in situ* leading to polyplexes that efficiently transfect cells. The robustness of the strategy entitles the simultaneous screening of several structural parameters enabling the accelerated screening and optimization of lead polymeric vectors.

Finally, a versatile approach towards coacervate-based artificial cells was also developed in the third section of this thesis. Cells represent the basic structural and functional units of all forms of life. In the last decade, a growing interest in creating artificial cell analogs to elucidate their inherent complexity has catalyzed the advancement of bottom-up synthetic biology. Among the structures commonly used as artificial cells, complex coacervates (CCs) are particularly noteworthy. These droplets, formed through liquid-liquid phase separation via the association of oppositely charged polyelectrolytes, are excellent mimics of the crowded cell interior and naturally occurring membrane-less organelles (MLOs), which play crucial roles in many vital processes. Variations in the concentration of the involved polyelectrolytes can effectively promote the formation or dissolution of the corresponding droplets, concept that has been largely exploited in living cells leading to regulatory processes. Inspired by this regulation, many scientific efforts have focused on translating such behavior into controlled coacervation methods, however the reported alternatives often fail in providing stabilization and structural diversity, which are essential for CCs function.

In the final section of this thesis, an adaptable method for inducing coacervation was described by using a dendritic BA that is activated due to the synergistic attachment of cationic and anionic catechols. This coupling affords zwitterionic polyboronates able to phase separate *in situ* into individual droplets with a mean diameter around 3 μm. The lack of a membrane to provide coacervates with structural integrity has been surpassed through the hierarchical assembly of PEG[G3]-BA onto the surface of the droplets.

An essential characteristic of CCs is their capacity to promote macromolecular sequestration, feature that can be enhanced by modulating the affinity of the cargo for the inner core of the coacervates. The robustness of the current strategy enabled the adaptation of the final droplets to enhance protein partitioning by adjusting the molar ratios between Cat-CA and Cat-G. This methodology allowed modulation of the inner environment of the droplets in a feasible manner without altering their polymeric scaffold. Glucose oxidase (GOX) and horseradish peroxidase (HRP), both fluorescently labeled with Cy5, were selected to assess the viability of this approach due to their largely different isoelectric points (pI), and their complementarity in enzymatic cascade reactions. Interestingly, a significant enhancement on the EE of both proteins was observed when using a 2-to-1 excess of Cat-G.

Since maintaining an active droplet-droplet communication after interfacial stabilization represents a challenge on synthetic biology, an archetypical example of enzymatic cascade reaction involving GOX and HRP was performed using these optimized coacervates. For qualitative studies, LSCM experiments were conducted. Initial images were captured before the addition of substrates to prove no protein exchange between the different populations. After the addition of substrates, glucose was oxidized by AF488-GOX@C, producing hydrogen peroxide (H_2O_2) as a byproduct. Effective communication was confirmed by the H_2O_2 transport between compartments in order Cy5-HRP@C to oxidize amplex red to resorufin. This was verified by monitoring the fluorescence signal from resorufin within the sample. While a dim initial resorufin fluorescence signal started to appear in Cy5-HRP@C, after 10 min, higher

fluorescence levels were detected within these compartments, also observing resorufin migration towards AF488-GOX@C. Consequently, these findings validate the ability of PEG[G3]-BA to promote the obtention of stabilized droplets, without preventing the diffusion of small molecules, thereby corroborating the life-like behavior of this polyboronate coacervates.

Recent reports have demonstrated that variations in the multivalency or charge density of polyelectrolytes undergoing phase separation can significantly affect internal dynamics and ribozyme/enzyme activity within CCs. Thereby, DCvC was envisaged as a promising tool to facilitate the investigation of CCs functionality by incorporating various functional moieties along a polymeric backbone. Three commercially available catechols were selected as a stress test for this adaptable methodology, which impact on the interactions between coacervates and protein cargo. Results obtained from fluorescence recovery after photobleaching (FRAP) experiments, pointed that the gel-like structure of the parent coacervates, similar to other reported guanidine-based CCs, was surpassed by the *in situ* modification of the zwitterionic polyboronates undergoing phase separation. Finally, since an enhanced protein mobility within CCs has been often correlated with enhanced ribozyme/enzyme activity, the influence of dopants on the ortho-phenylenediamine (*o*PD) to (2,3-diaminephenazine) 2,3-DAP enzymatic transformation was further analyzed. Enzymatic reaction profiles revealed enhanced kinetics for doped droplets, which is agreement with the already described fluorescence recovery values, highlighting the importance of manipulating protein diffusion on the activity of the final droplets.

In summary, the capability of DCvC to construct and stabilize dendritic protocell models was demonstrated. These findings emphasize how the modulation of the internal properties of the droplets can be achieved through a straightforward methodology based on *in situ* obtained zwitterionic polyboronates, paving the way for DCvC to impact synthetic biology.

These sections form the experimental base of the present thesis and are presented as pioneering examples of the robustness of the designed strategy.

USC
UNIVERSIDADE DE SANTIAGO DE COMPOSTELA

Resumo

As estruturas poliméricas xogaron un papel fundamental desde a orixe da vida e representan unha ferramenta única para o futuro da nosa sociedade. En canto ás funcións dos polímeros nun contexto biolóxico, son responsables de moitos procesos naturais, como a transmisión da información xenética ou o almacenamento de enerxía en substratos catabólicos. Ademais, nas últimas décadas, tamén se viron implicados no deseño de novos biomateriais. A súa exquisita capacidade de axuste estrutural inspirou aos científicos a investigar como as modificacións químicas ao longo das cadeas poliméricas poden alterar o rendemento dos materiais derivados das mesmas. Dada a importancia das relacións estrutura-actividade no descubrimento de sistemas de liberación de fármacos (DDS), así como na comprensión das regras que rexen as actividades biolóxicas, poden considerarse como un obxectivo de investigación punteiro con implicacións cruciais para o futuro da ciencia. Non obstante, o alcance de tales investigacións adoita verse limitado pola necesidade de introducir un gran número de modificacións estruturais.

Neste contexto, a Química Covalente Dinámica (DCvC) emerxe como unha ferramenta única para deseñar biomateriais sofisticados que poden formarse, axustarse e descompoñerse en condicións controladas. A DCvC refírese a transformacións químicas realizadas de forma reversible baixo condicións de equilibrio. Considerada como unha ligazón entre os sistemas estáticos convencionais e as ensamblaxes supramoleculares, a DCvC supera eficazmente as limitacións inherentes dos primeiros, ao tempo que permite a preparación de unións máis robustas ca os segundos. Entre as diferentes funcionalidades explotadas dentro da DCvC, os ácidos borónicos (BAs) representan un notable expoñente. Os BAs son compostos orgánicos sintéticos cun átomo de boro trivalente unido a unha cadea arilo ou alquilo e a dous grupos hidroxilo. A súa implicación na DCvC xorde a raíz da súa capacidade para formar ésteres con dioles 1,2- e 1,3-. Os procesos de equilibrio para a formación de ésteres de boronato dependen en gran medida do pK_a das especies implicadas e do pH da solución, que inmediatamente dita a hibridación do átomo de boro (sp^2 ou sp^3). Así, diferentes modificacións foron introducidas no anel aromático e nos substituíntes dos ácidos arilborónicos para axustar o seu pK_a e mellorar a eficiencia da formación de ésteres a pH fisiolóxico. En particular, os BAs do tipo Wulff engaden un átomo de nitróxeno adxacente ao boro, facilitando a formación de ésteres de boronato a través dunha unión dativa B−N. Isto induce un cambio de hibridación no átomo de boro que reduce o pK_a e permite a formación de ésteres de boronato máis estables. En medios próticos, este efecto é orixinado a través da inserción dunha molécula de disolvente no átomo de boro. Isto leva á obtención dun anión de boronato capaz de formar unha especie zwitteriónica co grupo de nitróxeno adxacente, o cal reduce o pK_a e permite o establecemento de ésteres estables a pH fisiolóxico pero capaces de seren hidrolizados en condicións ácidas.

A presente tese de doutoramento ten como obxectivo abordar os desafíos que dificultan o descubrimento de materiais poliméricos avanzados explotando as propiedades únicas da DCvC. Para este fin, combinarase a versatilidade química impartida polos BAs coas propiedades únicas das estruturas dendríticas. Descritos por primeira vez por Vötgle, Newkome e Tomalia, os dendrímeros son macromoléculas sintéticas e monodispersas con forma de árbore, caracterizadas por ter unha arquitectura globular. Están compostos por unidades repetitivas e ramificadas que xorden radialmente dun núcleo central. O control preciso sobre o peso molecular, a forma, e os grupos terminais logrado durante a súa síntese, permite o seu axuste específico para a aplicación desexada. Ademais, os dendrímeros tamén poden servir como bloques de construción para a formación de diferentes copolímeros e agregados

USC DE COMPOSTELA

supramoleculares. Por exemplo, nas últimas décadas, preparáronse copolímeros lineais-dendríticos que atoparon ampla aplicación no campo biomédico, particularmente no deseño de sistemas de liberación de fármacos (DDS) cando se incorporan cadeas lineais de polietilenglicol (PEG). Ao longo desta tese, empregáronse un copolímero de bloque PEG_{5k}-dendrítico (PEG[G3]-BA) e o seu análogo non PEGilado (3[G2]-BA), ambos da familia de dendrímeros derivados do ácido gálico (GATG) e funcionalizados con 27 BAs periféricos, como andamios estruturais. Seleccionáronse BAs do tipo *orto*-aminometilfenil debido ao seu conveniente pK_a de aproximadamente 6,5. Dado que o pH óptimo para a formación de ésteres de boronato é xeralmente superior ó pK_a, estes permitirán a formación de unións boronato estables a pH fisiolóxico, ao tempo que facilitarán a destrución controlada dos mesmos en presenza de medios ácidos. A adición de diferentes subunidades derivadas de catecol permite a obtención de poliboronatos dinámicos, cuxas propiedades están ditadas pola natureza das mencionadas subunidades. Esta tecnoloxía versátil representa a pedra angular da tese, que se centrou en analizar as súas implicacións na liberación de fármacos, a terapia xénica e a fabricación de células artificiais.

Os DDS para o tratamento do cancro intentan superar as limitacións da administración libre estándar de fármacos antitumorais mellorando a entrega dos compostos no tecido afectado. Non obstante, a eficacia da quimioterapia derivada de calquera DDS depende da óptima selección do vehículo. Tentando responder á crecente demanda de DDS capaces de interactuar co entorno tumoral, e considerando as propiedades únicas da DCvC para controlar tal interacción, o noso grupo desenvolveu un vehículo avanzado baseado nun copolímero PEG-GATG funcionalizado con BAs periféricos do tipo Wulff capaces de actuar como asas químicas. Este sistema permite a unión de fármacos que conteñen dioles 1,2 baixo condicións fisiolóxicas, facilitando a liberación controlada de fármacos por debaixo do pKa dos BAs. De xeito similar a enfoques como a autoensamblaxe inducida por polimerización (PISA), a unión *in situ* de fármacos na superficie dendrítica altera o equilibrio hidrofílico-hidrofóbico do copolímero, o cal resulta na súa autoagregación.

En canto á eficacia dos DDS, os parámetros estruturais teñen unha contribución importante. O tamaño do DDS identificouse como un parámetro fundamental a considerar en canto á farmacocinética e á retención tumoral. Non obstante, o control preciso sobre o tamaño do DDS segue sendo inalcanzábel mediante as metodoloxías químicas actuais. Neste contexto, o noso grupo demostrou recentemente como a ensamblaxe xerárquica dos dendrímeros pode programarse para enxeñar micelas PIC de tamaño controlado (dende 40 nm ata case 2 μm). Este estudo introduce un método para axustar o tamaño das micelas PIC empregando un par copolímero dendrítico-PEG/dendrímero, e un poliaminoácido de carga oposta. O control sobre o tamaño conséguese a través do axuste da PEGilación das micelas. Ao longo do estudo, deseñouse un modelo baseado en micelas esféricas para describir tal proceso organizado e para explicar a variación observada de tamaño co % PEG. A súa validación mediante medidas de dispersión de luz estática (SLS) confirmou que o modelo proposto pode describir perfectamente como o número de partículas (N), a superficie total das partículas (S) e a densidade de PEG por partícula (D) cambian co % PEG ao longo da serie de micelas. A primeira sección desta tese pretende unir as dúas últimas tecnoloxías nun DDS máis avanzado. Esta converxencia emerxe non só como un método poderoso para preparar DDS intelixentes con tamaños axustábeis, senón tamén como unha extrapolación do proceso de ensamblaxe xerárquica xa descrito, dirixida a superar a natureza electrostática das micelas PIC.

USC
UNIVERSIDADE DE SANTIAGO DE COMPOSTELA

Inspirado nos principios que rexen a formación de micelas, o método descrito anteriormente baseouse en reducir a PEGilación mantendo unha cantidade constante de unidades cargadas. Esta redución levou á obtención de micelas máis grandes capaces de acomodar un número reducido de cadeas PEG na coroa, ao tempo de incorporar unha maior cantidade de compoñentes no núcleo. Para desenvolver tal tecnoloxía, definiuse o grao de PEGilación (% PEG) como a porcentaxe entre PEG[G3]-BA e 3[G2]-BA. Entre os dioles comercialmente dispoñíbeis, seleccionouse o catecol (CAT) como modelo debido á súa alta solubilidade en auga e á súa coñecida capacidade para formar asociacións fortes cos BAs en solución acuosa. Preparáronse micelas con % PEG variábel a partir de PEG[G3]-BA/3[G2]-BA e CAT, engadindo unha mestura de compoñentes dendríticos sobre unha solución de CAT. A unión *in situ* de unidades CAT ao longo da superficie dos dendrímeros conduce á súa autoensamblaxe en micelas, cuxo tamaño está ditado polo % PEG empregado. O tamaño das estruturas resultantes analizouse mediante medidas de dispersión de luz dinámica (DLS), que revelou radios hidrodinámicos (R) que aumentan gradualmente de 16 a 535 nm ao reducir o % PEG de 100 a 0,15%. Curiosamente, reducións adicionais do % PEG por debaixo destes valores causaron a agregación das micelas, destacando o papel crucial das cadeas de PEG na coroa, que non só serven como modelos para a formación de micelas, senón que tamén son esenciais para a estabilidade coloidal. A caracterización física mediante microscopía electrónica de transmisión-escaneo (STEM) e microscopía confocal de varrido láser (LSCM) de micelas CAT preparadas a diferentes % PEG corroborou as tendencias observadas por DLS, e a ensamblaxe das cadeas de PEG ao longo da superficie das micelas. Curiosamente, os valores obtidos encaixan ben co modelo deseñado previamente, confirmando a súa tradución satisfactoria á micelas anfifílicas.

Obtivéronse DDS derivados destas partículas utilizando doxorrubicina (DOX) non só como carga terapéutica, senón tamén como un participante activo no proceso de autoensamblaxe. A dobre unión de DOX, a través da súa funcionalidade 2-ceto-1,3-diol, e CAT na capa externa dos dendrímeros facilitou a autoensamblaxe previamente descrita de micelas nanométricas con alta eficiencia de encapsulación (EE) e carga de fármaco (DL). A morfoloxía e a estabilidade dependente do tempo das últimas analizáronse mediante DLS. Curiosamente, os datos experimentais para estas micelas tamén se axustaron ao modelo desenvolvido para PIC. Realizáronse experimentos adicionais para avaliar o rendemento das micelas de DOX como DDS. Isto abordouse analizando o seu rendemento de entrega *in vitro* en termos de captación celular e citotoxicidade en células F-98, un modelo de liña celular de glioma derivado de ratas. Os resultados non revelaron diferenzas ao longo do % PEG probado.

En conclusión, seguindo un fluxo de traballo sistemático desenvolveuse unha nova tecnoloxía para obter DDS de tamaño axustable. A tradución satisfactoria da regulación de tamaño impartida pola ensamblaxe xerárquica de cadeas PEG a micelas de poliboronatos, permitiu a preparación de DDS de DOX sensíbeis ao pH, con diferentes tamaños e % PEG. O presente estudo arroxa luz sobre como estes últimos parámetros afectan á liberación desencadeada polo pH, ó tráfico intracelular, e a citotoxicidade das micelas preparadas.

A terapia xénica ofrece novas oportunidades terapéuticas máis alá do alcance dos tratamentos tradicionais. A pesar dos avances no uso de vectores virais, o seu alto custo, complexa fabricación e efectos secundarios graves incentivaron o desenvolvemento de alternativas non virais. Estas baséanse principalmente en polímeros catiónicos, péptidos e lípidos que interactúan electrostáticamente cos ácidos nucleicos (NAs). Sen embargo. aínda que representan alternativas máis seguras e rendíbeis, son menos eficientes en superar as barreiras

USC UNIVERSIDADE DE COMPOSTELA

celulares. Aquí é onde pode sobresaír a exquisita capacidade de axuste estrutural dos polímeros. Os avances recentes en metodoloxías sintéticas permiten aos investigadores impartir funcións desexadas aos vectores poliméricos de xenes. Non obstante, dado que as propiedades dos materiais deben ser enxeñadas para cada ácido nucleico, a identificación de polímeros que poidan substituír ós vectores virais na terapia xénica clínica resultou esquiva. A necesidade de axustar varios parámetros estruturais representa un obstáculo nos procesos de selección actuais, que só se mitigou parcialmente co auxe dos enfoques combinatorios. Polo tanto, existe unha urxente demanda de tecnoloxías que aceleren a optimización dos vectores poliméricos mediante o axuste simultáneo de múltiples variábeis. Neste contexto, a DCvC representa un piar prometedor para tales tecnoloxías innovadoras.

Ao longo desta sección, descríbese unha plataforma de entrega de xenes altamente adaptable empregando un ácido borónico polimérico que se activa na presenza de pDNA mediante a adición de catecois catiónicos. A unión rápida e forte do éster de boronato proporciona poliboronatos catiónicos dinámicos capaces de unir o pDNA *in situ* para formar poliplexos que, sen manipulación adicional, transfectan células de maneira eficiente. A robustez da estratexia permite a selección simultánea de varios parámetros estruturais: (i) % PEG, a proporción entre PEG[G3]-BA e 3[G2]-BA. (ii) A proporción N/P de átomos de nitróxeno ionizables no polímero (igual aos grupos BA) en relación cos grupos fosfato cargados negativamente no ácido nucleico. (iii) A proporción entre os catecois catiónicos engadidos e os grupos BA (proporción CBA). (iv) A composición química do policatión entre unha selección de catecois funcionalizados con grupos amina primaria (A) e terciaria (T), guanidinio (G), etilenodiamina (D) e imidazol (I). Finalmente (v), a incorporación de catecois con grupos hidrofóbicos, como un ácido graxo de cadea media (ácido octanoico, O), unha cadea de fluorocarbono (ácido perfluorobutanoico, P) e colesterol (C). Os poliplexos producíronse mediante bibliotecas dinámicas covalentes e avaliáronse polo seu tamaño e índice de polidispersidade (PDI), encapsulación de pDNA (pEGFP-N1) e eficiencia de transfección *in vitro*.

Deseñouse unha primeira biblioteca combinatoria para obter tendencias xerais sobre o efecto do % PEG, a proporción N/P e a natureza do grupo catiónico (G, A, D e mesturas deles) no rendemento do poliplexo. Os datos de DLS mostraron un diámetro medio de aprox. 125-150 nm para os poliplexos-G, independentemente do %PEG. Pola contra, revelaron un aumento de tamaño inversamente proporcional ó %PEG para os poliplexos -A e -D (ata 220 e 260 nm, respectivamente), probablemente asociado cunha menor capacidade de encapsulación de pDNA. A pesar das diferenzas no tamaño, revelouse unha encapsulación completa de pDNA para todos os poliplexos. En canto ás eficiencias de transfección, mentres algúns dos poliplexos-G superaron á LP 2000, ningún dos poliplexos -A ou -D produciu ningunha transfección, confirmando unha eficiencia de entrega moito menor. Do mesmo xeito, a incorporación de catecois A e, particularmente, D nos poliplexos-G reduciu drasticamente a eficiencia de transfección. Entre os poliplexos-G, observáronse transfeccións maiores para as proporcións N/P máis altas e % PEG máis baixos. A dopaxe dun dos mellores poliplexos-G con catecois catiónicos alternativos T e I ou catecois O, P e C para mellorar as interaccións hidrofóbicas con pDNA non proporcionou melloras nas transfeccións. A influencia do % PEG non se puido asociar inequivocamente cunha endocitose ou escape do endosoma deteriorados, xa que se sabe que a PEGilación dana drasticamente ambos pasos. Esta cuestión de endocitose vs escape do endosoma abordouse analizando en detalle a internalización celular de poliplexos seleccionados usando un plásmido etiquetado fluorescentemente. Unha captación celular cuantitativa, xunto cunha distribución intracelular indistinguible para todas as formulacións probadas, levou á asociación da falta de transfección observada cun problema de escape do endosoma. Para levar

a cabo á optimización dos poliplexos-G, planificouse unha segunda biblioteca combinatoria centrada en analizar menores % PEG e en avaliar o papel da proporción CBA. Curiosamente, os resultados indicaron que a proporción CBA modula a transfección dentro de cada N/P probado. Observáronse maiores transfeccións en CBA 10 para N/P 5, CBA 5 e 10 para N/P 10, e CBA 5 para N/P 15. Así, revelouse un equilibrio entre ambos parámetros, con proporcións CBA máis altas aumentando a transfección a proporcións N/P baixas pero comprometendo a viabilidade celular a proporcións N/P máis altas, especialmente para N/P 15. Deste estudo seleccionáronse dous poliplexos optimizados para estudos adicionais de transfección. Finalmente, realizáronse experimentos adicionais para corroborar a protección dos ácidos nucleicos impartida por estes vectores, así como a súa hemocompatibilidade.

En síntese da segunda parte desta tese, deseñouse unha plataforma de entrega de xenes altamente adaptable baseada na activación de estruturas dendríticas na presenza de pDNA, mediante a adición de catecois catiónicos. Os poliboronatos catiónicos resultantes poden complexar pDNA *in situ* formando poliplexos que transfectan células de forma eficiente. A robustez da estratexia permite a modulación simultánea de varios parámetros estruturais, permitindo a aceleración da selección e optimización dos vectores poliméricos principais.

Finalmente, tamén se conseguiu un enfoque versátil cara células artificiais. As células representan as unidades estruturais e funcionais básicas de todas as formas de vida. Na última década xurdiu un crecente interese por crear análogos artificiais de células para explicar a súa complexidade inherente, dando lugar ao campo da bioloxía sintética. Entre as arquitecturas máis empregadas, os coacervatos complexos (CCs) son especialmente notables. Estas gotas, formadas a través da separación de fases líquido-líquido mediante a asociación de polielectrólitos de carga oposta, son excelentes imitadores do interior celular e dos orgánulos sen membrana (MLOs) que desempeñan papeis cruciais en moitos procesos vitais. As variacións na concentración dos polielectrólitos implicados poden promover efectivamente a formación ou disolución das correspondentes gotas, concepto que se explotou amplamente nas células vivas levando a procesos reguladores. Inspirados por esta regulación, moitos esforzos científicos centráronse en traducir tal comportamento a métodos de coacervación controlada, non obstante, as alternativas reportadas a miúdo fallan en proporcionar estabilización e diversidade estrutural, que son esenciais para a función dos CCs. Entre outros métodos, DCvC constitúe unha metodoloxía prometedora para o desenvolvemento de redes adaptables e sensibles.

Ao longo da sección final desta tese, describiuse un método adaptable para inducir a coacervación empregando un ácido borónico dendrítico que se activa debido á unión sinérxica de catecois catiónicos e aniónicos. Esta unión promove a obtención de poliboronatos zwitteriónicos capaces de separarse en fases *in situ* formando gotas individuais cun diámetro medio de ao redor de 3 μm. A falta dunha membrana capaz de proporcionar integridade estrutural aos coacervados superouse mediante a ensamblaxe xerárquica do PEG[G3]-BA na superficie das gotas.

Unha característica esencial dos CCs é a súa capacidade para promover a captación de macromoléculas. Aínda que esta característica pode amplificarse modulando a afinidade da carga polo núcleo interno dos CCs, numerosos estudos dependen de modificacións nas proteínas para mellorar a súa acumulación no interior das gotas. A robustez da actual estratexia permitiu a adaptación das gotas finais para mellorar a partición de proteínas axustando as proporcións molares entre os catecois de carga oposta, sen alterar a súa arquitectura polimérica. A glucosa oxidase (GOX) e a peroxidasa de ravo picante (HRP), ambas etiquetadas fluorescente

con Cy5, foron seleccionadas para avaliar a viabilidade deste enfoque debido aos seus puntos isoeléctricos (pI) moi diferentes, e á súa complementariedade en reaccións enzimáticas en cascada. Curiosamente, observouse un aumento significativo na EE de ambas as proteínas ao empregar un exceso de 2 a 1 do compoñente catiónico.

Dado que manter unha comunicación gota-gota activa despois da estabilización interfacial representa un desafío en bioloxía sintética, realizouse un exemplo arquetípico de reacción en cascada enzimática, implicando GOX e HRP e empregando estes CCs optimizados. Para estudos cualitativos, realizáronse experimentos de LSCM. Capturáronse imaxes iniciais antes da adición de substratos para demostrar que non había intercambio de proteínas entre as diferentes poboacións. Despois da adición de substratos, a glucosa foi oxidada por AF488-GOX@C, producindo peróxido de hidróxeno (H_2O_2) como subproduto. Confirmouse unha comunicación efectiva mediante o transporte de H_2O_2 entre compartimentos para que Cy5-HRP@C oxidase amplex red a resorufina. Isto verificouse seguindo a produción de resorufina dentro da mostra. Mentres o sinal de fluorescencia de resorufina inicial comezou a aparecer en Cy5-HRP@C, despois de 10 minutos, detectáronse niveis de fluorescencia máis altos dentro destes compartimentos, observándose tamén a migración de resorufina cara a AF488-GOX@C. En consecuencia, estes resultados validan a capacidade de PEG[G3]-BA para evitar a migración de proteínas entre poboacións, ao tempo que permiten a difusión de pequenas moléculas, corroborando así o comportamento similar á vida dos CCs de poliboronatos.

Informes recentes demostraron que as variacións na multivalencia ou densidade de carga dos polielectrólitos involucrados na separación de fases, poden afectar de maneira significativa á dinámica interna e á actividade de ribozimas/enzimas dentro dos CCs. Polo tanto, a DCvC empregouse como unha ferramenta prometedora para facilitar a investigación da actividade dos CCs mediante a incorporación de diversas funcionalidades ao longo dunha cadea polimérica. Seleccionáronse tres catecois comercialmente dispoñíbeis como unha proba de estrés para esta metodoloxía, analizando o seu impacto nas interaccións entre CCs e proteínas. Os resultados obtidos a partir de experimentos de recuperación de fluorescencia despois do fotobranqueo (FRAP) indicaron que a estrutura similar a un xel dos CCs non dopados, similar a outros CCs baseados en guanidininio, superouse mediante a modificación *in situ* dos poliboronatos zwitteriónicos. Finalmente, dado cunha maior mobilidade das proteínas dentro dos CCs adoita relacionarse cunha maior actividade de ribozimas/enzimas, analizouse a influencia dos dopantes na transformación enzimática de *orto*-fenilendiamina (*o*PD) a 1,3-diamonifenazina (2,3-DAP). Os perfís de reacción enzimática revelaron cinéticas melloradas para as gotas dopadas, o que está de acordo cos valores de recuperación de fluorescencia xa descritos, destacando a importancia de manipular a mobilidade das proteínas na actividade das gotas finais.

En resumo, demostrouse a capacidade da DCvC para construír e estabilizar modelos de protocélulas dendríticas. Estes descubrimentos salientan como a modulación das propiedades internas das gotas pode lograrse mediante unha metodoloxía sinxela baseada en poliboronatos zwitteriónicos obtidos *in situ*, achaiado o camiño para que a DCvC impacte na bioloxía sintética.

Estas seccións forman a base experimental da presente tese, e preséntanse como exemplos pioneiros da robustez da estratexia deseñada.

USC
UNIVERSIDADE DE SANTIAGO DE COMPOSTELA

List of Abbreviations

A	Absorbance
AAV	Adeno-associated viral
AF 488	Alexa Fluor 488
Aq	Aqueous
AD	After dialysis
ARS	Alizarin Red S
ATPase	Adenosine triphosphatase
azoTAB	Azobenzenetrimethylammonium bromide
BA	Boronic acid
BBB	Blood brain barrier
bp	Base pairs
br	Broad (for spectroscopy signals)
BSA	Bovine serum albumin
BTZ	Bortezomib
CAT	Catechol
Cat-A	Dopamine hydrochloride
Cat-CA	3,4-Dihydroxyhydrocinnamic acid
Cat-C	(3S,10R,13R,17R)-10,13-dimethyl-17-((R)-6-methylheptan-2-yl)-2,3,4,7,8,9,10,11,12,13,14,15,16,17-tetradecahydro-1H-cyclopenta[a]phenanthren-3-yl (3,4-dihydroxyphenethyl)carbamate
Cat-D	*N*-(2-((2-aminoethyl)amino)ethyl)-3-(3,4-dihydroxyphenyl)propanamide hydrochloride
Cat-G	1-(3,4-dihydroxyphenethyl)guanidine hydrochloride
Cat-I	*N*-(3-(1H-imidazol-1-yl)propyl)-3-(3,4-dihydroxyphenyl)propanamide hydrochloride
Cat-O	*N*-(3,4-dihydroxyphenethyl) octanamide
Cat-P	*N*-(3,4-dihydroxyphenethyl)-2,2,3,3,4,4,4-heptafluorobutanamide
Cat-T	3-(3,4-dihydroxyphenyl)-*N*-(2-(dimethylamino)ethyl)propanamide hydrochloride
CBA	Ratio between added cationic catechols and boronic acids
CC	Complex coacervate
CED	Convection enhanced delivery
CMC	Critical micelle concentration

USC UNIVERSIDADE DE SANTIAGO DE COMPOSTELA

CPT	Camptothecin
CRS	Controlled release systems
Cy5	Cyanine 5
D	PEG density per particle
D_{app}	Apparent diffusion coeficient
Da	Dalton
d	Doublet
DCvC	Dynamic covalent chemistry
dd	Doublet of doublets
DD	Drug delivery
DDS	Drug delivery systems
DEAE	Diethylaminoethyl
DL	Drug loading
DLS	Dynamic light scattering
DMEM	Dulbecco's modified Eagle's medium
DMF	*N*,*N'*-Dimethylformamide
DMSO	Dimethyl sulfoxide
DNA	Deoxyribonucleic acid
DOX	Doxorubicin
DPPC	Dipalmitoylphosphatidylcholine
dsDNA	Double stranded deoxyribonucleic acid
DTS	Deoxyribonucleic acid nuclear targeting sequences
ECACC	European Collection of Authenticated Cell Cultures
ECM	Extracellular matrix
EDC	Ethyl-3-(3-dimethylaminopropyl)-carbodiimide
EDTA	Ethylendiaminetetraacetic acid
EE	Encapsulation efficiency
EGCG	Epigallocatechin gallate
EGFP	Enhanced green fluorescence protein
EMA	European Medicament Agency
EPI	Epicatechin

USC UNIVERSIDADE DE SANTIAGO DE COMPOSTELA

EPR	Enhanced permeation and retention
Eq	Equation
ESI	Electrospray ionization
EtOAc	Ethyl acetate
EtOH	Ethanol
FACS	Fluorescent activated cell sorter
FBS	Fetal bovine serum
FDA	Food and Drug Administration
FIA	Flow injection analysis
FITC	Fluorescein isothiocyanate
FRAP	Fluorescence recovery after photobleaching
FSC	Forward scattering
GATG	Gallic acid-triethylene glycol
GOX	Glucose oxidase
GUV	Giant unillamellar vesicle
HEPES	4-(2-Hydroxyethyl)piperazine-1-ethanesulfonic acid
HOBt	1-Hydroxybenzotriazol
Hoechst 33258	Bisbenzimide H-33258
HPLC	High performance liquid chromatography
HRMS	High resolution mass spectrometry
HRP	Horseradish peroxidase
Hz	Hertz
IR	Infrared
iRNA	Interference nucleic acids
IS	Ionic strength
J	Coupling constant
LB	Lysogeny broth
LDA	Laser doppler anemometry
LP 2000	Lipofectamine 2000
LSCM	Laser scanning confocal microscopy
m	Multiplet

USC UNIVERSIDADE DE SANTIAGO DE COMPOSTELA

M	Molar
MALDI	Matrix-assisted laser desorption/ionization
MLO	Membrane-less organelle
mPEG	Methoxy poly(ethylene glycol)
mPEG-TK-PTX	Methoxy poly(ethylene glycol) -thioketal-paclitaxel
MPLC	Medium pressure liquid chromatography
Mp	Peak molecular weight
MPS	Mononuclear phagocyte system
mRNA	Messenger ribonucleic acid
MS	Mass spectrometry
Mn	Number average molecular weight
Mw	Weight average molecular weight
MW	Molecular weight
MWCO	Molecular weight cut off
N	Number of particles
NA	Nucleic acid
NaOAc	Sodium acetate
NHS	*N*-Hydroxysuccinimide
NMR	Nuclear magnetic resonance
NQO1	Quinone oxidoreductase I
NPC	Nuclear pore complex
N/P	Nitrogen to phosphorous ratio
OA-P(Asp-API)	Octadecylaminepoly(aspartate-1-(3-aminopropyl) imidazole
ON	Oligonucleotide
***o*PD**	*Ortho*-phenylenediamine
PB	Phosphate buffer
PBS	Phosphate buffer saline
PCLgTMC	Poly(caprolactone-gradient-trimethylene carbonate)
PDC	Polymer-drug conjugates
PDDA	Polydiallyldimethyl ammonium
PDLLA	Poly (D,L-lactide)

USC UNIVERSIDADE DE SANTIAGO DE COMPOSTELA

pDNA	Plasmidic deoxyribonucleic acid
PDI	Polydispersity index
PEG	Poly(ethylene glycol)
pGLU	Poly(glutamic acid)
pI	Isoelectric point
PIC	Polyion complex
PISA	Polymerization-induced self-assembly
PK	Pharmacokinetics
Polyplex	Polyelectrolyte complex
PTC	Paclitaxel
q	Quartet
quint	Quintuplet
R	Hydrodynamic radii
^{rel}D	Relative PEG density per particle
^{rel}N	Relative number of micelles
^{rel}S	Relative total surface area of micelles
RFU	Relative fluorescence units
RITC	Rhodamine B isothiocyanate
RNA	Ribonucleic acid
RNP	Ribonucleoprotein
ROI	Region of interest
rpm	Revolutions per minute
rt	Room temperature
s	Singlet
S	Total surface area of particles
SC	Synthetic compartment
SLS	Static light scattering
SOD	Superoxide dismutase
ssDNA	Single-stranded DNA
SSO	Splice-switching oligonucleotide
SSC	Side scattering

USC UNIVERSIDADE DE SANTIAGO DE COMPOSTELA

STEM	Scanning transmission electron microscopy
t	Triplet
td	Triplet of doublets
TEM	Transmission electron microscopy
TLC	Thin-layer chromatography
TMLBQ	Trimethyl-locked benzoquinone
TMZ	Temozolomide
TOF	Time of flight
U	Units
uPIC	Monomeric unit PIC
V	Volt
ZP	Z potential
2-FPBA	2-formylphenylboronic
2,3-DAP	2,3-diaminephenazine
Å	Amstrom
% PEG	Degree of PEGylation
δ	Chemical shifts
ε	Extinction coefficient
$\tau_{1/2}$	Half-Life time

USC
UNIVERSIDADE DE SANTIAGO DE COMPOSTELA

1. INTRODUCTION

The concept of nanotechnology, as it is currently understood, arose from the speech given by Richard Feynman at the 1959 annual meeting of the American Physical Society. During his talk, Feynman emphasized the importance of manipulating matter at the molecular scale, which represented the starting point of a new vision of the world.[1] Over the years, and thanks to the collective effort of a huge number of researchers worldwide, this field has evolved into a scientific discipline with significant implications for the future of our society. This concept has been extended across a wide range of research areas, leading to pioneering applications in intelligent sensors,[2] self-propelled particles,[3] and in the assembly of complex architectures such as lipid membranes (liposomes) or micelles.[4] Additionally, we are gaining a deeper understanding of the fundaments behind natural processes.[5]

Nevertheless, these great advances in nanotechnology cannot be understood without the evolution of polymer chemistry. The term polymer, derived from the Greek words: '*poly*' meaning many, and '*meros*' meaning part, refers to large molecules built up from numerous and smaller molecular units, named monomers. Polymeric scaffolds have been largely employed in the development of solar cells,[6] in the construction of highly efficient batteries,[7] in the engineering of sensors with enhanced sensibility,[2] and in the construction of novel biomaterials.[8]

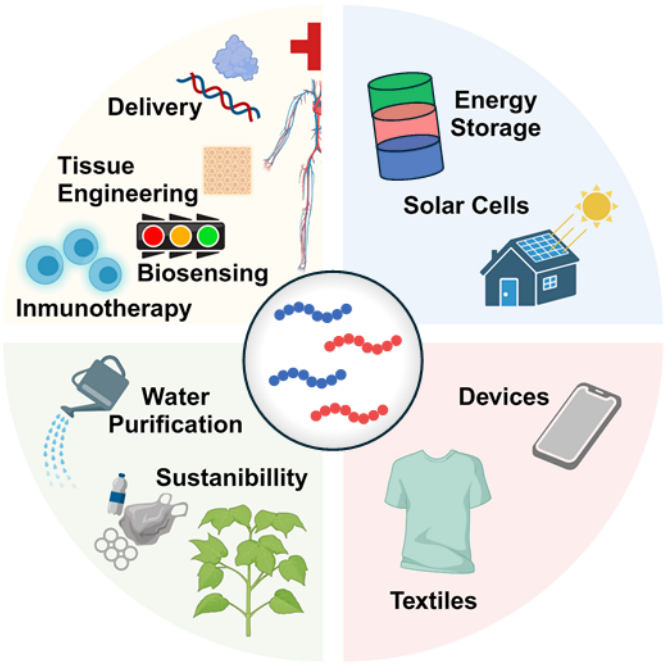

Figure 1. Schematic representation of applications of polymers in diverse areas and fields.

In fact, polymers have become promising candidates for developing efficient and safer drug delivery vehicles.[9] This term, whose origin and evolution will be discussed in the following section, arises from the application of nanotechnology in the treatment and diagnosis of different diseases. Over the years, the adaptability, ease of manufacture, and chemical variability of polymeric scaffolds have become powerful tools for tuning the properties of derived vehicles. In consequence, a wide array of polymeric structures has been discovered, characterized, and analyzed. Based on their structure, distinct types of polymers have been

designed. Linear homopolymers, characterized by a constant and uniform backbone, are the most commonly employed. The synthesis of different copolymers can be achieved through the introduction of two or more distinct monomers, thereby modifying the properties of the original scaffolds. Although the catalog of efficient, reproducible, and precise synthetic methods is growing every year,[10,11,12] achieving monodisperse products with an exact number of monomeric units remains elusive. In this context, dendritic structures have emerged as a promising option to overcome these limitations, thanks to the exceptional control over their structure and multivalency achieved during their preparation.

Apart from synthetic polymers, natural polymers represent the fundamental structures of natural living systems. Biopolymers produced by living organisms are responsible for a wide variety of vital processes, including the transmission of genetic information, the performance of vital functions, and the storage of energy within catabolic substrates. Although many classifications can be found in the literature, nucleic acids (NAs) and proteins are clearly differentiated from the rest. These share properties such as:

- Spontaneous organization and folding into intricate structures with minimal stability.
- Ability to resist hydrolysis and protect their partners through folding and heterogeneous assembly.

The aforementioned biopolymers are fundamental and active components of natural cells and, although the debate is still open, both have been postulated as potential starting points of life.[13] One theory, holds that abiotically synthesized ribonucleic acid (RNA) strands could have served as both genetic material and catalysts, thereby constituting a foundational unit of evolution. In contrast, alternative studies suggest that life might have emerged in an ecosystem where proteins and NAs could cross-catalyze each other's formation, following the principle of molecular mutualism.

As described above, polymeric structures have played crucial roles in the past, present, and future of our society. The following sections will explore the applications of polymers across various research fields.

USC
UNIVERSIDADE DE SANTIAGO DE COMPOSTELA

1.1 DRUG DELIVERY

1.1.1 Origin of Drug Delivery

In recent decades, drug delivery (DD) has evolved into a research discipline integrating fundamental fields such as biology, medicine, chemistry, pharmaceutical research, physics, and materials science. The efficacy of pharmacological compounds is often constrained by factors such as pharmacokinetics (PK), distribution, and dosage. Thus, drug delivery systems (DDS) aim to enhance their therapeutic effectiveness by facilitating their targeted transport and release at specific locations within the body. Despite numerous compounds showing positive *in vitro* results, challenges like poor water solubility, nonspecific effects, and inefficient biodistribution hinder their clinical application. Consequently, DDS represent a promising solution to address these limitations,[14] resulting in an increasing number of approved treatments after decades of research. [15]

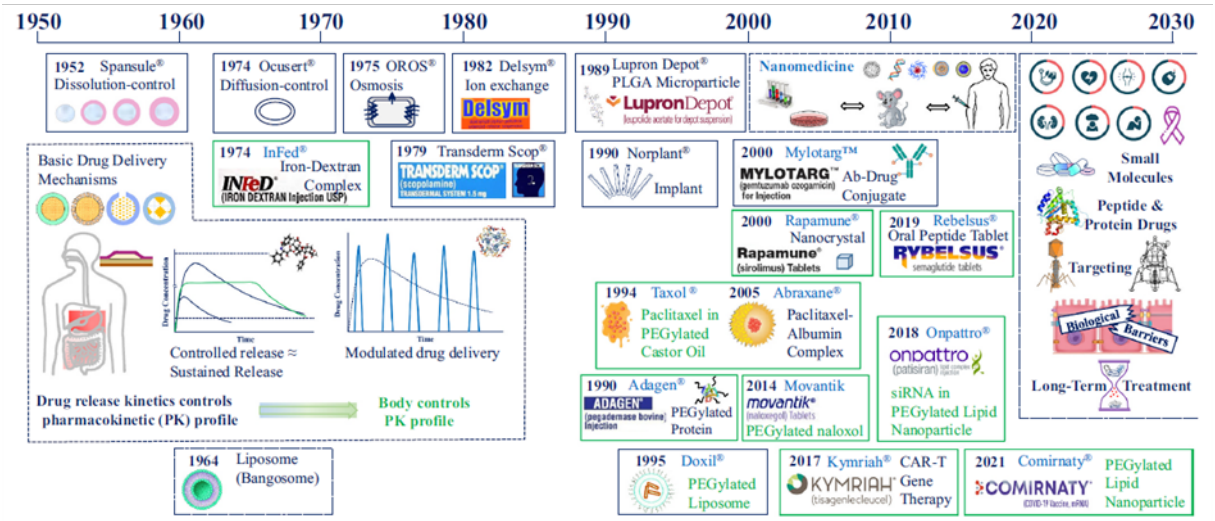

Figure 2. Evolution of drug delivery systems through the introduction of FDA-approved drug products from the Spansule® oral controlled release formulation to the lipid nanoparticle formulations for COVID-19 vaccine delivery. Adapted with permission from reference 16. Copyright 2022 Elsevier.

From an historical perspective, the field of DD has evolved from sustained release technologies to nanometric systems (Figure 2).[16] In the early stages, researchers were focused on developing controlled release systems (CRS) engineered to enable drug administration during long periods of time (weeks, months). The main advantage of CRS relies on mitigating the inherent fluctuations in drug concentration associated with standard administration, thereby maintaining consistent and therapeutic drug levels. The birth of this methodology dates back to 1952, when the sustained release technology Spansule® was launched. Since then, multiple therapies involving CRS based on the use of biodegradable polymeric implants have been developed, resulting in the introduction of innovative treatments for multiple pathologies, including psychotic disorders, and various types of cancer.[17]

Nevertheless, as the therapeutic landscape evolved, delivery systems underwent adaptations to address emerging demands. The introduction of nanometric DDS represented an inflexion point in the field, opening new and promising research avenues. While most CRS were designed with the sole objective of controlling the release of the entrapped drugs, the introduction of nanometric DDS resulted in improved biodistributions, PK, drug solubility and stability towards degradation, as well as notable reductions in side-toxicity values. A determinant moment for this trend was the approval of Doxil® in 1995.[18] This vehicle, based on liposomes,

facilitated the delivery of the antineoplastic drug doxorubicin (DOX), improving its half-life in blood circulation and hampering its acute cardiotoxicity.

1.1.2 Engeeniring Drug Delivery Systems

Although multiple materials, from macromolecules[19] to supramolecular architecures,[20,21] have been employed in the construction of nanometric DDS, high aqueous solubility, biocompatibility, or drug protection are some fundamental parameters that must be accomplished. However, over the years, the list of factors to consider when developing novel carriers keeps growing. The subsequent section will examine the key structural parameters essential for a successful carrier.

1.1.2.1 Surface Properties

A common limitation of nanosized DDS is their inability to deliver sufficient amounts of the therapeutic cargo to the target site due to nonspecific accumulation. After intravenous injection, the mononuclear phagocyte system (MPS) can sequester DDS in the liver and spleen.[22] The process usually starts with the opsonization of the DDS by the incorporation of proteins and plasma macromolecules. After molecular absorption, the conjugated aggregates are attached to the receptors on the surface of phagocytes, which finally drive the degradation of DDS.[23] In this context, different methodologies have been designed to prevent the formation of the protein corona. These involve the introduction of an external layer to prevent the adhesion of plasma proteins, thereby inhibiting uptake by the MPS. Among the reported approaches, the most employed strategy involves grafting poly(ethylene glycol) (PEG) chains onto the surface of DDS, often referred to as PEGylation. PEG is a hydrophilic polymer approved by the Food and Drug Administration (FDA) characterized by a reduced toxicity and immunogenicity, as well as a stealth character for increased solubility and circulation times in the blood stream.[24] PEG superficial chains form associations with water molecules, leading to the construction of a hydrating layer that is ultimately responsible of the protective character of PEGylation. An archetypical example of this methodology is the already mentioned Doxil®, which, thanks to the PEG stealth effect, is able to enhance the stability and PK of DOX. Other strategies rely on coating the DDS with different cell membranes. As an example, Parodi *et al*. developed a biomimetic particle coating consisting of cell membranes isolated from leukocytes.[25] Upon surface functionalization, particles showed about a ten-fold decrease in protein adsorption to the surface, which consequently resulted in less particle uptake in phagocytic cells. When the wrapped DDS were examined in murine models, functionalized particles displayed lower accumulation in the liver after systemic administration, which finally led to an enhanced concentration of particles in a model of melanoma. This procedure also represents an attractive option for targeting. For example, particles wrapped with platelet membranes display those ligands present on native platelets, allowing them to target injury sites and being accumulated around activated platelets.[26]

USC
UNIVERSIDADE DE SANTIAGO DE COMPOSTELA

1.1.2.2 Targetting

Over time, our understanding of the biological processes behind every disease is growing every day, and in consequence, novel therapeutic targets are unlocked. However, compounds against these targets often fail in later stages of development.[27] The minimal therapeutic impact observed following nanoparticle delivery is a direct consequence of the nanoparticle's inability to overcome many of the biological barriers it must face before reaching the target tissue. Thus, achieving successful delivery remains a challenge in the field. In the last decades, multiple paths have been pursued to address this issue.

Local Delivery. This strategy offers the simplest way to deliver drugs to a diseased tissue[18] and consists in introducing the DDS directly into the target location. Although it is limited by the accessibility of the affected tissue, localized therapies such convection enhanced delivery (CED) have been successfully employed for the treatment of localized tumors.[28]

Passive Transport or off-Target Delivery. This strategy relies on the use of DDS targeting diseases displaying the enhanced permeation and retention (EPR) effect. Described by Maeda *et al*. in 1986,[29] the EPR effect is based on the differences between tumoral and healthy tissues (Figure 3). These include angiogenesis, increased vascularization, altered tissue drainage, and a significant increase in permeability mediators. The combination of these processes constitutes the EPR effect and have become a cornerstone in DDS research for cancer therapy. Essentially, macromolecules are allowed to easily permeate tumor tissues due to the hypervascularization and, owing to the lack of tissue drainage, they remain retained for extended periods.

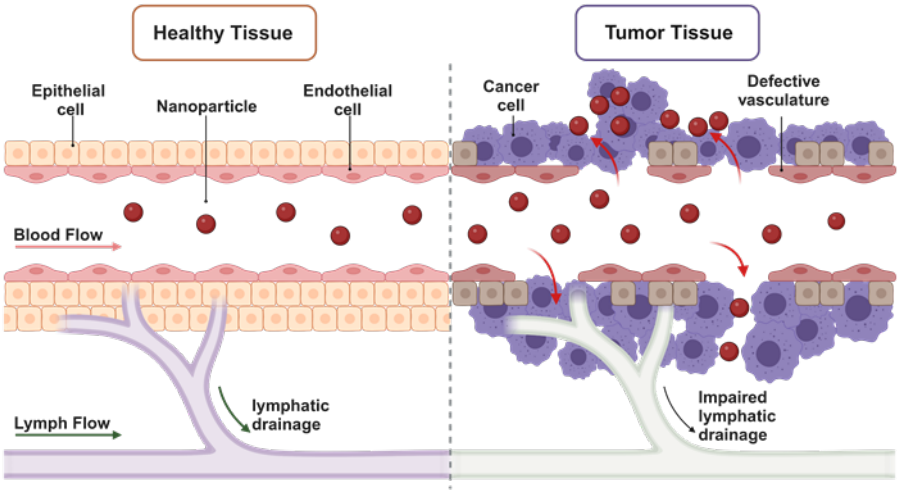

Figure 3. Schematic representation of the differences between tumoral and healthy tissues, and the EPR effect.

Active Transport or Targeted-Delivery. Active targeting represents an advanced form of delivery in which the surface of DDS is decorated with targeted ligands such as vitamins, glucose, antibodies, or aptamers, to enhance their uptake by the targeted cells (Figure 4).[30] Although targeting has been shown to enhance the pharmacological activity of many DDS, it is not considered a definitive solution. Due to the variation of disease markers between affected cells, and among potential patients, the identification of a target should be performed on a case-by-case basis at different disease stages. Furthermore, the employment of general targets can lead to nonspecific uptake by healthy cells, coming back to a form of passive transport.[31]

USC UNIVERSIDADE DE SANTIAGO DE COMPOSTELA

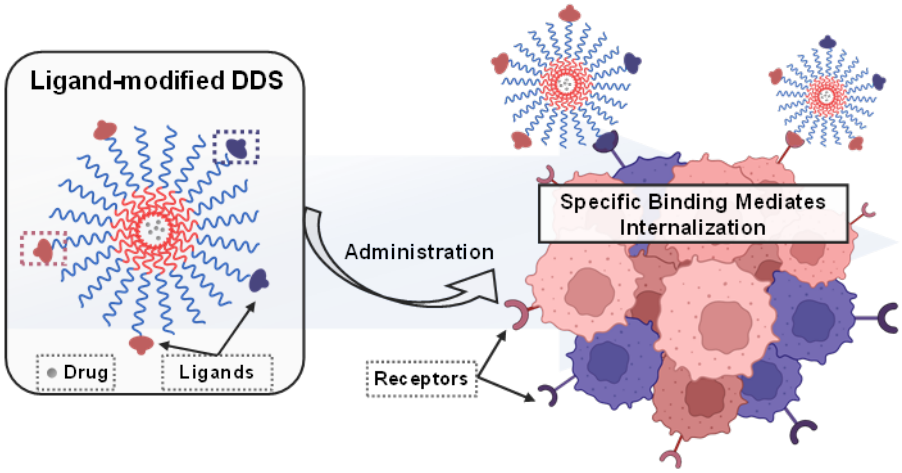

Figure 4. Schematic representation of the active transport of a DDS through the incorporation of different ligands.

1.1.2.3 Physico-chemical Properties of DDS

DDS size. The size of a DDS represents an important design parameter to consider regarding the *in vivo* systemic administration of the vehicle. While particles with diameters below 5 nm rapidly undergo renal clearance after intravenous administration, those ones with dimeters in the micrometric scale have demonstrated accumulation in the capillaries of the lungs. Intermediate sized DDS, those ones with diameters above 200 nm are normally trapped during splenic filtration and the ones with diameters below 100 nm can be easily sequestered in the vascular fenestrations of the noncontinuous endothelia of the liver (50-100 nm). Taken together, those DDS with sizes around 100 nm are considered better candidates for improving circulation half-lives, which also increases their tendency to extravasate through fenestrations in tumor vasculature.[32]

Particle shape. Geometry affects hemorheological dynamics, cellular uptake, and *in vivo* fate of DDS. In terms of internalization, discoidal particles exhibit unique margination dynamics that favor vessel wall interaction in comparison with spherical particles (Figure 5).[33] Regarding the circulation half-times, Discher and co-workers[34] have demonstrated that filomicelles have long-circulating lifetimes (>1 week after administration) compared with their spherical counterparts (2–3 days), owing to their tendency to align with blood flow. Overall, particle shape should be also considered and modulated, if feasible, for obtaining more efficient DDS.

Surface charge. While DDS with cationic surfaces are rapidly cleared from circulation by the MPS, DDS with neutral and negative surface charges have shown reduced adsorption of serum proteins, resulting in longer circulation half-lives.[35] On the other hand, positively charged nanoparticles have a higher rate of nonspecific uptake in most cells. Interestingly, McDonald and co-workers[36] showed that cationic liposomes are preferentially bound and internalized by tumor-associated angiogenic endothelial cells compared with normal vasculature, a phenomenon also observed in sites of chronic inflammation. Thus, for effective nanoparticle delivery to tumors, a neutral or slightly negative nanoparticle surface charge is usually preferred upon intravenous administration, but a switch to a positive charge upon arrival at the tumor site can enhance their performance. However, there is no consensus regarding the issue of charge, as cationic DDS can become entrapped within the altered extracellular matrix (ECM), thereby impeding their capacity to deliver cargo to the target cells.

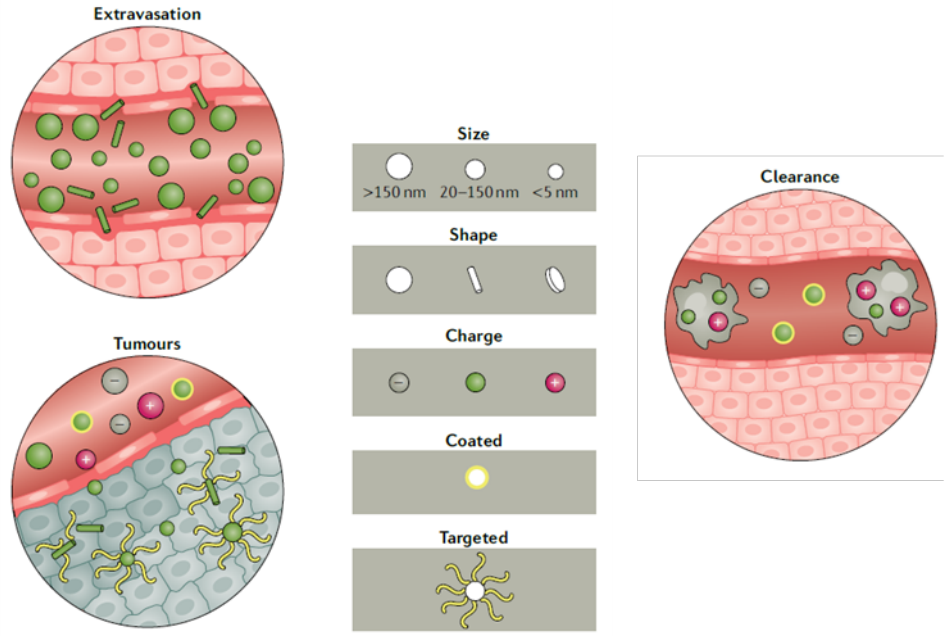

Figure 5. Schematic representation of the distribution of nanoparticles based on their architecture. Larger, spherical nanoparticles stick to vessel walls, while rod-shaped ones exit vessels more readily. Uncoated or positively charged particles are cleared faster. For local distribution, rod-shaped, neutral, or positive, and targeted nanoparticles penetrate tumors better. Adapted from reference 31. Copyright 2021 with permission from Springer Nature.

1.1.3 Polymers in Drug Delivery

To adhere to the aforementioned guidelines and to modulate DDS for a deeper understanding of these structure-activity relationships, versatile platforms for DDS design are needed. Among the materials employed in the construction of DDS, polymeric scaffolds have emerged as promising candidates due to their biodegradability, water solubility, biocompatibility, and stability. The first polymer-based, therapeutic vehicle was a polymer-drug conjugate for mescaline delivery reported in 1955 by Jatzkewitz,[37] and this approach represented the starting point of a large array of DDS involving polymeric structures.

Polymer-based DDS can be prepared from both natural and synthetic materials, enabling the creation of diverse structures with tailored properties. The structural versatility of polymers permits different interactions between the carrier and the active cargo, which can be encapsulated within the DDS core, entrapped in the polymer matrix, chemically conjugated to the polymer, or displayed along the surface. Such flexibility allows the delivery of various types of cargo, including hydrophobic and hydrophilic compounds with different molecular weights.[38,39] Up to date, several types of polymeric scaffolds have been reported as effective DDS, some of which further described in the present section.

Polymer-Drug Conjugates (PDCs). Generally, PDCs consist of a water-soluble polymeric carrier with the therapeutic cargo attached via a cleavable spacer, which often includes a targeting moiety (Figure 6). This strategy has been translated into commercially available formulations as Oncaspar, or into technologies in clinical trials such Prothecan.[37,40]

USC UNIVERSIDADE DE SANTIAGO DE COMPOSTELA

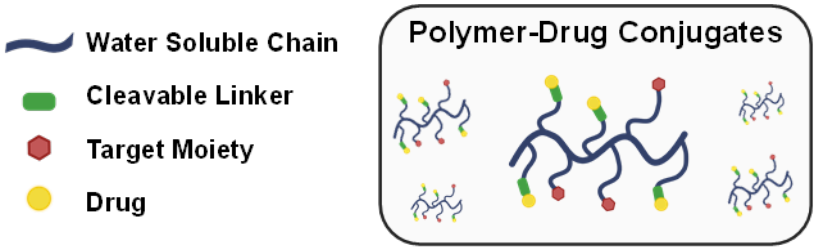

Figure 6. Schematic representation of a polymer-drug conjugate.

Polymersomes. These artificial vesicles, with membranes made from amphiphilic block copolymers (Figure 7), can be considered the polymeric analogs of liposomes. Polymersomes are known for their improved stability and cargo retention efficiency, [41] which makes them effective DDS. They have been the focus point of many research and, as a result, have formed the basis of sophisticated and successful DDS.[42,43]

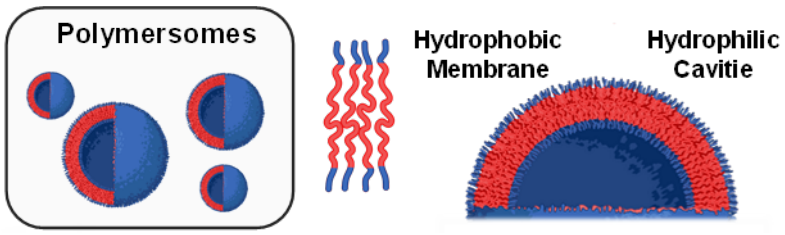

Figure 7. Schematic representation of a polymersome.

Polymeric Micelles. These are supramolecular architectures typically formed by the spontaneous arrangement of amphiphilic block-copolymers (Figure 8). Once the critical micelle concentration (CMC) of the polymer is reached, polymeric chains self-assemble into ordered aggregates, creating hydrophobic cores surrounded by a hydrophilic shell. Research into this self-assembly process highlights the superior stability of polymeric micelles compared to their surfactant-based counterparts.[21] Prove of their role as DDS has resulted in therapeutics such as Genexol® [PM], which consists of paclitaxel (PCT) encapsulated in methoxy-PEG: poly (D,L-lactide) (mPEG:PDLLA) polymeric micelles with sizes between 20 and 50 nm. This formulation has been approved for the treatment of metastatic breast cancer in South Korea and several other countries, and its currently under clinical trials in the US.[44]

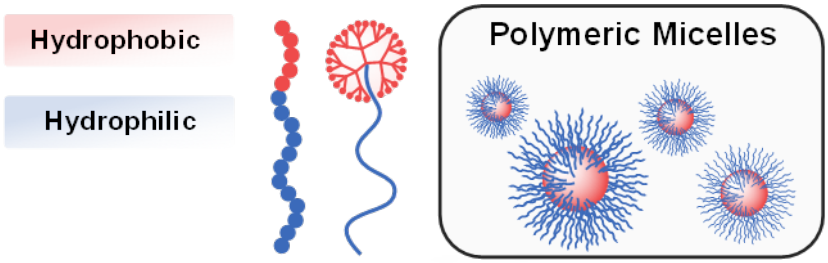

Figure 8. Schematic representation of a polymeric micelle.

Dendrimers. First described by Vötgle, Newkome[45] and Tomalia,[46] dendrimers are synthetic, tree-like, and monodisperse macromolecules characterized for having a globular architecture in solution. Dendrimers are composed of branched repeating units emerging radially from a central core. Along the dendritic structure, three differentiated parts can be distinguished: i) the core, responsible for the three-dimensional shape of the dendrimer, ii) the internal ramifications, and iii) the periphery of the dendrimer, which can be decorated with a large array of functional groups (Figure 9B).

USC
UNIVERSIDADE DE SANTIAGO DE COMPOSTELA

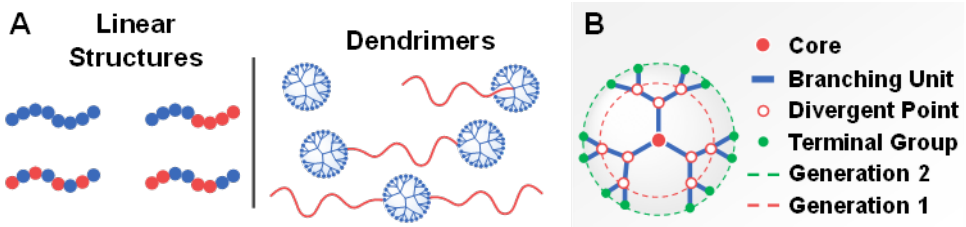

Figure 9. Schematic representation of diverse polymeric (left) and dendritic structures (right) (A). Description of the inner structure of a dendrimer (B).

The precise control over molecular weight, shape, and terminal groups achieved during their synthesis allow dendrimers to be specifically tuned for the treatment of a targeted disease. Thanks to their structure, drugs can be either displayed bounded on the surface[47] or sheltered within the internal cavities.[48] Additionally, dendrimers can also serve as building blocks for the construction of polymeric DDS. Thus, in the last decades, linear-dendritic block copolymers have been prepared and found wide application in the biomedical field, particularly for the design of DDS when incorporating linear PEG chains.[49] In this context, our research group has a large background in studying the biomedical applications of Gallic Acid-Triethylene Glycol (GATG) dendrimers and block-copolymers.[50] This dendritic family, first introduced by Roy *et al.*,[51] is characterized by a high solubility, ease of modulation, and enhanced stability. Regarding the impact of the dendritic structure, our group have proven that linear-dendritic block-copolymers overcome their linear counterparts when assembling polyion complex (PIC) micelles.[52] The stability of these micelles, formed by electrostatic interaction in aqueous media between oppositely charged block copolymers in a stoichiometric charge ratio, highly depends on the ionic strength (IS) of the aqueous medium. The outstanding stability obtained by the incorporation of dendritic units (up to 3 M NaCl) in comparison with linear polymeric chains (150 mM NaCl), highlights the beneficial outcomes of branched structures.

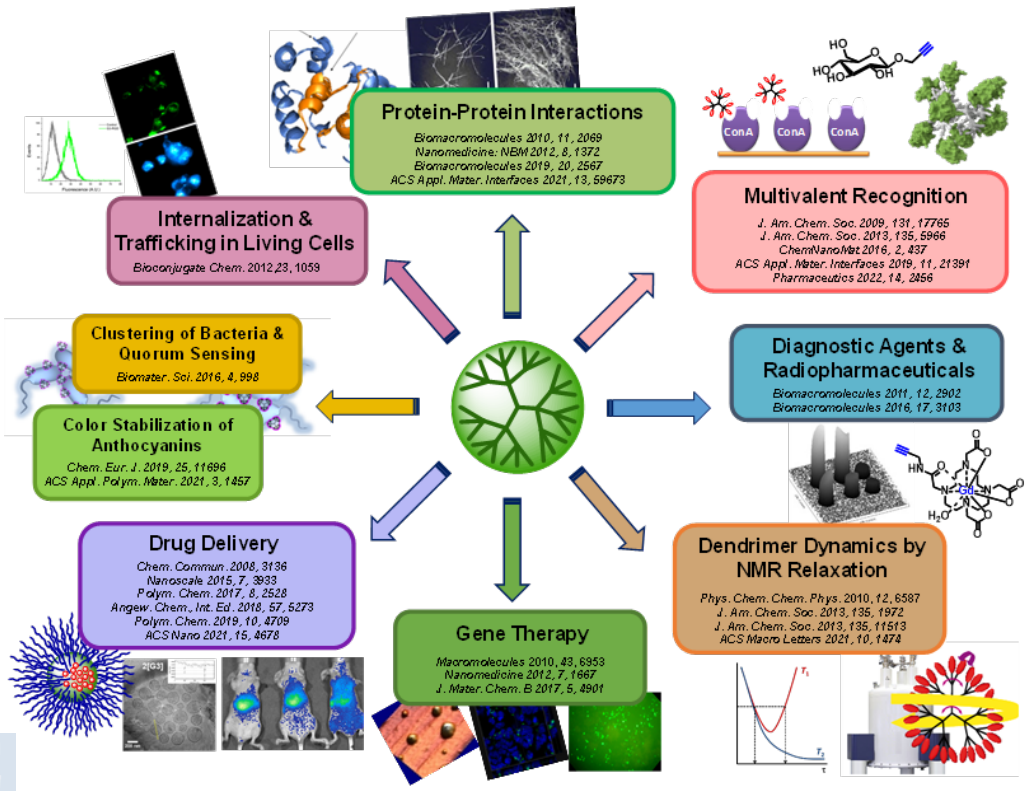

Figure 10. Diagram illustrating the primary biomedical applications of GATG family dendrimers developed by our research group.

1.1.4 Smart Polymers for DDS

The preceding sections highlight the significant advancements in polymeric drug delivery over the last few decades. Starting with the development of CRS, the field has progressed to finely engineered carriers capable of delivering therapeutic cargo in specific locations. However, despite the remarkable efforts made, particularly in cancer therapy, the number of FDA-approved DDS remains limited.[53] This limitation may arise from issues such as ineffective targeting, premature cargo release, or rapid particle clearance. Thus, in recent years there has been increased interest in smart delivery scaffolds. These active DDS are able to interact with biological environments and release cargo in response. Achieving such control demands not only a profound understanding of the properties of the target site, but also a deep comprehension of the molecular interactions that trigger the response. Over time, scientists have taken advantage of different stimuli to promote the release of drugs: temperature, pH, redox potential, sound, or light are the most commonly employed examples. Among them, those ones based on interactions between polymers and the particular characteristics of the targeted tissue will be discussed below.

Regarding the characteristics of the tumoral environment, its altered metabolism leads to uncommon levels of different enzymes. In a recent report by Wang *et al*. advantage was taken of the upregulated quinone oxidoreductase I (NQO1) to produce redox sensitive polymeric micelles.[54] This enzyme reduces quinones to hydroquinones, producing highly oxidative stress and elevated levels of reactive oxygen spices (ROS) in solid tumors. In this study, the authors employed the redox chemistry of trimethyl-locked benzoquinone (TMLBQ) to prepare smart scaffolds. The copolymers were expected to eliminate lactones under redox conditions, leading to the exposure of amino groups, which initiate intramolecular cyclization and trigger the depolymerization of the structure. This technology was translated into smart DDS by encapsulating DOX. It was proved that the micelles could rapidly release DOX under intracellular redox conditions. Furthermore, *in vitro* studies demonstrated that release can be hampered by inhibiting NQO1 in different cell lines. However, the overexpression of some enzymes within solid tumors has been also targeted to design DDS with enzyme -degradable segments that can promote cargo release in the tumoral environment. As an example, Li *et al.* have recently designed enzyme-sensitive, and amphiphilic PEGylated dendrimer-paclitaxel prodrug-based nanoparticles in which, the oligopeptide Gly-Phe-Leu-Gly (GFLG) was used to bind the dendritic structure with PTC.[55] Degradation of this linker by cathepsin B, a lysosomal cysteine protease overexpressed in tumor cells such as breast cancer, triggered cargo release. The carefully designed polymers allowed prolonged circulation times, tumor accumulation, and significantly higher toxicity towards tumoral cells in comparison with healthy tissues.

Another peculiarity of solid tumors is the slight decrease in pH they typically exhibit. Tumor cells often undergo rapid and continuous growth, which implies an increased energy requirement for survival. Therefore, they tend to employ rapid energy-producing metabolic routes, such as the catabolism of carbohydrates, ATP, and amino acids. These pathways promote the release of protons into the extracellular environment, which often diffuse from the interstitial space till the blood vessels for being eliminated. However, due to the lack of drainage observed in tumoral tissues, these protons tend to be temporarily and locally accumulated, resulting in the more acidic pH of solid tumors (6.0 - 6.5).[56] In consequence, many DDS have been tailored to release the therapeutic cargo in response to pH variation. Wang *et al.* designed a zwitterionic polyacetal dendrimer, *via* alternant aza-Michael addition and thiol–ene click reactions, able to promote DOX encapsulation and pH-triggered release.[57] In this system, pH

USC DE COMPOSTELA

variations induced not only the rupture of the polyacetal scaffold, but also a charge reversal transformation on the superficial zwitterionic chains. Thanks to this tailored design, the systems showed hampered protein adhesion, high biodegradability, and pH responsiveness, highlighting the role of structural-activity relations in the field of polymeric drug delivery. More recently, Li *et al.* developed a pH/ROS cascade-responsive prodrug micelle with long-circulating, deep tumor-penetration, cancer cell active targeting, and self-accelerated drug release for effective drug delivery.[58] This micelle, was formed from four parts: a ROS-responsive polymeric prodrug (mPEG-thioketal-paclitaxel (mPEG-TK-PTX), a tumor tissue penetration and cancer cell-targeting part (iRGD peptide),[30] a pH-responsive part for endosomal escape based on octadecylaminepoly(aspartate-1-(3-aminopropyl) imidazole) (OA-P(Asp-API)), and a ROS generation agent (β-Lapachone). *In vitro* and *in vivo* experiments demonstrated that these micelles could be actively targeted to the tumor site, penetrate into tumor tissue, escape from lysosomes, and show self-amplified drug release. This study represents a remarkable example of how the structure of the polymer can vary the activity of the final DDS. Furthermore, it facilitates the introduction of the concept "endosomal escape", that although has not significantly impacted the delivery of small hydrophobic drugs, it has hindered the development of gene delivery carriers, which will be the focal point of the following section.

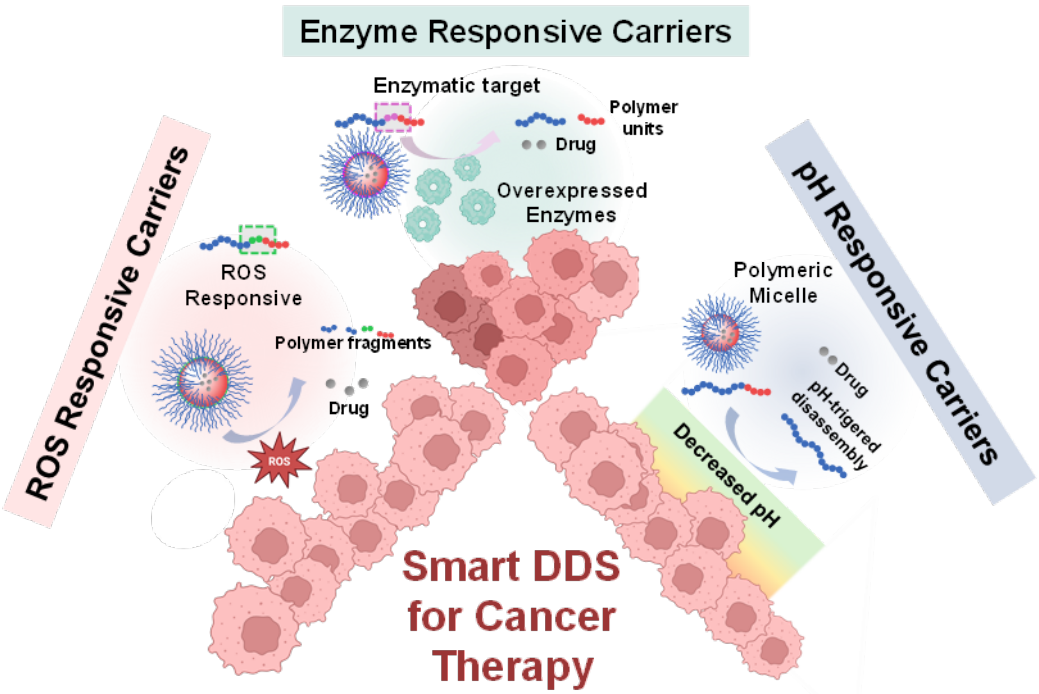

Figure 11. Schematic representation of polymeric micelles able to response towards variations in redox conditions (left), tumor overexpressed enzymes (middle), and pH (right).

USC UNIVERSIDADE DE SANTIAGO DE COMPOSTELA

1.2 Gene Delivery

1.2.1 Origin and Current Status of Gene Delivery

The preceding section provided a comprehensive overview of the delivery of small therapeutics. Nevertheless, the basic principles derived from this research have been extended to facilitate the transport of other therapeutic cargoes, including proteins, antibodies, and NAs. Notably, NAs-based therapies provide promising new therapeutic avenues that surpass the limitations of conventional treatments.[15] They have promoted significant advancements in treating cardiovascular, infectious, and monogenic diseases, as well as various types of cancer.[59] Such accomplished goals have positioned gene therapy as the third major therapeutic platform, alongside small bioactive molecules, and biologic compounds.[60]

Therapeutic NAs can perform their function at different stages along the gene expression process (Figure 12). The introduction of DNA represents the origin of the "gene therapy" concept. It consists of incorporating exogenous DNA into the target cells in order to achieve the expression of a therapeutic protein. Similar effect is pursued when introducing a messenger ribonucleic acid (mRNA), that intervenes in an advanced stage of gene expression. Due to the advances in biological sciences, a profound understanding of the mechanisms that regulate gene expression has been achieved. Consequently, novel NAs, known for regulating the expression of genes, have been employed as effective therapeutics. As an example, during the splicing process, while some introns are deleted from the primary RNA to obtain mature and functional NAs, anormal exons can be also removed by the action of splice-switching oligonucleotides (SSOs), that can join those exons triggering alternative splicing to the following ones. In more advanced stages, antisense oligonucleotides, and interference nucleic acids (iRNA), can inhibit the target mRNA translation by steric effects and/or by RNA degradation. Thus, their tailored design, and effective cytosolic delivery, can lead to the inhibition of the targeted mRNA.[61]

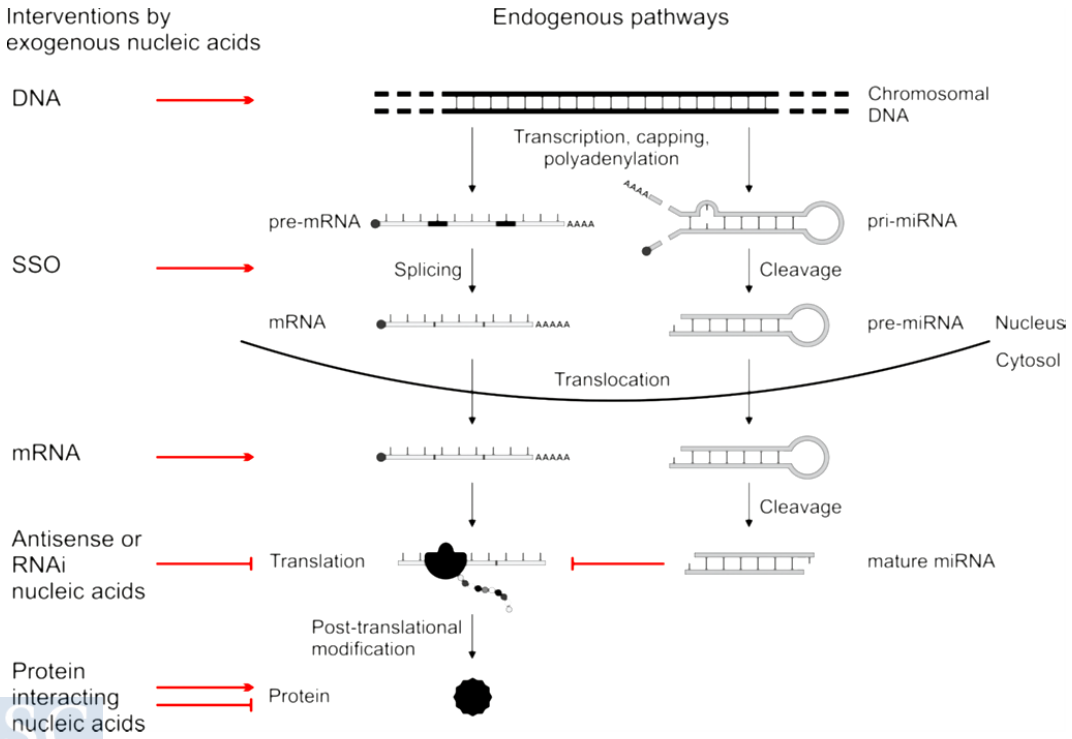

Figure 12. Schematic illustration of the endogenous pathways through which various NAs payloads are processed. Adapted with permission from reference 61. Copyright 2015 American Chemical Society.

The efficient delivery of therapeutic nucleic acids (NAs) to target cells and tissues is a critical step in gene therapy, achievable either via viral or nonviral vectors. Viral vectors, extensively researched over the past decades, are highly effective for NA delivery due to their evolved tropism for specific cell types and their ability to transport payloads directly to the nucleus. Numerous drug products employing recombinant viral vectors for *in vivo* transgene delivery have gained approval, with adeno-associated viral (AAV) vectors being the most prevalent exponent. AAV is a small, nonenveloped parvovirus (~25 nm) with a ≈ 4.7-kb single-stranded DNA (ssDNA) genome. Recombinant AAV vectors used for delivery typically retain their original capsid structure, while replacing viral coding sequences with therapeutic gene expression cassettes.[62] This strategy maximizes their packaging capacity and diminishes immunogenicity.[63] Because AAV tropism has a broad range, AAVs can be used for targeted transduction in a large variety of tissues, potentially providing cellular specificity. Receptor-bound AAVs internalize cells by endocytosis, are released into the cytosol by acidification of the early endosome, and, following perinuclear accumulation, can enter into the nucleus.[64] The first commercial product employing AAV-based vectors (and first gene therapy for genetic disease), Alipogene tiparvovec (Glybera, uniQure), was approved by the European Medicament Agency (EMA) in 2012 for the treatment of recurrent or severe pancreatitis in patients with a rare genetic lipid disorder. More recently, in 2016, the FDA approved the use of an antisense oligonucleotide for the treatment of the spinal muscular atrophy.[65]

However, although the obtention of promising results, various safety concerns have arisen. AAV-based gene therapies have been linked to significant side effects, including hepatotoxicity, genotoxicity, and thrombotic microangiopathy.[66] These effects are mainly motivated by the high doses of viral vehicles needed to treat some target diseases, which increase the risk of adverse events. Beyond their nonideal safety profiles, viral vehicles also pose financial and logistical challenges during manufacturing, resulting in expensive costs and long production times.[67]

1.2.2 Biological Barriers

Based on the above, there is a pressing demand for more affordable and safer nonviral gene delivery carriers. These alternatives primarily employ cationic polymers, peptides, and lipids, which electrostatically interact with NAs to form various types of particles that offer further advantages such as a large payload accommodation, and redosing.[68] However, in comparison to viral vectors, which have naturally evolved to efficiently express their genes in host cells, nonviral vectors struggle to overcome biological barriers, leading to substantially lower transfection efficiencies.

As discussed in the previous section, drug or gene carriers need to be carefully engineered to surpass those barriers. While targeting, surface properties, and DDS architecture are already-considered factors, additional parameters must be balanced in the context of nonviral gene delivery vectors to facilitate the successful delivery of NAs.

1.2.2.1 Carrier and Cargo Degradation

USC SANTIAGO

Opsonization of DDS constitutes the first step towards DDS sequestration by the MPS (Section 1.1.1.2). Although particle-protein association relies on different attractive forces, the cationic character commonly found in gene carriers as well as the high concentration of anionic

proteins in blood and serum are responsible for protein corona formation, which ultimately causes colloidal systems to aggregate or be sequestrated by the MPS.[69] Thus, while the introduction of positively charged groups can facilitate NAs encapsulation by interaction with the negatively charged phosphate groups, they can compromise DDS stability under physiological conditions. Other consequences of the nonspecific binding of the complexing molecules with serum proteins, or the proteoglycans and glycosaminoglycans found in the ECM, are the displacement of the cargo and the degradation of the particle.[70] Another limitation can arise from NAs degradation in biological media via serum nucleases; thus, nonviral vectors need to prolong the half-life of DNA in circulation. The ability of NAs to activate the immune system after *in vivo* administration also represents a hurdle to obtain successful gene therapies. As reported by Reineke *et al.*[67] the major immune responses caused by the introduction of exogeneous NAs, are the activation of toll-like receptors and the complement system, which can trigger an innate immune response after detecting foreign material. Among nonviral vectors, polymeric scaffolds have demonstrated great potential to avoid the aforementioned limitations. While undesirable interactions can be avoided by introducing a protective polymeric layer or by the introduction of charge reversal polymers, the activation of the immune response has been seen to decrease by reducing the number of unpaired cationic charged units. Herein, PEGylation emerges as a common solution for both issues, as it can provide stealth against protein absorption and also shields the DDS surface charge.[71]

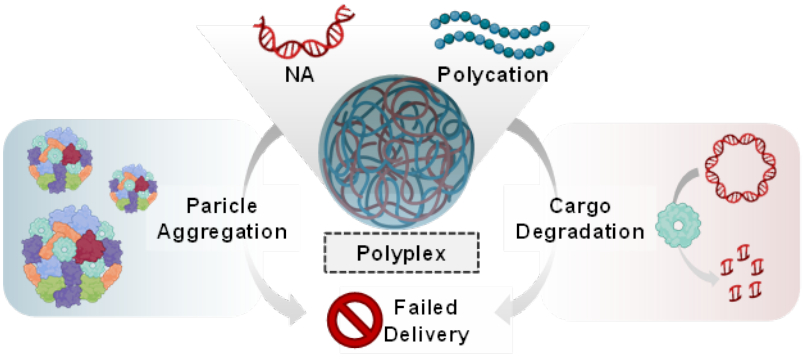

Figure 13. Schematic representation of the degradation of gene delivery carriers.

1.2.2.2 Cytotoxicity

For effective gene delivery, achieving maximal transfection efficiency while minimizing cytotoxicity, is imperative. Thus, cellular toxicity stands as an important parameter to consider when designing novel gene carriers.[72] The positive charges that allow the complexation and efficient cytosolic delivery of NAs are also often involved in cytotoxicity issues, primarily due to their interactions with negatively charged membranes and proteins. In particular, its toxicity is known to be caused by the disruption of the mitochondrial integrity. In addressing these challenges, the addition of shielding layers to cationic polymers has shown promise in mitigating toxicity during transfection.[67]

1.2.2.3 Cellular Internalization

After binding to the cell surface, either by electrostatic or tailored interactions, polyplexes need to be internalized to deliver their cargo (Figure 14). It is known that most

USC
UNIVERSIDADE DE COMPOSTELA

polyplexes enter cells by endocytosis,[67] however determining the endocytic pathway represents a major challenge in the field. Many studies have reported the use of inhibitors of specific routes to identify how a particular system internalizes in a certain cell type. Nevertheless, giving the diversity of employed materials, cargos, cells, and environmental conditions, a specific path cannot be determined.[73]

1.2.2.4 Endosomal Escape

With few exceptions, most endocytic processes direct polyplexes towards the endosomes. Initially, following internalization via endocytosis, polyplexes are sequestered into early endosomes. Subsequently, two potential trajectories can be followed. In the first trajectory, polyplexes are recycled back to the cell surface for exocytosis. In the second trajectory, they progress to late endosomes, which undergo gradual acidification through the action of adenosine triphosphatase (ATPase) proton pumps (pH 6.0−4.8). These late endosomes eventually merge with lysosomes, whose acidic lumen and high hydrolase content facilitate the degradation of the cargo.[74] Thus, the success of gene delivery vectors is strongly related to their ability to escape from the endosomal compartment. This process has constituted a bottleneck for the field of gene therapy,[75] and in consequence, significant effort has been dedicated to developing and adapting polymer-based systems to overcome this obstacle. Although it is a controversial area of debate, the "proton-sponge" effect has been the most widely accepted hypothesis to explain the mechanism of endosomal escape.[76] This hypothesis was based on the observation that carriers possessing titratable cationic groups, able to be protonated in response to pH variations within the late endosomes, promoted higher transfection efficiencies. Briefly, the hypothesis suggests that during the active acidification of vesicles by the ATPase pumps, titratable groups along the polymeric structure will absorb protons, leading to an uncontrolled accumulation of chloride counterions and the subsequent elevation of osmotic pressure within the vesicle, that ultimately results in its rupture. However, many reports have postulated some variations due to the lack of experimental evidence to support the latter part of the theory. Recent hypotheses rely on a different mechanism, which involves a polycation-membrane interaction. As recently reviewed by Monnery[73] and Reineke *et al.,*[67] endosomal escape might be promoted as a consequence of the interaction between polycations and the endosomal membrane. This interaction would be performed not only by those chains complexed within the polyplex, but also by the free polymeric chains engulfed with the carrier.

1.2.2.5 Diffusion to Nuclei

The nucleus of the cell is contained by a phospholipid bilayer envelope that consists of two separate membranes (outer and inner) interspaced by the perinuclear space. These membranes are fused at multiple points by protein pores, named as nuclear pore complexes (NPCs).[77] Once knowing that complexed NAs are unable to cross the NPCs, their transport will depend on their structure. Although low molecular weight (MW) cargo can cross the NPC by passive diffusion, large payloads such plasmids need to be actively transported into the nucleus. For large NAs, expression in dividing cells greatly surpasses that in nonmitotic cells owing to the disintegration of the nuclear membrane, which facilitates nuclear uptake. To enhance nuclear transport in nondividing cells, some strategies such as affixing nuclear localization signals (NLS) or integrating DNA nuclear targeting sequences (DTS) are employed to recruit importins, which facilitate the passage of the plasmid through the NPCs.

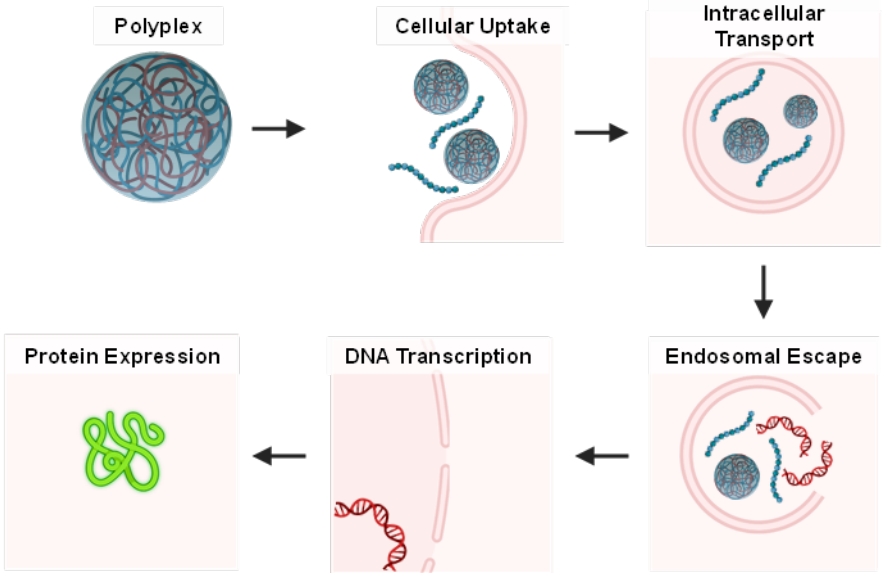

Figure 14. Schematic representation of the transfection process.

1.2.3 Polycation Architecture Mediates Polyplex Activity

Recent advancements in synthetic methodologies have enabled researchers to introduce specific functionalities into polymeric gene carriers by evaluating a variety of monomer functionalities and polymeric scaffolds. Nevertheless, this process comes with additional challenges, as the material properties must be tailored for each type of NAs. This adaptation requires careful consideration of the nature of the charged groups, the polymer structure, and the molecular weight. Numerous architectures have been employed in the construction of gene delivery vectors, prompting researchers to investigate a wide array of options, including natural, synthetic, branched, dendritic, linear, and mixed polymers. The forthcoming discussion aims to elucidate how the functional groups of polymers can intricately modulate the efficacy of the resultant polyplexes.

Nitrogenous cations are predominantly used throughout the nonviral gene delivery literature.[67] The type of amine-based cationic center determines the pK_a of the obtained polymers, which is often related with its ability to undergo endosomal escape. Most employed vectors rely on amine-functionalized moieties to promote DNA binding, encapsulation, and delivery. Apart from enhancing the proton-sponge effect, no significant variation in the gene delivery performance has been found when varying the degree of amine alkylation. However, other cationic nitrogen-containing groups have yielded good delivery performances. An example of such technology was reported by Pun *et al.*, who have demonstrated how the incorporation of imidazolium[78] or guanidinium[79,80] groups can promote greater transfection efficiencies than their amine-functionalized counterparts.

Regarding the introduction of hydrophilic moieties, although PEGylation has been associated with immune responses after multiple administrations, as well as with reduced internalization and endosomal escape abilities, it remains a prevalent method for optimizing gene delivery vectors. As discussed earlier, PEGylation enhances the colloidal stability of the carriers, diminishes protein absorption, and prolongs circulation times. Other hydrophilic chains have been also explored to promote similar shielding effects as PEG, including zwitterionic polymers[81,82] and the incorporation of carbohydrate chains.[83] On the other hand, introducing

hydrophobicity is one of the parameters in the polymer chemist's toolbox to modulate polyplex performance in DNA encapsulation, stability in serum, cellular uptake, and endosomal escape. Incorporating cholesteryl groups,[84] fatty acid derivatives,[85] or fluorinated alkyl chains[86] into terminal amine polymers can bolster cargo protection and transfection efficiency. These effects have been linked to an enhanced ability to interact with biological membranes and to a tailored electrostatic interaction with the encapsulated NAs, thereby facilitating carrier decomplexation at the right moment during intracellular transport.

However, the successful development of delivery vehicles has remained elusive when analyzing these modifications one-by-one. Consequently, combinatorial approaches have emerged as a promising strategy to circumvent the inherent limitations of individual studies. This methodology was introduced by the Langer group in the early 00s. They reported the parallel synthesis of a large library of degradable cationic polymers via the conjugate addition of primary or secondary amines to diacrylates, and test them as gene carriers through rapid cell-based screening assays (Figure 15A).[87,88,89] Over the course of three different articles, these authors described up to 140 structurally unique polymers, of which 70 displayed enough water solubility to be included in further studies. During NA complexation studies, 14 polymers were excluded since they did not interact sufficiently with DNA to retard migration through the agarose gel matrix. Among the 56 remaining formulations, 2 showed higher transfection efficiency than the commercial agent Lipofectamine 2000 (LP 2000). Regarding these two hits, one was based on a histidine-like polymer, whose ability to promote enhanced transfection was related with its ability to promote endosomal escape. The other effective polymer was formed by an amino alcohol containing monomer, whose efficacy could not be related to any known biological process, validating their parallel approach, and highlighting the value of incorporating structural diversity.

More recently, works by Chen *et al.* and Reineke *et al.* have employed similar approaches to produce large libraries of polymers and facilitate the obtention of structural-activity relationships. In the first study, Chen *et al.*[90] designed modified dendrimers to test the role of the attached ligands in promoting higher siRNA delivery. A total of 301 surface-engineered dendrimers were obtained by reacting the primary amine groups from a G5-PAMAM dendrimer with carboxyl, anhydride, isocyanate, isothiocyanate, halogen or epoxy groups (Figure 15B). Structure-activity relationship studies demonstrated that hydrophobic ligands such as aliphatic chains and aromatic rings, as well as functional ligands incorporating halogen atoms, boronic acids, and guanidine groups resulted in a high gene silencing efficacy. Above all, the optimized materials in the library enable efficient delivery of various siRNA into different cell lines with minimal cytotoxicity and allowed the design of a second-generation library of surface-engineered dendrimers with high gene silencing efficacy. In the second study, a combinatorial design allowed Reineke *et al.* to create a large polymer library with diverse physicochemical properties for efficient intracellular ribonucleoprotein (RNP) delivery (Figure 15C).[91] Through parallelized experimentation, they acquired data about polymer composition, molecular weight distribution, pK_a, polyplex size distribution, RNP binding affinity, charge density, cellular toxicity, RNP uptake, and RNP delivery efficiency. Over 43 formulations tested, a hit polymer outperformed commercial RNP delivery reagents used as benchmarked. To identify the physicochemical basis underlying its RNP delivery capabilities, correlations between polymer structure, properties, and biological performance were studied. A library-wide evaluation of editing efficiency, cellular viability, and internalization formed the basis for machine learning models that were able to capture key trends. They also applied data science tools to identify

USC UNIVERSIDADE DE SANTIAGO DE COMPOSTELA

physicochemical determinants of payload delivery, providing highly valuable experimental guidance to tailor vector properties for specific applications.

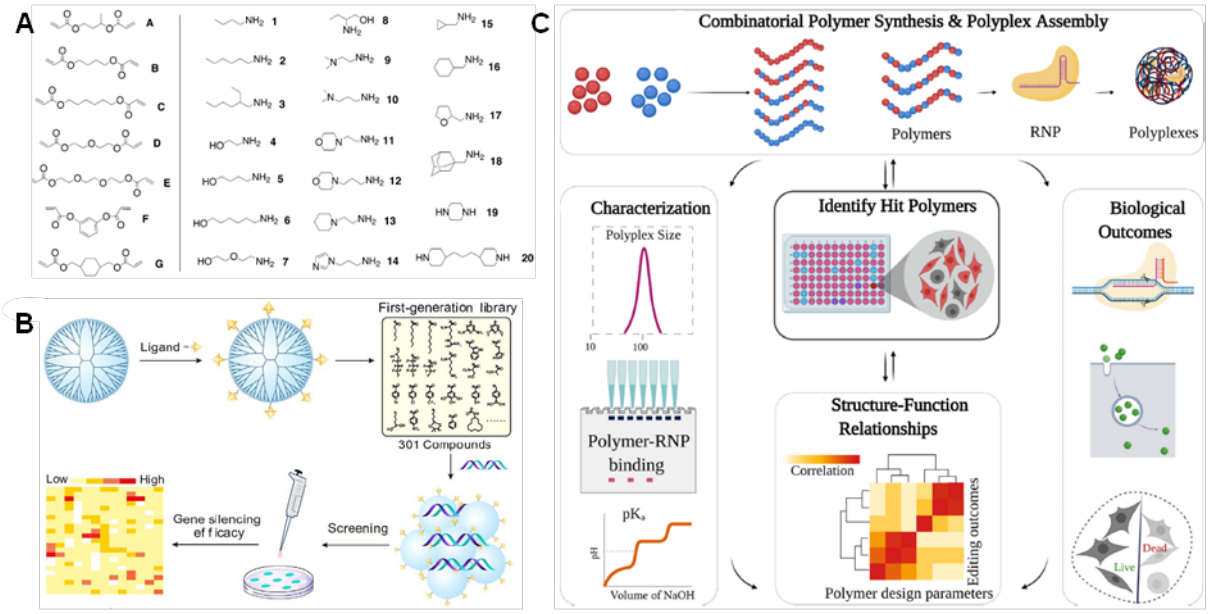

Figure 15. Combinatorial approaches for the screening of gene delivery vectors. Structures employed in the studies by Langer *et al*. Adapted with permission from reference 89. Copyright 2003 American Chemical Society (A). Methodology employed in the combinatorial study performed by *Liu et al*. Adapted from reference 90. Copyright 2016 with permission from Springer Nature (B). Working diagram displaying the optimization process performed by Kumar *et al*. adapted with permission from reference 91. Copyright 2020 American Chemical Society (C).

The exploration of structural-activity relationships has shown considerable potential in optimizing gene delivery carriers. Nevertheless, these relationships have also illuminated fundamental aspects of life. In the following section, the contribution of polymer's versatility in elucidating the molecular principles governing DNA packaging, protein activity, and other biological processes will be examined from the perspective of creatin novel models of natural cells.

USC
UNIVERSIDADE DE SANTIAGO DE COMPOSTELA

1.3 Complex Coacervates As Artificial Cell Models

1.3.1 Bottom-up Synthetic Biology

Since their discovery in the first half of the 18th century, cells have been considered the basic structural and active units of all forms of life. These self-contained structures are characterized by a multitude of functionalities, including compartmentalization, metabolism, replication, and adaptation. Modern cells have emerged through a continuous process of natural selection, leading to complex and highly efficient microreactors. To date, a profound comprehension of the events occurring within natural cells has been gained. However, the intricate connections among these processes, which represent the fundamental functions of living organisms, remain indecipherable by current scientific techniques.[92] Over history, many theories have been elucidated to explain this evolution. For example, the Oparin theory suggested that life evolved from simple molecules through the enhancement of molecular complexity.[93] In recent decades, these theories have been translated into the emerging research field of bottom-up synthetic biology. This aims to create minimal cell analogs to understand the origins of cellular life and to engineer technologies with promising applications in delivery, biomedical devices, and biotechnology.[94,95]

Currently, one of the main goals in synthetic biology is the obtention of compartmentalized structures able to act as individual entities. Since compartmentalization process is a stablished condition for the origin and operation of living systems,[96] the concept of semi-permeable compartmentalization, which enables selective diffusion, retention, and release of structural components, arises as a central tenet in the field.[97]Although a large array of synthetic microcompartments exhibiting such behavior have been studied (Figure 1), there are two main employed candidates for creating novel artificial cells: Giant Unillamellar Vesicles (GUVs) and Complex Coacervates (CCs).

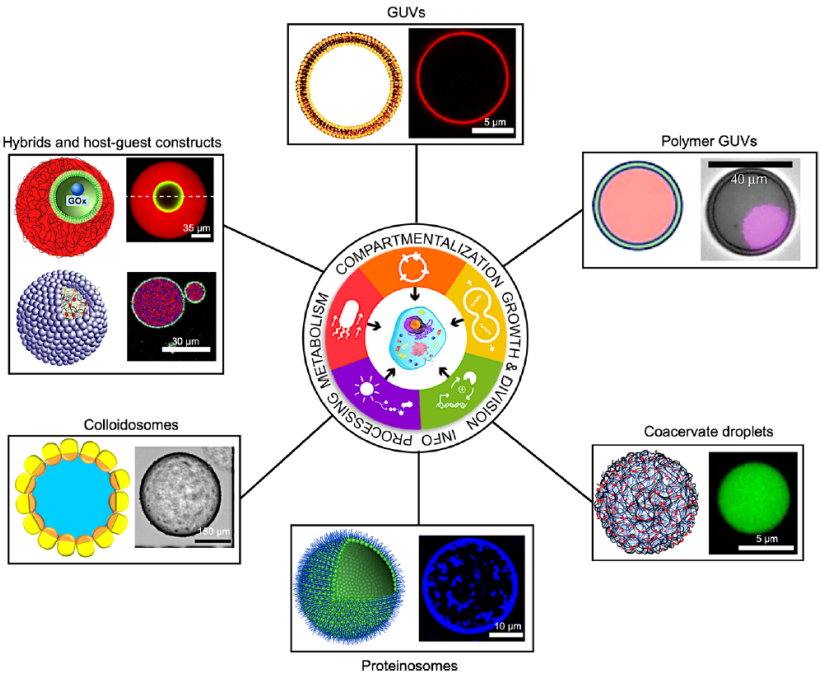

Figure 16. Diverse soft micro-compartmentalized assemblages used for synthetic cell modeling. Single and nested compartments are shown as graphical representations (left panels) and experimental microscopy images (right panels). Adapted from reference 97. Copyright 2021 with permission from Springer Nature.

1.3.2 The Importance of Macromolecular Crowding

The relevance of vesicles in living systems has inspired scientists to employ these architectures in the construction of GUVs, which have demonstrated typical properties of cells, such as small-molecule diffusion, macromolecular encapsulation, enzymatic catalysis, replication, and division.[98,99] Multiple components could be employed in the bottom up assemble of GUVs, including phospholipids, amphiphilic polymers, proteins, or nanoparticles. Inspired by the general assumption that early membranes might be formed by simply amphiphiles,[13] liposomes have been largely considered for synthetic cells construction. Since the first example in the sixties,[99] phospholipid bilayers have evolved towards sophisticated artificial cell models able to mimic multiple life-like properties. However, in recent decades, polymers have served as advanced synthetic analogs of phospholipids for the construction of GUVs (polymersomes). These hollow entities, also useful as DDS as described in Section 1.1.3, are prepared by the self-assembly of amphiphilic block-copolymers which nature, composition, and chemical properties can influence the behavior of the final GUVs. The use of polymersomes as synthetic cells, similar to liposomes, relies on the encapsulation of active components like enzymes, NAs, or natural cell extracts in the aqueous lumen. The membrane properties of GUVs (fluidity, permeability, stability…) are strongly dependent on the MW of the building blocks. Consequently, the increase in MW that encompasses the use of polymeric structures for the preparation of vesicles, is often accompanied by an increase in membrane thickness, which limits the permeability of polymersomes and their wide employment as building blocks for artificial cells by hindering continuous activity within the vesicles due to mass transfer constraints.[41] However, the increasing versatility on polymer chemistry has facilitated the development of strategies to overcome the mentioned issue. Currently, the integration of crystalline (or semicrystalline) polymers through the hydrophobic segments, the use of pore-forming proteins, polyion complex vesicles, or the introduction of stimuli responsive groups represent strategies towards the obtention of semipermeable membranes, opening the door of synthetic biology to polymersomes.[100]

Although GUVs have demonstrated valuable in the development of novel synthetic cell analogs, they often suffer from limitations regarding their inability to mimic aspects of natural cells, such the viscous, macromolecularly crowded, and polyelectrolyte-rich interior. As defined by the Natural Human Genome Research Institute "the cytoplasm is the gelatinous liquid that fills the inside of a cell, which is composed of water, salts, and organic molecules and multiple kind of intracellular organelles.*"* Besides providing physical support for multiple vital processes, cytoplasm plays a major role in maintaining cell integrity. This function arises from its viscous nature, which is motivated by the high total concentration of macromolecules and solutes it contains. Indeed, the cytoplasm of natural cells is occupied by macromolecules in a 20-30% (Figure 17).[101] This phenomenon is termed as crowded rather than concentrated, as it results from the sum of the concentrations of multiple macromolecules rather than from a high content of an individual one.[101] Crowding has been recognized for modifying the association of macromolecules,[102] which immediately affects the reaction equilibria in biological processes. Another consequence of crowding is the reduction of the diffusion rates of all molecules,[103] with those bigger ones being more influenced. Overall, although the role of crowding in biological processes has not been always analyzed, naturally occurring processes cannot be completely understood without considering it. In fact, crowding cannot be obviated when trying to understand or reproduce cellular capacities, thus it should be incorporated into novel artificial cell models. In this context, despite exceptions using novel approaches,[104] GUVs often fail to achieve the high encapsulation efficiencies required to produce the molecularly

crowded and structured milieu of natural cells. Alternative synthetic aggregates developed for mimicking natural cells with crowded interiors include water-in-water and water-in-oil droplets, hydrogels, and especially droplets produced by liquid-liquid phase separation, named complex coacervates.[105] The origin, characteristics and applications of the latter will be discussed in the following section.

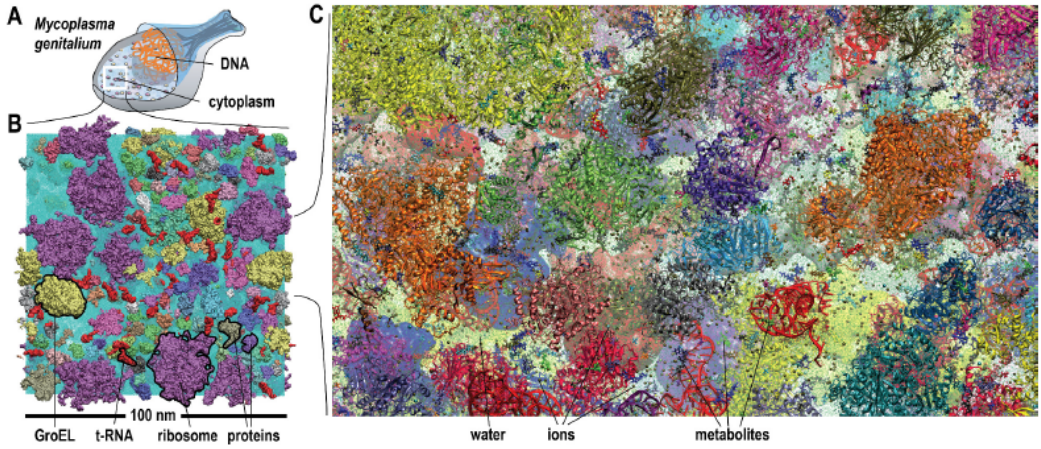

Figure 17. Molecular model of a bacterial cytoplasm. Schematic illustration of Mycoplasma genitalium (MG) (A). Equilibrated MGh system highlighted with proteins, transfer RNA, GroEL, and ribosomes. (C) MG close-up showing atomistic level of detail (B). Adapted from reference 102. Copyright 2020 with permission from ELife.[102]

1.3.3 Complex Coacervates: Origin, Characteristics, and Applications

CCs are condensed liquid-liquid phase separated droplets produced by the association of oppositely charged polyelectrolytes in aqueous solution, usually into a dense phase (the coacervate; Figure 18). Regarding the naming, although the term complex aims to create a distinction with simple coacervation, which involves a single-phase separating molecule, the barrier is becoming ambiguous with the increasing research on the field. In fact, some zwitterionic polymers can self-associate to form auto CCs,[106] whose denotation attempts to merge the properties of CCs to the only presence of one polymeric structure. As the relevance of GUVs in the construction of synthetic cells arises from the attempts to mimic cellular membranes, the concept of phase separation that leads to CCs formation emerges to resemble the interior of natural cells. This process also mimics the formation of biomolecular condensates observed within living systems, usually named as membrane less organelles (MLOs). MLOs are condensed bodies able to carry out essential cellular functions originated *via* liquid–liquid phase separation of intrinsically disordered proteins. Their first observation in 1830,[107] triggered the discovery of many other compartments within cells, which were found encapsulated into cellular compartments, such as nucleoli, or freely spread through the cytoplasm. The observation of P granules in *Caenorhabditis elegans,* and their description as liquid-like condensates,[108] entailed an inflexion point for determining phase separation as the principle that governs MLO formation. Since MLOs and CCs are both formed through liquid-liquid phase separation, CCs emerge as an ideal platform not only to create sophisticated and faithful artificial analogs of cells, but also as an outstanding technology to get further understanding on MLOs function and properties. In fact, giving their viscous, electrolyte-rich, and dynamic interior, their use as artificial cells has been redefined and extended to reproduce various life-like activities.[105]

USC UNIVERSIDADE DE SANTIAGO DE COMPOSTELA

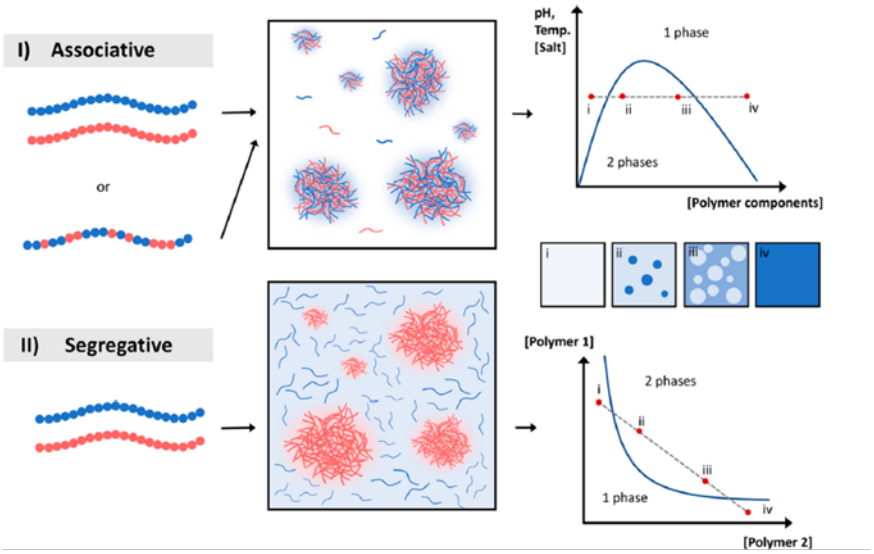

Figure 18. Schematic representation of segregative and associative phase separation processes. Adapted with permission from reference 105. Copyright 2023 American Chemical Society.[105]

Promoting the formation of subcompartments able to act as individual entities represents a significant challenge in artificial cell research. In this context, the development of coacervate-in-coacervate systems has been explored through two different methods based on the principle of phase separation. Some studies rely on the addition of an extra nonmiscible phase over already prepared CCs. For example, in a recent work by Chen *et al.*[109] a coacervate-in-coacervate multi-compartment was constructed via a bottom-up layer-by-layer assembly method (Figure 19A). During a first stage, the inner sub-compartment is formed by liquid–liquid phase separation of strong polyelectrolytes: polydiallyldimethyl ammonium (PDDA) / DNA. Then, carboxymethyl-dextran and diethylaminoethyl-dextran are deposited onto the surface of the previous-prepared droplets through layer- by-layer assembly. The immobilization of active enzymes in such structured compartments was tested through an enzymatic cascade reaction, in which the localization of a catalase can allow or inhibit the obtention of the final fluorescent product. On the other hand, other examples reported the obtention of coacervate-in-coacervate organizations based on multiphase separated compartments (Figure 19B).[110] To understand this concept, a deeper view on the phase separation process should be taken. As already described, CCs are formed by the associative electrostatic combination of two oppositely charged polyelectrolytes. This coupling leads to the formation of a liquid-like droplet, whose properties are dictated by the nature of the associative force and the characteristics of the involved polyelectrolytes. In this context, the presence of multiphased coacervates can be achieved by introducing a third charged polyelectrolyte that matches certain requirements. Recent work by Spruijt *et al*. has proposed an easy-applicable theory to predict the formation of multiphased systems[111] highlighting the role of polyelectrolyte structure on such process. The proposed model was based on the differences on critical salt concentration and interfacial tension values of individual coacervates prepared using different polyanions and polycations. The authors concluded that multiphase separation is favored when the interfacial tension between coacervates is lower than the interfacial tension between one of the coacervates and the surrounding dilute phase. In the same study, they propose that the identity of the inner coacervate can be predicted from the values of critical salt concentration. Thus, coacervates with higher critical salt concentration will be usually engulfed and found in the inner part of the multiphased coacervate due to a stronger density, and lower water content.

USC
UNIVERSIDADE
DE SANTIAGO
DE COMPOSTELA

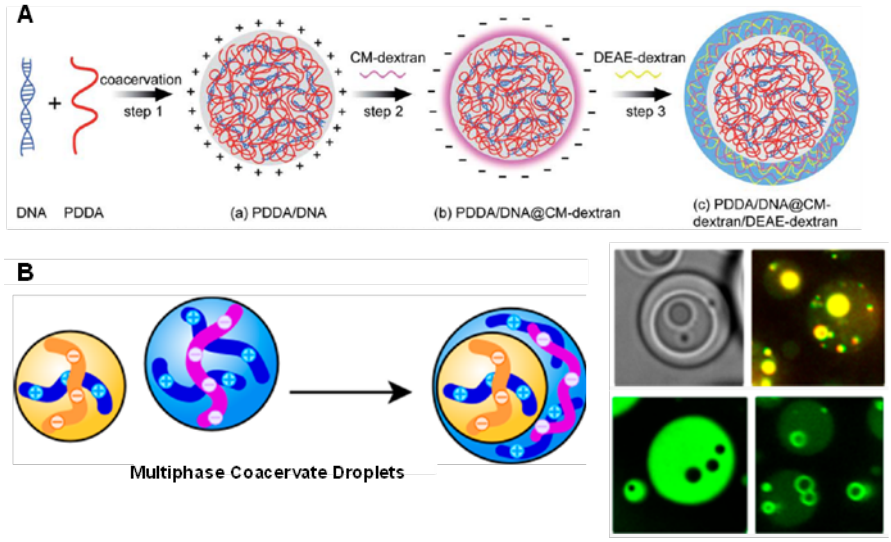

Figure 19. Multi-compartmentalized coacervates. Schematic representation of coacervate-in-coacervate system reported by Chen *et al*. Adapted with permission from reference 109. Copyright 2020 Royal Society of Chemistry (A). Schematic representation and fluorescence microscopy images of multiphase coacervates described by Spruijt *et al*. Adapted with permission from reference 111. Copyright 2020 American Chemical Society (B).

Phase separation processes are mainly governed by the concentration of the components within the droplet. Thus, variations in their concentration can effectively alter the formation or dissolution of phase-separated droplets. This concept has been largely exploited in living cells giving rise to multiple regulatory processes based on changes in the molecular composition, which finally affect the solubility of certain molecules. For example, in nephrin signaling assemblies an increased number of phosphotyrosine residues promote phase separation, facilitating a regulatory system that modulates kinase and phosphatase activity.[112] Inspired by such regulation, many scientific efforts have been focused on achieving controlled coacervation methods by taking advantage on modulations of pH, light irradiation, or enzymatic processes. Regarding the light-controlled coacervation, Martin *et al.*[113] reported CCs prepared from double stranded DNA (dsDNA) and a light-responsive azobenzene cation (trans-azobenzenetrimethylammonium bromide; trans-azoTAB; Figure 20A). Due to the photoisomerization between trans-azoTAB and the metastable cis-azoTAB isomer, droplets could be assembled, disassembled, and reassembled within a few seconds by blue and UV light irradiation. Applying this methodology, they demonstrated a light-mediated transfer of genetic material between droplet populations, unravelling the possible role of light irradiation on synthetic cell modulation. Recently, interesting, and pioneering examples have been reported in which phase separation is controlled by an enzymatic network. Nakashima *et. al*[114] developed active coacervate protocells that were able to grow in size through a pyruvate kinase (PyK) catalyzed mechanism (Figure 20B). Lysine-rich protein K72 does not form droplets in the presence of ADP. However, when pyruvate kinase (PyK) and phosphoenolpyruvate are introduced, the latter is hydrolyzed to pyruvate, generating ATP. This ATP enables the formation of droplets with K72, whose growth can be precisely controlled by adjusting the concentration of phosphoenolpyruvate. Another interesting work was reported by the Martin group, who performed the self-induced phase separation of glucose oxidase (GOX) in the presence of an oppositely charged polyelectrolyte based on enzyme-driven pH changes (Figure 20C).[115] This methodology allowed the obtention of stable enzyme-rich coacervate droplets with programmable lifetime depending on the amount of glucose added to the system.

USC UNIVERSIDADE DE SANTIAGO DE COMPOSTELA

Furthermore, they combined this system with a typical pLys/ATP coacervate to demonstrate the enzyme-driven formation of multiphased CCs.

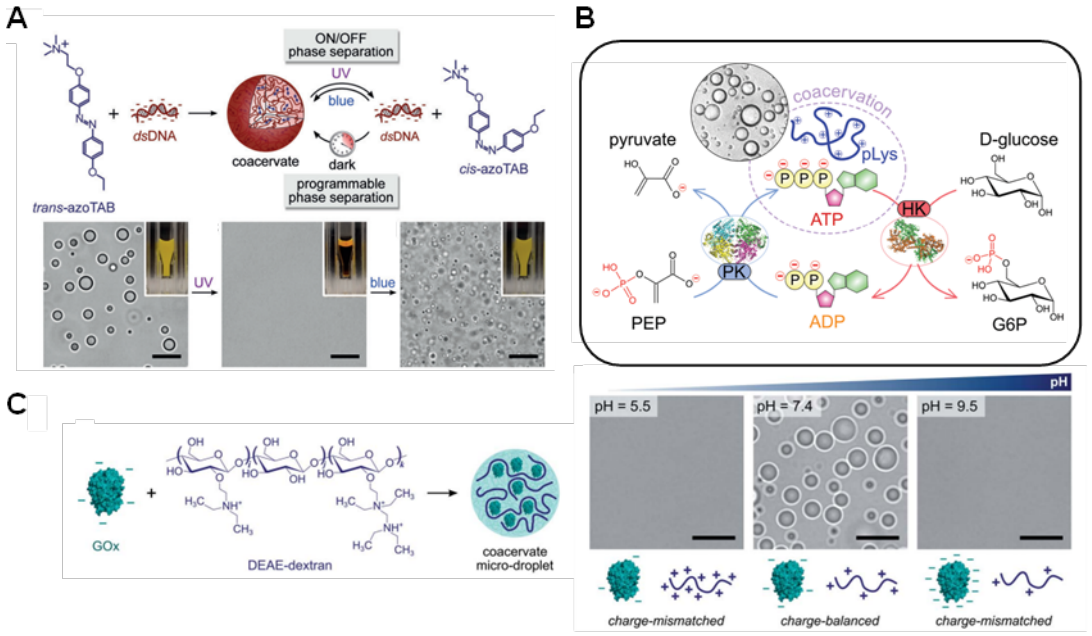

Figure 20. Controlled coacervation technologies. Light-driven coacervation reported by Martin *et al*. Adapted with permission from reference 113. Copyright 2019 John Wiley and Sons (A). Enzymatic control over coacervation reported by Nakashima *et al*. Adapted with permission from reference 114. Copyright 2018 Royal Society of Chemistry (B). GOX induced self-phase separation in presence of cationic dextran. Adapted with permission from reference 115. Copyright 2021 Royal Society of Chemistry (C).

Recently, the obtention of functional coacervates has represented a major objective in bottom-up synthetic biology. As discussed in the previous sections, the physicochemical properties of the components employed in the assembly of novel materials are highly associated with the performance of the obtained aggregates. Thus, part of the current investigations on CCs attempts to answer how the nature, composition, and structure of the components which undergo phase separation influence the properties of the resulting droplets. Because of this approach, fundamental parameters such as multivalency, hydrophobicity, and functionality have been studied, highlighting the impact of fundamental chemistry in synthetic biology. Keating *et al.* reported the effect of multivalency over the phase separation process of homopeptides.[116] These authors focused on understanding the role of low molecular weight, more prebiotically available short oligomers on complex coacervation and functionality. Thus, positively, and negatively charged homopeptides with 1–100 residues, and adenosine mono-, di-, and triphosphate nucleotides were employed as model polyions. The obtained results showed that low multivalency components can match or exceed the performance of those formed by higher-multivalency counterparts in all areas tested, except salt resistance. Notably, the lower multivalency (Lys)n/(Asp)n coacervates ($n < 30$) were more effective at providing distinct pH and at accumulating RNA than those with higher n. (Lys)10/ATP, in which the anion is a nucleotide rather than an oligopeptide, also formed coacervates able to concentrate RNAs and support their duplex formation. In other study, Kreysing *et al.* reported that the interspacing of cationic and neutral amino acids in peptides of limited length increased RNA mobility, that along-side with sequence-dependent Mg^{2+} partitioning, enable enhanced ribozyme activity.[117] Finally, in a recent study, Cook *et al.* used a synthetically modified carboxymethyl amylose and multiple polycations, synthetized by the reversible addition-fragmentation chain-transfer polymerization, to shed light on the role of the cationic functional

group on β-galactoxidase activity. From this sdtudy, reduced charge density polycations gave condensates with higher protein mobility and higher enzyme activity.[118]

Despite their ideal characteristics, the utilization of CCs as artificial cells has been often limited by their tendency to coalesce due to the lack of a membrane that provides structural integrity and prevents the diffusion of large molecules to the aqueous phase. To overcome this limitation, there is a growing interest on chemical-based strategies for achieving the membranization of CCs without compromising their ability to participate in active processes.[105] Membrane-stabilized droplets would serve as ideal mimics of natural cells, combining the advantages of a membrane with the crowded interiors characteristic of CCs. First reports were focused on elucidating how liquid phase separated compartments could have been stabilized in the early earth. With that purpose, lipidic membranes were employed as stabilizers that, giving the higher surface tension of liposomes, prevented droplets to coalesce.[119] As reported by Keating *et al.* individual liposomes have been also applied to stabilize coacervates without inhibiting ribozyme cleavage reaction within the droplets.[120] More recently, amphiphilic synthetic polymers have been also employed for interfacial membrane stabilization. A remarkable study was reported in 2017 by the van Hest group[121] in which a terpolymer comprising PEG, poly(caprolactone-gradient-trimethylene carbonate) (PCLgTMC), and poly(glutamic acid) (pGlu) was used for stabilizing amylose-derived coacervates. All the mentioned components had important functions during the stabilization process. While PEG and pGlu stablished strong interactions with the aqueous and droplet phases respectively, PCLgTMC allowed internal configuration and membrane flexibility. In another example Jobdeedamrong *et al.*[122] demonstrated that silica nanocapsules can create a protective shell around droplets. This shell was able to regulate molecular transport as a function of nanocapasule size, consequently modifying the activity of the stabilized droplets. More recently, Caruso *et al*. reported the first example of a coacervate stabilized with a metal-phenolic network. In their report, they showed how the metal identity can modify the membrane properties, which have a large influence on coacervates functionality. [123]

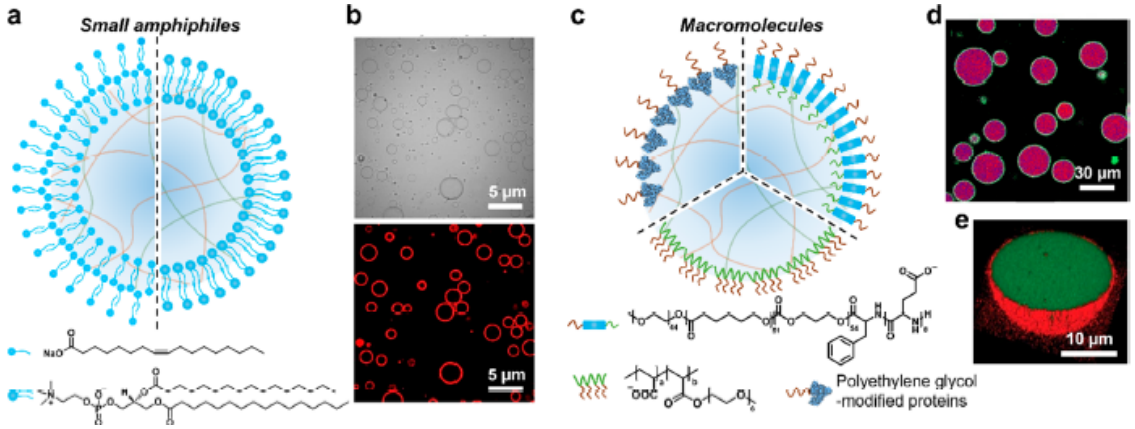

Figure 21. Membranized coacervate microdroplets based on molecular/macromolecular interfacial self-assembly. Scheme showing coacervate microdroplets coated with a multilayer fatty acid (left side) or a phospholipid bilayer (right side) (A). Brightfield (top) and fluorescence (bottom) images of phospholipid (DPPC, Dil stain, red fluorescence) bilayer-bounded DEAE-dextran/DNA coacervate microdroplets (B). Scheme showing coacervate microdroplets coated with macromolecules (terpolymer, top right), PEG-modified proteins (top left), or comb polyelectrolytes (bottom) (C). Laser scanning confocal microscopy (LSCM) image showing terpolymer-bounded coacervate microdroplets (purple) (D). 3D CLSM image showing PEG-modified protein-coated coacervate microdroplet: red fluorescence, RITC-labeled protein; green fluorescence, FITC-tagged coacervate(E). Adapted with permission from reference 208. Copyright 2023 American Chemical Society.

USC UNIVERSIDADE DE SANTIAGO DE COMPOSTELA

The last three sections of this introduction highlight three distinct research areas with a particular emphasis on elucidating structure-activity relations. At this point, the chemical structure of polymeric scaffolds has been postulated as a path for developing more advanced delivery materials and for getting deeper knowledge about the principles that govern biological processes. Nevertheless, the investigation in structure-activity relationships has often been hampered by the need to introduce a large number of chemical modifications. In consequence, there is an urgent demand for technologies to speed up the design of polymeric structures by simultaneous adjustment of multiple variables. In this context, the concept of Dynamic Covalent Chemistry arises as an interesting tool that will be discussed in the following section.

USC
UNIVERSIDADE DE SANTIAGO DE COMPOSTELA

1.4 Dynamic Covalent Chemistry

The synthesis of organic compounds has been often performed by kinetically controlled reactions, which result in the irreversible formation of strong covalent bonds. The irreversible nature of the reaction ensures that, once a particular product is formed, it neither reverts to the starting materials, nor evolves into another product. Following this approach, synthetic chemists have historically described efficient syntheses of numerous products.[124] Nevertheless, in recent decades, interest has shifted to reactions in which the covalent bonds can be formed and cleaved reversibly under equilibrium control. These processes, grouped under the concept of Dynamic Covalent Chemistry (DCvC), constitute a recurrent technology for the construction of novel and sophisticated materials.[125] Notable examples of DCvC include disulfides, hydrazones, and boronate esters.

1.4.1 DCvC Reactions

1.4.1.1 Disulfide Exchange

Disulfide bonds are among the most commonly employed dynamic covalent linkages in the creation of reversible chemical systems.[126] The essence of the disulfide exchange mechanism involves three steps: initial ionization of the thiol to form a thiolate anion, nucleophilic attack of the thiolate on the sulfur atom of the disulfide moiety to cleave the original S–S bond and create a new one, and protonation of the generated thiolate anion.

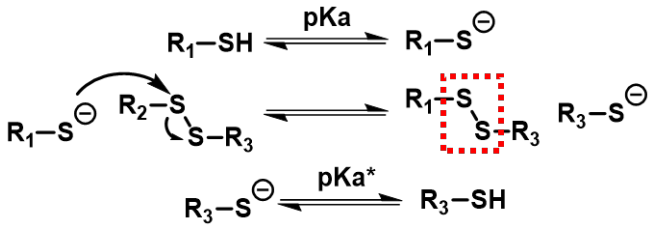

Figure 22. Schematic representation of the three steps involved in disulfide exchange mechanism.

Since exchange requires a deprotonated thiol, the reaction is highly pH-sensitive, allowing the process to be ‘‘frozen’’ by lowering the pH. In most cases, a pH range of 7–9 is used to obtain enough thiolate anions to promote the exchange. This equilibrium has important implications within natural processes, such the assembly of protein’s secondary structures, where disulfide bridges are stablished between thiol-containing cysteine residues.

1.4.1.2 Formation of Oximes and Hydrazones

Another largely explored DCvC reaction involves the reversible formation of hydrazones,[127] a versatile conjugation that finds application across various scientific disciplines. As detailed in Figure 23, the process hinges on the reaction between a hydrazine and a carbonyl compound to yield the corresponding hydrazones.

The reaction begins with an acid-catalyzed attack of the hydrazine on the carbonyl of the electrophile, resulting in the formation of the corresponding hemiaminals after proton transfer. These intermediates can undergo dehydration via protonation of the hydroxyl group, followed by the elimination of water. The resulting protonated intermediate must undergo deprotonation

to yield the final hydrazone (Figure 23). The reversibility of these reactions has been exploited not only in dynamic combinatorial chemistry, but also in certain biological applications, such as the reverse formaldehyde fixation of cells.

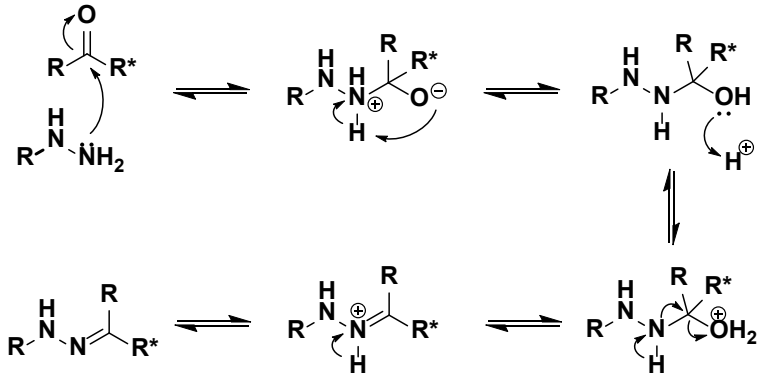

Figure 23. Schematic representation of the formation of oximes and hydrazones.

1.4.1.3 Formation of Boronate Esters

Boronic acids (BAs) are synthetic organic compounds composed by a trivalent boron atom bonded to an aryl or alkyl chain and two hydroxyl groups. Their chemical properties are dictated by their ability to act as Lewis acids due to a vacant p-orbital on the boron center. This characteristic allows them to form complexes with Lewis bases, such the hydroxide anion, or with electron-donating atoms, such as nitrogen. Upon complexation, the hybridization of the boron center shifts from sp^2 to sp^3, which leads to the formation of anionic tetrahedral and hydroxyl coordinated boronates.[128] In fact, in aqueous solutions BAs exist in equilibrium between the neutral form and the boronate anion. This equilibrium is highly influenced by the pK_a of the BA, which typically ranges from 5 to 10.[129]

The relevance of BAs in DCvC relies on their ability to form esters with 1,2- and 1,3- diols. While diols can form esters with both neutral BAs and boronates, sp^2 esters are significantly less stable than the sp^3 counterparts, a fact attributed to the stabilization of five- and six-membered rings by sp^3 boron atoms.[130]

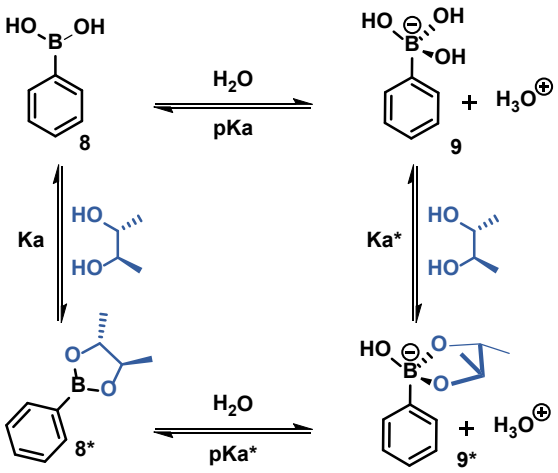

Figure 24. Schematic representation of the equilibriums of BAs in aqueous solution.

USC UNIVERSIDADE DE SANTIAGO DE COMPOSTELA

The equilibrium processes leading to the formation of boronate esters are highly dependent on the pK_a of BA and diol, as well as the pH of the medium, which dictates the hybridization state of the BA (sp^2 or sp^3). Most BAs used in biomedical applications are arylboronic acids (pK_a *ca.* 10). Considering the importance of BA's pK_a in the formation of boronate esters, a large number of modifications have been introduced into their aromatic ring and its substituents for enhancing the efficiency of ester formation at physiological pH by lowering the pK_a. Interestingly, Wulff and coworkers found that the incorporation of an aminomethyl substituent in *ortho* to the boron atom facilitates the formation of boronate esters at pH 7.0 thanks to the formation of a B−N dative bond. This postulated interaction has been often related to the induction of a hybridization change in the boron center (from sp^2 to sp^3), that for both secondary and tertiary amines lowers the pK_a till similar values close to 7.0, and allows for the formation of more stable boronate esters.[131] More recent studies have suggested that an intramolecular H bond may be favored over B−N dative bond formation in protic media, such as methanol or water.[132,129] This insertion would create a zwitterionic specie, with cationic ammonium and anionic sp^3 boronate centers. Such ionic stabilization would potentially explain the lowered pK_a of Wulff-Type BAs in water *ca.* 6.5[133] and its enhanced binding of diols at neutral pH.[134,135] These structures have been specially employed as diols sensors and in pH sensitive delivery, since the resulting esters would be stable at physiological pH, while hydrolyzed under acidic conditions.[136]

1.4.2 Applications of DCvC

The usefulness of DCvC could be associated with its capacity to enable the preparation of novel architectures that can be formed, adjusted, and disrupted under controlled conditions. Positioned as a link between conventional static systems and supramolecular assemblies, DCvC not only surpasses the inherent limitations of the former, while allowing the formation of more robust conjugates than the latter.[137] Although DCvC was initially exploited in medicinal chemistry, the field has rapidly evolved towards sophisticated applications, such as the development of covalent organic frameworks, self-assembled polymers, and optical sensors. Nevertheless, a notable inflection point has arisen in recent years with the emergence of smart delivery systems, that thanks to the unique properties of DCvC, can be easily tailored for specific applications, and precisely disassembled to enhance cargo delivery efficiency.

1.4.2.1 DCvC for Drug Delivery

Dynamic bonds have been employed to facilitate the controlled release of small drugs in response to different stimuli, such as ROS, pH variations, or competitive bonding agents. The strategies employed to achieve this goal are primarily focused on establishing dynamic bonds either between the carrier and the drug, or within the carrier scaffold itself.

In an interesting example, Liu *et al.*[138] reported the employment of two different dynamic covalent bonds for the delivery of anticancer drugs. They employed a salicylhydroxamate-containing polymer to conjugate the chemotherapeutic agent bortezomib (BTZ) *via* a boronate ester bond (P1-BTZ; Figure 25A), which induced the self-assembly of the resulting products and facilitated drug delivery. Furthermore, these authors also reported the use of synthetic linkers to surpass the need of BA -containing therapeutics. This technology was validated through the complexation of camptothecin (CPT) using two different approaches, wherein its

tertiary alcohol served as chemical handle for the conjugation of cleavable linkers. In a first approach, a linker containing a BA moiety facilitated the attachment of the drug to the polymeric backbone through boronate bonds (P1-CPT^{ROS}; Figure 25B), whose inherent reactivity with oxidants enabled the ROS-responsive release of the drug. In a second approach, a disulfide linker was employed not only to separate the conjugation site from the sensitive group, but also to introduce an additional responsive moiety, facilitating glutathione-triggered drug release (P1-CPT^{redox}; Figure 25C). The efficient cellular activity, in terms of cell mortality, exhibited by these polymer–drug nanoconjugates highlights the potential utility of DCvC in nanomedicine.

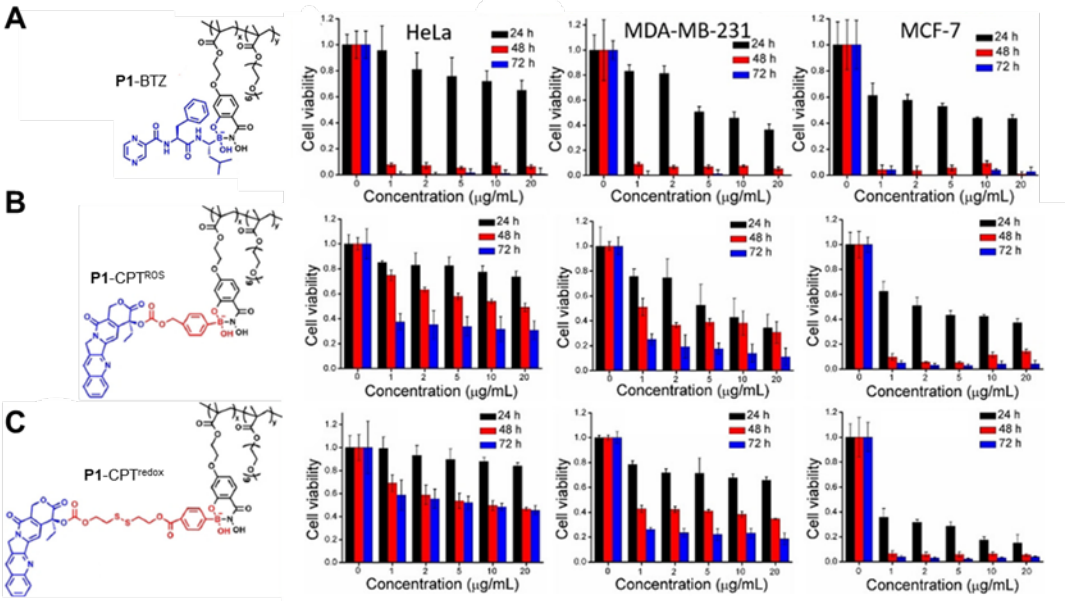

Figure 25. Studies performed by Liu *et al*. based on the drug conjugation induced self-assembly. Structure (left) and cytotoxicity (right) toward different cell lines at different times of P1-BTZ drug-conjugate (A). Structure (left) and cytotoxicity (right) toward different cell lines at different times of P1-CPT^{ROS} (B). Structure (left) and cytotoxicity (right) toward different cell lines at different times of P1-CPT^{redox} (C). Adapted with permission from reference 138. Copyright 2016 John Wiley and Sons.

DDS based on DCvC have also been designed for the delivery of DOX. In a recent study reported by Wang *et al.* [139] the authors employed multifunctional cylindrical polymer brushes bearing BAs and hydrazides for the delivery of DOX (Figure 26A). The incorporation of BAs aimed to enhance cellular uptake and endosomal escape through interactions with sialic acid receptors, while the conjugation of DOX was achieved via acylhydrazone bonds formed with the free ketone group in the side chain of the drug. These DDS demonstrated extraordinary therapeutic efficacy in tumor treatment, attributed to the enhanced tumor targeting, penetration, and endosomal escape facilitated by the BAs. Another interesting example reported by Wang *et al.*[140] describes the encapsulation of a tumor specificity ROS inducer NQO1-responsive hemicyanine fluorescent dye ($NCyNH_2$) into a ROS-responsive self-immolative polymeric nanoparticle for programmed oxidation-chemotherapy (Figure 26B). In response to ROS, this polymer therapeutic degrades to release DOX through a domino-like fragmentation. Accordingly, the $NCyNH_2$-loaded self-immolative nanoparticle could be dissociated, triggering further release of DOX and $NCyNH_2$. Consequently, free $NCyNH_2$ could be activated by intratumorally overexpressed NQO1 to generate additional ROS, which further induces the degradation of the particle to release more drugs. This complex system was validated in both *in vitro* and *in vivo* studies, demonstrating the efficiency of these nanoparticles.

USC
UNIVERSIDADE DE SANTIAGO DE COMPOSTELA

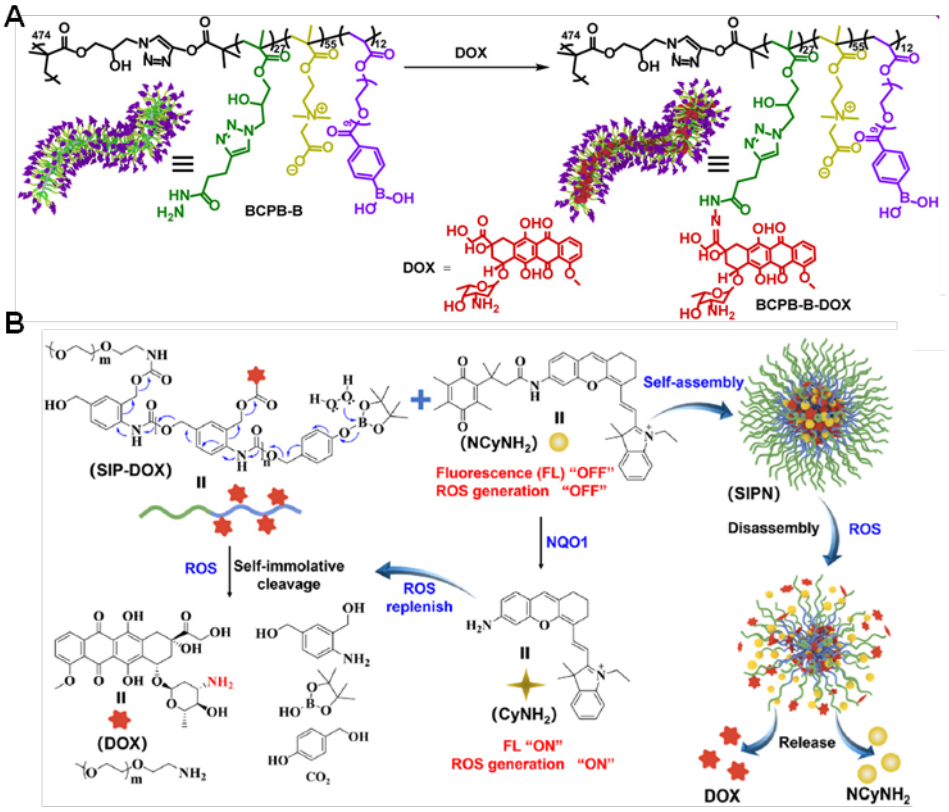

Figure 26. DCvC for DOX delivery. Polymeric structure and schematic representation of fibromicelles employed by Wang *et al*. for DOX delivery. Adapted with permission from reference 139. Copyright 2021 American Chemical Society (A). Schematic representation of the self immolative polymeric nanoparticles and its degradation mechanism employed in the studies of Wang *et al*. Reproduced with permission from reference 140. Copyright 2022 Elsevier (B).

1.4.2.2 DCvC for Delivery of Biopharmaceuticals

Recently, there have been remarkable advances in sophisticated DCvC methodologies for protein and NAs delivery focused either on the assembly of polymeric vectors, or the use of self-polymerizing polymers for the construction of templated vehicles. As part of the first approach, the research conducted by the groups of Chen and Montenegro is noteworthy, since they have respectively demonstrated how BAs and hydrazones can be employed to create active scaffolds through optimized processes. In a recent example, Chen *et al.*[141] employed a BA-catechol coupling to attach hydrophobic alkyl chains of different length to a BA -functionalized polylysine for improving protein delivery efficiency (Figure 27). Applying such technology, the efficient delivery of multiple proteins with different isoelectric points and molecular weights was achieved. Furthermore, they also proved that the lead system delivered superoxide dismutase (SOD), an enzymatic antioxidant that can protect cells, to downregulate the ROS levels in colon tissues and efficiently ameliorated *ulcerative colitis in vivo*.

USC UNIVERSIDADE DE SANTIAGO DE COMPOSTELA

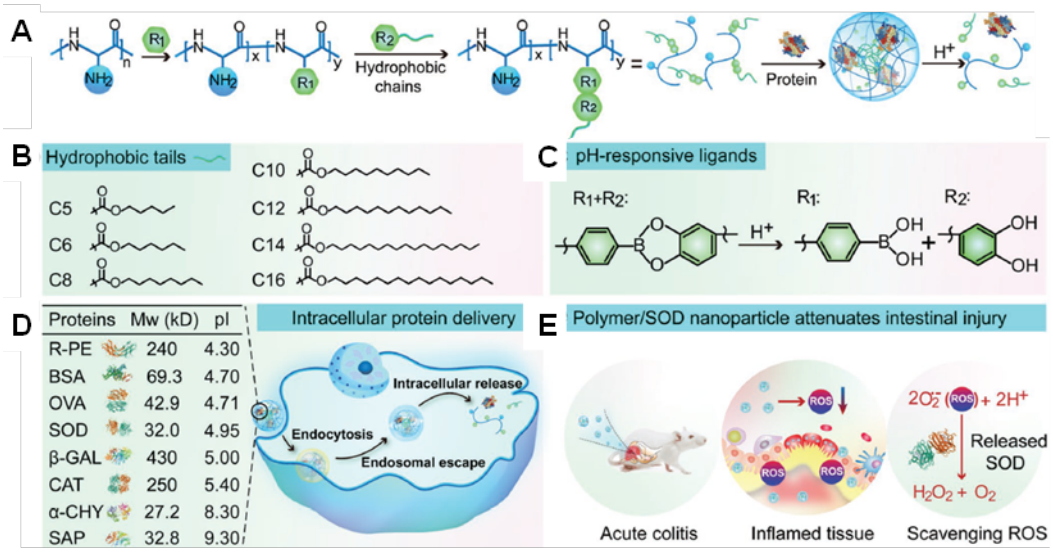

Figure 27. Dynamic polymers for protein delivery described by Chen and coworkers. Hydrophobic lipids were tagged to PBA-modified PLL via a dynamic covalent chemistry (A). Ejmployed lipidated catechols (B). pH-responsive boronate-catechol linkages (C). Cargo proteins in this study (D). *In vivo* SOD delivery (E). Reproduced with permission from reference 141. Copyright 2021 John Wiley and Sons.

On the other hand, Montenegro *et al.* described the multiple acyhydrazones sidechain functionalization of different length polyhydrazide polymers, and use them for both siRNA[142] and plasmid DNA[143] delivery (Figure 28). Their results provided a suitable strategy for the screening and identification of customized polymeric vehicles for NAs delivery, avoiding the typical drawbacks of traditional screening processes, such as purification and characterization steps.

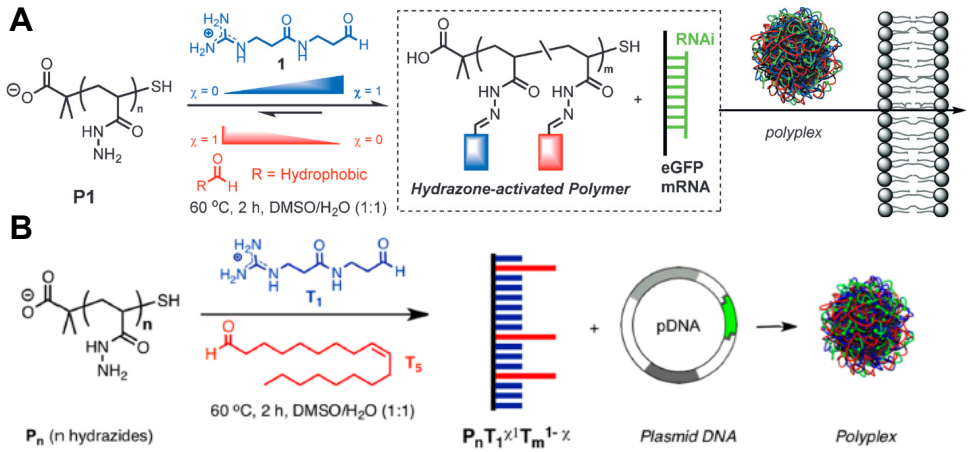

Figure 28. Reported works by Montenegro and coworkers. Post-polymerization functionalization with cationic and hydrophobic aldehydes, followed by supramolecular conjugation of activated polymers with cargo (siRNA) and polyplex delivery. x=molar fraction. Adapted with permission from reference 142. Copyright 2016 John Wiley and Sons (A). Schematic representation of polyplex formation through the reaction between the polymer with n hydrazides sites (P_n) with the cationic T_1 and the hydrophobic T_5 to afford the amphiphilic polyhydrazone $P_n T_1^{x} T_5^{1-x}$ that is then combined with the plasmid DNA for polyplex formation (the x superindex corresponds to the molar fraction of the guanidinium aldehyde tail). Adapted with permission from reference 143. Copyright 2019 American Chemical Society (B).

Other studies have focused on developing technologies for the *in situ* preparation of delivery vectors. These approaches involve the construction of scaffolds via DCvC in the presence of the macromolecules that they ultimately encapsulate. In this context, some important contributions should be remarked. An interesting example was reported by Aida *et al.* in

2015.[144] Along this study, they reported the preparation of a small siRNA/carrier conjugate with a uniform size of 7 ± 2 nm by oxidative polymerization of a water-soluble telechelic dithiol monomer carrying multiple guanidinium ion pendants in the presence of siRNA as a template (Figure 29A). From a screening process, they concluded that a monomer containing a triethylene glycol (TEG) chain and 4 interspaced guanidinium groups ($^{TEG}Gu_4$) was able to form nanocapplets with siRNA *via* an *in situ* polymerization. These aggregates, able to retardate siRNA migration in agarose gel electrophoresis, were stable after incubation with serum, and facilitated siRNA uptake by Hep3b cells. Finally, they also confirm that the obtained nanocaplets significantly reduced luciferase expression in Hep3b-Luc cells. This study introduced a novel method for obtaining advanced systems for siRNA delivery, in which the formation of the obtained vectors was templated by the NAs. More recently Yang *et al.*[145] employed a similar approach for gene delivery based on an oligonucleotide (ON)-template-assisted polymerization (Figure 29B). In this system, guanidinium-containing disulfide monomers adhered strongly to ON templates via multiple salt bridges between the phosphate (ON) and guanidinium (monomer) groups. Organization along the ON templates brought the disulfide monomers into close proximity, which increased their local concentrations and kinetics of ring-opening disulfide-exchange polymerization. This afforded -ON/oligomer complexes, which further self-assembled into ONs nanoparticles able to achieve cytosolic delivery through thiol-mediated uptake. These nanoparticles were able to effectively deliver ON into HeLa cells and demonstrated a remarkable efficiency in gene regulation assays.

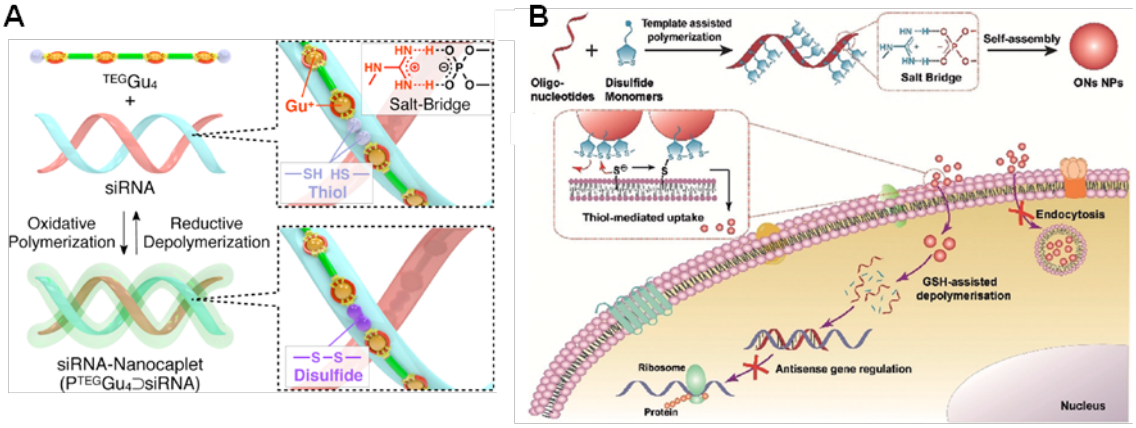

Figure 29. Reported works by the groups of Aida (A) and Yang (B) on cationic poly(disulfides). Oxidative polymerization of $^{TEG}Gu_4$ with siRNA as the template. $^{TEG}Gu_4$ adheres to siRNA *via* the formation of multiple salt bridges and undergoes oxidative polymerization to form a siRNA-containing nanocaplets able to be disrupted under reductive conditions. Adapted with permission from reference 144. Copyright 2015 American Chemical Society (A). ON-template-assisted polymerization for the formation of ONs nanoparticles and effective intracellular gene delivery by thiol-mediated uptake, followed by disassembly through GSH-assisted depolymerization. Adapted with permission from reference 145. Copyright 2019 John Wiley and Sons (B).

Following a similar approach, Ulrich and coworkers have reported the *in situ* templated self-assembly of hydrazone containing scaffolds. This technology was employed for the generation of biomolecular clusters able to bind DNA.[146] In this study, the authors create multivalent biomolecular clusters for DNA recognition, generated *in situ* through the formation of hydrazone linkages. These clusters effectively bind DNA via multivalent interactions and, due to the reversibility of their formation, facilitate template effects where DNA promotes the formation of the most active DNA-binding clusters. Additionally, the authors explore exchange reactions to control DNA decomplexation. More recently, the same group has reported the use of hydrazone-based dynamic covalent polymers for cell-selective siRNA delivery.[147] In this

USC UNIVERSIDADE DE SANTIAGO DE COMPOSTELA

work, the templated assembly process was conducted employing polymers functionalized with multivalent carbohydrates, which allowed a cell-selective targeted delivery.

1.4.2.3 DCvC for the Construction of Artificial Cells

Despite the significant contributions of DCvC to drug delivery, its implementation in the field of synthetic biology remains largely unexplored. The closest approach has been reported this year by Yu *et al.* offering a functional strategy to mitigate the severity of hypoglycemia in a rodent model of insulin overdose.[148] Briefly, CCs were obtained by incubating a cationic phenylboronic acid-containing peptide amphiphile, glucose and dasiglucagon (a cationic glucagon analogue) in aqueous solution. The coupling between BAs and glucose facilitated the reduction of positive charge density along the surface of the amphiphiles, which leads to phase separation in presence of dasiglucagon (Figure 30). It was demonstrated that glucose is mandatory for the obtention droplets and exploited this fact for creating dasiglucagon controlled release systems. Since under conditions of low glucose, the droplets typically coalesce, an enhanced release of dasiglucagon is promoted as therapeutic remedy for low blood glucose.

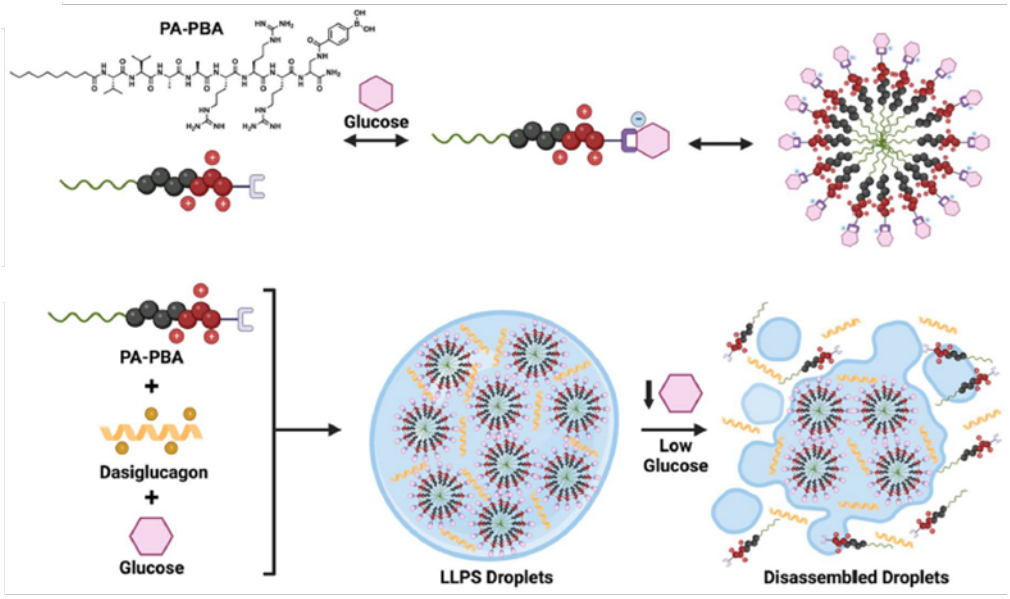

Figure 30. Molecular structure of the BA modified peptide amphiphile and schematic representation of its assembly into spherical aggregates upon the addition of glucose (up). Assembly of the dasiglucagon containing CCs and its coalescence process in absence of glucose (down). Reproduced with permission from reference 148. Copyright 2024 American Chemical Society.

Overall, the unique properties of DCvC have been exploited in various applications. DCvC not only facilitates the development of smart materials capable of interacting with biological environments, but also serves as a valuable tool for studying structural modifications. Recent studies have shown that DCvC can impact the controlled release of therapeutic cargo, facilitate the optimization of DDS, and also effectively introduce sensitive moieties into formed systems.

USC
UNIVERSIDADE DE SANTIAGO DE COMPOSTELA

2. OBJECTIVES

The tremendous impact of structure-activity relationships in the discovery of advanced DDS, as well as in understanding the rules that govern biological activities, makes them an attractive research field. On the other hand, DCvC has emerged as a unique tool to design sophisticated and innovative materials able to surpass some of the limitations impose by classical covalent methodologies. This thesis aims to bridge the gap between these two concepts by exploiting the dynamic covalent coupling between BAs and catechols as cement. This offers an exciting technology with implications in drug delivery, gene therapy, and the fabrication of artificial cell models. These elements form the cornerstone of this thesis, which will be divided in the subsequent objectives.

1. Since the precise control of the size of DDS remains elusive by current chemical technologies, the relationship between size and efficacy *in vivo* remains largely unexplored. The first part of this thesis aims to address this limitation by focusing on the construction of size-controlled DOX therapeutics through the hierarchical assembly of *in situ* functionalized dendrimers. The *in situ* binding of diol drugs to a PEG-dendritic copolymer/dendrimer pair via boronate esters leads to the assembly of the resulting amphiphilic structures into micelles, where the PEGylation degree templates the size between *ca.* 30 nm up to the micron. This section will elucidate the effects of PEGylation and size on the *in vitro* and *in vivo* performance of DOX therapeutics.

2. Despite the tremendous progress of viral gene delivery vectors, their high cost, complex manufacturing, and side effects have encouraged the development of nonviral alternatives, including cationic polymers. However, these are less efficient in overcoming cellular barriers, resulting in lower transfection efficiencies. Although the exquisite structural tunability of polymers might be envisaged as a versatile tool for improving transfection, the need to fine-tune several structural parameters represents a bottleneck in current screening technologies. By taking advantage of the fast-forming and strong boronate ester bond, in the second part of this thesis a highly adaptable gene delivery platform will be described in which the polycation synthesis and pDNA complexation occur *in situ*. The robustness of the strategy entitles the simultaneous evaluation of several structural parameters at will, enabling the accelerated screening and adaptive optimization of lead polymeric vectors using dynamic covalent libraries.

3. The creation of synthetic models of natural cells represents a promising approach for elucidating the origin and governing principles of cellular life. In this context, coacervates obtained through liquid-liquid phase separation emerge as ideal mimics of the crowded cell interior. Although different approaches have been reported to control coacervate formation, they typically fail in providing stabilization and modulation. In the third part of this thesis, a DCvC approach based on BA will be followed to (i) promote the formation of coacervates, (ii) induce their stabilization through the hierarchical assembly of a PEGylated dendrimer, and (iii) modulate the coacervate inherent properties, such as protein partitioning and internal dynamics.

USC UNIVERSIDADE DE SANTIAGO DE COMPOSTELA

3. MATERIALS AND METHODS

3.1 Experimental data for A Hierarchical Assembly of *In Situ* Prepared Boronate-Ester Dendrimers Regulates the Size of Doxorubicin Polymer Therapeutics

3.1.1 Materials

Dulbecco's modified Eagle's medium (DMEM), fetal bovine serum (FBS), penicillin, streptomycin, and LysoTracker Green DND-99 were purchased from Invitrogen Thermo Fisher. DOX·HCl was purchased from Apollo Scientific. Bisbenzimide H-33258 (Hoechst 33258) was purchased from Sigma Aldrich. All other chemicals were purchased from Acros Organics, Fluka, Sigma-Aldrich, or Thermo Fisher Scientific, unless otherwise noted. All solvents were HPLC grade, purchased from Scharlab, or Sigma-Aldrich. Et_3N was dried under 4Å molecular sieves. H_2O was of Milli-Q grade obtained using a Millipore water purification system. PEG[G3]-BA and 3[G2]-BA were prepared following procedures previously described by our group.[149]

3.1.2 Instrumentation

Determination of pH Values. pH values were measured with a portable pH-meter (Crison PH25) connected to a glass electrode (Crison 52 09).

Dialysis and Ultrafiltration. Dialysis was performed with an 18 mm Spectra/Por 6 MWCO 1 kDa membrane tubing from SpectrumLabs. Ultrafiltration was performed on Amicon Ultra-15 Centrifugal Filter Unit MWCO 3 kDa from Sigma-Aldrich.

Scanning Transmission Electron Microscopy (STEM). STEM measurements were performed on a FESEM-UltraPlus (Zeiss, Oberkochen, Germany) operated at 20.00 kV electron microscope equipped with a STEM detector. A drop of a solution of micelles (0.1 mg/mL in H_2O) was settled on a copper grid (Ted Pella, Inc.) and allowed to dry at room temperature for 12 h. Size of polyplexes were determined with ImageJ software (version 1.51j8) measuring the line intensity profile across the assemble. Average diameters were obtained by measuring the size of a representative number of polyplexes.

Laser Scanning Confocal Microscopy (LSCM). Confocal images were obtained on an Andor Dragonfly spinning disk confocal system mounted on a Nikon TiE microscope equipped with a Zyla 4.2 PLUS sCMOS digital camera (Andor, Oxford Instruments) and an OKO-lab incubator to maintain cells at 37 °C.

Spectroscopic Measurements. Absorbance and fluorescence measurements were performed in a plate reader Tecan Infinite F200 PRO.

USC UNIVERSIDADE DE SANTIAGO DE COMPOSTELA

3.1.3 Micelles Preparation

3.1.3.1 CAT Micelles

Preparation of the Solutions of Components. PEG[G3]-BA (1.50 mg/mL; 95.0 μM) and 3[G2]-BA (1.05 mg/mL; 95 μM) were separately dissolved in 50 mM PB pH 7.4 and the resulting solutions were aged for 1 h at rt before use. A fresh catechol solution (0.57 mg/mL; 51.7 mM) was prepared in 50 mM PB pH 7.4 just before the preparation of micelles. All solutions were filtered through 0.45 μm nylon filters before the preparation of micelles.

Preparation of Micelles. For each % PEG, solutions of PEG[G3]-BA and 3[G2]-BA were mixed in different volume ratios (Table 1) to afford a total volume of 700 μL. A 667 μL portion of the obtained mixtures was immediately added over the solution of catechol (333 μL) under stirring at 37 ºC. The formation of micelles was left for18 h under vigorous stirring (1000 rpm) at 37 ºC in the dark.

Table 1. Volume (μL) of PEG[G3]-BA and 3[G2]-BA solutions used in the preparation of CAT micelles with different % PEG, and corresponding values of micelle concentration.

%PEG	PEG[G3]-BA	3[G2]-BA	Micelle Concentration (mg/mL)
100	700	0	1.19
80	560	140	1.13
60	420	280	1.07
40	280	420	1.01
20	140	560	0.95
10	70	630	0.92
5	35	665	0.90
1	7	693	0.89
0.4	2.8	697.2	0.89
0.25	1.75	698.25	0.89
0.15	1.05	698.95	0.89

3.1.3.2 DOX Micelles

Preparation of the Solutions of Components. PEG[G3]-BA (1.50 mg/mL; 95.0 μM) and 3[G2]-BA (1.05 mg/mL; 95.0 μM) were separately dissolved in 50 mM Na_2HPO_4 and the resulting solutions were aged for 1 h at rt before use. Fresh solutions of catechol (0.75 mg/mL; 6.77 mM) and DOX·HCl (1.67 mg/mL; 3.10 mM) were prepared in 50 mM NaH_2PO_4 just before the preparation of micelles. All solutions were filtered through 0.45 μm nylon filters before the preparation of micelles.

Preparation of Micelles. For each % PEG, solutions of PEG[G3]-BA and 3[G2]-BA were mixed in different volume ratios (Table 2) to afford a total volume of 700 μL. A 667 μL portion of the obtained mixtures was immediately added over a mixture of the catechol (100 μL) and DOX·HCl (233 μL) solutions under stirring at 37 ºC. The formation of micelles was left for18 h under vigorous stirring (1000 rpm) at 37 ºC in the dark. The pH of the resulting solution of micelles was around 7.4.

USC DE COMPOSTELA

Table 2. Volume (μL) of PEG[G3]-BA and 3[G2]-BA solutions used in the preparation of DOX micelles with different % PEG.

%PEG	PEG[G3]-BA	3[G2]-BA
100	700	0
80	560	140
60	420	280
40	280	420
20	140	560
10	70	630
3	21	679
2	14	186
1	7	693

Encapsulation efficiency (EE) and Drug loading (DL)

- **EE** describes the fraction of drug incorporated into a micelle compared to the total amount of drug used in its preparation (EE = weight of drug in micelle × 100/weight of feeding drug).

- **DL** refers to the mass fraction of a micelle that is composed of the drug (DL = weight of drug in micelle × 100/weight of drug-loaded micelle).

Encapsulation of DOX. After micelle formation, unloaded DOX was removed by dialysis (Spectra/Por 6, MWCO 1 kDa) against 250 mL of PBS for 6 h in the dark at 37 ºC. To determine the EE and DL of DOX, an aliquot of the buffer solution was taken at the end of the dialysis (150 μL) and placed in a 96-well microplate (done in triplicate). Then, 500 mM acetate buffer pH 4.0 (50 μL) was added to each well and the fluorescence of the samples was measured in a microplate reader (λ_{ex} 485 nm, λ_{em} 535 nm; Tecan Infinite F200 PRO). The concentration of unloaded DOX in solution was determined by comparison with a standard calibration curve made from the fluorescence emission of fresh solutions of DOX of known concentrations prepared under identical conditions. An average EE of 82 % and an average DL of 28 % were obtained regardless of the % PEG.

USC
UNIVERSIDADE DE SANTIAGO DE COMPOSTELA

Table 3. EEs, DLs, and calculated values of DOX, and micelle concentration of DOX micelles prepared with different % PEG.

% PEG	EE (%)	DL (%)	DOX Concentration (mg/mL)
100	81.5	23.9	0.32
80	80.8	25.1	0.32
60	82.6	26.8	0.32
40	82.9	27.6	0.32
20	79.5	28.6	0.31
10	80.0	29.8	0.31
3	79.0	30.4	0.31
2	81.8	30.2	0.32
1	80.3	31.0	0.31

3.1.4 Dynamic Light Scattering (DLS), Size, and Stability of Micelles

DLS measurements were performed on a Malvern Nano ZS (Malvern Instruments, U.K.), operating at 633 nm with a 173º scattering angle, at 25 or 37 ºC. DLS mean diameters were obtained from the intensity particle size distribution provided by Malvern Zetasizer Software (5 independent measurements). DLS histograms were obtained from the intensity particle size distributions. Filtering of samples before DLS measurements was avoided to prevent the removal of larger assemblies or aggregates that could obscure analysis.

CAT Micelles. Micelles were measured at two different time points (temperature of DLS recording in brackets): (a) after 18 h of formation at 37 ºC (referred as "upon formation", DLS at 37 ºC), and (b) after dialysis (3 × 500 mL H_2O, Spectra/Por 6, MWCO 1 kDa) and 1 month of storage at 4 ºC (DLS at 25 ºC).

DOX Micelles. Micelles were measured at four consecutive time points (temperature of DLS recording in brackets): (a) immediately after 18 h of formation at 37 ºC (referred as "upon formation", DLS at 37 ºC), (b) after dialysis (1 mL of micelles against 250 mL PBS, Spectra/Por 6, MWCO 1 kDa, 6 h, 37 °C; DLS at 37 ºC), (c) after additional 24 h of heating at 37 ºC (DLS at 37 ºC), and lastly (d) after 1 month of storage at 4 ºC (DLS at 25 ºC).

USC UNIVERSIDADE DE SANTIAGO DE COMPOSTELA

3.1.4.1 CAT-Micelles

Table 4. Mean hydrodynamic radius (*R*, nm) and PDI (in brackets) of CAT micelles obtained after 18 h of formation at 37 ºC, and after storage for 1 month at 4 ºC.

% PEG	Upon Formation (37 ºC)	1 month at 4 ºC (25 ºC)
100	16 ± 1 (0.10 ± 0.02)	18 ± 1 (0.28 ± 0.02)
80	22 ± 1 (0.12 ± 0.01)	-
60	37 ± 1 (0.08 ± 0.02)	-
40	51 ± 1 (0.02 ± 0.01)	51 ± 1 (0.05 ± 0.02)
20	73 ± 1 (0.02 ± 0.01)	-
10	83 ± 1 (0.04 ± 0.01)	80 ± 1 (0.05 ± 0.02))
5	104 ± 2 (0.03 ± 0.02)	-
1	160 ± 4 (0.16 ± 0.02)	154 ± 6 (0.16 ± 0.03)
0.4	263 ± 3 (0.02 ± 0.01)	293 ± 12 (0.16 ± 0.02)
0.25	368 ± 6 (0.10 ± 0.06)	*
0.15	535 ± 17 (0.16 ± 0.02)	*

USC
UNIVERSIDADE DE SANTIAGO DE COMPOSTELA

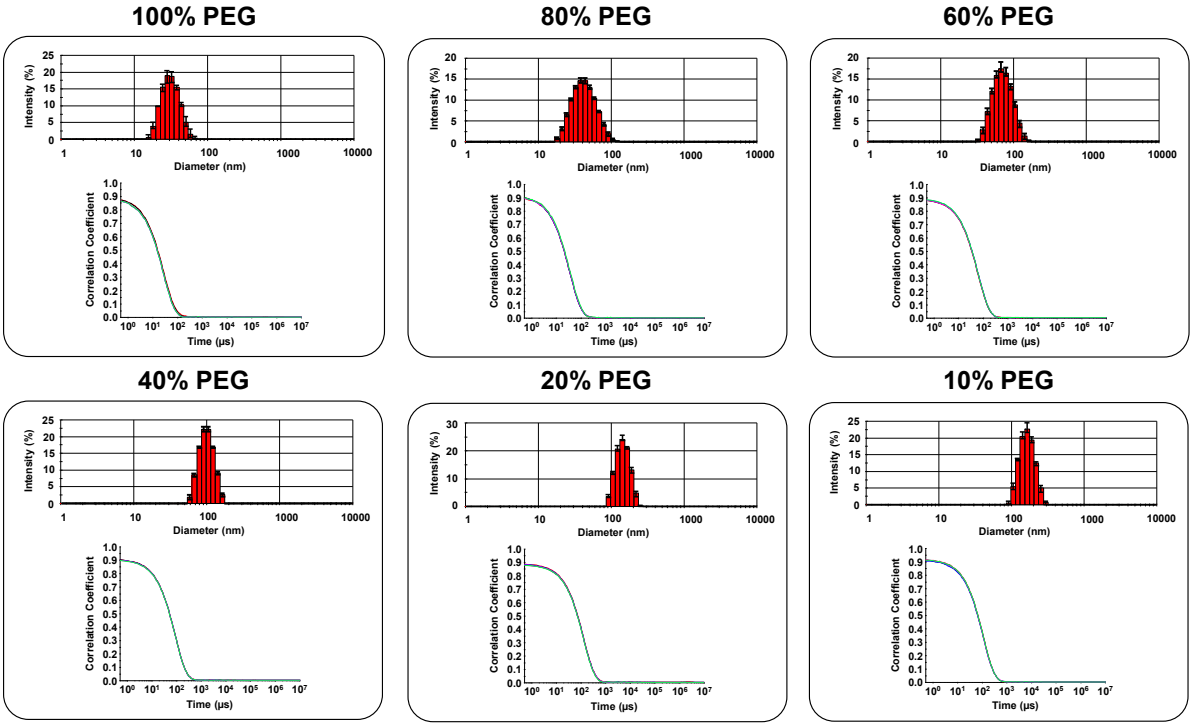

Figure 31. DLS histograms and correlation functions of CAT micelles with different % PEG recorded at 37 ºC immediately after formation.

USC
UNIVERSIDADE DE SANTIAGO DE COMPOSTELA

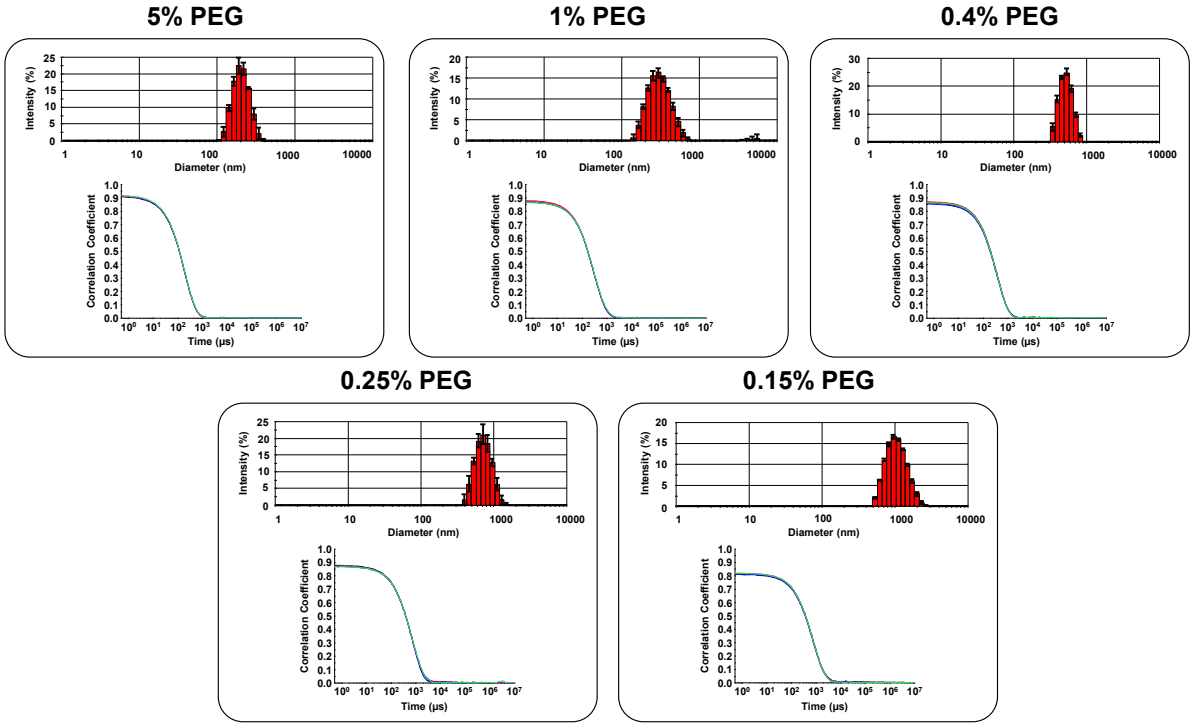

Figure 32. DLS histograms and correlation functions of CAT micelles with different % PEG recorded at 37 ºC immediately after formation.

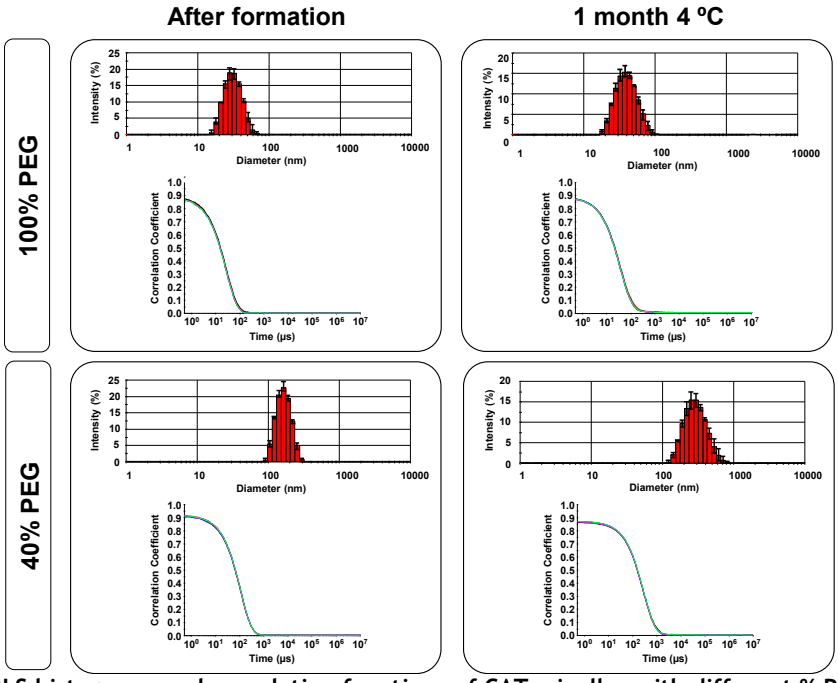

Figure 33. DLS histograms and correlation functions of CAT micelles with different % PEG recorded immediately after formation (37 ºC), and after 1 month of storage at 4 ºC (25 ºC).

USC
UNIVERSIDADE DE SANTIAGO DE COMPOSTELA

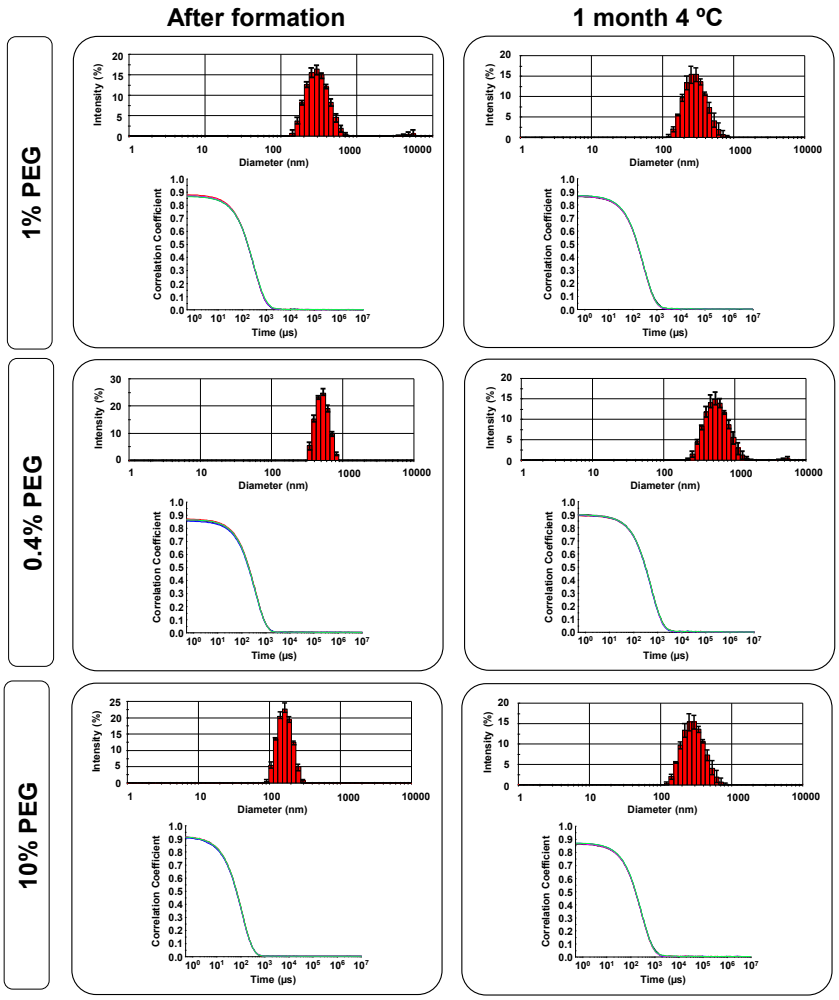

Figure 34. DLS histograms and correlation functions of CAT micelles with different % PEG recorded immediately after formation (37 ºC), and after 1 month of storage at 4 ºC (25 ºC).

USC UNIVERSIDADE DE SANTIAGO DE COMPOSTELA

3.1.4.2 DOX Micelles

Table 5. Mean hydrodynamic radius (*R*, nm) and PDI (in brackets) of DOX micelles obtained immediately after 18 h of formation at 37 ºC, after dialysis, after 24 h at 37 ºC, and after storage for 1 month at 4 ºC.

% PEG	Upon formation (37 ºC)	Dialysis (37 ºC)	24 h at 37 ºC (37 ºC)	1 month at 4 ºC (25 ºC)
100	14 ± 1 (0.16 ± 0.01)	22 ± 1 (0.21 ± 0.01)	27 ± 1 (0.13 ± 0.01)	18 ± 1 (0.28 ± 0.02)
80	27 ± 1 (0.22 ± 0.01)	28 ± 1 (0.28 ± 0.03)	26 ± 1 (0.19 ± 0.01)	-
60	39 ± 1 (0.06 ± 0.01)	41 ± 1 (0.14 ± 0.03)	39 ± 1 (0.09 ± 0.03)	-
40	50 ± 1 (0.05 ± 0.02)	48 ± 1 (0.04 ± 0.01)	43 ± 1 (0.04 ± 0.01)	51 ± 1 (0.05 ± 0.02)
20	71 ± 1 (0.02 ± 0.01)	71 ± 1 (0.03 ± 0.01)	72 ± 1 (0.03 ± 0.01)	-
10	93 ± 9 (0.03 ± 0.01)	92 ± 1 (0.06 ± 0.02)	91 ± 1 (0.04 ± 0.01)	90 ± 1 (0.05 ± 0.02)
3	244 ± 9 (0.14 ± 0.03)	237 ± 5 (0.13 ± 0.02)	254 ± 3 (0.13 ± 0.01)	241 ± 10 (0.16 ± 0.03)
2	294 ± 5 (0.12 ± 0.02)	295 ± 6 (0.07 ± 0.03)	300 ± 16 (0.17 ± 0.02)	289 ± 14 (0.16 ± 0.02)
1	348 ± 12 (0.16 ± 0.02)	345 ± 16 (0.26 ± 0.03)	358 ± 25 (0.21 ± 0.02)	371 ± 40 (0.24 ± 0.05)

USC UNIVERSIDADE DE SANTIAGO DE COMPOSTELA

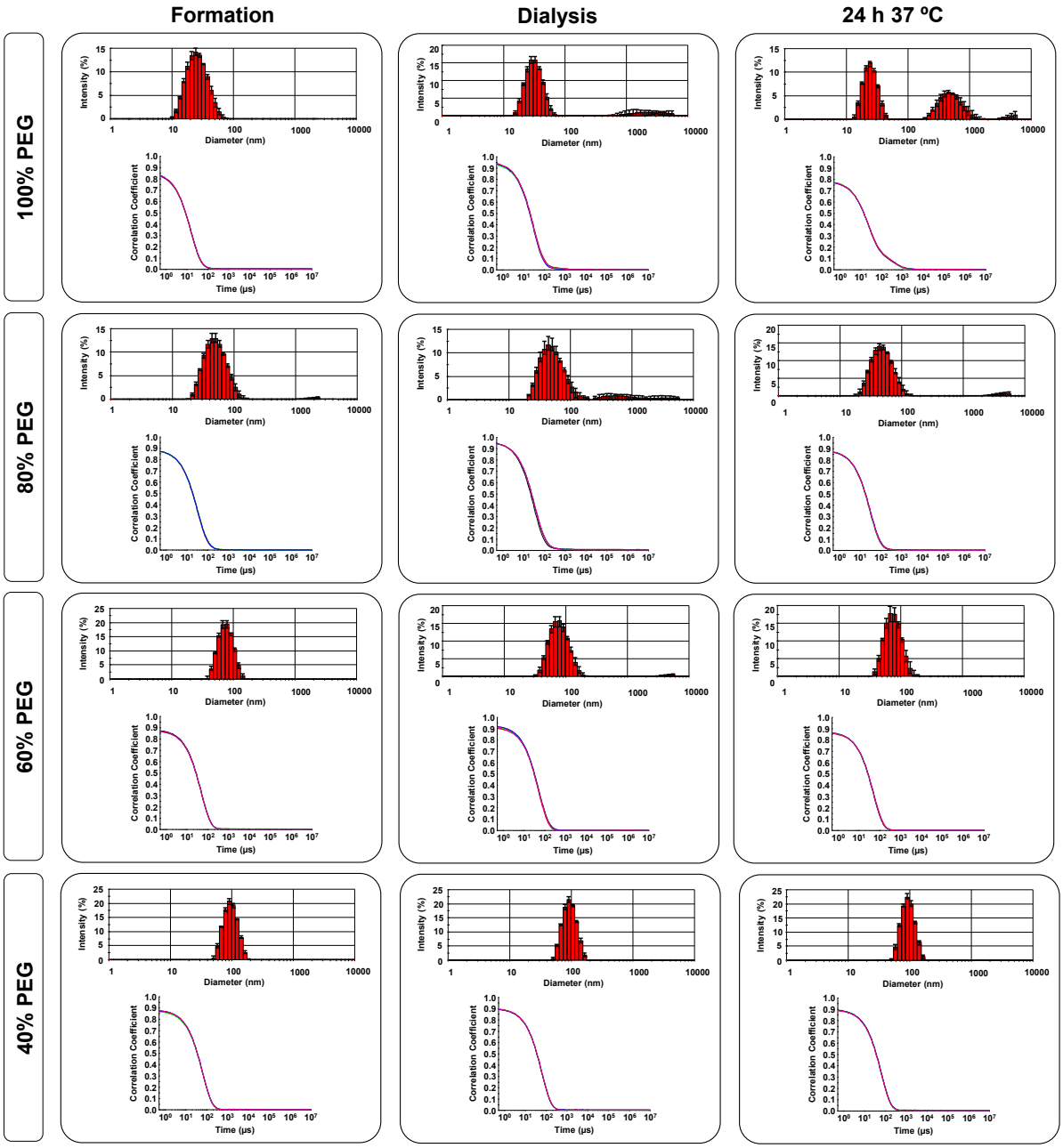

Figure 35. DLS histograms and correlation functions of DOX micelles with different % PEG recorded immediately after formation (37 ºC), after dialysis (37 ºC), and after 24 h at 37 ºC (37 ºC).

USC
UNIVERSIDADE DE SANTIAGO DE COMPOSTELA

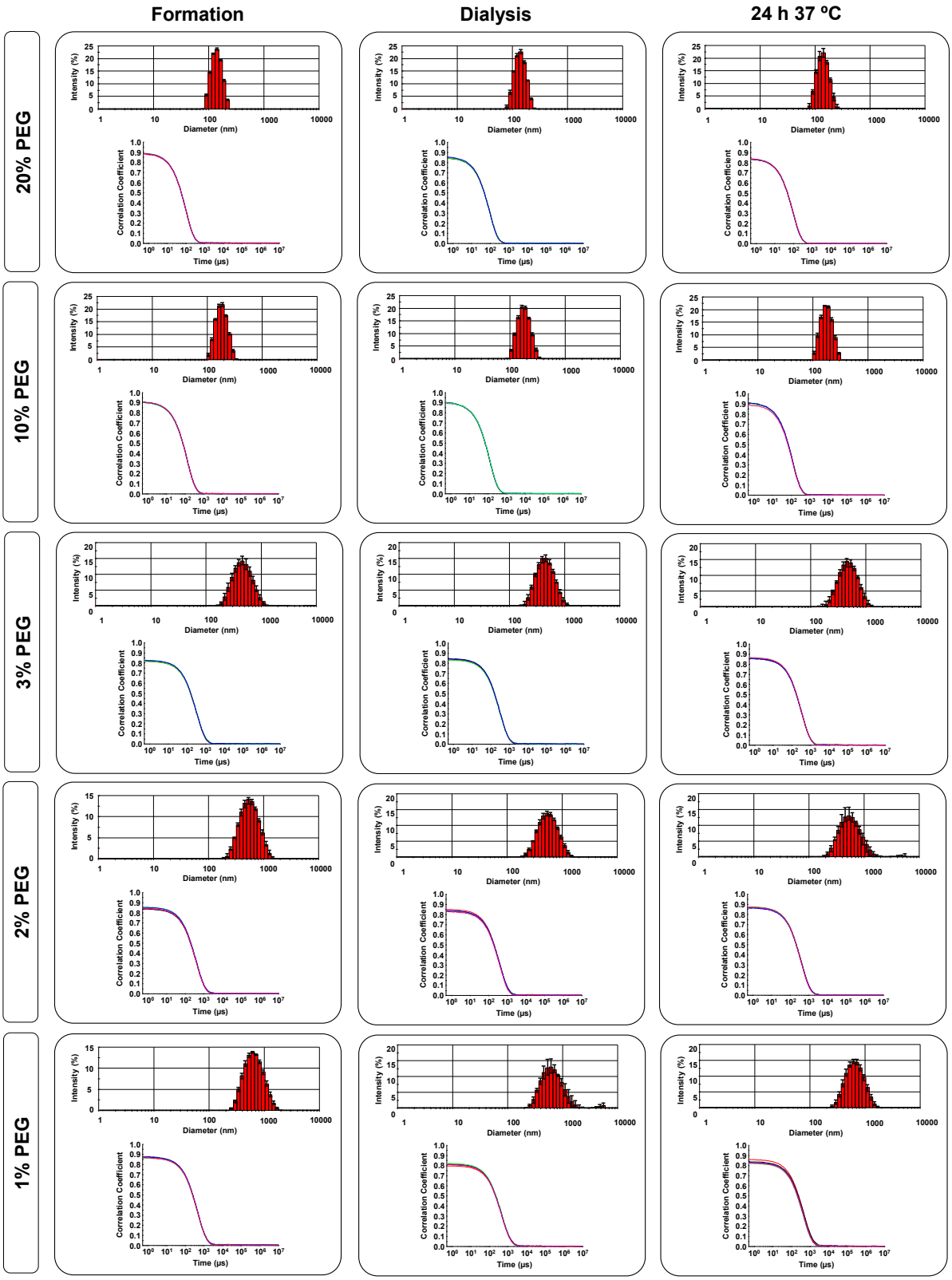

Figure 36. DLS histograms and correlation functions of DOX micelles with different % PEG recorded immediately after formation (37 ºC), after dialysis (37 ºC), and after 24 h at 37 ºC (37 ºC).

USC
UNIVERSIDADE
DE SANTIAGO
DE COMPOSTELA

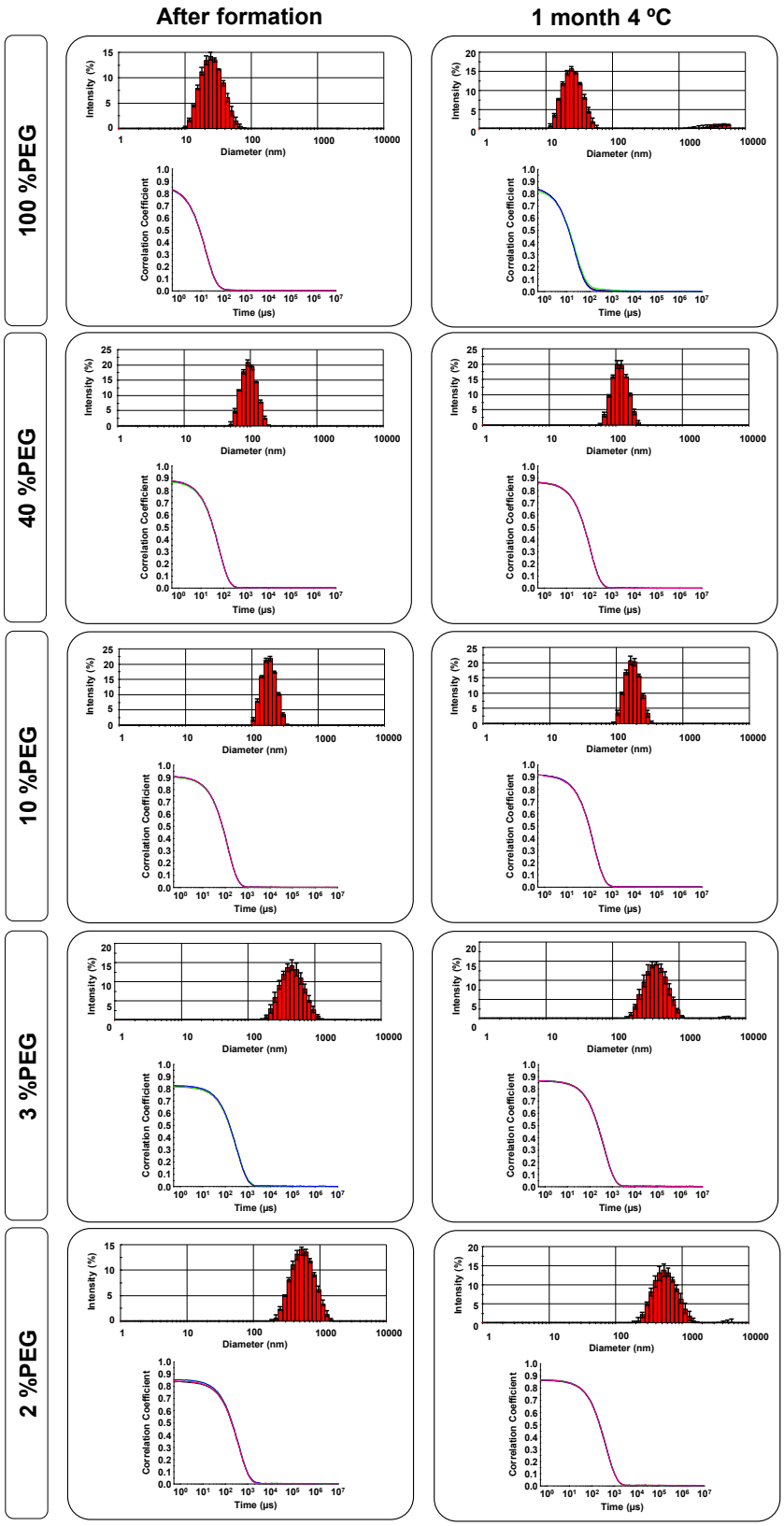

Figure 37. DLS histograms and correlation functions of DOX micelles with different % PEG recorded immediately after formation (37 ºC), and after 1 month of storage at 4 ºC (25 ºC).

USC UNIVERSIDADE DE SANTIAGO DE COMPOSTELA

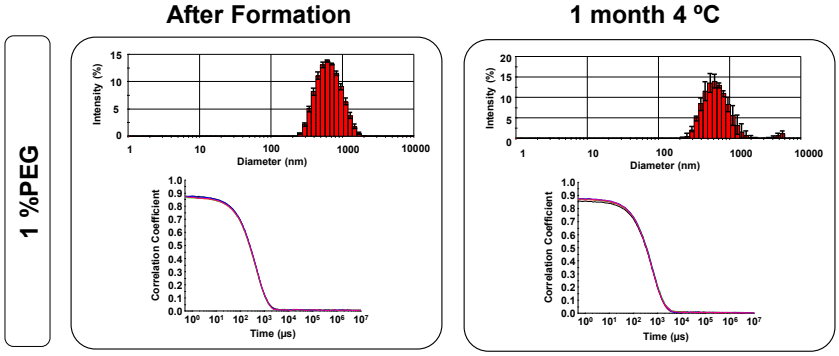

Figure 38. DLS histograms and correlation functions of DOX micelles with different % PEG recorded immediately after formation (37 ºC), and after 1 month of storage at 4 ºC (25 ºC).

3.1.5 Characterization Assays

Alizarin Red Sulfate (ARS) Fluorescence Assay. CAT-micelles were prepared at different %PEG (100 and 5%) following the above-described procedure. Then, micelle solutions (100 µL) were mixed with an ARS solution (100 µL, 0.23 mM, PBS) in 96-well microplates (Nunc F96 MicroWell flat black from Thermo Scientific), keeping the final concentration of ARS and boronic fixed to 0.1 mM and 1.0 mM respectively. Before performing fluorescence measurements, the final mixture containing micelles and ARS was keep under agitation for 1 h at rt protected from light. To confirm the absence of free BA in solution, the emission spectra of the mixtures was recorded by exciting the samples at 495 nm and measuring the fluorescence between 500 and 650 nm. Standard calibration curves were done with solutions of PEG[G3]-BA and 3[G2]-BA solutions at different molar ratios that were treated under the same conditions.

LSCM of Micelles. The micellar structures of CAT and DOX micelles were analyzed by LSCM by measuring FITC-PEG[G3]-BA and DOX fluorescence, respectively. Briefly, 100 µL of the corresponding micelle solution were transferred to Cellvis 4-Chamber microwells (35mm Glass Bottom Dish with 20 mm, #1.5 cover glass) and imaged with an Andor Dragonfly spinning disk confocal system mounted on a Nikon TiE microscope equipped with a Zyla 4.2 PLUS sCMOS digital camera (Andor, Oxford Instruments). Once an area containing a representative population of micelles was identified, images were obtained in triplicates. Filtering of samples before LSCM analysis was avoided to prevent the removal of larger assemblies or aggregates that could obscure analysis.

Release study of DOX. DOX micelles were prepared as described above and dialyzed (Spectra/Por 6, MWCO 1 kDa; 0.5 mL of micelles against 125 mL of PBS, 6 h, 37 °C, in the dark) to remove the nonencapsulated drug. Then, dialysis bags were transferred to new buffer solutions: (i) 125 mL of 50 mM PB pH 7.4, 150 mM NaCl, (ii) 125 mL of 50 mM PB pH 6.8, 150 mM NaCl, and (iii) 125 mL of 50 mM acetate buffer pH 5.0, 150 mM NaCl, and dialysis continued at 37 °C in the dark. At fixed times, aliquots (100 µL) were taken and placed in 96-well microplates (Nunc F96 MicroWell flat black from Thermo Scientific; done in triplicate). Then, 500 mM acetate buffer pH 4.0 (100 µL) were added to each well and the fluorescence of the samples was measured in a microplate reader (λ_{ex} 485 nm, λ_{em} 535 nm; Tecan Infinite F200 PRO). The amount of released DOX was determined by comparison with a standard calibration

USC UNIVERSIDADE DE SANTIAGO DE COMPOSTELA

curve made from the fluorescence emission of fresh solutions of DOX of known concentration prepared under identical conditions.

3.1.6 Cell Studies

Cell Cultures. Glial-like F98 cells, obtained from the American Type Culture Collection ATCC, were cultured at 37 °C in a 5% CO_2 atmosphere in DMEM with high glucose, containing 10% FBS and supplemented with 50 U/mL penicillin and 50 U/mL streptomycin, in 75 cm^2 cell culture flasks. All cell experiments were performed at 37 °C in a 5% CO^2 atmosphere with this modified DMEM, simply referred as "medium".

Cell Viability. DOX micelles were prepared at different % PEG (100, 40 and 2) following the above-described procedure and dialyzed (Spectra/Por 6, MWCO 1 kDa; 1 mL of micelles against 250 mL PBS, 6 h, 37 °C, in the dark) to remove nonencapsulated DOX. Then, samples were diluted with medium to reach final DOX concentrations between 30 and 0.1 μM. F-98 cells were seeded in 96-well culture plates (Corning Costar 96-Well microplates from Thermo Scientific) at a density of 75000 cells/mL. After 24 h of incubation, medium was replaced with the solutions of micelles (100 μL). After 24 and 48 h of incubation, cell viability was determined by a colorimetric assay with CCK-8 following the manufacturer's protocol. After 2 h of incubation at 37 °C in 5% CO_2 with a 6% solution of CCK-8 in fresh medium, supernatant solution was transferred to a new 96-well plate. Viability was determined by measuring the supernatant absorbance at 450 nm in a plate reader Tecan Infinite F200 PRO. Absorbance (A) from a 6% CCK-8 solution in medium was subtracted from all data points. Results show the average and standard deviation of three independent experiments. Viability was calculated as follows:

$$\text{Cell Viability (\%)} = 100 \times \frac{(A_{\text{sample}} - A_{6\%\ \text{CCK-8}})}{(A_{\text{control}} - A_{6\%\ \text{CCK-8}})}$$

Control cell viability experiments were conducted with PEG[G3]-BA, 3[G2]-BA, and free DOX at concentrations of these components found in the micelle samples.

Intracellular Trafficking by LSCM. DOX Micelles were prepared at different % PEG (100, 40 and 2%) following the above-described procedure and dialyzed (Spectra/Por 6, MWCO 1 kDa; 1 mL of micelles against 250 mL PBS, 6 h, 37 °C, in the dark) to remove nonencapsulated DOX. F-98 cells were seeded in 24-well glass bottom 15 mm plates (Cellvis) at a density of 100000 cells/mL in 500 μL of medium. After 24 h of incubation at 37 °C in 5% CO_2, medium was replaced by a solution of 30 μL of the corresponding DOX micelle in 470 μL of medium, and incubation was continued at 37 ºC for 30 min. Afterwards, medium was removed, and fresh medium was added to the cell culture plates. Cells were left incubating at 37 ºC for 1 h or 2 h. Half an hour before observation, acidic organelles were stained by adding 10 μL of 10 μM LysoTracker Green and nuclei were stained by adding 10 μL of 200 μM Hoechst 33258. Before observation, medium was replaced with fresh medium. Confocal images were obtained on an Andor Dragonfly spinning disk confocal system mounted on a Nikon TiE microscope equipped with a Zyla 4.2 PLUS sCMOS digital camera (Andor, Oxford Instruments) and an OKO-lab incubator to maintain cells at 37 °C. Samples were excited with three different lasers (405, 561, and 637 nm) and the emitted fluorescence was collected by the filter wheel (450/50 nm, 620/50 nm, and 725/40 nm) with appropriate combinations of them.

USC UNIVERSIDADE DE SANTIAGO DE COMPOSTELA

Internalization Studies by Flow Cytometry. F-98 cells were seeded in a 24-well culture plate (Corning Costar 96-Well microplates from Thermo Scientific) at a density of 100000 cells/mL in 500 μL of medium. After 24 h of incubation at 37 °C in 5% CO_2, medium was replaced with by a solution of 30 μL of the corresponding DOX micelle in 470 μL of medium. After 30 min of incubation at 37 °C in 5% CO_2, medium was removed, and fresh medium was added to the cell culture plates and incubation was continued at 37 ºC for 1 h. Then, cells were washed with PBS (3 × 500 μL) and trypsinized (100 μL 0.25% Trypsin–EDTA) for 5 min followed by trypsin quenching with 350 μL of serum-supplemented PBS. Then, cells were transferred to 96-well plates and analyzed by flow cytometry collecting at least 5000 events per well using a Guava Millipore flow cytometer equipped with a 488 nm blue laser coupled with a 525/30 nm filter. All reported data represent the average of at least three independent experiments. Data analysis was performed with InCyte software included in Millipore GuavaSoft 3.2 or with FlowJo. Gating was conducted by performing control experiments in which cells were untreated or treated with CAT micelles (100% PEG).

USC
UNIVERSIDADE DE SANTIAGO DE COMPOSTELA

3.2 Experimental data for Dynamic Boronate Chemistry Accelerates the Screening of Polymeric Gene Delivery Vehicles *via In Situ* Complexation of Nucleic Acids.

*The results from this section have already been published as Bruno Delgado Gonzalez,[a] Roi Lopez-Blanco,[a] Samuel Parcero-Bouzas,[a] Natalia Barreiro-Piñeiro,[b] Lucas Garcia-Abuin,[a] and Eduardo Fernandez-Megia[a]. Dynamic Covalent Boronate Chemistry Accelerates the Screening of Polymeric Gene Delivery Vectors via *In Situ* Complexation of Nucleic Acids. *J. Am. Chem. Soc.* **2024**, 146, 17211-17219. https://doi.org/10.1021/jacs.4c03384

[a] Centro Singular de Investigación en Química Biolóxica e Materiais Moleculares (CIQUS), Departamento de Química Orgánica, Universidade de Santiago de Compostela, Jenaro de la Fuente s/n, 15782 Santiago de Compostela, Spain

[b] Centro Singular de Investigación en Química Biolóxica e Materiais Moleculares (CIQUS), Departamento de Bioquímica e Bioloxía Molecular, Universidade de Santiago de Compostela, Jenaro de la Fuente s/n, 15782 Santiago de Compostela, Spain

3.2.1 Materials

DMEM, FBS, penicillin, streptomycin, LP 2000, and LysoTracker Red DND-99 were purchased from Invitrogen Thermo Fisher. Hoechst 33258 was purchased from Sigma Aldrich. Cy5 Label IT Nucleic Acid Labelling Kit was purchased from Mirus. All other chemicals were purchased from Acros Organics, Fluka, Sigma-Aldrich, or Thermo Fisher Scientific, unless otherwise noted. All solvents were HPLC grade, purchased from Scharlab, or Sigma-Aldrich. DMF and CH_3CN were dried using a SPS800 solvent purification system from MBRAUN. Et_3N was dried under 4Å molecular sieves. H_2O was of Milli-Q grade obtained using a Millipore water purification system. Thin-layer chromatography (TLC) was done on silica ($60F_{254}$ from Merck) aluminum-backed plates. 1-(3,4-dihydroxyphenethyl)guanidine hydrochloride (Cat-G) and 3-(2,2-dimethylbenzo[d][1,3]dioxol-5-yl)propanoic acid were prepared following known procedures.[150,151] PEG[G3]-N_3 and 3[G2]-N_3 were prepared following procedures previously described by our group.[152, 153]

3.2.2 Instrumentation

NMR Spectroscopy. NMR spectra were recorded on Varian Mercury 300 MHz or Bruker DRX 500 MHz spectrometers. Chemical shifts (δ) are reported in ppm relative to the residual solvent peak (7.26 ppm for $CDCl_3$, 4.79 ppm for D_2O, 3.31 ppm for CD_3OD, 2.50 ppm for DMSO-d_6, 1.94 ppm for CD_3CN). MestReNova 14.2.2 software (Mestrelab Research) was used for spectral processing.

Infrared Spectroscopy. FT-IR spectra were recorded on a Perkin-Elmer Spectrum Two equipped with a UATR accessory.

Determination of pH Values. pH values were measured with a portable pH-meter (Crison PH25) connected to a glass electrode (Crison 52 09).

USC UNIVERSIDADE DE SANTIAGO DE COMPOSTELA

Dialysis and Ultrafiltration. Dialysis was performed with a 18 mm Spectra/Por 6 MWCO 1 kDa membrane tubing from SpectrumLabs. Ultrafiltration was performed on Amicon Ultra-15 Centrifugal Filter Unit MWCO 3 kDa from Sigma-Aldrich.

Zeta Potential. Zeta potential values of polyplexes were measured by laser doppler anemometry (LDA), measuring the mean electrophoretic mobility (Malvern Zetasizer Nano ZS, Malvern Instruments). Measurements were performed in 10 mM HEPES pH 7.1 using the Smoluchowski approximation.

Column Chromatography. Automated column chromatography was performed on a MPLC Teledyne ISCO CombiFlash RF 200 psi. Samples were adsorbed onto silica 40-63 μm from VWR Chemicals and loaded into solid cartridges. RediSep Rf 12 g columns refilled with silica 40-63 μm from VWR Chemicals were used.

Transmission Electron Microscopy (TEM). TEM measurements were performed on a JEOL JEM-1011 operated at 100 kV electron microscope equipped with a camera S5 MegaView G2. A drop of a solution of polyplexes (0.37 mg/mL) was settled on a TEM carbon type-B film copper grid (Ted Pella, Inc.) and allowed to dry at room temperature for 12 h. Size of polyplexes were determined with ImageJ software (version 1.51j8) measuring the line intensity profile across the assemble. Average diameters were obtained by measuring the size of a representative number of polyplexes.

Mass Spectrometry. Mass spectra were recorder on a Bruker MicroTOF spectrometer using electrospray ionization (ESI) in negative or positive modes. Samples were dissolved in $CHCl_3/CH_3OH$ or CH_3OH acidified with 0.1% formic acid, and injected *via* flow injection analysis (FIA) using a 1:1 CH_3OH/0.1% formic acid aq solution, flow 0.2 mL/min.

Fluorescence Microscopy. Fluorescence microscopy was performed using a Nikon Eclipse TiE microscope. Images were processed with ImageJ (1.51j8) software.

LSCM. Confocal images were obtained on an Andor Dragonfly spinning disk confocal system mounted on a Nikon TiE microscope equipped with a Zyla 4.2 PLUS sCMOS digital camera (Andor, Oxford Instruments) and an OKO-lab incubator to maintain cells at 37 °C.

USC
UNIVERSIDADE DE SANTIAGO DE COMPOSTELA

3.2.3 Synthesis and Characterization of New Compounds

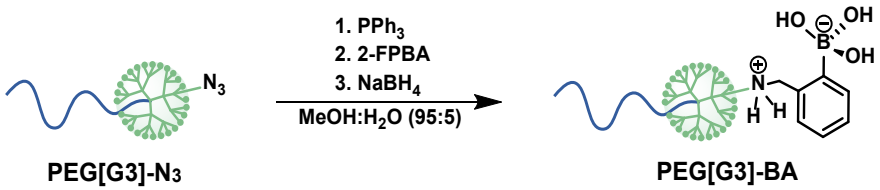

PEG[G3]-BA. PPh_3 (60.0 mg, 0.23 mmol) was added to a solution of PEG[G3]-N_3 (100.0 mg, 7.70 µmol) in MeOH:H_2O (95:5, 2.1 mL). The mixture was stirred at rt for 12 h and then, 2-formylphenylboronic acid (46.7 mg, 0.31 mmol; 2-FPBA) was added. Stirring was continued for 12 h at rt before the addition of $NaBH_4$ (11.8 mg, 0.31 mmol). After 4 h of stirring at rt, the solvent was evaporated. The crude product was dissolved in H_2O and purified by dialysis [8 × 1 L MeOH:H_2O (2:3), 8 × 1 L H_2O; MWCO 1 kDa, Spectra/Por 6]. After freeze-drying, PEG[G3]-BA (89.3 mg, 73%) was obtained as a white solid.

^{1}H NMR (500 MHz, D_2O) δ: 7.40-7.37 (m, 27H), 7.18-6.94 (m, 105H), 4.15-3.51 (m, ~1028H), 3.42 (s, 3H), 3.25 (br s, 2H), 3.04 (br s, 54H). ^{13}C NMR (125 MHz, D_2O) δ: 168.4, 151.5, 145.5, 140.9, 139.3, 128.9, 127.4, 126.9, 122.4, 106.0, 71.9, 70.9, 69.8, 69.5, 68.9, 68.1, 66.7, 66.6, 58.0, 52.4, 45.6, 39.6, 39.3. IR (ATR, cm^{-1}): 3437, 2874, 1714, 1352, 1113. MALDI-TOF MS (DHB, linear mode) *m/z*: M_p 15192, M_n 15010, M_w 15052.

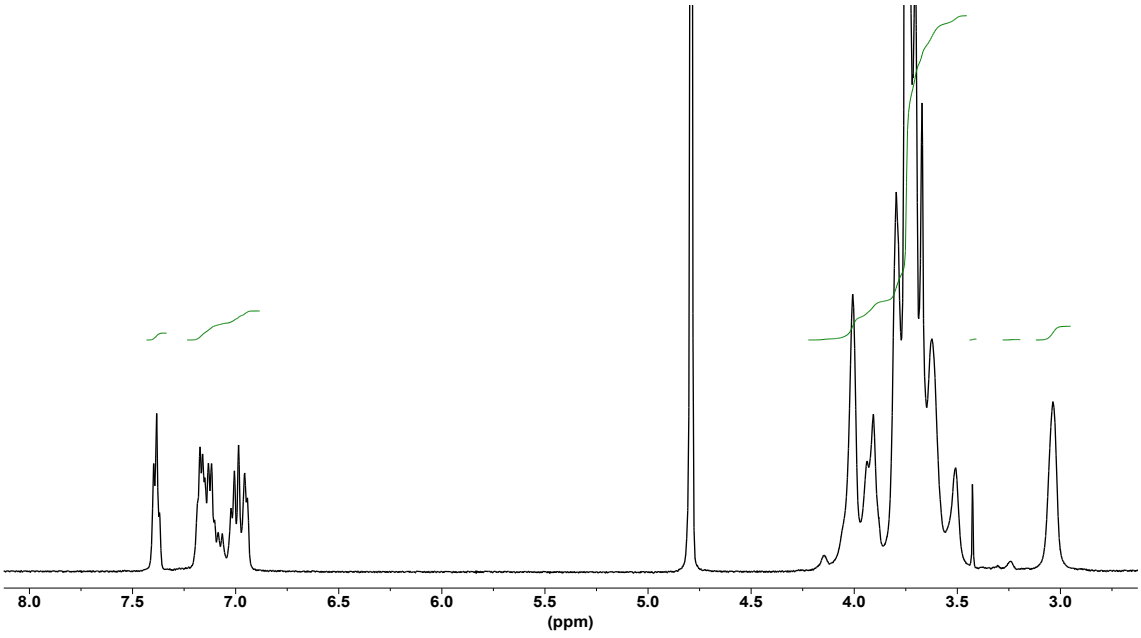

Figure 39. ^{1}H NMR spectrum (D_2O, 500 MHz) of PEG[G3]-BA.

USC
UNIVERSIDADE DE SANTIAGO DE COMPOSTELA

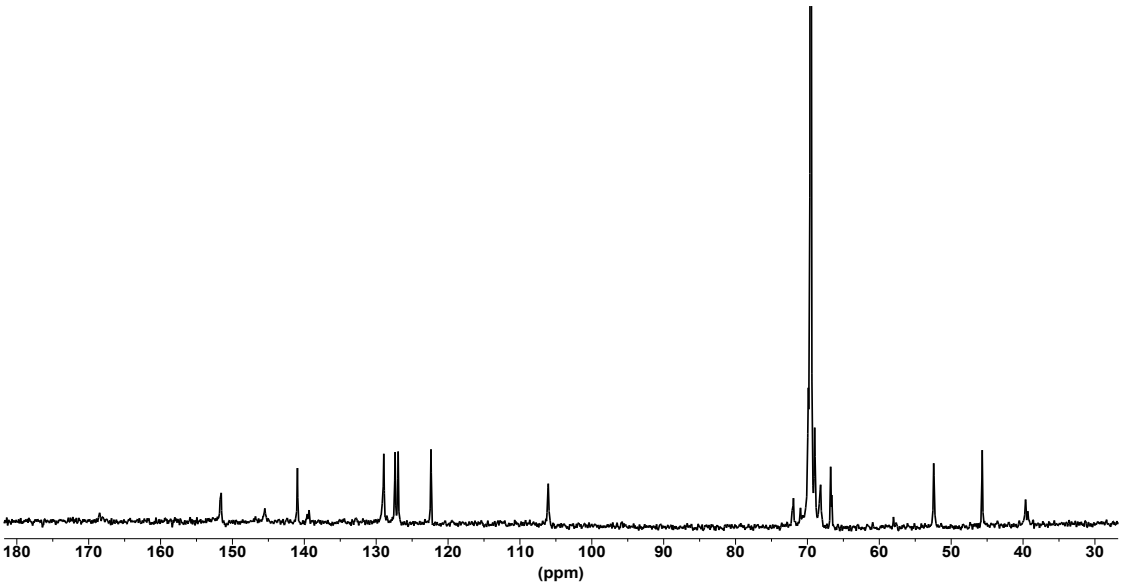

Figure 40. ^{13}C NMR spectrum (D_2O, 125 MHz) of PEG[G3]-BA.

Figure 41. IR spectrum of PEG[G3]-BA.

USC
UNIVERSIDADE DE SANTIAGO DE COMPOSTELA

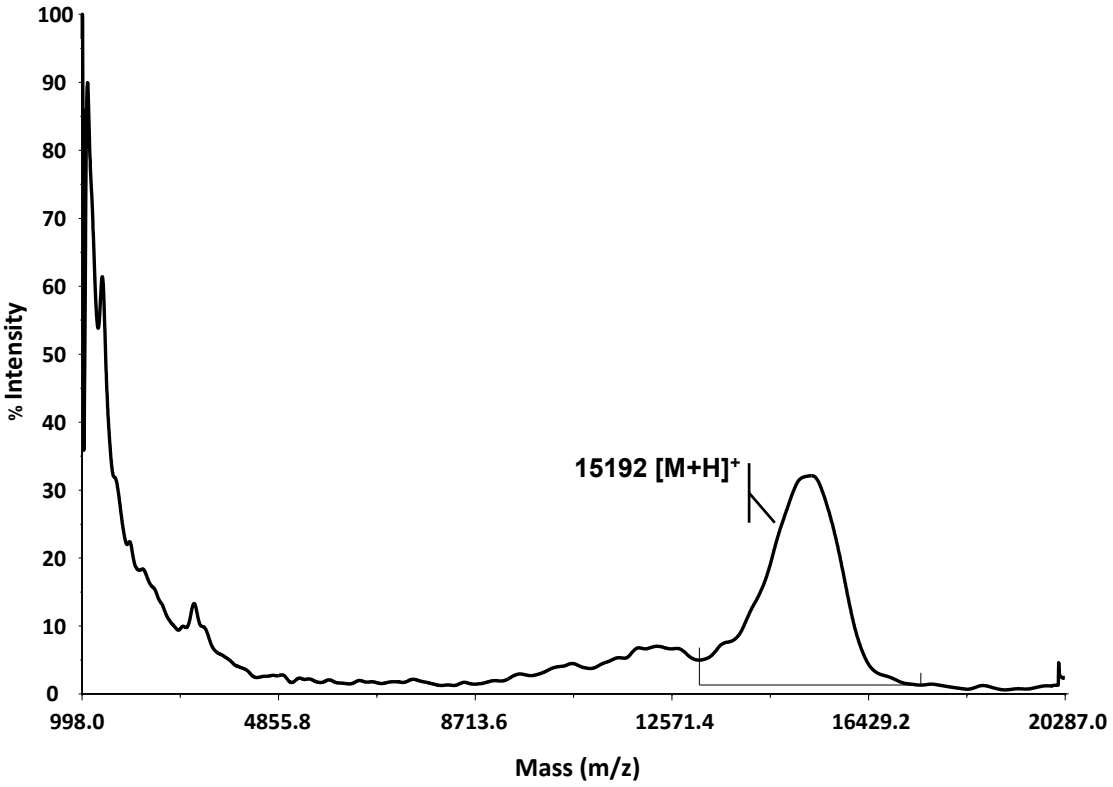

Figure 42. MALDI-TOF MS of PEG[G3]-BA.

USC
UNIVERSIDADE DE SANTIAGO DE COMPOSTELA

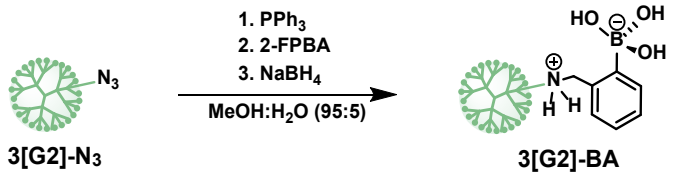

3[G2]-BA. PPh_3 (60.1 mg, 0.23 mmol) was added to a solution of 3[G2]-N_3 (60.0 mg, 7.70 µmol) in MeOH:H_2O (95:5, 2 mL). The mixture was stirred at rt for 12 h and then, 2-formylphenylboronic acid (46.8 mg, 0.31 mmol; 2-FPBA) was added. Stirring was continued for 12 h at rt before the addition of $NaBH_4$ (12.0 mg, 0.31 mmol). After 4 h of stirring at rt, the solvent was evaporated, and the crude product was dissolved in H_2O (10 mL). Then, 1 M HCl was added till pH 3. The resulting solution was washed with $CHCl_3$ (6 × 20 mL) and purified by dialysis [1 L MeOH:H_2O (2:1), 2 × 1 L H_2O; MWCO 1 kDa, Spectra/Por 6]. After freeze-drying, 3[G2]-BA (74.0 mg, 87 %) was obtained as a white solid.

^{1}H NMR (500 MHz, CD_3OD) δ: 7.41-7.36 (m, 27H), 7.10-7.08 (m, 81H), 7.08-7.01 (m, 24H), 6.02 (s, 3H), 4.15-3.91 (m, 138H), 3.83-3.41 (m, ~561H), 3.07-2.97 (m, 54H). ^{13}C NMR (125 MHz, CD_3OD) δ: 169.2, 161.5, 153.1, 142.4, 141.2, 130.7, 128.3, 127.6, 123.5, 107.4, 95.3, 73.2, 71.3, 71.1, 70.9, 70.4, 69.5, 67.8, 54.0, 47.5, 40.7. IR (ATR, cm^{-1}): 3326, 2874, 1582, 1334, 1103.

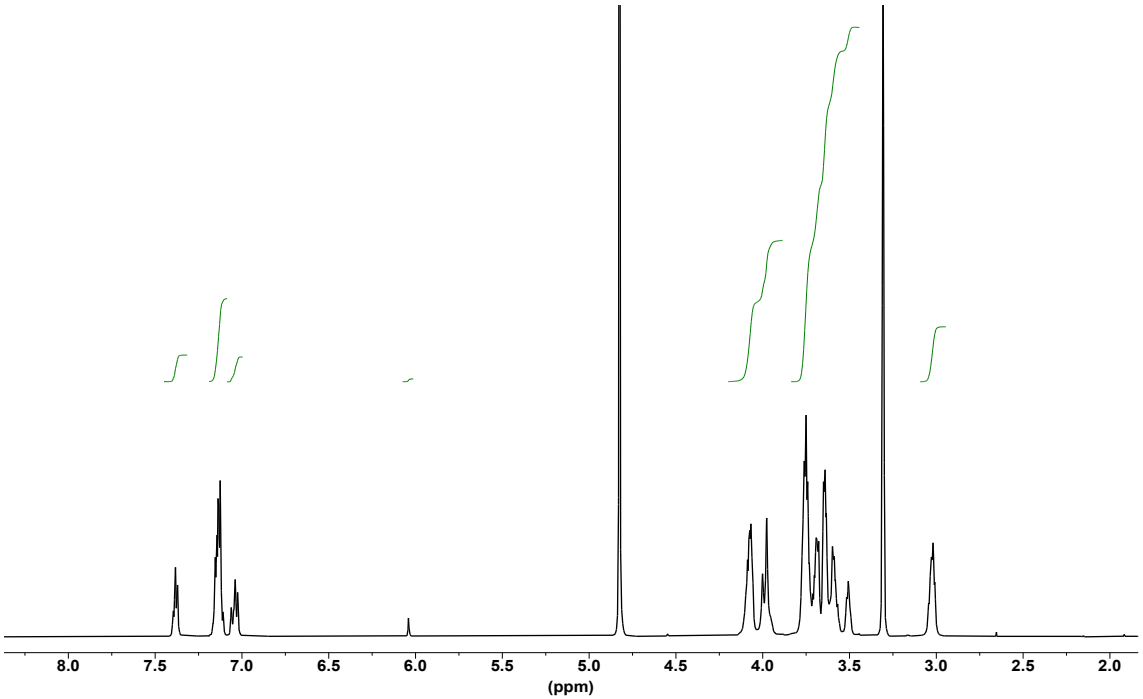

Figure 43. ^{1}H NMR spectrum (CD_3OD, 500 MHz) of 3[G2]-BA.

USC
UNIVERSIDADE DE SANTIAGO DE COMPOSTELA

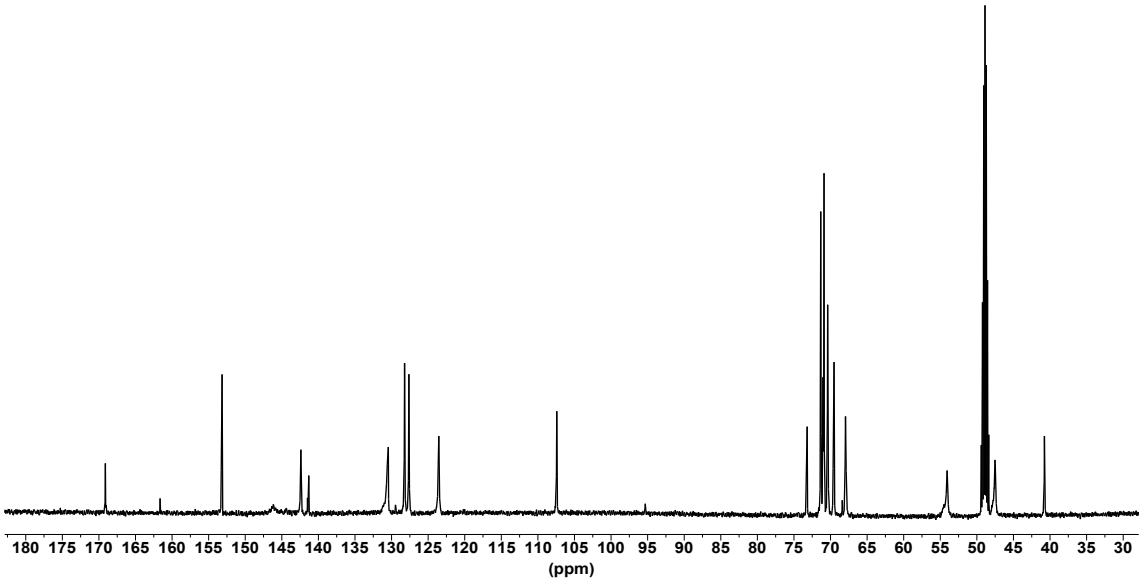

Figure 44. ^{13}C NMR spectrum (CD_3OD, 125 MHz) of 3[G2]-BA.

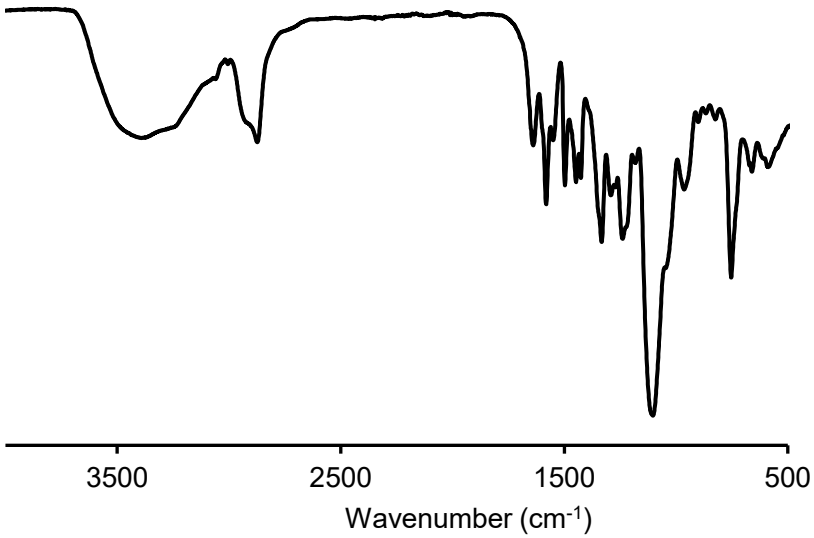

Figure 45. IR spectrum of 3[G2]-BA.

USC
UNIVERSIDADE DE SANTIAGO DE COMPOSTELA

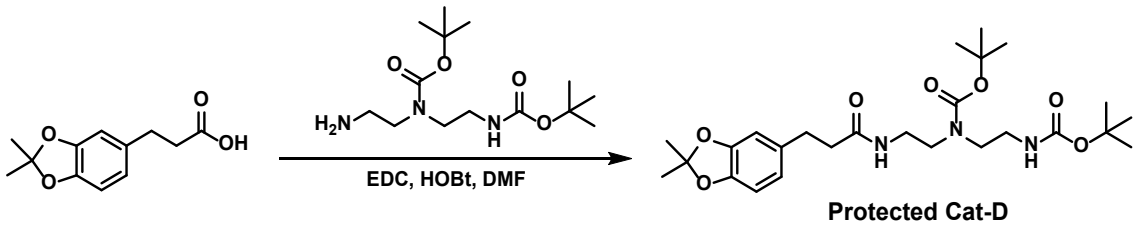

Tert-butyl(2-((tert-butoxycarbonyl)amino)ethyl)(2-(3-(2,2-dimethylbenzo[*d*][1,3]dioxol-5-yl)propanamido)ethyl)carbamate (Protected Cat-D). HOBt (19.0 mg, 0.14 mmol), EDC·HCl (27.0 mg, 0.14 mmol), and tert-butyl (2-aminoethyl)(2-((tert-butoxycarbonyl)amino)ethyl)carbamate (43.0 mg, 0.20 mmol) were added to a solution of 3-(2,2-dimethylbenzo[d][1,3]dioxol-5-yl)propanoic acid (25.0 mg, 0.10 mmol) in anhydrous DMF (1.15 mL). After stirring overnight at rt under Ar, the reaction mixture was diluted with EtOAc (50 mL) and sequentially washed with 0.1 M HCl (3 × 50 mL), sat $NaHCO_3$ (3 × 50 mL), and brine (50 mL). The organic layer was dried ($MgSO_4$) and concentrated. The crude product was purified by automated MPLC (gradient from hexane to 50% EtOAc:hexane, silica, 15 min) to afford Protected Cat-D (30.1 mg, 65%) as a pale-yellow oil.

^{1}H NMR (500 MHz, DMSO-d_6) δ: 7.80-7.77 (m, 1H), 6.85-6.72 (m, 1H), 6.67 (td, J = 7.9, 1.7 Hz, 2H), 6.57 (dd, J = 7.9, 1.7 Hz, 1H), 3.13 (br s, 6H), 3.00 (br s, 2H), 2.68 (t, J = 6.7 Hz, 2H), 2.33-2.25 (m, 2H), 1.59 (s, 6H), 1.39 (s, 9H), 1.36 (s, 9H). ^{13}C NMR (125 MHz, CD_3CN) δ: 172.5, 171.5, 156.7, 148.2, 146.3, 135.7, 121.5, 118.6 108.9, 108.1, 80.3, 79.1, 60.9, 39.9, 38.9, 31.9, 28.5, 28.4, 25.8, 21.0, 14.4. IR (ATR, cm^{-1}): 3320, 2934, 1582, 1668, 1244, 1154. ESI-HRMS (*m/z*): 508.3004 Calcd. for $[M+H]^+$, $C_{26}H_{42}N_3O_7^+$: 508.3017.

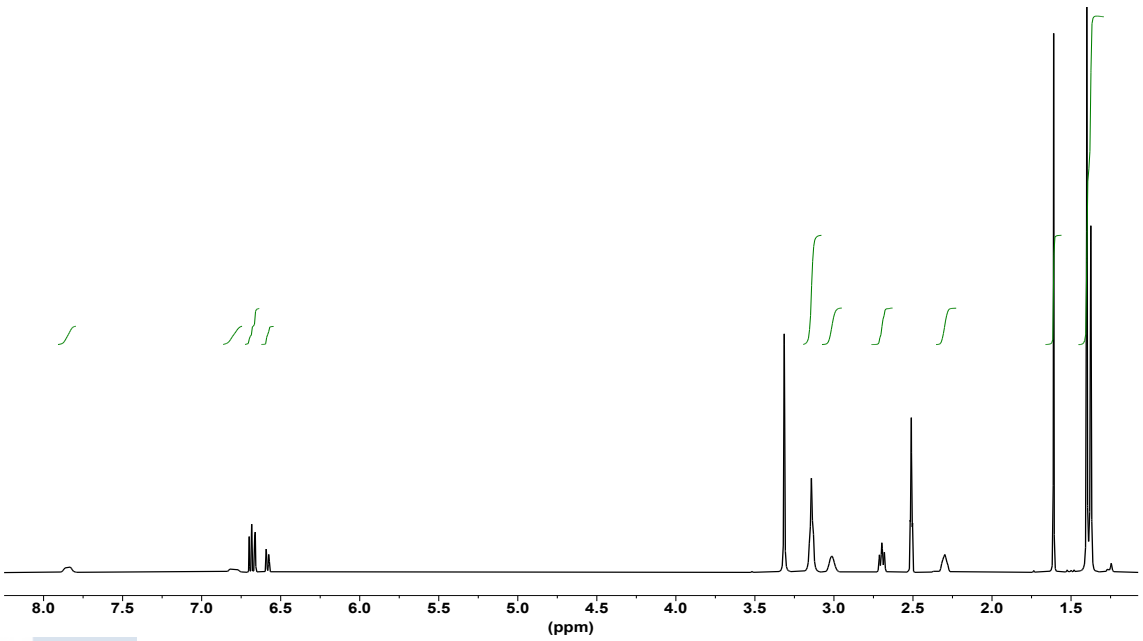

Figure 46. ^{1}H NMR spectrum (DMSO-d_6, 500 MHz) of Protected Cat-D.

USC UNIVERSIDADE DE SANTIAGO DE COMPOSTELA

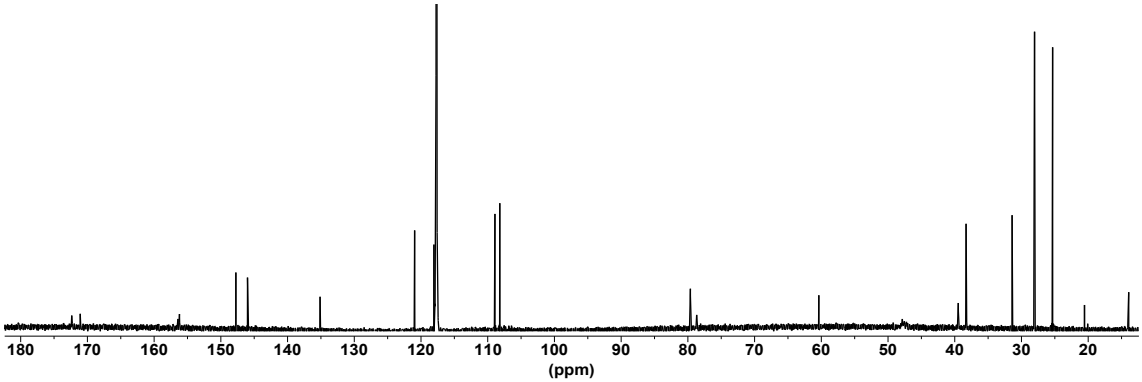

Figure 47. ^{13}C NMR spectrum (CD_3CN, 125 MHz) of Protected Cat-D.

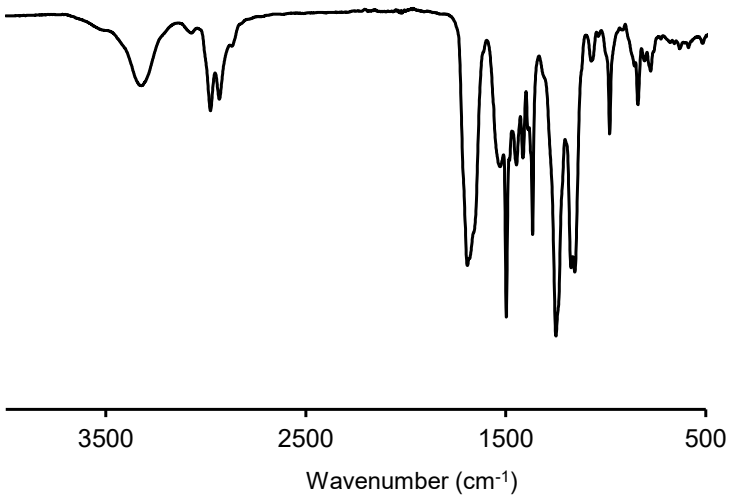

Figure 48. IR spectrum of Protected Cat-D.

USC
UNIVERSIDADE DE SANTIAGO DE COMPOSTELA

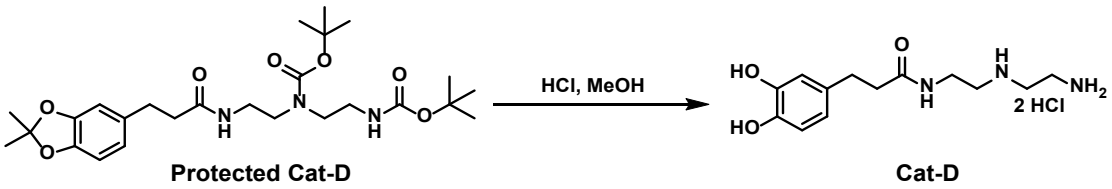

***N*-(2-((2-aminoethyl)amino)ethyl)-3-(3,4-dihydroxyphenyl)propanamide hydrochloride (Cat-D).** Protected Cat-D (24.0 mg, 46.1 μmol) was dissolved in a mixture of CH_3OH (1.8 mL) and 37% HCl (0.45 mL). After 5 h of stirring at rt, the mixture was concentrated to afford Cat-D (13.8 mg, 88%) as a pale-yellow foam.

^{1}H NMR (500 MHz, CD_3OD) δ: 6.67 (td, J = 8.1, 2.1 Hz, 2H), 6.55 (dd, J = 8.1, 2.1 Hz, 1H), 3.49 (t, J = 5.8 Hz, 2H), 3.46-3.43 (m, 4H), 3.19 (t, J = 5.8 Hz, 2H), 2.78 (t, J = 6.9 Hz, 2H), 2.49 (t, J = 6.9 Hz, 2H). ^{13}C NMR (125 MHz, CD_3OD) δ: 177.6, 147.0, 145.4, 134.7, 121.2, 117.3, 117.1, 50.1, 46.4, 39.8, 37.8, 37.6, 32.5. IR (ATR, cm^{-1}): 3027, 1642, 1280, 1233. ESI-HRMS (*m/z*): 268.1655 Calcd. for $[M+H]^+$, $C_{13}H_{22}N_3O_3^+$: 268.1656.

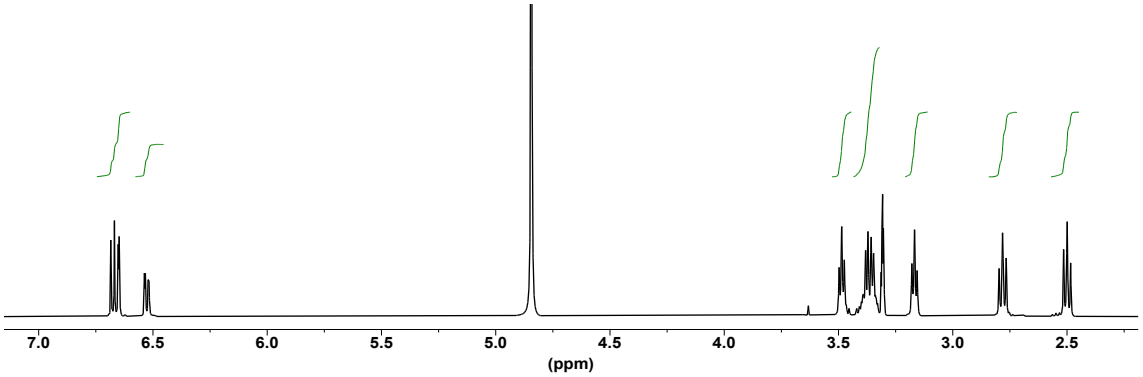

Figure 49. ^{1}H NMR spectrum (CD_3OD, 500 MHz) of Cat-D.

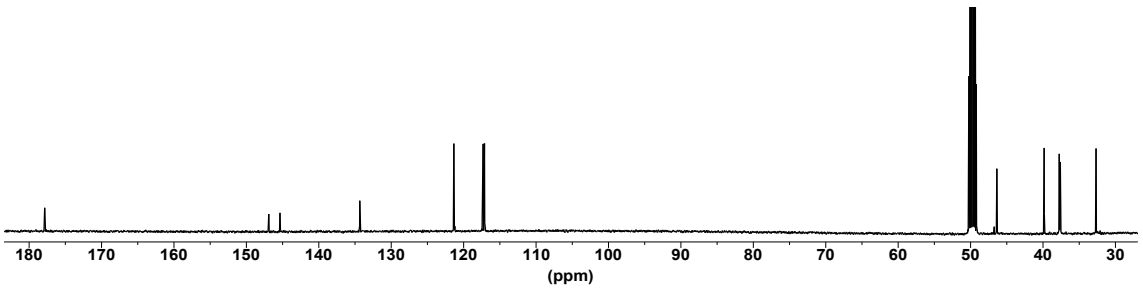

Figure 50. ^{13}C NMR spectrum (CD_3OD, 125 MHz) of Cat-D.

USC
UNIVERSIDADE DE SANTIAGO DE COMPOSTELA

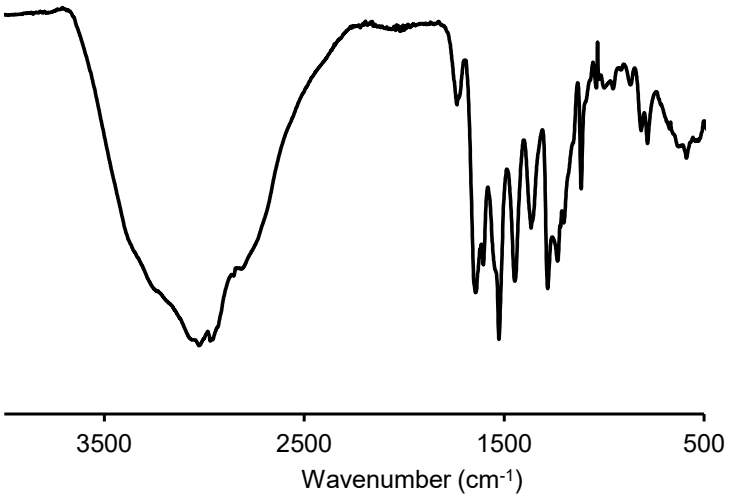

Figure 51. IR spectrum of Cat-D.

USC
UNIVERSIDADE DE SANTIAGO DE COMPOSTELA

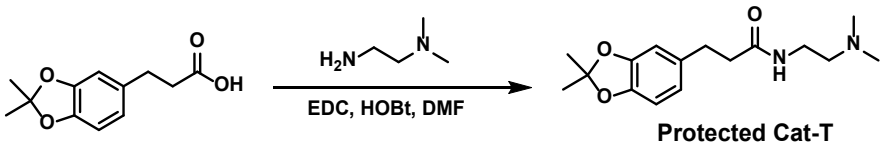

***N*-(2-(dimethylamino)ethyl)-3-(2,2-dimethylbenzo[*d*][1,3]dioxol-5-yl)propanamide (Protected Cat-T).** HOBt (48.6 mg, 0.36 mmol), EDC·HCl (69.0 mg, 0.36 mmol), and *N*,*N*-dimethylethylenediamine (40 µL, 0.36 mmol) were added to a solution of 3-(2,2-dimethylbenzo[d][1,3]dioxol-5-yl)propanoic acid (40.0 mg, 0.18 mmol) in anhydrous DMF (1.80 mL). After stirring overnight at rt under Ar, the reaction mixture was diluted with EtOAc (50 mL) and sequentially washed with 0.1 M NaOH (3 × 50 mL) and brine (50 mL). The organic layer was dried ($MgSO_4$) and concentrated. The crude product was purified by automated MPLC (gradient from CH_2Cl_2 to 5% CH_3OH:CH_2Cl_2, (silica, 15 min) to afford Protected Cat-T (40.5 mg, 77%) as a pale-yellow solid.

^{1}H NMR (500 MHz, $CDCl_3$) δ: 6.62-6.53 (m, 3H), 6.23 (br s, 1H), 3.29 (q, J = 5.6 Hz, 2H), 2.83 (t, J = 7.7 Hz, 2H), 2.45-2.36 (m, 4H), 2.21 (s, 6H), 1.62 (s, 6H). ^{13}C NMR (125 MHz, $CDCl_3$) δ: 172.7, 147.7, 146.5, 134.4, 120.8, 1179, 109.0, 108.3, 58.2, 42.3, 39.0, 36.8, 31.8, 26.1. IR (ATR, cm^{-1}): 3298, 2778, 1648, 1228, 970. ESI-HRMS (*m/z*): 293.1871 Calcd. for $[M+H]^+$, $C_{13}H_{22}N_3O_3^+$: 293.1860.

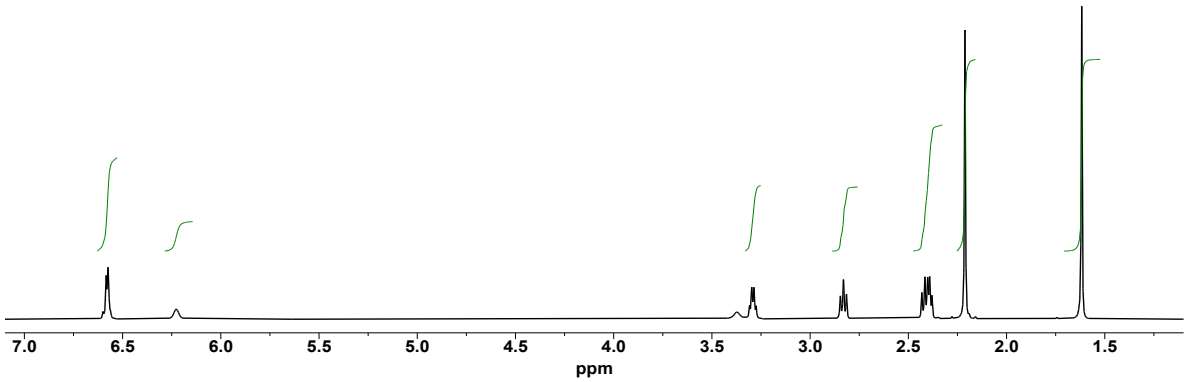

Figure 52. ^{1}H NMR spectrum ($CDCl_3$, 500 MHz) of Protected Cat-T.

USC
UNIVERSIDADE DE SANTIAGO DE COMPOSTELA

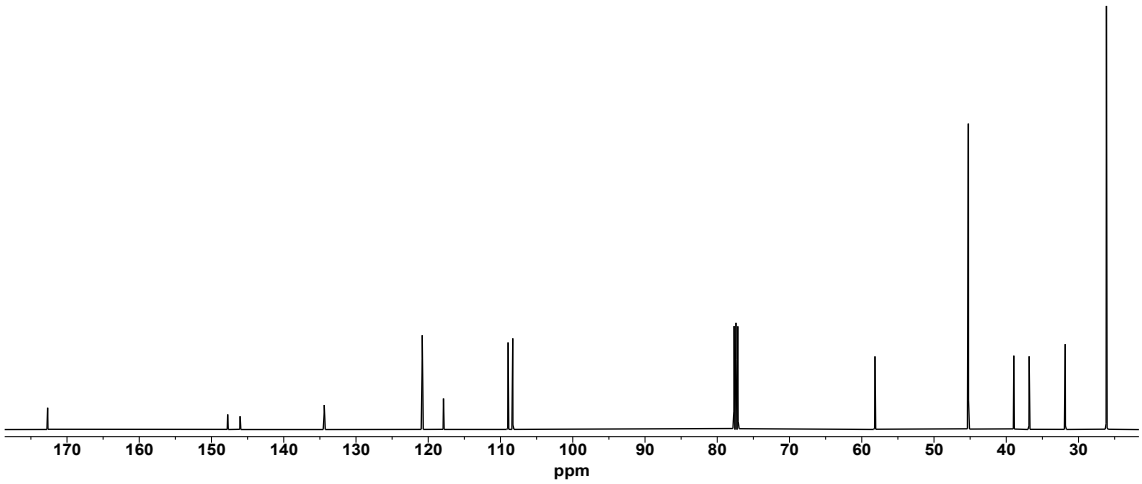

Figure 53. ^{13}C NMR spectrum ($CDCl_3$, 125 MHz) of Protected Cat-T.

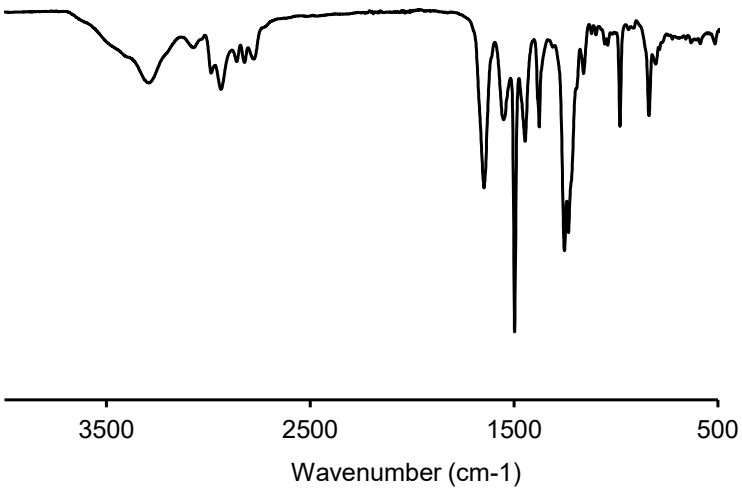

Figure 54. IR spectrum of Protected Cat-T.

USC
UNIVERSIDADE DE SANTIAGO DE COMPOSTELA

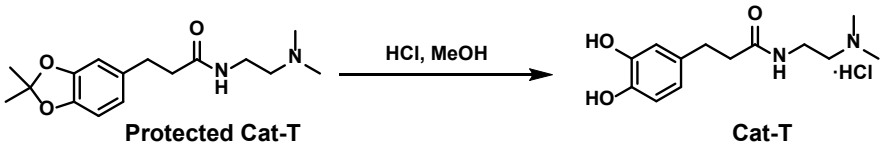

3-(3,4-dihydroxyphenyl)-*N*-(2-(dimethylamino)ethyl)propanamide hydrochloride (Cat-T). Protected Cat-T (15.0 mg, 51.1 µmol) was dissolved in a mixture of CH_3OH (2.24 mL) and 37% HCl (0.56 mL). After 5 h of stirring at rt, the mixture was concentrated to afford Cat-T (11.2 mg, 77%) as a pale-yellow foam.

^{1}H NMR (500 MHz, CD_3OD) δ: 6.72-6.61 (m, 2H), 6.53 (dd, J = 8.0, 2.1 Hz, 1H), 3.5 (t, J = 5.8 Hz, 2H), 3.16 (t, J = 5.9 Hz, 2H), 2.88 (s, 6H), 2.78 (t, J = 7.5 Hz, 2H), 2.49 (t, J = 7.5 Hz, 2H). ^{13}C NMR (125 MHz, CD_3OD) δ: 176.7, 146.2, 144.7, 135.5, 120.6, 116.6, 116.4, 58.7, 43.8, 39.0, 35.8, 31.9. IR (ATR, cm^{-1}): 3192, 2720, 1644, 1522, 1274. ESI-HRMS (*m/z*): 253.1542 Calcd. for $[M+H]^+$, $C_{13}H_{22}N_3O_3^+$: 253.1547.

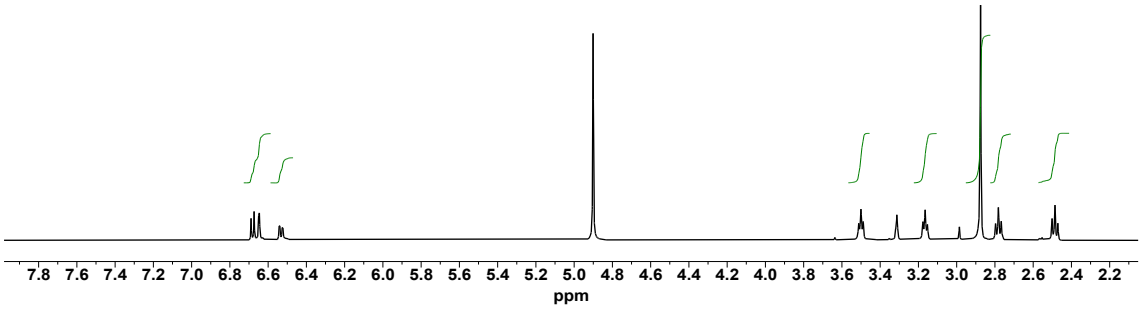

Figure 55. ^{1}H NMR spectrum (CD_3OD, 500 MHz) of Cat-T.

USC
UNIVERSIDADE DE SANTIAGO DE COMPOSTELA

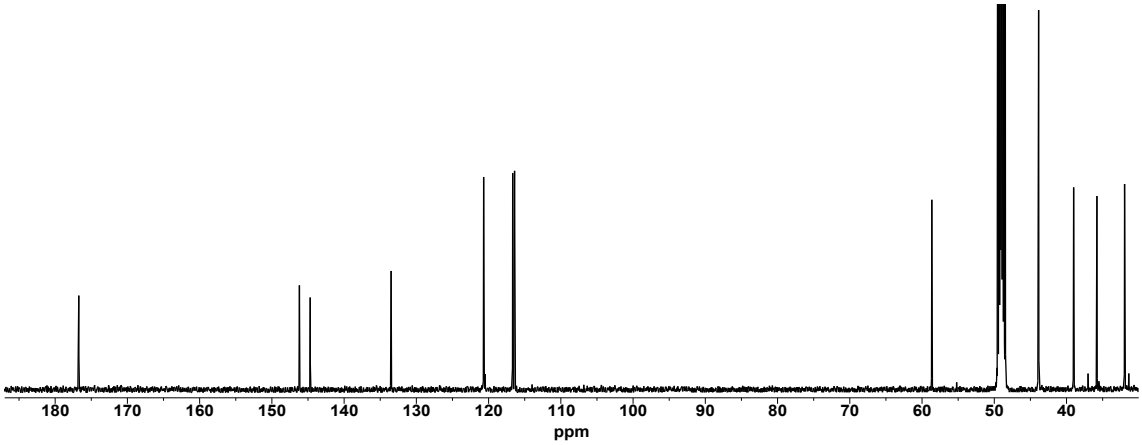

Figure 56. ^{13}C **NMR spectrum (CD_3OD, 125 MHz) of Cat-T.**

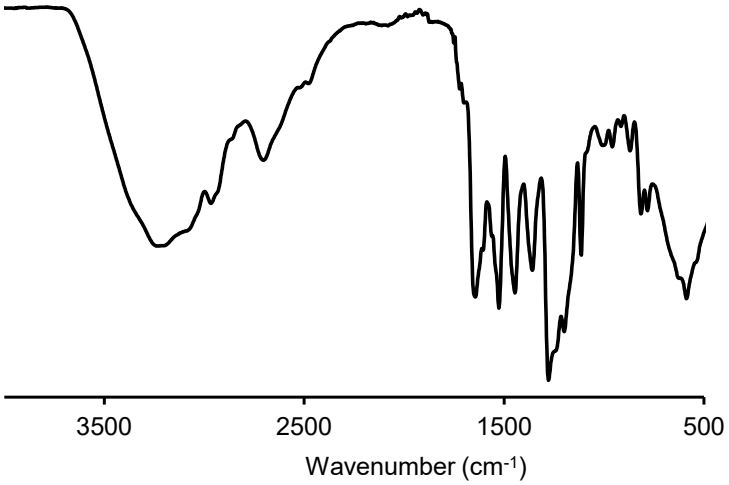

Figure 57. IR spectrum of Cat-T.

USC
UNIVERSIDADE DE SANTIAGO DE COMPOSTELA

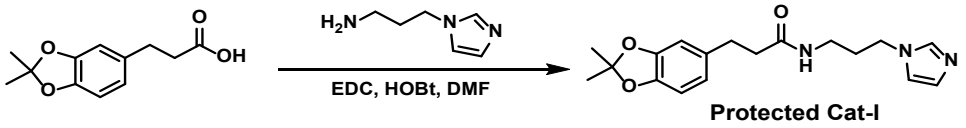

***N*-(3-(1*H*-imidazol-1-yl)propyl)-3-(2,2-dimethylbenzo[*d*][1,3]dioxol-5-yl)propanamide (Protected Cat-I).** HOBt (48.6 mg, 0.36 mmol), EDC·HCl (69.0 mg, 0.36 mmol), and 1-(3-aminopropyl)imidazole (45.0 mg, 0.36 mmol) were added to a solution of 3-(2,2-dimethylbenzo[d][1,3]dioxol-5-yl)propanoic acid (40.0 mg, 0.18 mmol) in anhydrous DMF (1.80 mL). After stirring overnight at rt under Ar, the reaction mixture was diluted with EtOAc (50 mL) and sequentially washed with 0.1 M NaOH (3 × 50 mL) and brine (50 mL). The organic layer was dried ($MgSO_4$) and concentrate. The crude product was purified by automated MPLC (gradient from CH_2Cl_2 to 5% CH_3OH:CH_2Cl_2, silica, 15 min) to afford Protected Cat-I (43.9mg, 74%) as a pale-yellow solid.

^{1}H NMR (500 MHz, $CDCl_3$) δ: 7.40 (br s, 1H), 7.00 (br s, 1H), 6.87 (br s, 1H), 6.63-6.45 (m, 3H), 3.85 (t, J = 6.9 Hz, 2H), 3.17 (q, J = 6.4 Hz, 2H), 2.9 (br s, 1H), 2.83 (t, J = 7.6 Hz, 2H), 2.4 (t, J = 7.5 Hz, 2H), 1.9 (quint, J = 6.8 Hz, 2H), 1.62 (s, 6H). ^{13}C NMR (125 MHz, $CDCl_3$) δ: 172.8, 147.6, 145.9, 137.2, 134.0, 129.3, 120.6, 119.1, 117.8, 108.7, 108.4, 44.5, 38.6, 36.5, 31.6, 31.1, 25.9. IR (ATR, cm^{-1}): 3268, 2938, 1740, 1644, 970. ESI-HRMS (*m/z*): 330.1827 Calcd. for $[M+H]^+$, $C_{13}H_{22}N_3O_3^+$: 330.1812.

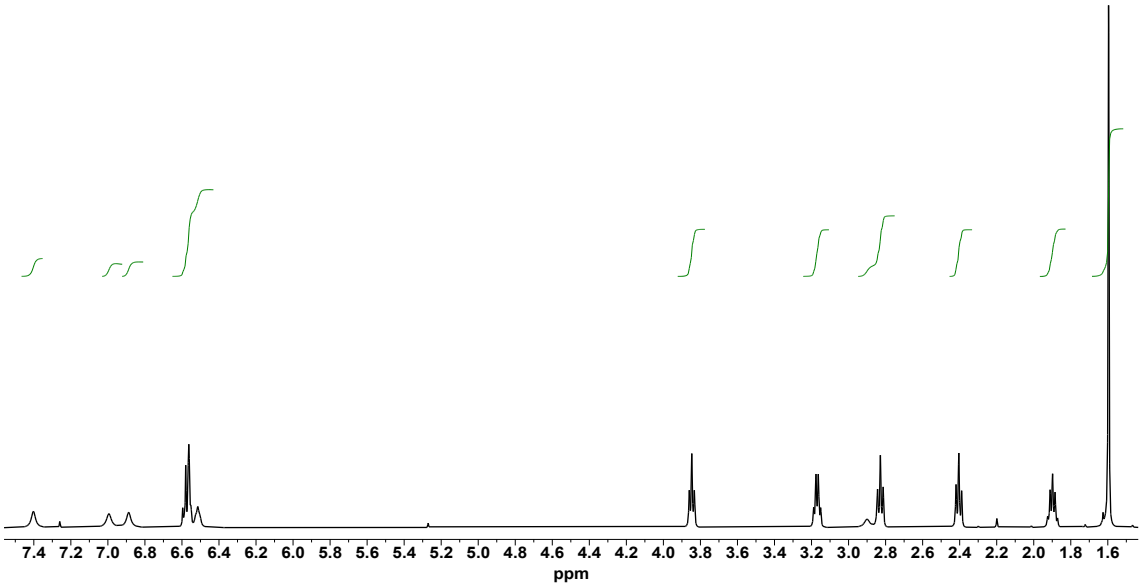

Figure 58. ^{1}H NMR spectrum ($CDCl_3$, 500 MHz) of Protected Cat-I.

USC UNIVERSIDADE DE SANTIAGO DE COMPOSTELA

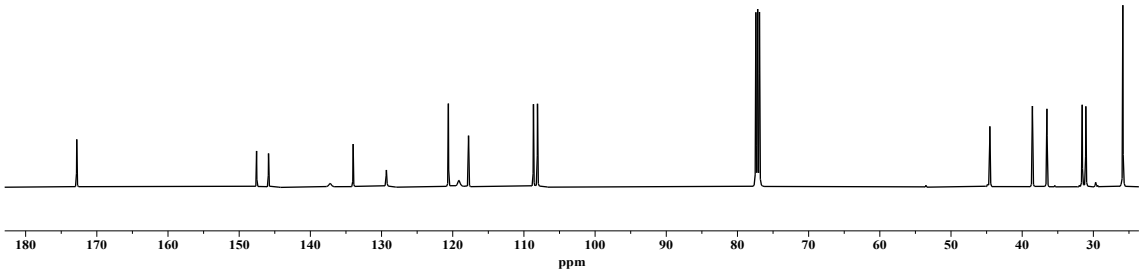

Figure 59. ^{13}C NMR spectrum ($CDCl_3$, 125 MHz) of Protected Cat-I.

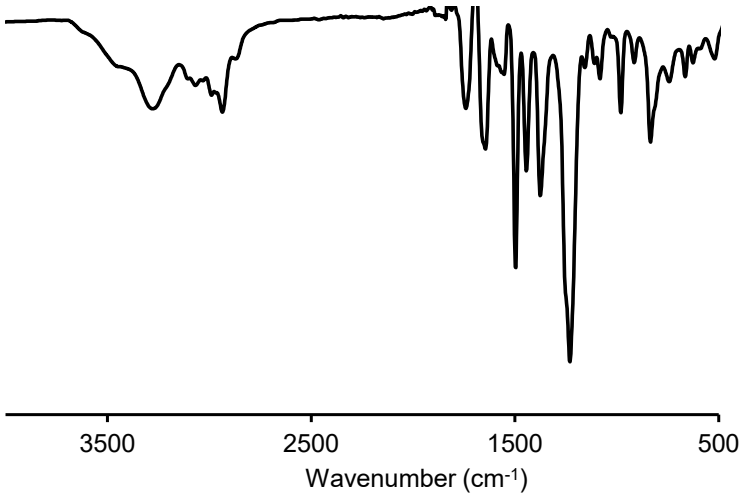

Figure 60. IR spectrum of Protected Cat-I.

USC
UNIVERSIDADE DE SANTIAGO DE COMPOSTELA

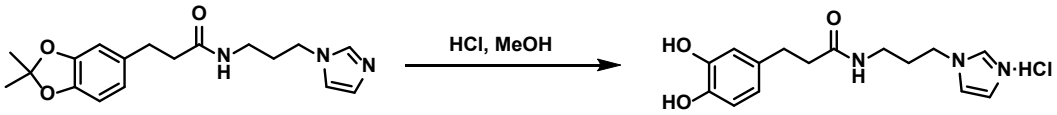

Protected Cat-I Cat-I

***N*-(3-(1*H*-imidazol-1-yl)propyl)-3-(3,4-dihydroxyphenyl)propanamide hydrochloride (Cat-I).** Protected Cat-I (26.0 mg, 78.9 µmol) was dissolved in a mixture of CH_3OH (2.72 mL) and 37% HCl (0.68 mL). After 5 h of stirring at rt, the mixture was concentrated to afford Cat-I (20.2 mg, 79%) as a pale-yellow foam.

^{1}H NMR (500 MHz, CD_3OD) δ: 8.83 (s, 1H), 7.58 (s, 1H), 7.56 (s, 1H), 6.70-6.65 (m, 2H), 6.58-6.53 (m, 1H), 4.00 (t, J = 7.0 Hz, 2H), 3.19 (t, J = 6.3 Hz, 2H), 2.80 (t, J = 7.2 Hz, 2H), 2.51 (t, J = 7.2 Hz, 2H), 1.97 (quint, J = 6.8 Hz, 2H). ^{13}C NMR (125 MHz, CD_3OD) δ: 176.0, 146.1, 144.8, 136.5, 133.3, 123.3, 121.1, 120.9, 116.8, 116.4, 47.8, 38.7, 37.7, 32.1, 30.1. IR (ATR, cm^{-1}): 3140, 1640, 1520, 1283. ESI-HRMS (*m/z*): 290.1505 Calcd. for $[M+H]^+$, $C_{13}H_{22}N_3O_3^+$: 290.1499

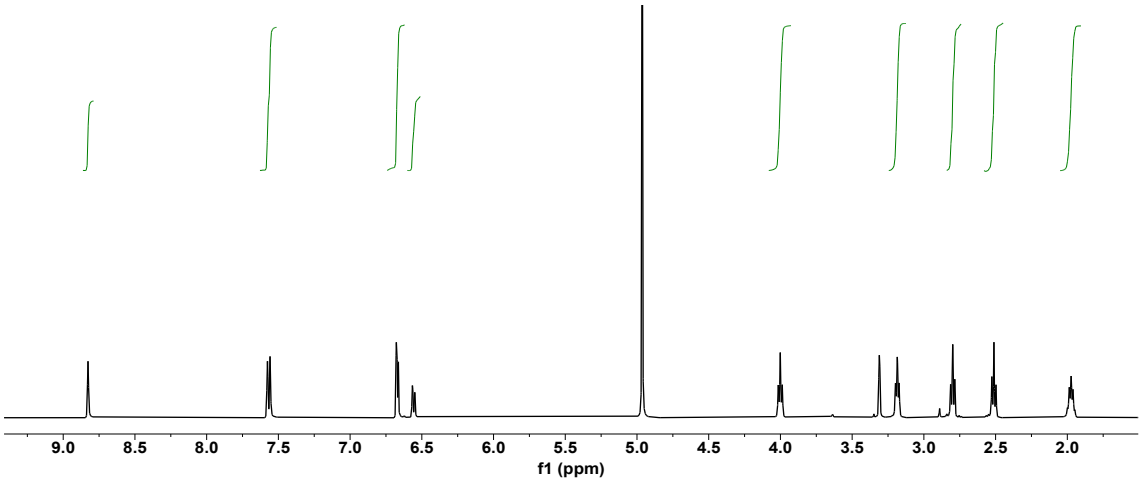

Figure 61. ^{1}H NMR spectrum (CD_3OD, 500 MHz) of Cat-I.

USC
UNIVERSIDADE DE SANTIAGO DE COMPOSTELA

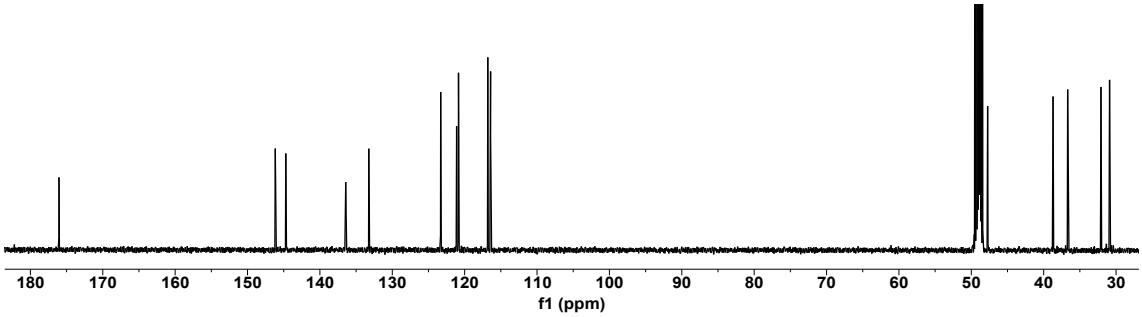

Figure 62. ^{13}C NMR spectrum (CD_3OD, 125 MHz) of Cat-I.

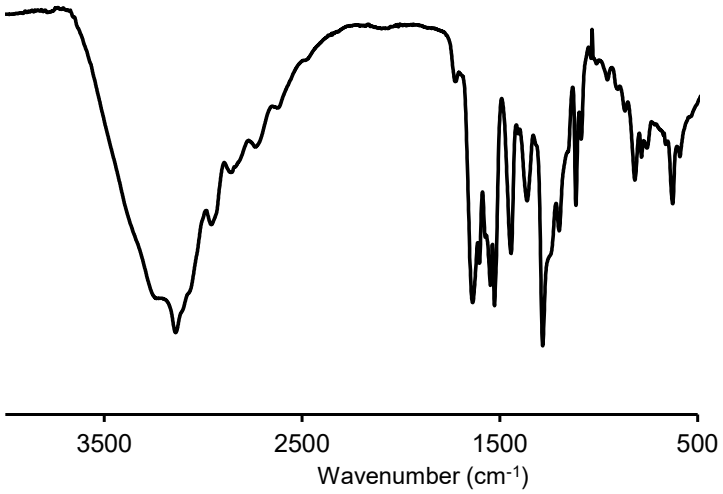

Figure 63. IR spectrum of Cat-I.

USC
UNIVERSIDADE DE SANTIAGO DE COMPOSTELA

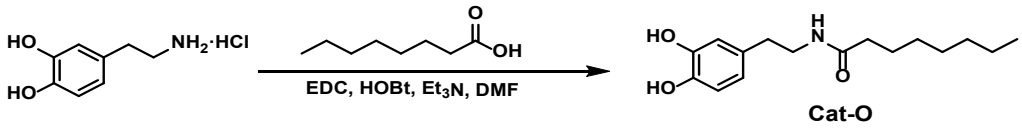

Cat-O

***N*-(3,4-dihydroxyphenethyl) octanamide (Cat-O).** HOBt (140.0 mg, 1.04 mmol), EDC·HCl (200.0 mg, 1.04 mmol), Et_3N (290 µL, 2.08 mmol), and dopamine hydrochloride (197.0 mg, 1.04 mmol) were added to a solution of octanoic acid (100.0 mg, 0.69 mmol) in anhydrous DMF (6.94 mL). After stirring overnight at rt under Ar, the reaction mixture was diluted with EtOAc (50 mL) and sequentially washed with 0.1 M HCl (3 × 50 mL), sat. $NaHCO_3$ (3 × 50 mL), and brine (50 mL). The organic layer was dried ($MgSO_4$) and concentrated. The crude product was purified by automated MPLC (gradient from hexane to 55% EtOAc:hexane, silica, 20 min) to afford Cat-O (203.8 mg, 99%) as a white solid.

^{1}H NMR (500 MHz, $CDCl_3$) δ: 7.82-7.61 (m, 1H), 7.44-7.31 (m, 1H), 6.85-6.69 (m, 2H), 6.55 (dd, J = 8.0, 2.0 Hz, 1H), 5.57 (br s, 1H), 3.47 (q, J = 6.7 Hz, 2H), 2.68 (t, J = 7.1 Hz, 2H), 2.14 (t, J = 7.6 Hz, 2H), 1.66-1.47 (m, 2H), 1.24 (br s, 8H), 0.86 (t, J = 6.5 Hz, 3H). ^{13}C NMR (125 MHz, $CDCl_3$) δ: 175.3, 145.0, 143.6, 130.9, 121.2, 116.1, 115.8, 41.7, 37.5, 35.4, 32.1, 30.2, 29.6, 26.5, 23.1, 14.6. IR (ATR, cm^{-1}): 3590, 1599. ESI-HRMS (*m/z*): 278.1755 Calcd. for [M-H]$^-$, $C_{16}H_{24}NO_3^-$: 278.1762.

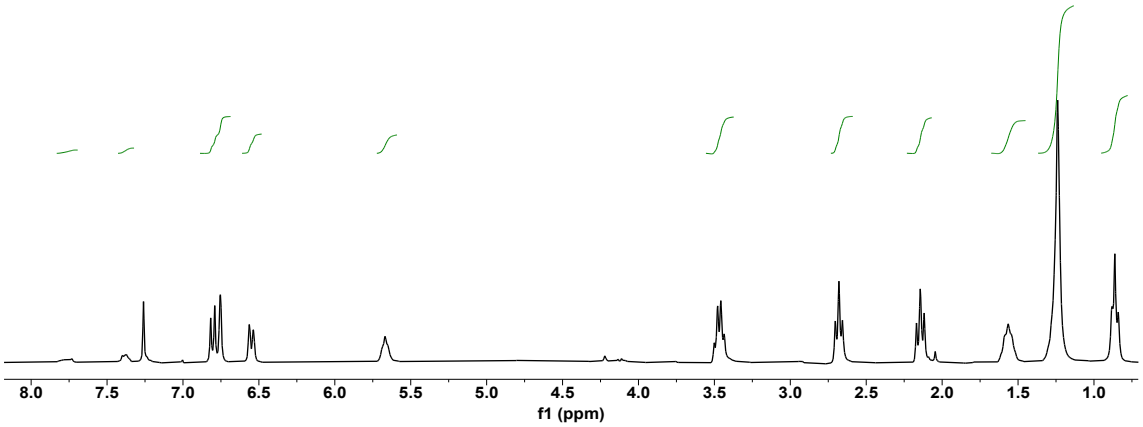

Figure 64. ^{1}H NMR spectrum ($CDCl_3$, 500 MHz) of Cat-O.

USC
UNIVERSIDADE DE SANTIAGO DE COMPOSTELA

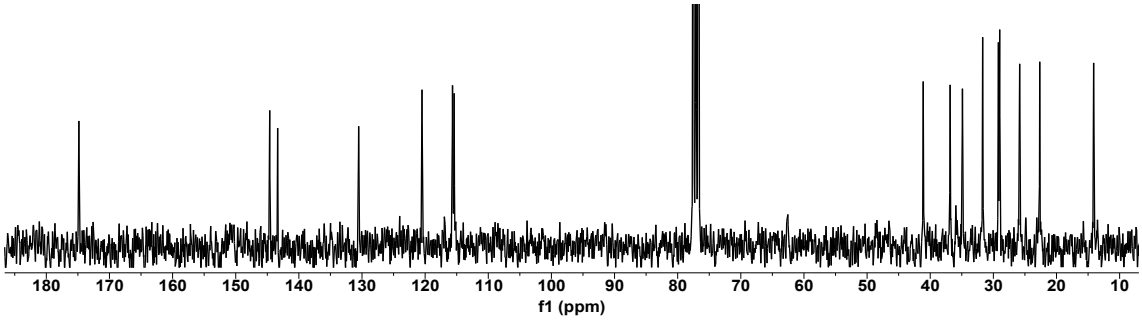

Figure 65. ^{13}C NMR spectrum ($CDCl_3$, 125 MHz) of Cat-O.

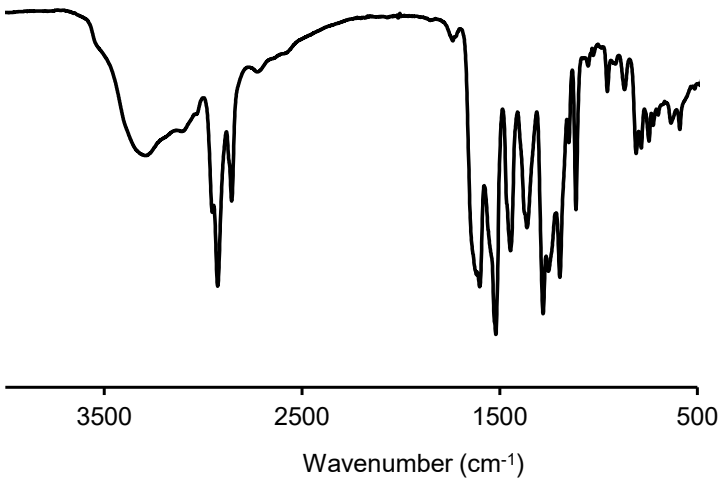

Figure 66. IR spectrum of Cat-O.

USC
UNIVERSIDADE DE SANTIAGO DE COMPOSTELA

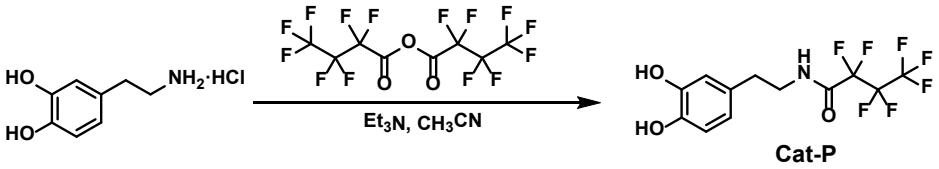

Cat-P

***N*-(3,4-dihydroxyphenethyl)-2,2,3,3,4,4,4-heptafluorobutanamide (Cat-P).** Heptafluorobutyric anhydride (59.7 µL, 0.24 mmol) was added dropwise to a solution of Et_3N (100 µL, 0.73 mmol) and dopamine hydrochloride (70.0 mg, 0.37 mmol) in anhydrous CH_3CN (2.44 mL). After stirring overnight at rt under Ar, the reaction mixture was diluted with EtOAc (50 mL) and sequentially washed with 0.1 M HCl (3 × 50 mL) and brine (50 mL). The organic layer was dried ($MgSO_4$) and concentrated. The crude product was purified by automated MPLC (gradient from hexane to 40% EtOAc:hexane, silica, 15 min) to afford Cat-P (70 mg, 74%) as a white solid.

^{1}H NMR (300 MHz, CD_3OD) δ: 6.73-6.61 (m, 2H), 6.52 (d, J = 8.3 Hz, 1H), 3.45 (t, J = 7.5 Hz, 2H), 2.69 (t, J = 7.5 Hz, 2H). ^{13}C NMR (125 MHz, CD_3OD) δ: 159.1, 146.5, 145.0, 131.2, 121.1, 119.0, 117.0, 116.4, 110.0, 109.7, 42.9, 35.3. ^{19}F NMR (282 MHz, CD_3OD) δ: -86.3, -126.9, -133.5. IR (ATR, cm^{-1}): 3320, 2970, 1738, 1362, 1218, 1120. ESI-HRMS (*m/z*): 348.0471 Calcd. for $[M-H]^-$, $C_{12}H_9F_7NO_3^-$: 348.0476.

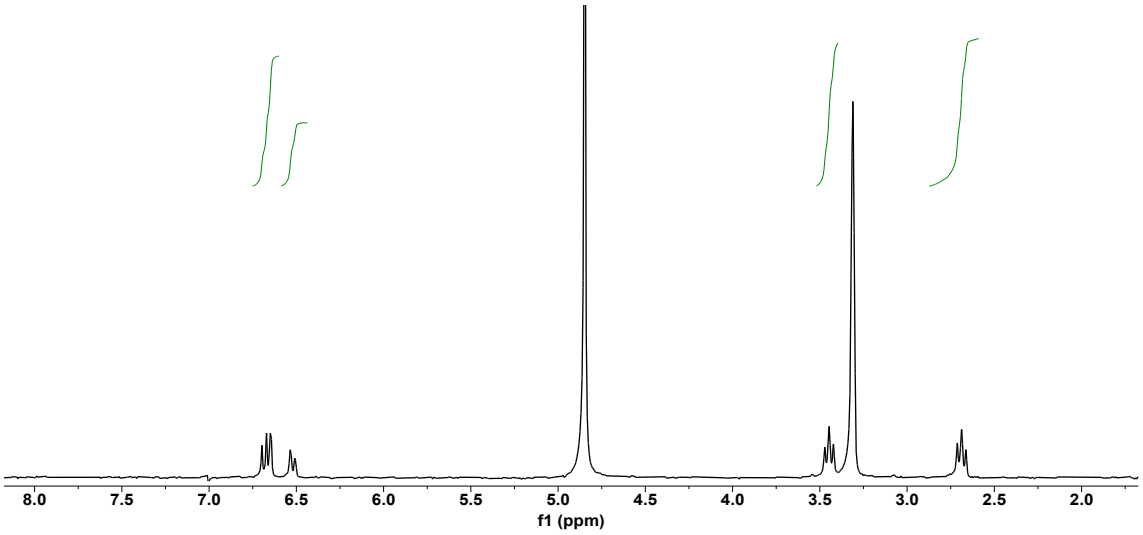

Figure 67. ^{1}H NMR spectrum (CD_3OD, 300 MHz) of Cat-P.

USC
UNIVERSIDADE DE SANTIAGO DE COMPOSTELA

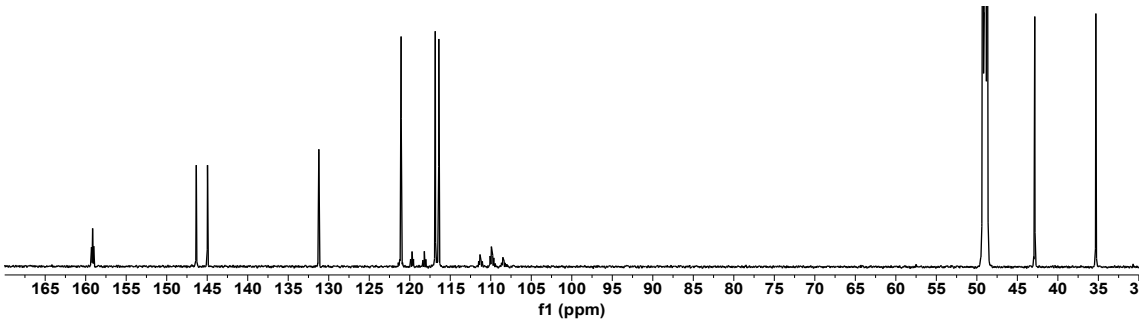

Figure 68. ^{13}C NMR spectrum (CD_3OD, 125 MHz) of Cat-P.

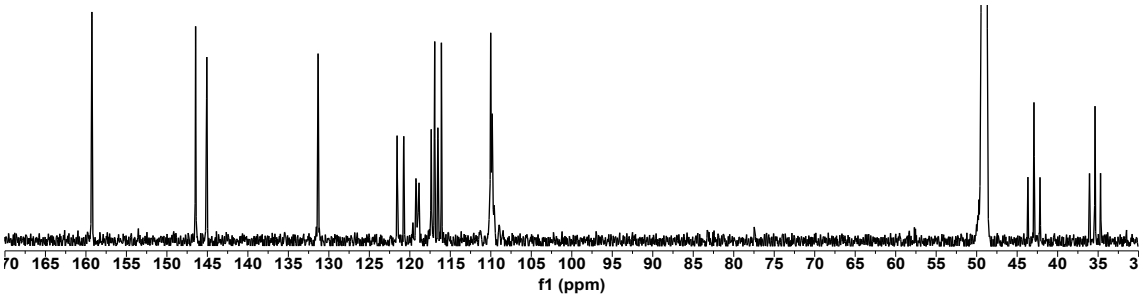

Figure 69. ^{13}C NMR spectrum (CD_3OD, 125 MHz, ^{19}F decoupled, ^{1}H coupled) of Cat-P.

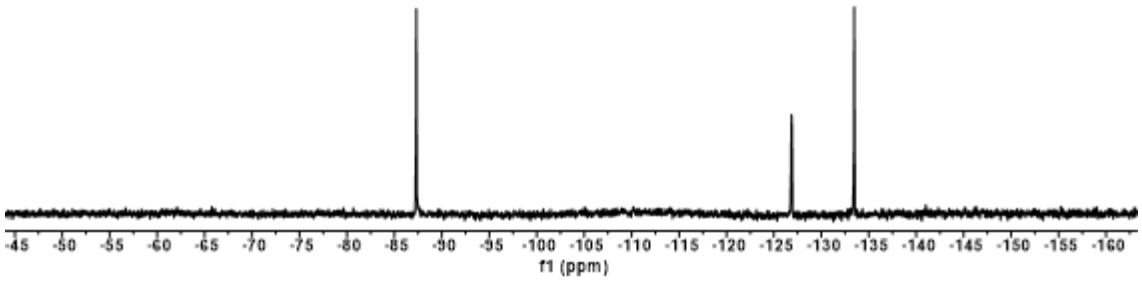

Figure 70. ^{19}F NMR spectrum (CD_3OD, 282 MHz, ^{13}C decoupling) of Cat-P.

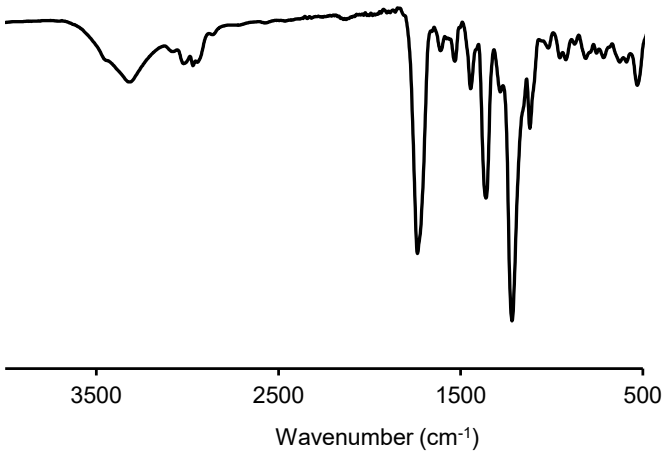

Figure 71. IR spectrum of Cat-P.

USC UNIVERSIDADE DE SANTIAGO DE COMPOSTELA

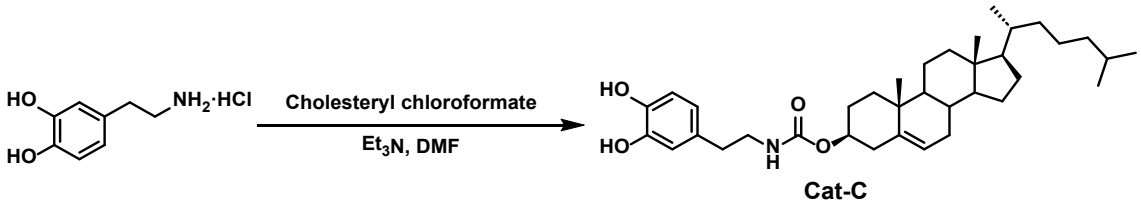

(3*S*,10*R*,13*R*,17*R*)-10,13-dimethyl-17-((*R*)-6-methylheptan-2-yl)-2,3,4,7,8,9,10,11,12,13,14,15,16,17-tetradecahydro-1*H*-cyclopenta[*a*]phenanthren-3-yl (3,4-dihydroxyphenethyl)carbamate (Cat-C). Cholesteryl chloroformate (100.0 mg, 0.22 mmol) was added to a solution of Et_3N (92 µL, 0.67 mmol) and dopamine hydrochloride (63.1 mg, 0.33 mmol) in anhydrous DMF (2.22 mL). After stirring overnight at rt under Ar, the reaction mixture was diluted with EtOAc (50 mL) and sequentially washed with 0.1 M HCl (3 × 50 mL) and brine (50 mL). The organic layer was dried ($MgSO_4$) and concentrated. The crude product was purified by automated MPLC (gradient from hexane to 40% EtOAc:hexane, silica, 20 min) to afford Cat-C (98.0 mg, 80%) as a white solid.

^{1}H NMR (500 MHz, $CDCl_3$) δ: 6.70 (d, J = 8.0 Hz, 1H), 6.62 (d, J = 2.0 Hz, 1H), 6.50–6.44 (m, 1H), 5.30-5.23 (m, 1H), 4.46-4.45 (br s, 1H), 3.32-3.20 (m, 2H), 2.61-2.51 (m, 2H), 2.28-2.14 (m, 2H), 2.01-1.67 (m, 5H), 1.64-1.13 (m, 14H), 1.13-0.71 (m, 23H), 0.60 (s, 3H). ^{13}C NMR (125 MHz, $CDCl_3$) δ: 157.7, 144.4, 143.1, 143.0, 131.4, 123.1, 121.2, 116.1, 115.8, 71.2, 57.1, 56.5, 50.3, 42.7, 42.6, 40.2, 39.9, 38.9, 37.4, 37.0, 36.6, 36.2, 35.8, 32.3, 30.1, 28.6, 28.5, 28.4, 26.3, 24.6, 24.3, 23.2, 22.9, 21.4, 19.7, 19.1, 12.3. IR (ATR, cm^{-1}): 3340, 2938, 2866, 1734, 1218, 1680, 1440, 1228. ESI-HRMS (*m/z*): 564.4052 Calcd. for $[M-H]^-$, $C_{36}H_{54}NO_4^-$: 564.4058.

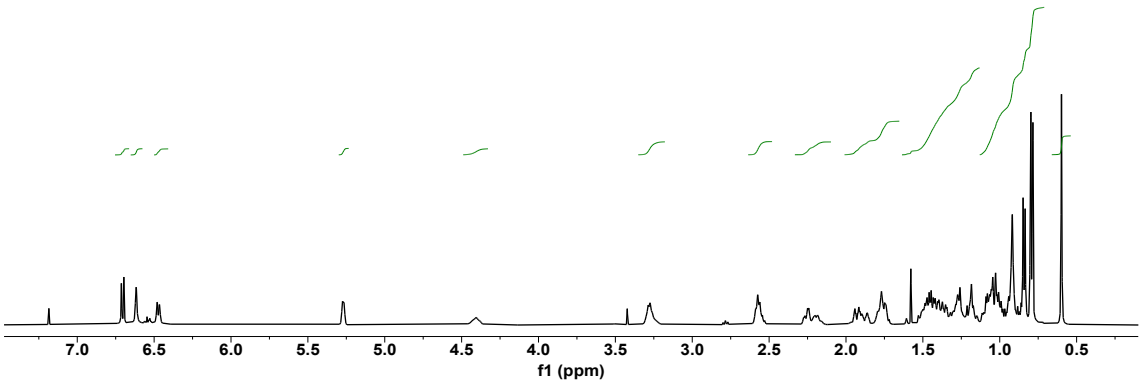

Figure 72. ^{1}H NMR spectrum ($CDCl_3$, 500 MHz) of Cat-C.

USC
UNIVERSIDADE DE SANTIAGO DE COMPOSTELA

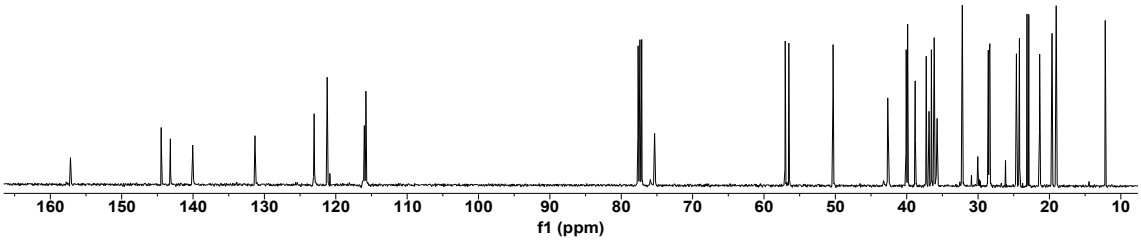

Figure 73. ^{13}C NMR spectrum ($CDCl_3$, 125 MHz) of Cat-C

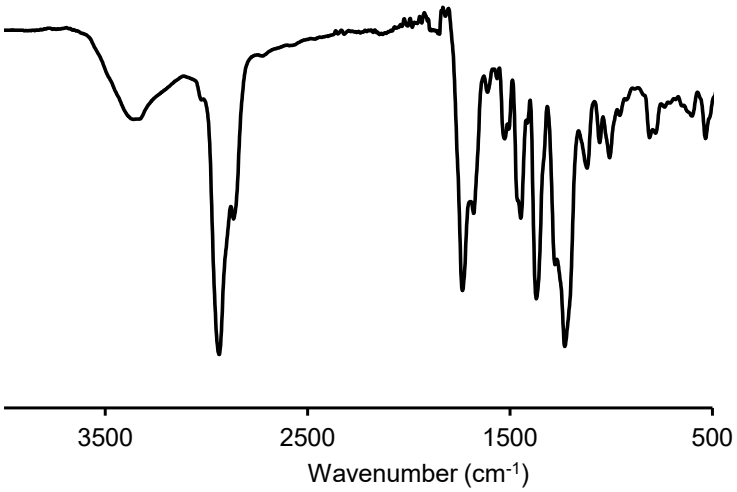

Figure 74. IR spectrum of Cat-C.

USC
UNIVERSIDADE DE SANTIAGO DE COMPOSTELA

3.2.4 pEGFP-N1 Production

Bacteria Transformation. Competent bacteria (XL1Blue, Stratagene) were thawed on ice and a 100 µL aliquot was mixed with transforming pEGFP-N1 (1-10 ng). Following incubation on ice for 30 min, a heat shock was performed at 42 °C for 1 min. After additional incubation on ice for 2 min, 1 mL of LB (Lysogeny Broth) medium was added, and the mixture was incubated at 37 °C for 1 h under orbital stirring. Finally, bacteria were collected by centrifugation and spread onto an LB-agar plate supplemented with kanamycin (50 µg/mL).

Plasmid Production. A single colony of transformed bacteria was mixed with 50 mL of LB medium and incubated overnight at 37 ºC under orbital stirring (250 rpm).

Plasmid Purification. pEGFP-N1 was isolated from 50 mL of bacterial culture using PureYield™ Plasmid Midiprep System (Promega, Madrid, Spain) following manufacturer's instructions. After isolation, pEGFP-N1 was precipitated in a mixture of 500 mM NaOAc pH 5.5 and cold EtOH (1:20 v/v). Precipitation process was continued for at least 2 h at -20 ºC and then, samples were centrifugated at 4 ºC for 30 min (4000 *g*). The resulting pellet was resuspended in sterile H_2O and washed to remove the excess of salts by ultracentrifugation (3 × 5 mL H_2O; Amicon MWCO 10 kDa).

Cy5 Fluorescent Labelling of pEGFP-N1. Labelling was conducted using 20 µg of pEGFP-N1 in 10 mM HEPES pH 7.1 (1 µg/µL) following the manufacter's recommendations. Purification was done by precipitation in a mixture of 5 M NaCl and cold EtOH (1:20 v/v). Precipitation process was continued for 24 h at -20 ºC and then, samples were centrifugated at 4 ºC for 30 min (4000 g). The resulting pellet was washed at room temperature with 500 µL of 70% EtOH and centrifugated at 4 ºC for 30 min (4000 *g*). Finally, the pellet was resuspended in sterile H_2O and washed to remove the excess of salts by ultrafiltration (3 × 5 mL H_2O; Amicon MWCO 10 kDa).

USC UNIVERSIDADE DE SANTIAGO DE COMPOSTELA

3.2.5 Polyplex Preparation and Dynamic Light Scattering Measurements

Preparation of the Solutions of Components. PEG[G3]-BA and 3[G2]-BA were separately dissolved in 10 mM HEPES pH 7.1 (Table 8), and the resulting solutions were aged for 1 h at rt before polyplexing. Fresh catechol solutions were prepared in 10 mM HEPES pH 7.1 (Cat-G in Table 9; Cat-A, Cat-D, Cat-T, and Cat-I in Table 10) or DMSO (Cat-O, Cat-P, and Cat-C in Table 11) just before polyplex preparation. All solutions were filtered through sterile 0.22 μm nylon filters before polyplex formation.

Table 6. Concentration (mg/mL) of solutions of PEG[G3]-BA and 3[G2]-BA used in the preparation of polyplexes with N/P 5, 10, and 15.

	N/P 5	N/P 10	N/P 15
PEG[G3]-BA	1.58 (99.1 μM)	3.16 (198.2 μM)	4.74 (297.3 μM)
3[G2]-BA	1.10 (99.1 μM)	2.20 (198.2 μM)	3.29 (297.3 μM)

Table 7. Concentration (mg/mL) of Cat-G solutions used in the preparation of polyplexes with N/P 5, 10, and 15.

	N/P 5	N/P 10	N/P 15
CBA 2	2.63 (11.4 mM)	5.27 (22.8 mM)	7.90 (34.2 mM)
CBA 5	6.58 (28.4 mM)	13.16 (56.8 mM)	19.75 (85.2 mM)
CBA 10	13.16 (56.8 mM)	26.33 (113.6 mM)	39.49 (170.4 mM)

Table 8. Concentration (mg/mL) of solutions of catechols A, D, T, and I used in the preparation of polyplexes with CBA 5. These concentrations account for 28.4, 56.8, and 85.2 mM for N/P 5, 10, and 15, respectively.

	N/P 5	N/P 10	N/P 15
Cat-A	4.35	8.70	13.06
Cat-D	8.63	17.26	25.89
Cat-T	-	16.36	-
Cat-I	-	18.45	-

Table 9. Concentration (mg/mL) of solutions of catechols O, P, and C used in the preparation of G polyplexes with N/P 10 and CBA 5. A 3:1 volume ratio between Cat-G (15.8 mg/mL, 68.2 mM) and the hydrophobic catechols was used, which accounts for a 10 mol% of the latter.

Polyplex	Cat-O	Cat-P	Cat-C
5-10-5G.O	6.35 (22.7 mM)	-	-
5-10-5G.P	-	7.94 (22.7 mM)	-
5-10-5G.C	-	-	12.86 (22.7 mM)

USC UNIVERSIDADE DE SANTIAGO DE COMPOSTELA

Preparation of Polyplexes. For each N/P ratio and % PEG, solutions of PEG[G3]-BA and 3[G2]-BA (Table 6) were mixed in different volume ratios (Table 10) to afford a total volume of 40 µL. Then, 18.8 µL of a cationic catechol solution (Tables 7 and 8 for catechols G, A, D, T, and I; Table 9 for O, P, and C) or mixtures thereof were added according to the desired N/P and CBA ratios. A 50 µL portion of this solution was immediately added over a pEGFP-N1 (4733 bp) solution (30 µL, 20 ng/µL in 10 mM HEPES pH 7.1) and polyplex formation was left overnight at 21 ºC under orbital stirring (300 rpm) in an Eppendorf Thermomixer C.

Table 10. Volume (µL) of PEG[G3]-BA and 3[G2]-BA solutions used in the preparation of polyplexes with different % PEG.

% PEG	PEG[G3]-BA	3[G2]-BA
100	40	0
50	20	20
25	10	30
12.5	5	35
7.5	3	37
5	2	38
2.5	1	39
1	0.4	39.6

Dynamic Light Scattering of Polyplexes. DLS measurements were performed after 16-24 h of polyplexing on a Malvern Nano ZS (Malvern Instruments, U.K.), operating at 633 nm with a 173º scattering angle, at 25 ºC. DLS mean diameters were obtained from the intensity particle size distribution provided by Malvern Zetasizer Software (5 independent measurements). DLS histograms were obtained from the intensity particle size distributions. Filtering of samples before DLS measurements was avoided to prevent the removal of larger assemblies or aggregates that could obscure analysis.

USC
UNIVERSIDADE DE SANTIAGO DE COMPOSTELA

Table 11. Mean hydrodynamic diameter (nm) and PDI of Cat-G polyplexes.

	N/P 5		N/P 10		N/P 15	
	Polyplex	Diameter (PDI)	**Polyplex**	Diameter (PDI)	**Polyplex**	Diameter (PDI)
CBA 2	**7.5-5-2**	144 ± 4 (0.14 ± 0.01)	**7.5-10-2**	150 ± 3 (0.12 ± 0.01)	**7.5-15-2**	142 ± 5 (0.19 ± 0.04)
	5-5-2	157 ± 2 (0.20 ± 0.02)	**5-10-2**	157 ± 3 (0.20 ± 0.02)	**5-15-2**	140 ± 4 (0.21 ± 0.02)
	2.5-5-2	167 ± 1 (0.10± 0.01)	**2.5-10-2**	167 ± 1 (0.15 ± 0.01)	**2.5-15-2**	153± 5 (0.14 ± 0.03)
	1-5-2	147 ± 1 (0.16 ± 0.01)	**1-10-2**	148 ± 1 (0.16 ± 0.01)	**1-15-2**	167± 3 (0.09 ± 0.01)
CBA 5	**25-5-5**	147 ± 5 (0.20 ± 0.01)	**25-10-5**	138 ± 5 (0.19 ± 0.01)	**25-15-5**	150± 4 (0.16 ± 0.01)
	12.5-5-5	124 ± 4 (0.16 ± 0.02)	**12.5-10-5**	135 ± 2 (0.20 ± 0.01)	**12.5-15-5**	146 ± 1 (0.07 ± 0.01)
	7.5-5-5	140 ± 3 (0.15 ± 0.02)	**7.5-10-5**	136 ± 3 (0.16 ± 0.01)	**7.5-15-5**	150 ± 2 (0.16 ± 0.01)
	5-5-5	128 ± 4 (0.14 ± 0.01)	**5-10-5**	148 ± 3 (0.16 ± 0.02)	**5-15-5**	137 ± 5 (0.16 ± 0.01)
	2.5-5-5	148 ± 3 (0.17 ± 0.02)	**2.5-10-5**	148 ± 4 (0.17 ± 0.01)	**2.5-15-5**	167 ± 3 (0.13 ± 0.01)
	1-5-5	152 ± 3 (0.13 ± 0.02)	**1-10-5**	143 ± 3 (0.17 ± 0.01)	**1-15-5**	141 ± 3 (0.17 ± 0.01)
CBA 10	**7.5-5-10**	144 ± 5 (0.22 ± 0.01)	**7.5-10-10**	159 ± 6 (0.21 ± 0.01)	**7.5-15-10**	161 ± 7 (0.04 ± 0.02)
	5-5-10	148 ± 3 (0.20 ± 0.01)	**5-10-10**	150 ± 2 (0.17 ± 0.01)	**5-15-10**	139 ± 2 (0.16 ± 0.02)
	2.5-5-10	166 ± 3 (0.18 ± 0.02)	**2.5-10-10**	164 ± 5 (0.20 ± 0.01)	**2.5-15-10**	142 ± 5 (0.19 ± 0.02)
	1-5-10	147 ± 4 (0.17 ± 0.01)	**1-10-10**	149 ± 2 (0.15 ± 0.01)	**1-15-10**	154 ± 4 (0.20 ± 0.02)

USC UNIVERSIDADE DE SANTIAGO DE COMPOSTELA

Table 12. Mean hydrodynamic diameter (nm) and PDI of Cat-A polyplexes.

N/P 5		N/P 10		N/P 15	
Polyplex	Diameter (PDI)	**Polyplex**	Diameter (PDI)	**Polyplex**	Diameter (PDI)
25-5-5	124 ± 1 (0.14 ± 0.01)	**25-10-5**	133 ± 1 (0.18 ± 0.01)	**25-15-5**	134 ± 1 (0.18 ± 0.01)
12.5-5-5	155 ± 3 (0.17 ± 0.02)	**12.5-10-5**	160 ± 3 (0.14 ± 0.01)	**12.5-15-5**	146 ± 1 (0.07 ± 0.01)
5-5-5	219 ± 3 (0.07 ± 0.01)	**5-10-5**	222 ± 6 (0.14 ± 0.01)	**5-15-5**	200 ± 3 (0.10 ± 0.02)

Table 13. Mean hydrodynamic diameter (nm) and PDI of Cat-D polyplexes.

N/P 5		N/P 10		N/P 15	
Polyplex	Diameter (PDI)	**Polyplex**	Diameter (PDI)	**Polyplex**	Diameter (PDI)
25-5-5	159 ± 5 (0.15 ± 0.01)	**25-10-5**	153 ± 2 (0.15 ± 0.02)	**25-15-5**	164 ± 3 (0.12 ± 0.01)
12.5-5-5	181 ± 3 (0.12 ± 0.02)	**12.5-10-5**	185 ± 3 (0.09 ± 0.01)	**12.5-15-5**	192 ± 3 (0.08 ± 0.02)
5-5-5	261 ± 3 (0.13 ± 0.02)	**5-10-5**	255 ± 3 (0.11 ± 0.01)	**5-15-5**	260 ± 5 (0.15 ± 0.01)

Table 14. Mean hydrodynamic diameter (nm) and PDI of mixed polyplexes.

N/P 10		N/P 15	
Polyplex	Diameter (PDI)	**Polyplex**	Diameter (PDI)
5-10-5G.A	157 ± 4 (0.23 ± 0.01)	**5-15-5G.A**	149 ± 1 (0.14 ± 0.02)
5-10-5G.D	169 ± 5 (0.13 ± 0.02)	**5-15-5G.D**	197 ± 5 (0.33 ± 0.01)
5-10-5G.AD	167 ± 5 (0.13 ± 0.01)	**5-15-5G.AD**	196 ± 3 (0.24 ± 0.05)
5-10-5G.T	158 ± 4 (0.18 ± 0.01)	-	-
5-10-5G.I	164 ± 4 (0.22 ± 0.01)	-	-
5-10-5G.TI	180 ± 3 (0.18 ± 0.01)	-	-

USC UNIVERSIDADE DE SANTIAGO DE COMPOSTELA

Table 15. Mean hydrodynamic diameter (nm) and PDI of polyplexes dopped with catechols O, P, and C.

Polyplex	Diameter (PDI)
5-10-5 G.O	241 ± 6 (0.26 ± 0.01)
5-10-5 G.P	185 ± 5 (0.14 ± 0.02)
5-10-5 G.C	233 ± 5 (0.32 ± 0.02)
5-10-5 G.OPC	216 ± 3 (0.22 ± 0.03)

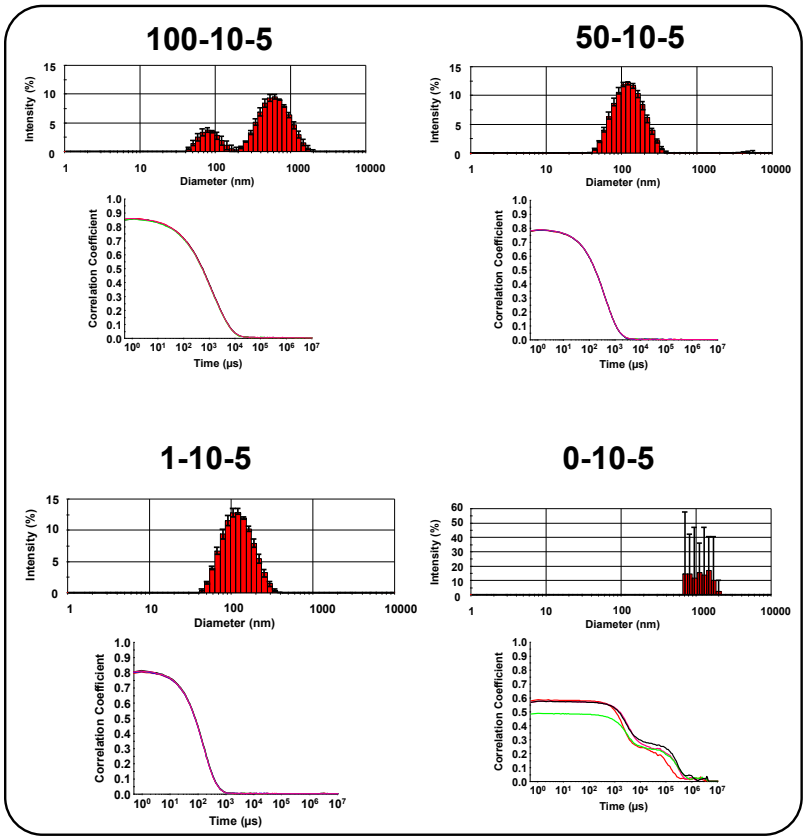

Figure 75. DLS histograms and correlation functions of polyplexes prepared with Cat-G at different % PEG.

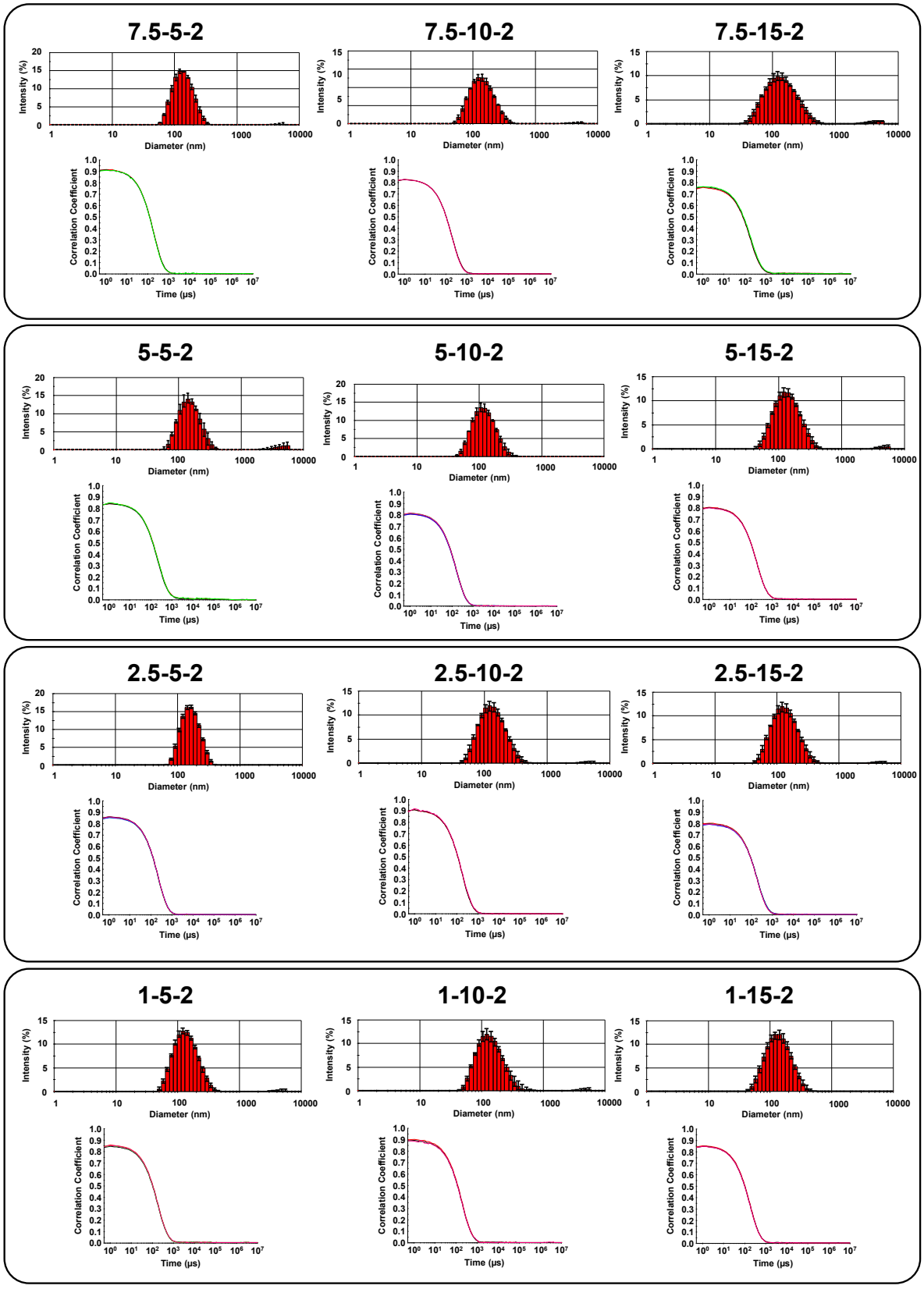

Figure 76. DLS histograms and correlation functions of polyplexes prepared with Cat-G at different N/P and CBA ratios.

USC
UNIVERSIDADE DE SANTIAGO DE COMPOSTELA

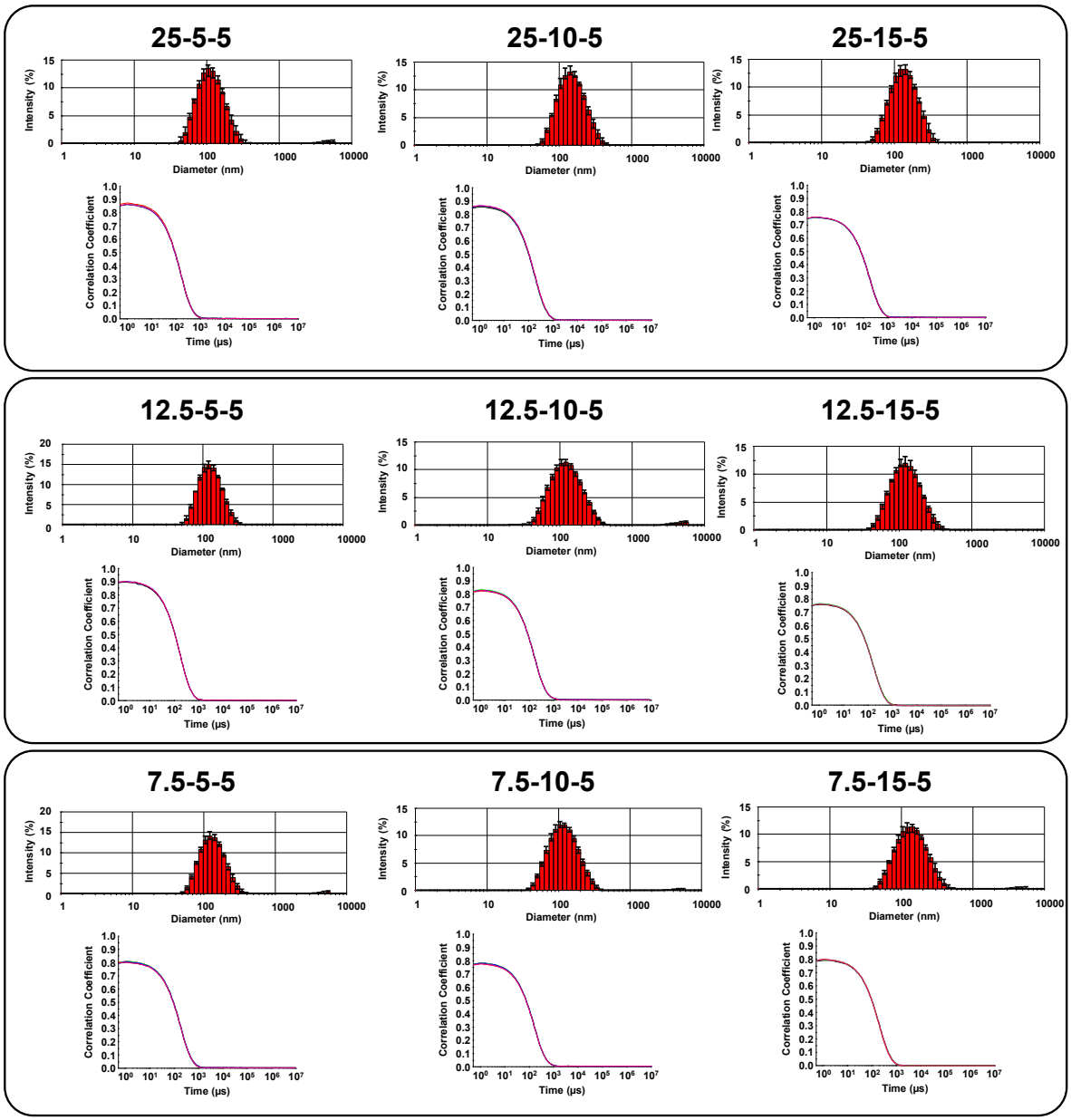

Figure 77. DLS histograms and correlation functions of polyplexes prepared with Cat-G at different N/P and CBA ratios.

USC
UNIVERSIDADE DE SANTIAGO DE COMPOSTELA

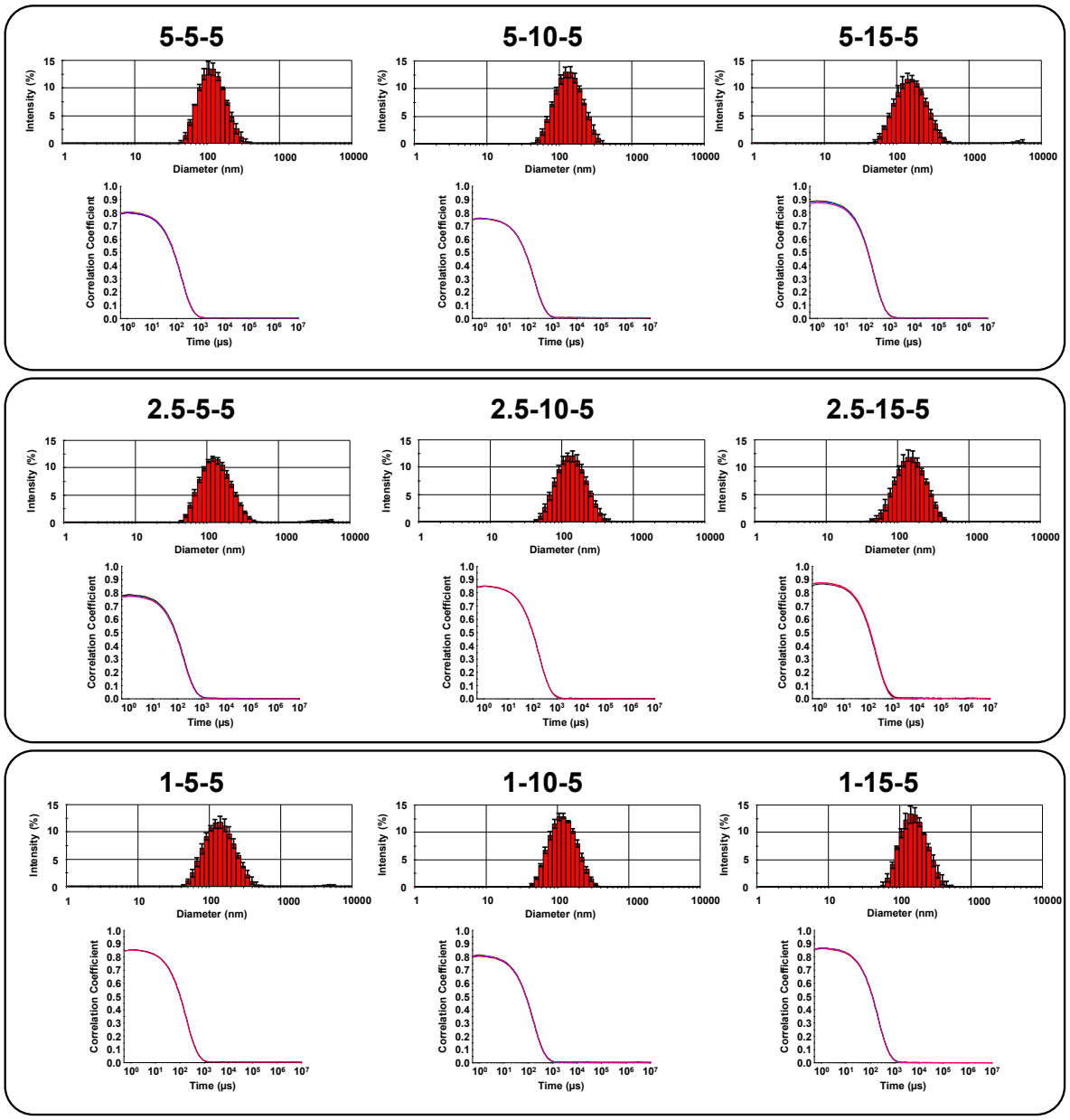

Figure 78. DLS histograms and correlation functions of polyplexes prepared with Cat-G at different N/P and CBA ratios.

USC
UNIVERSIDADE DE SANTIAGO DE COMPOSTELA

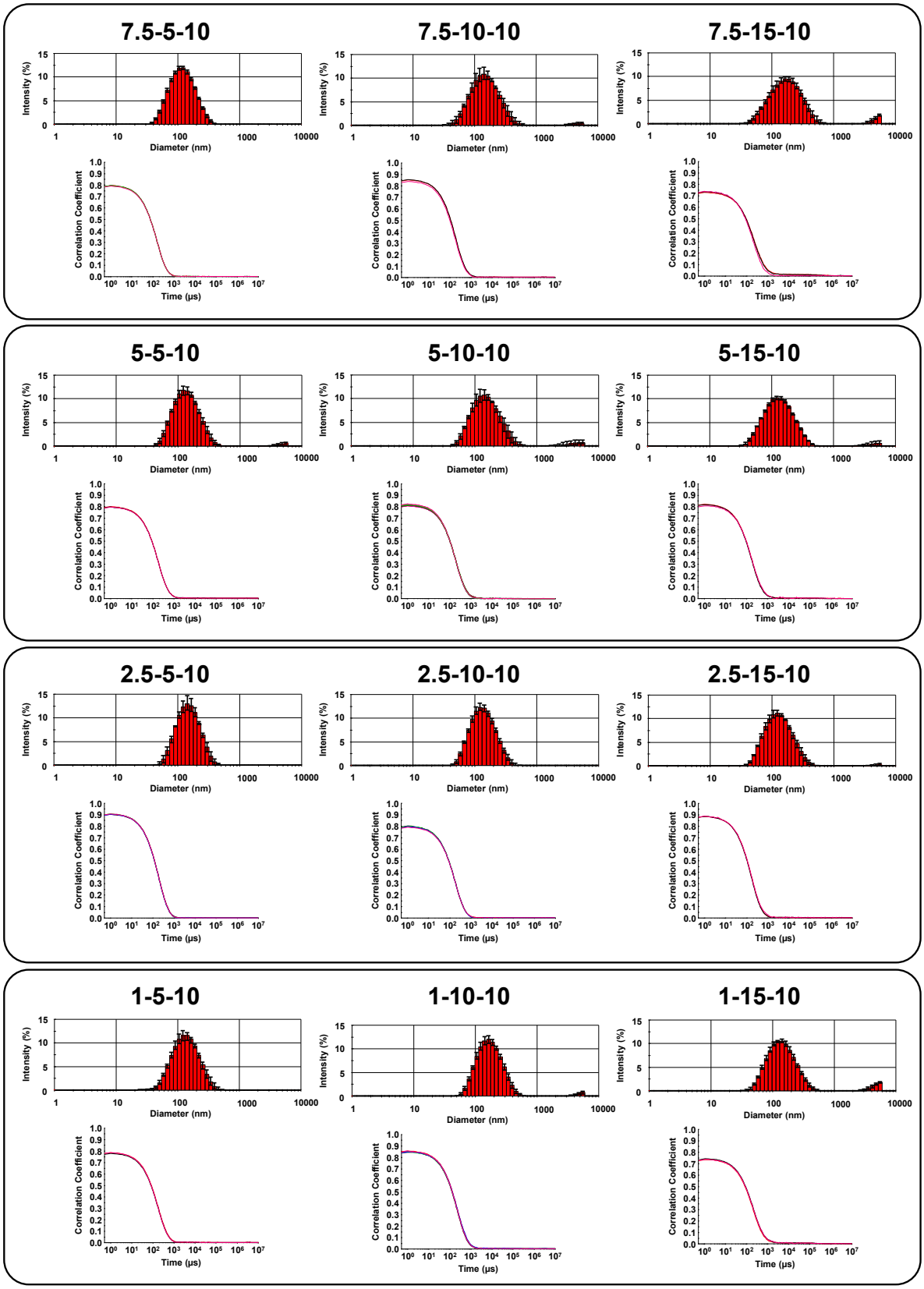

Figure 79. DLS histograms and correlation functions of polyplexes prepared with Cat-G at different N/P and CBA ratios.

USC UNIVERSIDADE DE SANTIAGO DE COMPOSTELA

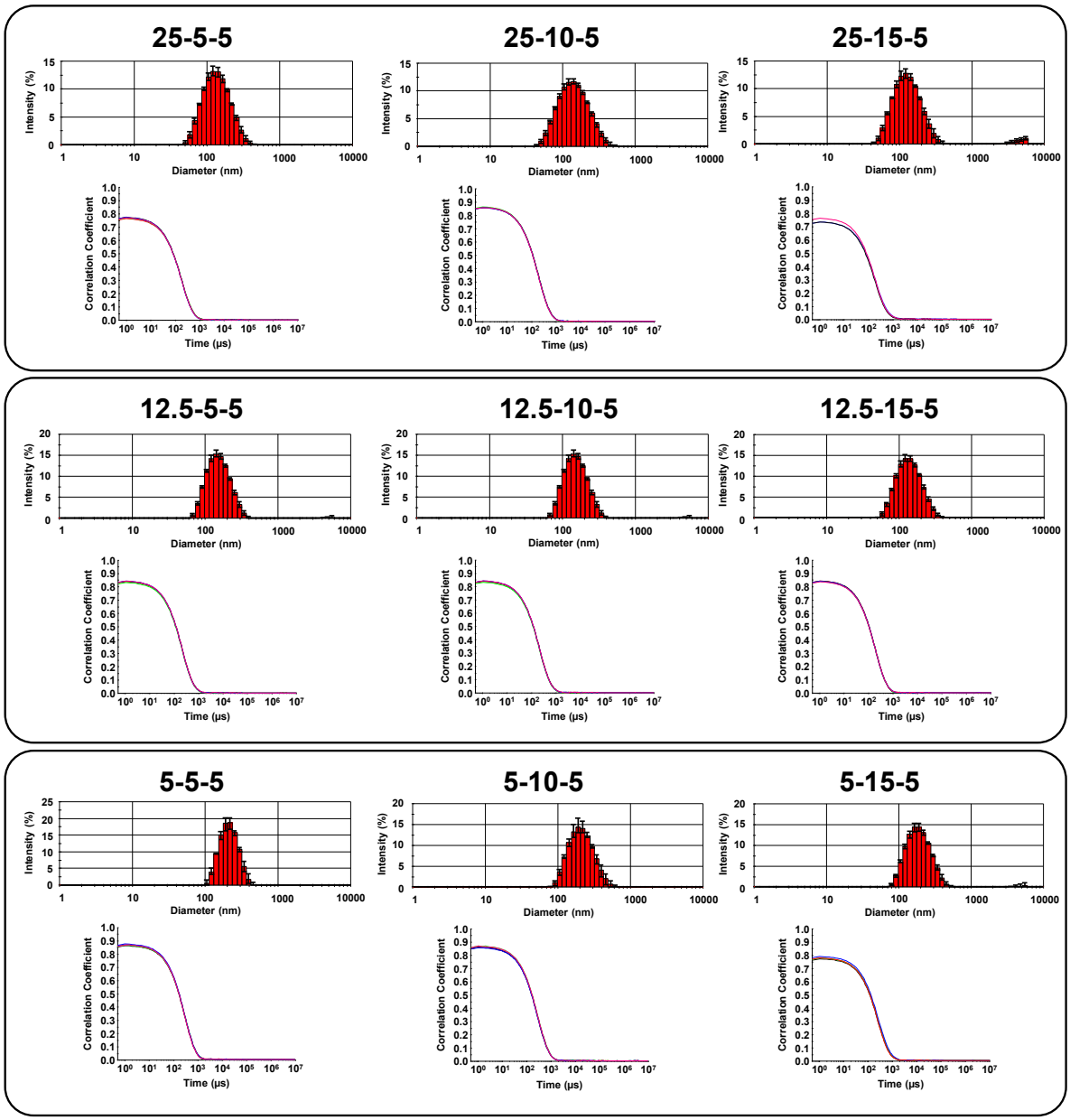

Figure 80. DLS histograms and correlation functions of polyplexes prepared with Cat-A at different N/P.

USC
UNIVERSIDADE DE SANTIAGO DE COMPOSTELA

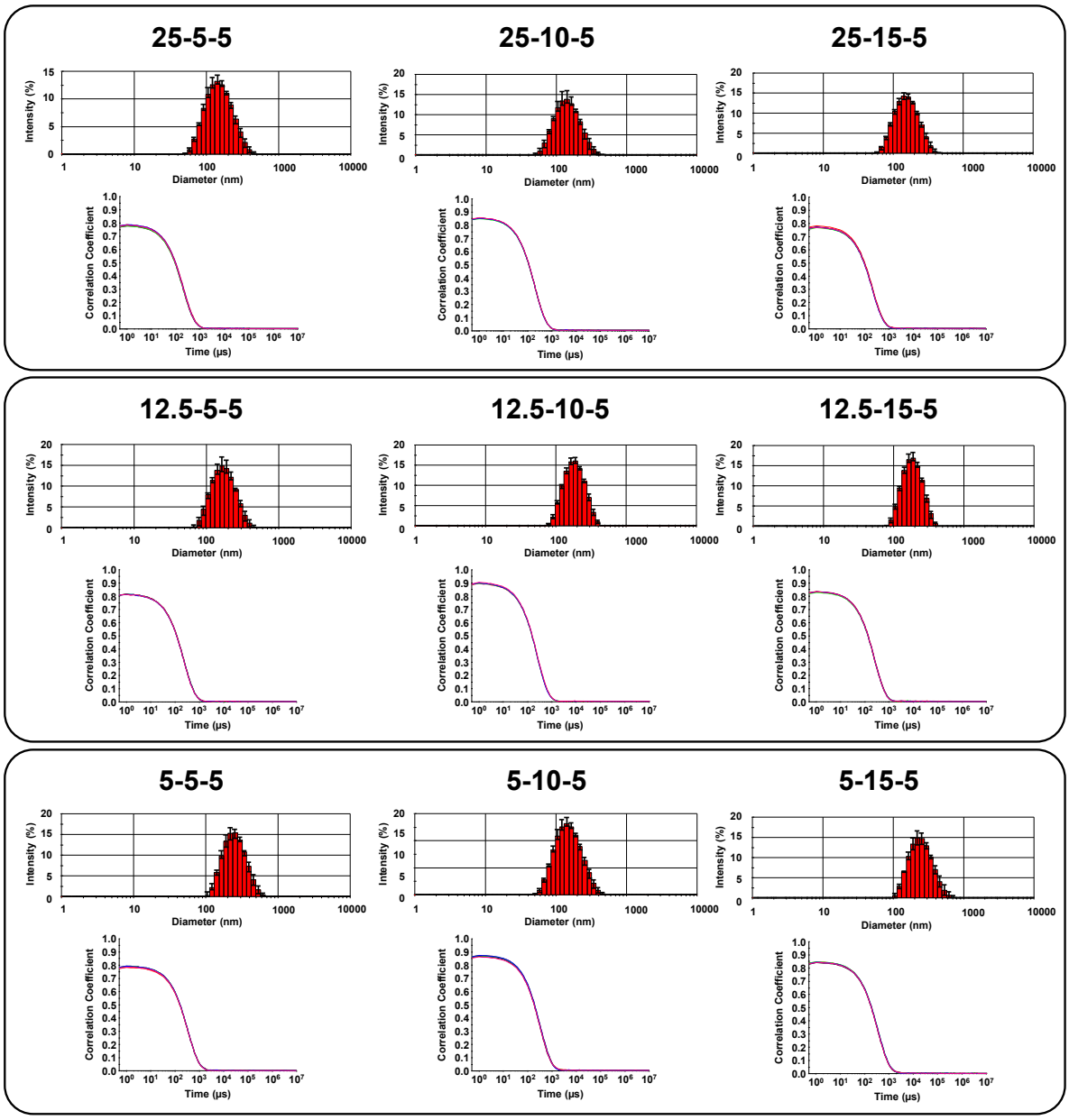

Figure 81. DLS histograms and correlation functions of polyplexes prepared with Cat-D at different N/P.

USC
UNIVERSIDADE DE SANTIAGO DE COMPOSTELA

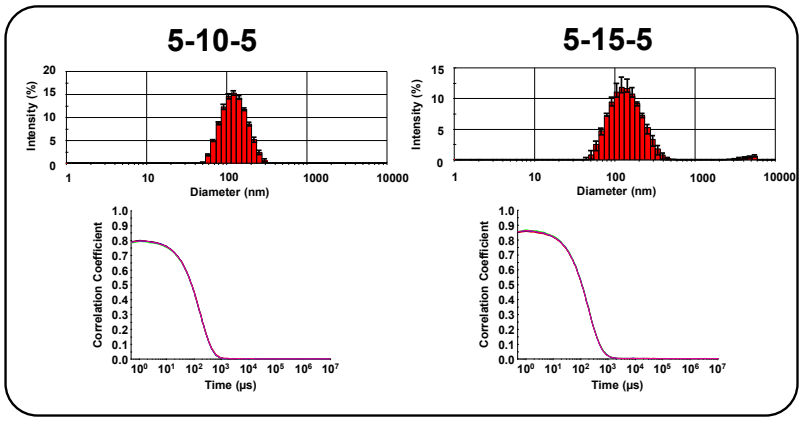

Figure 82. DLS histograms and correlation functions of polyplexes prepared with a mixture of Cat-G (75 %) and Cat-A (25 %) at different N/P.

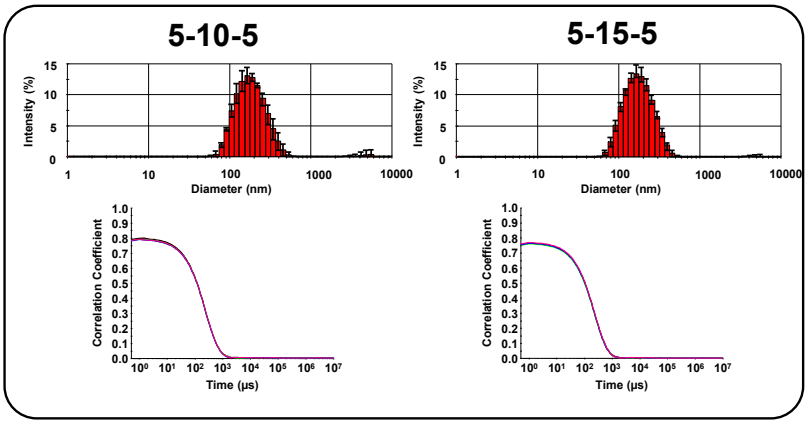

Figure 83. DLS histograms and correlation functions of polyplexes prepared with a mixture of Cat-G (75 %) and Cat-D (25 %) at different N/P.

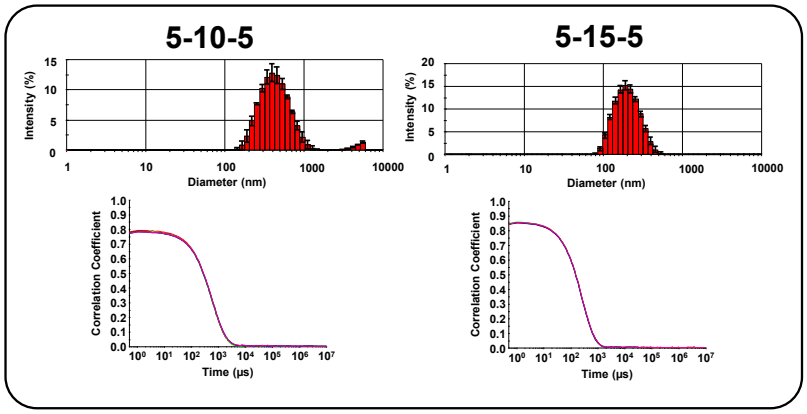

Figure 84. DLS histograms and correlation functions of polyplexes prepared with a mixture of Cat-G (50 %), Cat-A (25 %), and Cat-D (25 %) at different N/P.

USC
UNIVERSIDADE DE SANTIAGO DE COMPOSTELA

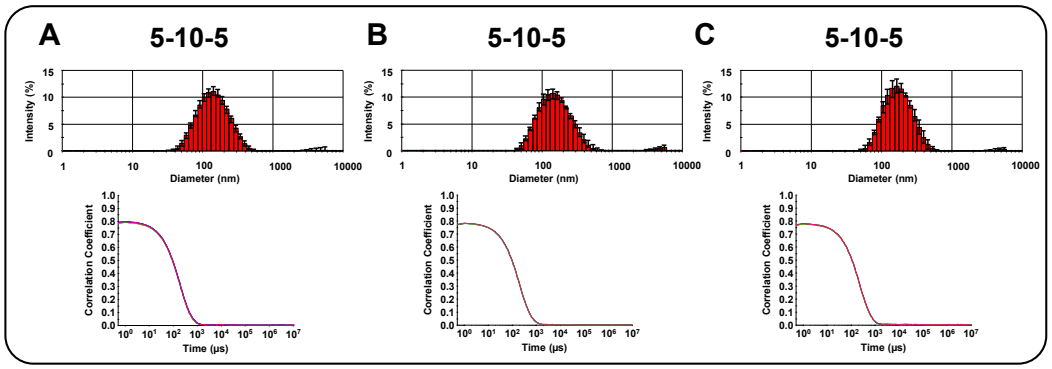

Figure 85. DLS histograms and correlation functions of polyplexes prepared with mixtures of 75% Cat-G and 25% Cat-T (A), 75% Cat-G and 25% Cat-I (B), and 50% Cat-G, 25% Cat-T, and 25% Cat-I (C).

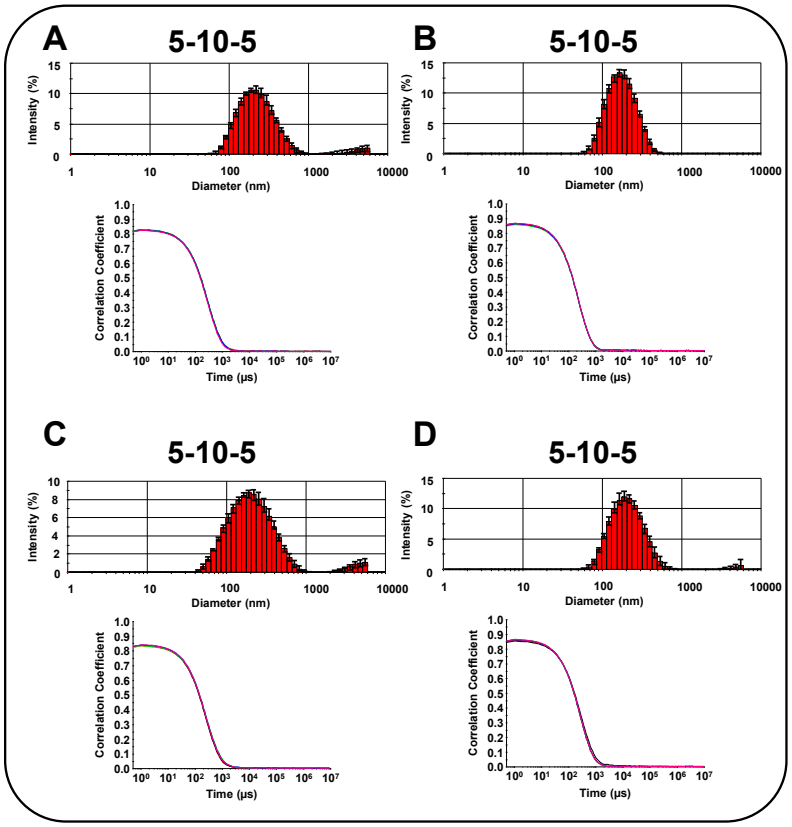

Figure 86. DLS histograms and correlation functions of G polyplexes dopped with 10 mol% Cat-O (A), 10 mol% Cat-P (B), 10 mol% Cat-C (C), and 3.33 mol% each of Cat-O, Cat-P, and Cat-C (D).

USC
UNIVERSIDADE DE SANTIAGO DE COMPOSTELA

3.2.6 Cell Studies

Cell Cultures. HEK-293, COS-7, HepG2, and HeLa cells, obtained from the European Collection of Authenticated Cell Cultures (ECACC), were cultured at 37 °C in a 5% CO_2 atmosphere in DMEM with high glucose, containing 10% FBS and supplemented with 50 U/mL penicillin and 50 U/mL streptomycin, in 75 cm^2 cell culture flasks. All cell experiments were performed at 37 °C in a 5% CO_2 atmosphere with this modified DMEM, simply referred as "medium".

***In vitro* Transfection.** Cells were seeded in 24-well plates at a density of 200000 cells/mL for HEK-293, 150000 cells/mL for COS-7, 125000 cells/mL for HepG2, and 100000 cells/mL for HeLa. After 24 h of incubation, medium was replaced with fresh medium (250 µL) and then, the polyplex solution was added (1 µg pEGFP-N1/well). Cells were incubated with the polyplex for 5 h. Afterwards, the medium was replaced with fresh medium (500 µL) and incubation continued for up to a total of 48 h (COS-7, HepG2, and HeLa) or 72 h (HEK-293). Transfection with LP 2000 was performed following manufacturer's protocol (FBS-free medium). To verify cell tolerance towards medium replacement, duration of transfection, and washing procedures, controls were conducted by subjecting the cells to the same treatments.

Flow Cytometry. EGFP expression of transfected cells was analyzed by flow cytometry. After 48 h (COS-7, HepG2, and HeLa) or 72 h (HEK-293) of incubation with the polyplexes, cells were washed with PBS (3 × 500 µL) and trypsinized (100 µL of 0.25% Trypsin–EDTA) for 5 min, followed by trypsin quenching with 350 µL of PBS supplemented with 5% FBS. Cells were transferred to 96-well culture plates (Corning Costar 96-Well microplates from Thermo Scientific) and analyzed by flow cytometry collecting at least 5000 events per well using a Guava Millipore flow cytometer equipped with a 488 nm blue laser coupled with a 525/30 nm filter. All reported data represent the average of at least three independent experiments. Data analysis was performed with InCyte software included in Millipore GuavaSoft 3.2 or with FlowJo. Gating was conducted by performing control experiments in which cells were untreated or treated with different control samples. Results are reported as the percentage of EGFP positive cells and as the median fluorescence intensity of positive cells.

USC
UNIVERSIDADE DE SANTIAGO DE COMPOSTELA

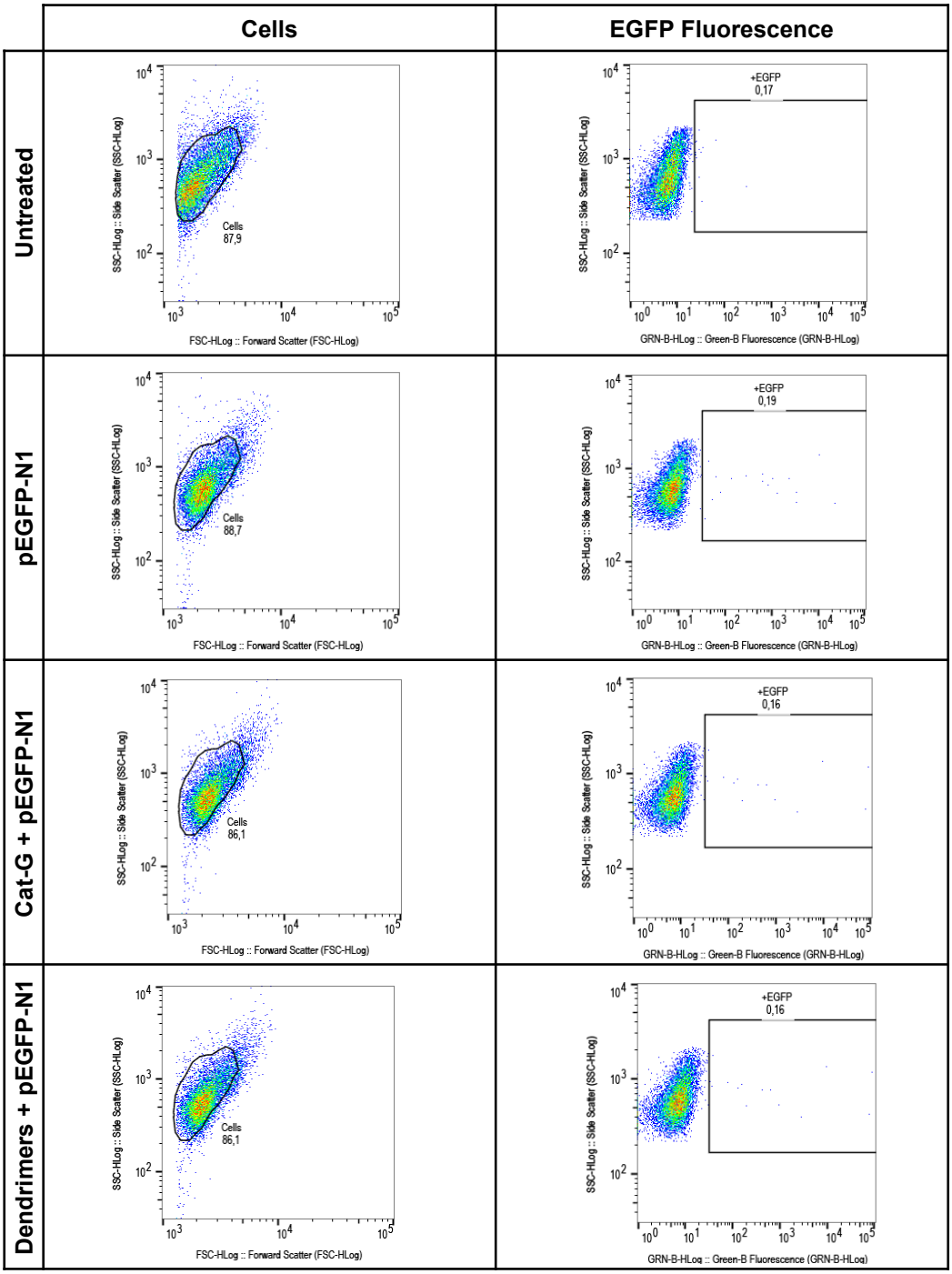

Figure 87. Gating for analyzing *in vitro* transfection efficiency by flow cytometry. Dot plot displaying SSC *vs* FSC showing the region selected as cells for subsequent analysis (first column). Dot plot displaying SSC *vs* EGFP fluorescence intensity showing the region selected as EGFP positive cells (second column). Experiments performed with (i) untreated HEK-293 cells, and cells after 72 h of incubation with (ii) pEGFP-N1, (iii) a mixture of pEGFP-N1 and Cat-G (equivalent to polyplex 5-10-5G devoid of PEG[G3]-BA and 3[G2]-BA), and a mixture of pEGFP-N1 and dendrimers (equivalent to polyplex 5-10-5G devoid of Cat-G).

USC
UNIVERSIDADE DE SANTIAGO DE COMPOSTELA

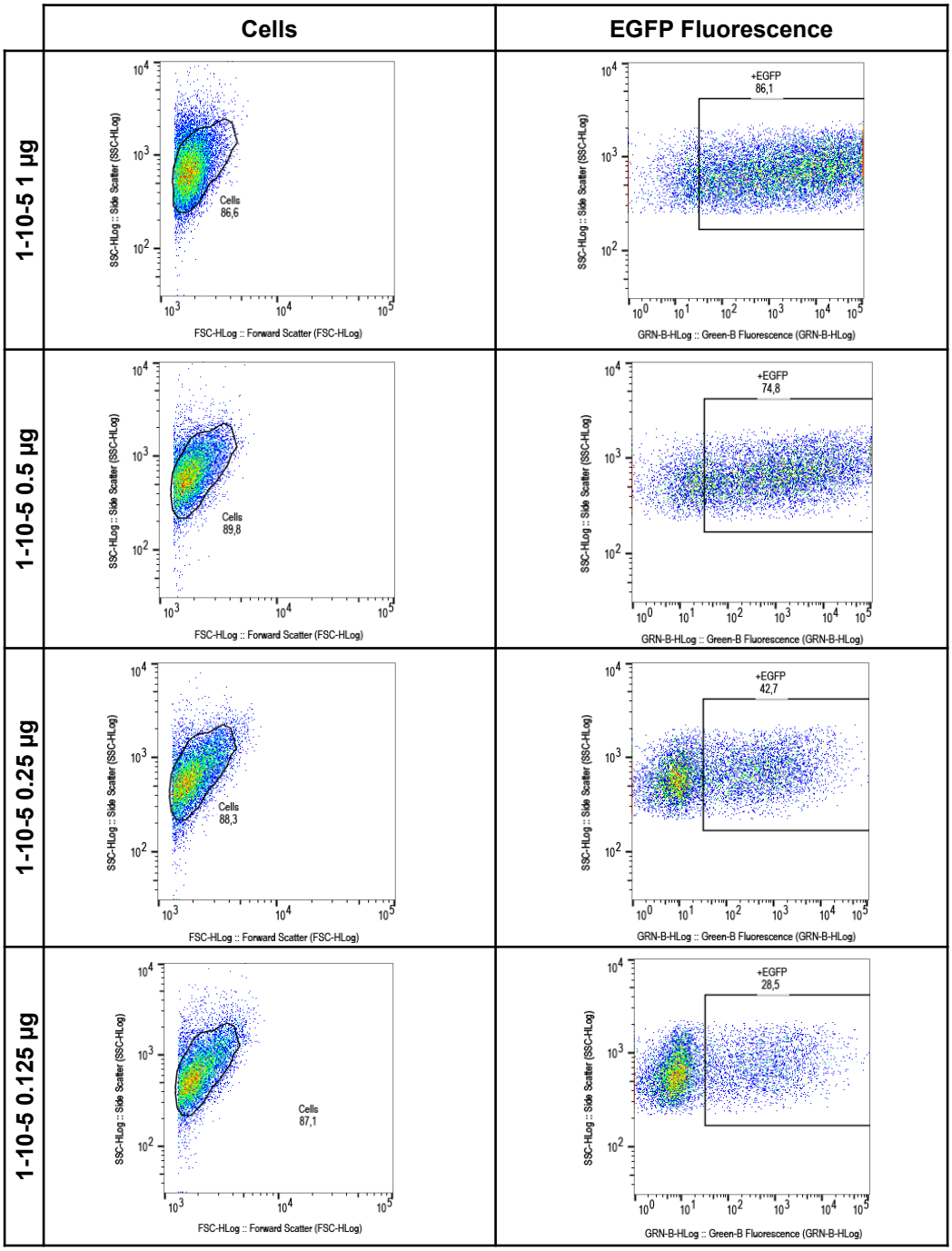

Figure 88. Gating for analyzing *in vitro* transfection efficiency by flow cytometry. Dot plot displaying SSC *vs* FSC showing the region selected as cells for subsequent analysis (first column). Dot plot displaying SSC *vs* EGFP fluorescence intensity showing the region selected as EGFP positive cells (second column). Dose-dependent transfection of polyplex 1-10-5G after 72 h in HEK-293 cells.

USC
UNIVERSIDADE DE SANTIAGO DE COMPOSTELA

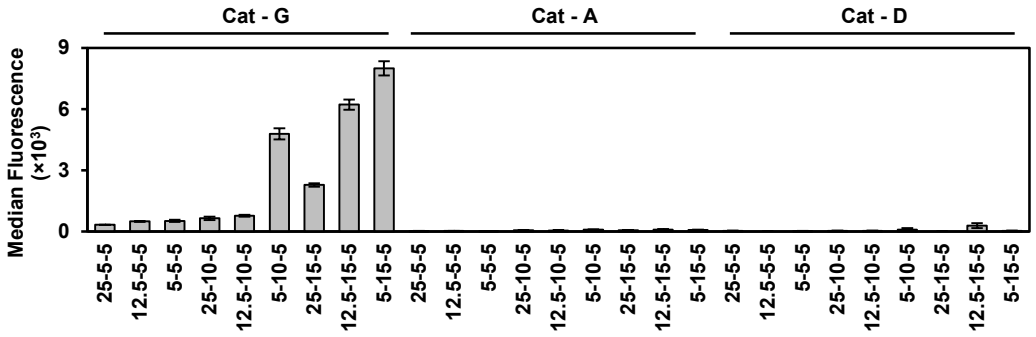

Figure 89. Median EGFP fluorescence of HEK-293 cells transfected for 72 h with G-, A-, and D-polyplexes of different % PEG and N/P ratios (CBA 5) measured by flow cytometry.

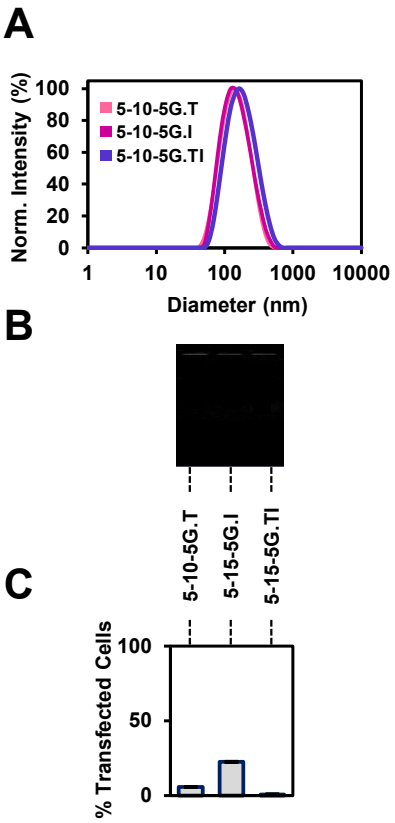

Figure 90. Polyplex 5-10-5G dopped with Cat-T and Cat-I. DLS histograms (A), gel retardation experiments with ethidium bromide on agarose gel electrophoresis (B), and percentage of transfected HEK-293 cells after 72 h of incubation (C).

Cell Viability. After 72 h of transfection, cell viability was determined by a colorimetric assay with CCK-8 following manufacturer's protocol. After 2 h of incubation at 37 °C in 5% CO_2 with a 6% solution of CCK-8 in fresh medium, supernatant solution was transferred to 96-well culture plates (Corning Costar 96-Well microplates from Thermo Scientific). Viability was determined by measuring the supernatant absorbance at 450 nm in a plate reader Tecan Infinite F200 PRO. Absorbance (*A*) from a 6% CCK-8 solution in medium was subtracted from all data points. Viability was calculated as follows:

$$\text{Cell Viability (\%)} = 100 \times \frac{(A_{\text{sample}} - A_{6\%\ \text{CCK-8}})}{(A_{\text{control}} - A_{6\%\ \text{CCK-8}})}$$

Fluorescence Microscopy. HEK-293 cells were seeded in 24-well glass bottom 15 mm plates (Cellvis) at a density of 200000 cells/mL in 500 µL of medium. After 24 h of incubation at 37 °C in 5% CO_2, culture media was replaced with 250 µL of medium and polyplex solution (1 µg pEGFP-N1/well). Cells were then incubated at 37 °C in 5% CO_2 for 5 h, followed by a replacement of culture media with fresh medium and a new incubation for 72 h at 37 °C in 5% CO_2. Then, EGFP expression was detected by fluorescence microscopy using a Nikon TiE microscope equipped with a Zyla 4.2 PLUS camera (Andor, Oxford Instruments). Excitation 475/35 nm; emission 530/43 nm.

Internalization Studies by Laser Scanning Confocal Microscopy (LSCM). HEK-293 were seeded in 24-well glass bottom 15 mm plates (Cellvis) at a density of 200000 cells/mL in 500 µL of medium. After 24 h of incubation at 37 °C in 5% CO_2, culture media was replaced with 250 µL of medium and polyplex solution (1 µg pEGFP-N1-Cy5/well). Cells were then incubated at 37 °C in 5% CO_2 for 5 h. Half an hour before observation, acidic organelles were stained by adding 10 µL of LysoTracker Red (10 µM in 10% DMSO:H_2O) and nuclei were stained by adding 10 µL of Hoechst 33258 (200 µM in 10% DMSO:H_2O). Before observation, culture media was removed, cells were washed with DMEM and 500 µL of fresh medium was added.

Confocal images were obtained on an Andor Dragonfly spinning disk confocal system mounted on a Nikon TiE microscope equipped with a Zyla 4.2 PLUS sCMOS digital camera (Andor, Oxford Instruments) and an OKO-lab incubator to maintain cells at 37 °C. Samples were excited with three different lasers (405, 561, and 637 nm) and the emitted fluorescence was collected by the filter wheel (450/50 nm, 620/50 nm, and 725/40 nm) with appropriate combinations of them.

Internalization Studies by Flow Cytometry. HEK-293 cells were seeded in a 24-well plate at a density of 200000 cells/mL. After 24 h of incubation at 37 °C in 5% CO_2, medium was replaced with 250 µL of medium and polyplex solution (1 µg pEGFP-N1-Cy5/well). After 5 h of incubation at 37 °C in 5% CO_2, cells were washed with PBS (3 × 500 µL) and trypsinized (100 µL 0.25% Trypsin–EDTA) for 5 min followed by trypsin quenching with 350 µL of serum-supplemented PBS. Then, cells were pelleted by centrifugation (5 min, 700 *g*), washed with 500 µL of serum-supplemented PBS, and pelleted again using the same conditions. Finally, cells were resuspended with 500 µL of serum-supplemented PBS and the suspension was transferred into FACS tubes for analysis by flow cytometry. At least 10000 events were collected using a Becton-Dickinson FACSCalibur Flow Cytometer equipped with a 635 nm red laser coupled with a BP 660/13 nm filter. For the analysis, cells population was selected by representing FSC vs SSC. Then, histograms displaying the number of events (count) vs Cy5 fluorescence were obtained. The region of Cy5 positive cells was delimited referring to untreated cells (control). Results are reported as the percentage of Cy5 positive cells.

USC
UNIVERSIDADE DE SANTIAGO DE COMPOSTELA

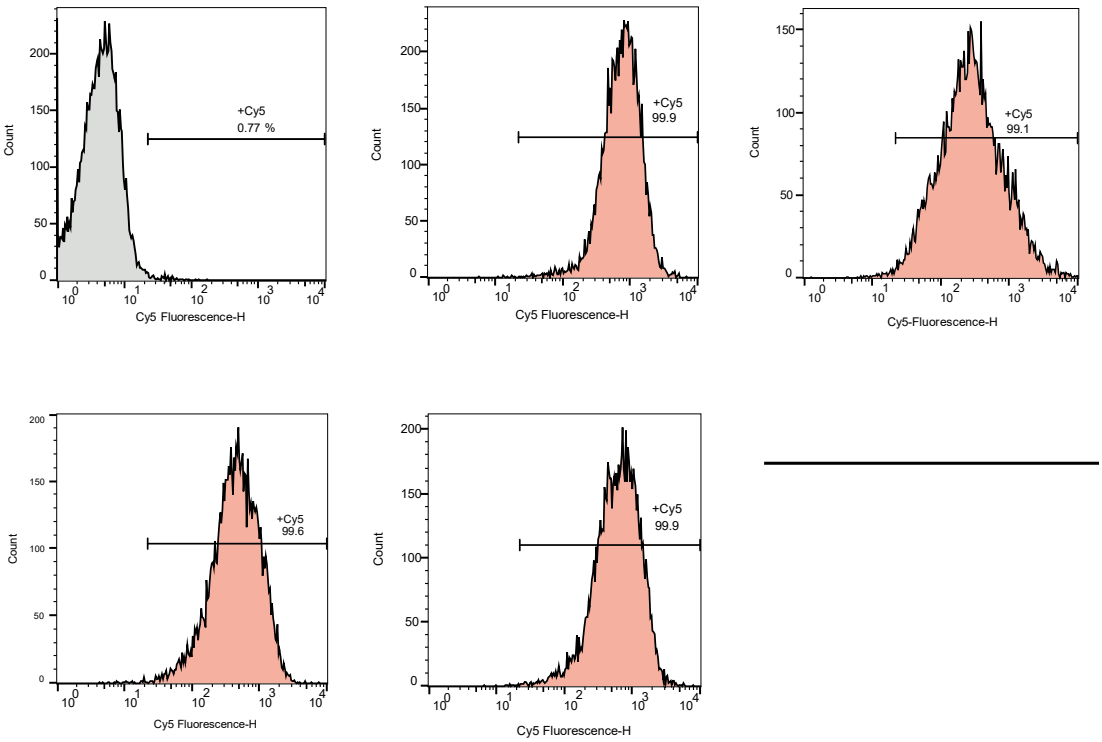

Figure 91. Histograms displaying number of cells (count) vs Cy5 fluorescence intensity showing the region selected as Cy5 positive cells. Experiments performed with untreated HEK-293 cells (A), and cells after 5 h of incubation with 25-10-5G (B), 5-10-5G (C), 5-10-5A (D) and 5-10-5D (E). Results are reported as the percentage of Cy5 positive cells (F).

Erythrocyte Aggregation Assay. Fresh rat blood was collected and immediately mixed with sodium citrate to a final concentration of 25 mM. Erythrocytes were obtained after multiple rounds of centrifugation in cold PBS, until the supernatant became clear (1600 *g* at 4 °C for 10 min). A 3% (w/v) suspension of erythrocytes was then prepared in PBS. Aliquots of an erythrocyte suspension (100 µL, 1% w/v in PBS) were mixed with 100 µL of solutions with increasing concentrations of PEG[G3]-BA or 3[G2]-BA and Cat-G at a CBA ratio of 5 in PBS (final concentrations: 25, 50, 100, and 250 µg/mL). The resulting suspensions were transferred to 24-well glass bottom 15 mm plates (Cellvis) and incubated at 37 °C in 5% CO_2. After 1 h of incubation, the degree of erythrocyte aggregation was analyzed by imaging the samples using a Nikon TiE microscope equipped with a Zyla 4.2 PLUS camera (Andor, Oxford Instruments).

Hemolysis Assay. Aliquots of an erythrocyte suspension (100 µL, 3% w/v in PBS) were mixed with 100 µL of solutions with increasing concentrations of PEG[G3]-BA or 3[G2]-BA and Cat-G at a CBA ratio of 5 in PBS (final concentrations: 5, 25, 50, 100, and 250 µg/mL). The resulting suspensions were incubated for 1 h at 37 °C under orbital shaking. Then, cells were removed by centrifugation (1600 *g*, 10 min) and hemoglobin release was analyzed by measuring the supernatant absorbance (*A*) at 540 nm. PBS and 2% Triton X-100 were used as negative (nonhemolytic, 0% hemoglobin release) and positive (hemolytic, 100% hemoglobin release) controls, respectively. Absorbance measurements were performed in a plate reader Tecan Infinite F200 PRO. The percentage of hemolysis was calculated as follows:

$$\text{Hemolysis (\%)} = 100 \times \frac{(A_{\text{sample}} - A_{\text{control}})}{(A_{2\%\ \text{Triton X-100}} - A_{\text{control}})}$$

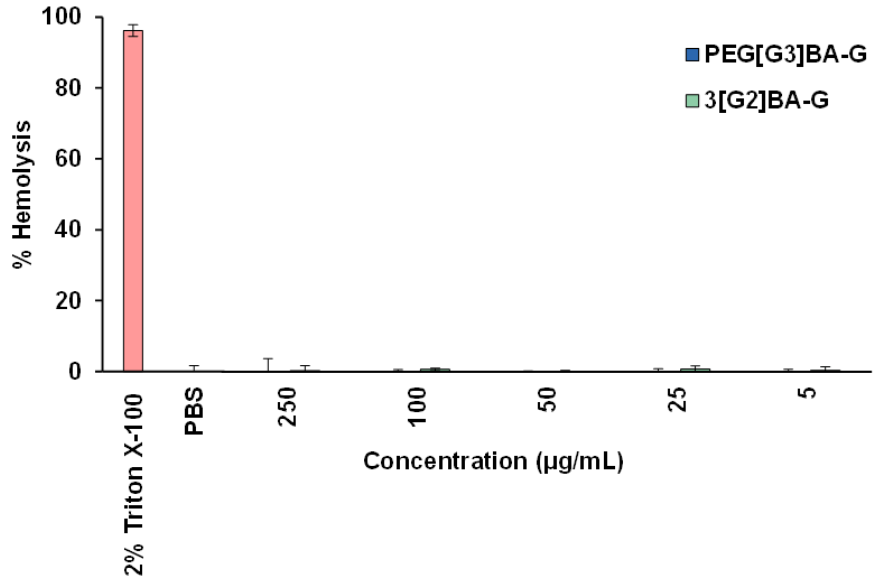

Figure 92. Percentage of hemoglobin released upon incubation of erythrocytes (3% w/v in PBS) with increasing concentrations of PEG[G3]-BA or 3[G2]-BA and Cat-G at a CBA ratio of 5, for 1 h at 37 ºC. The amount of hemoglobin released was determined by absorbance of the supernatant (540 nm), using PBS and 2% Triton X-100 as negative and positive controls, respectively.

3.2.7 *In vitro* Assays

Protection against decomplexation. The ability of cationic polyboronate vectors to protect pEGFP-N1 against decomplexation by glycosaminoglycans/polyanions was assessed in 96-well plates by monitoring the fluorescence increase of ethidium bromide permeating the polyplex and intercalating into pDNA. Untreated polyplexes (no fluorescence) and naked pDNA (maximum fluorescence, complete ethidium bromide accessibility to pDNA) were employed as negative and positive controls, respectively.

Briefly, polyplexes 1-10-5G and 1-15-5G (0.6 µg of pEGFP-N1, 8 µL per well) were incubated for 2 h at 37 ºC under horizontal shaking with increasing concentrations of hyaluronic acid, heparin, and dextran sulfate (92 µL, PBS), which accounted for up to a 18 charge ratio relative to the negative phosphate groups of pEGFP-N1 (equivalent to 138 µg/mL of hyaluronic acid, 55 µg/mL of heparin, and 43 µg/mL of dextran sulfate). Once at room temperature, ethidium bromide (0.5 µg) was added to each well and its fluorescence measured in a plate reader Tecan Infinite F200 PRO (λ_{ex} 300 nm, λ_{em} 600 nm).

DNase I Protection Assay. DNase I (1 U DNase/µg pEGFP-N1) was added over 100 µL of polyplexes 1-10-5G and 1-15-5G (10 ng of pEGFP-N1/µL) in 10 mM HEPES 7.1. After incubation for 60 min at 37 °C, samples were cooled at 0 °C and the enzymatic reaction was quenched by adding 5 µL of 0.5 M EDTA. Complexed pEGFP-N1 was partially dissociated from polyplexes by treatment with dextran sulfate (4 µL of a 50 mg/mL solution in 10 mM HEPES 7.1) for 60 min at 37 °C. The topology of the released pEGFP-N1 was examined by 0.7% agarose gel electrophoresis using naked pEGFP-N1 as control.

3.3 Experimental data for Dynamic Covalent Boronate Chemistry for the *In Situ* Preparation, Stabilization, and Activity Optimization of Coacervate Artificial Cells

3.3.1 Materials

All chemicals were purchased from Acros Organics, Fluka, Sigma-Aldrich, or Thermo Fisher Scientific, unless otherwise noted. Cy5-NHS was obtained from Lumiprobe. All solvents were HPLC grade, purchased from Scharlab, or Sigma-Aldrich. CH_2Cl_2 was dried using a SPS800 solvent purification system from MBRAUN. DMSO and Et_3N were dried under 4Å molecular sieves. H_2O was of Milli-Q grade obtained using a Millipore water purification system. Cat-G was prepared following known procedures.[150] PEG[G3]-BA and 3[G2]-BA were prepared following procedures previously described by our group.[149]

3.3.2 Instrumentation

Determination of pH Values. pH values were measured with a portable pH-meter (Crison PH25) connected to a glass electrode (Crison 52 09).

UV-Vis Spectroscopy. UV-Vis spectra were recorded on a Jasco V-630 spectrometer.

Dialysis. Dialysis was performed with an 18 mm Spectra/Por 6 MWCO 1 kDa or 10 kDa membrane tubing from SpectrumLabs.

Zeta Potential. Zeta potential values were measured by laser doppler anemometry (LDA), measuring the mean electrophoretic mobility (Malvern Zetasizer Nano ZS, Malvern Instruments) in 10 mM PB pH 7.0, 100 mM NaCl using the Smoluchowski approximation.

Fluorescence Measurements. Fluorescence measurements were performed in a plate reader Tecan Infinite F200 PRO. Gain was fixed or selected as optimal for dynamic and static measurements, respectively.

LSCM. Confocal images were obtained on an Andor Dragonfly spinning disk confocal system mounted on a Nikon TiE microscope equipped with a Zyla 4.2 PLUS sCMOS digital camera (Andor, Oxford Instruments).

Fluorescence Recovery After Photobleaching (FRAP) Measurements. FRAP experiments were performed on an inverted LSCM Leica Stellaris 8 FALCON (Leica Microsystems, Wetzlar, Germany) employing the FRAP interface available in Leica Application Suite X (LAS X) software.

3.3.3 Preparation Of Fluorescently Labeled Compounds

FITC-PEG[G3]-BA. A solution of fluorescein 5(6)-isothiocyanate (0.90 mg, 2.40 μmol) in dry DMSO (188 μL) was added to a solution of PEG[G3]-BA (5.00 mg, 0.30 μmol) and Et_3N (0.20 μL, 1.21 μmol) in CH_2Cl_2 (262 μL). After stirring overnight at rt under Ar and protected from light, the solvent was evaporated. The crude product was dissolved in 0.1 M $NaHCO_3$ and purified by dialysis (2 × 1.5 L 0.1 M $NaHCO_3$, 2 × 1.5 L H_2O, Spectra/Por 6, MWCO 1 kDa). After freeze-drying, FITC-PEG[G3]-BA (4.40 mg, 86%) was obtained as an orange solid. A

USC
DE SANTIAGO
DE COMPOSTELA

degree of functionalization of 100% in fluorescein was determined by absorbance at 490 nm (ε_{490}: 93200 $cm^{-1}M^{-1}$ as provided by supplier).

General Procedure for Labelling Proteins. Proteins were dissolved at 5.00 mg/mL in 0.1 M $NaHCO_3$ pH 9.0. A fresh solution of the fluorescent dye in DMSO was added and the reaction mixture was stirred overnight at rt protected from light. After freeze-drying, the crude products were dissolved in 150 µL of 300 mM NaCl and purified in a PD-10 column (Sephadex G-25) to remove any unreacted dye. Then, the fractions containing pure fluorescently labeled proteins were desalted by dialysis (5 × 500 mL H_2O, Spectra/Por 6, MWCO 1 kDa,) and lyophilized. The dye functionalization degrees were determined by measuring the relative UV absorbances of the proteins and fluorescent dyes using the following extinction coefficients: GOX ε_{280} 241500 $M^{-1}cm^{-1}$, HRP ε_{405} 102000 $M^{-1}cm^{-1}$, BSA ε_{280} 43824 $M^{-1}cm^{-1}$, AF488 ε_{495} 71800 $M^{-1}cm^{-1}$, Cy5 ε_{646} 250000 $M^{-1}cm^{-1}$.

GOX-AF488. From a solution of AF488-NHS (0.40 mg, 0.51 µmol, 9 eq) in dry DMSO (80 µL) and a solution of GOX (9.00 mg, 0.06 µmol) in 0.1 M $NaHCO_3$ (2.0 mL), GOX-AF488 (8.30 mg) labeled with an average of 2.3 molecules of AF488 was obtained following the General Procedure.

HRP-Cy5. From a solution of Cy5-NHS (3.40 mg, 5.1 µmol, 24 eq) in dry DMSO (70 µL) and a solution of HRP (9.00 mg, 0.21 µmol) in 0.1 M NaHCO3 (2.0 mL), HRP-Cy5 (8.10 mg) labeled with an average of 2.2 molecules of Cy5 was obtained following the General Procedure.

BSA-Cy5. From a solution of Cy5-NHS (1.0 mg, 1.7 µmol, 12 eq) in dry DMSO (100 µL) and a solution of BSA (9.00 mg, 0.14 µmol) in 0.1 M $NaHCO_3$ (1.8 mL), BSA-Cy5 (8.1 mg) labeled with an average of 1.0 molecules of Cy5 was obtained following the General Procedure.

3.3.4 Coacervate Preparation

Preparation of the Solutions of Components. PEG[G3]-BA (2.16 mg/mL, 135 µM) and 3[G2]-BA (1.50 mg/mL 135 µM) were separately dissolved in 10 mM PB pH 7.0, and the resulting solutions were aged for 1 h at rt before coacervation. Fresh solutions of catechols were prepared in 10 mM PB pH 7.0 (Cat-G, Cat-CA in Table 18, EPI, EGCG and CAT in Table 19) just before coacervate preparation. All solutions were filtered through sterile 0.22 µm nylon filters before coacervate formation.

Table 16. Concentration (mg/mL) of solutions of Cat-G, and Cat-CA used in the preparation of coacervates at different CBA. These concentrations account for 3.65, 7.3, and 11.0 mM for CBA 1, 2, and 3 respectively.

	CBA 1	CBA 2	CBA 3
Cat-G	0.85	1.69	2.54
Cat-CA	0.67	1.33	2.00

USC UNIVERSIDADE DE SANTIAGO DE COMPOSTELA

Table 17. Concentration (mg/mL) of solutions of EPI, EGCG and CAT used in the preparation of coacervates at CBA 1.

10% EPI	2.00
10% EGCG	1.64
10% CAT	0.80

Preparation of Coacervates. For each charge ratio solutions of Cat-G and Cat-CA were mixed in different volume ratios (Table 20) to afford a total volume of 120 µL. A 100 µL portion of this solution was immediately added over a solution of 3[G2]-BA (100 µL) at 21 ºC under orbital stirring (350 rpm) in an Eppendorf Thermomixer C. After 15 min of stirring, ionic strength was adjusted to 100 mM NaCl with 5 M NaCl, and the mixture was incubated for 15 additional min before stabilization with PEG[G3]-BA (9 µL).

Table 18. Volume (µL) of Cat-G and Cat-CA solutions used for coacervate preparation.

	2:1	**1:1**	**1:2**
Cat-G	80	60	40
Cat-CA	40	60	80

Protein Encapsulation. The encapsulation of proteins into coacervates was done by adding the corresponding protein solution (1.7 µL, 2.0 mg/mL) to the coacervates solution immediately after coacervation. Protein encapsulation was confirmed by LSCM and the corresponding EE values obtained by comparing the fluorescence of the supernatant after centrifugation (2500 *g*, 2.5 min), with a standard calibration curve made from the fluorescence emission of fresh solutions of the proteins of known concentration prepared under identical conditions. Measurements performed in a plate reader Tecan Infinite F200 PRO.

Doped Coacervates. Coacervates doped with different catechols were prepared by adding 5 µL of the corresponding catechol solution (Table S3) to 120 µL of Cat-G and Cat-CA mixture. The molar ratio of dopant accounts for an extra 10 % of catechols. Then coacervation and protein encapsulation were conducted following the general procedure previously described.

USC UNIVERSIDADE DE SANTIAGO DE COMPOSTELA

3.3.5 Characterization of Coacervates

The presence of spherical coacervates and the absence of aggregates were monitored by optical microscopy. The size distribution of the samples was determined by image analysis using Image-J.

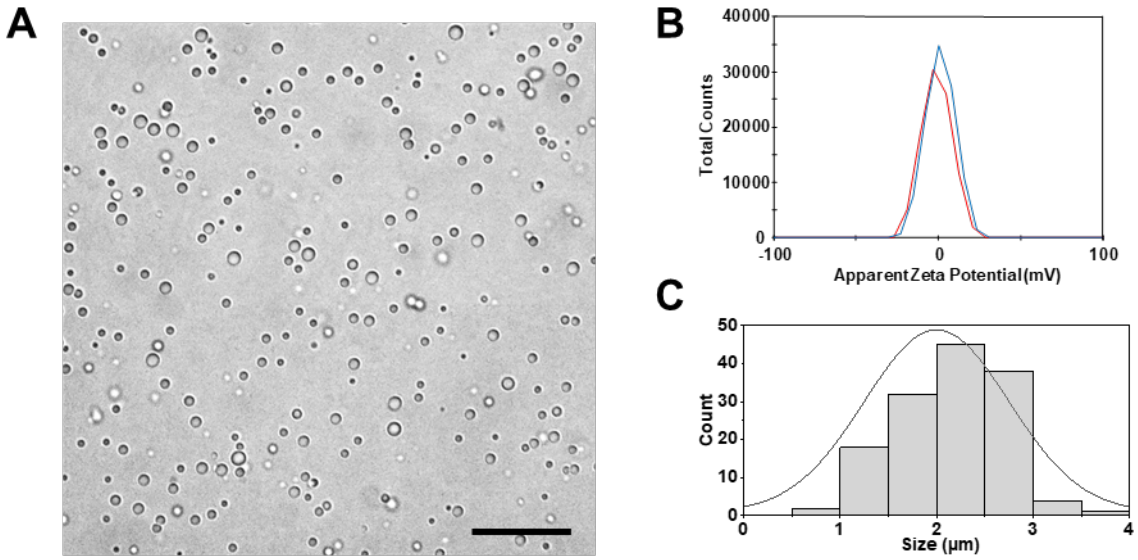

Figure 93. Characterization of coacervates prepared at CBA = 1, and stoichiometric ratio of charges. Brightfield image of coacervate population. (A) Z-Potential measurements of coacervates (ZP = 0 mV). (B) Histogram showing the size distribution of coacervates (C).

USC
UNIVERSIDADE DE SANTIAGO DE COMPOSTELA

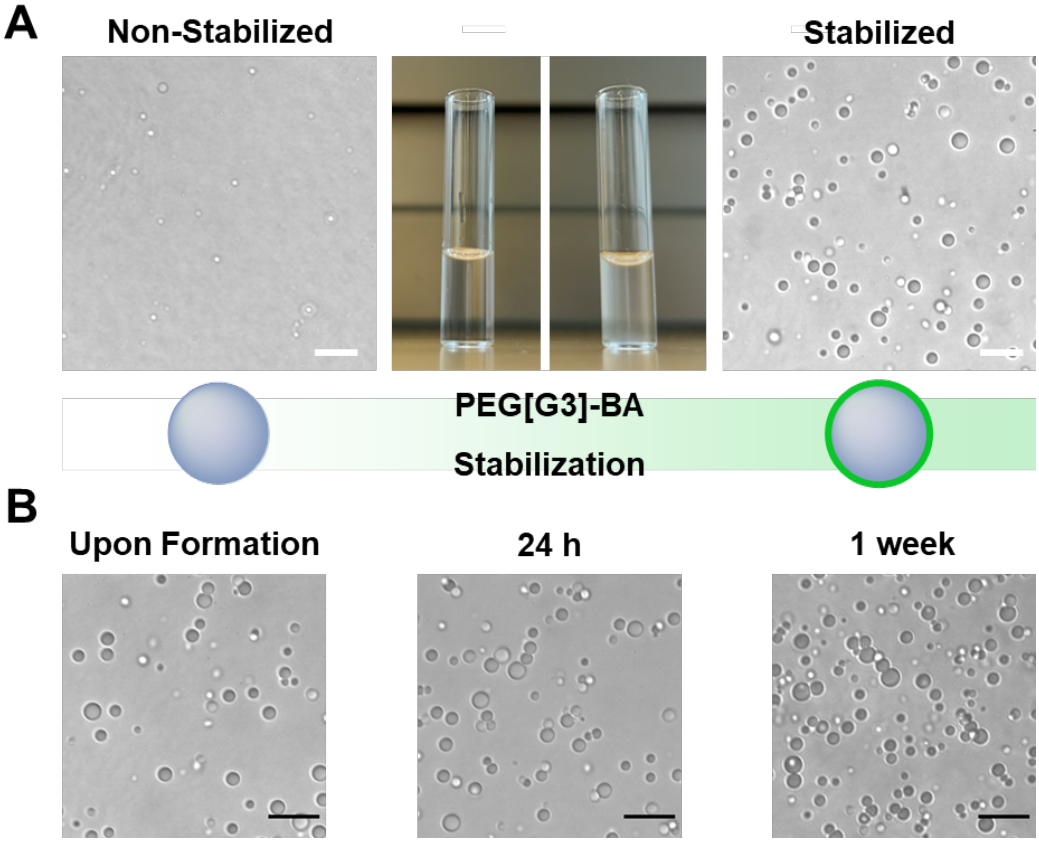

Figure 94. Stabilization of coacervates with PEG[G3]-BA. Brightfield microscopy images of nonstabilized (left) and stabilized (right) coacervates. The center image shows the presence of turbidity in the tube containing the stabilized coacervates (A). Brightfield images of stabilized coacervates upon formation (left), 24 h (middle), and 1 week (right) (B).

3.3.6 Enzymatic Cascade Reaction

Enzymatic Cascade by LSCM. Coacervates (CBA 1, Charge ratio 2:1) containing either AF488-GOX (green) or Cy5-HRP (blue) were mixed in a 1:1 volume ratio to a volume of 100 µL in a Cellvis 4-Chamber microwells (35mm Glass Bottom Dish with 20 mm, #1.5 cover glass). Controls experiments were performed to discard protein exchange between both populations of coacervates. Once an area of interest containing similar number of coacervates from both populations was selected, 3 µL of 6 µM Amplex Red in DMSO were added into the well. The enzymatic cascade reaction was triggered by gentle pippeting 3 µL of 0.12 mM glucose into the coacervate solution. The sample was imaged at different times to monitor production and localization of resorufin (red) and diffusion. Experiments performed in the absence of any of the enzymes (being replaced by 10 mM PB 7.0, 150 mM NaCl) did not result in the production of resorufin.

USC UNIVERSIDADE DE SANTIAGO DE COMPOSTELA

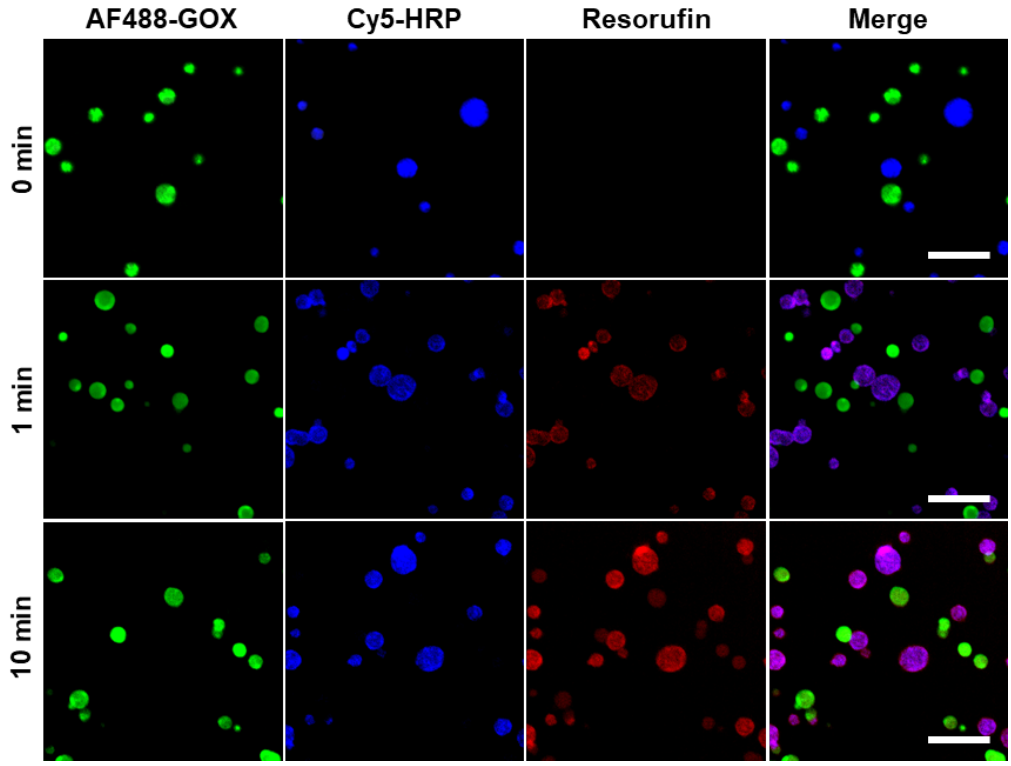

Figure 95. Enzymatic Cascade Reaction by LSCM. Experimental was conducted as described in the previous section. LSCM images show the GOX/HRP enzymatic production of resorufin (red) from AF488@C-GOX and Cy5-HRP@C droplets, identified by AF-488 (green) or Cy5 (blue), respectively.

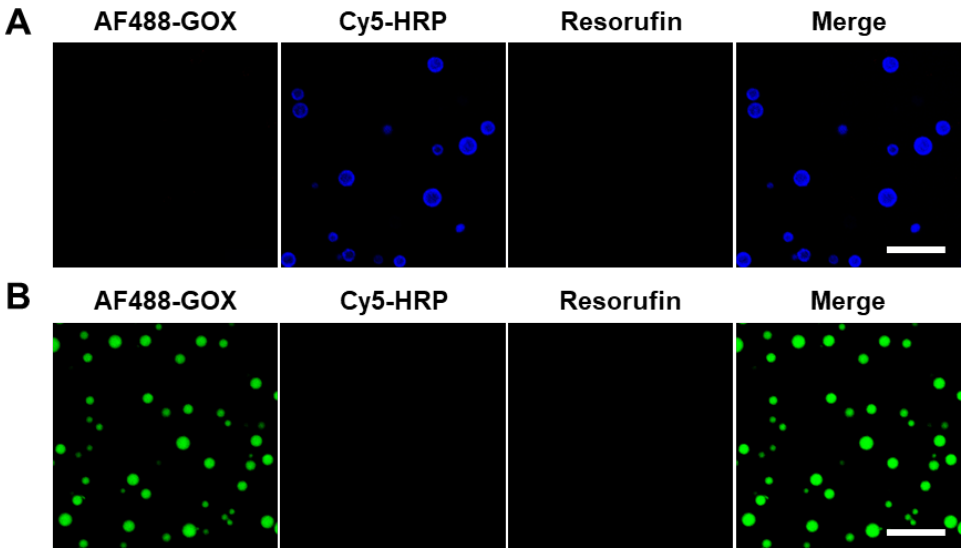

Figure 96. Enzymatic cascade control experiments by LSCM. LSCM images show the GOX/HRP enzymatic production of resorufin (red) from AF488@C-GOX and Cy5-HRP@C droplets, identified by AF-488 (green) or Cy5 (blue), respectively. Experiment conducted after 10 min in the absence of GOX (A) or HRP (B)

USC
UNIVERSIDADE DE SANTIAGO DE COMPOSTELA

Monitorization of the Enzymatic Cascade. Coacervates encapsulating GOX (60 µl) and HRP (30 µL) were placed in a 96-well microplate (Nunc F96 MicroWell flat black from Thermo Scientific) to achieve final protein concentrations of 10 µg/mL and 5 µg/mL, respectively. Then, Then, *ortho*-phenylenediamine (oPD, 2 µL, 27.7 mM) and glucose (6 µL, 16.7 mM) were added stepwise to initiate the enzymatic cascade reaction. The reaction progression was followed by measuring the appearance of the fluorescence of the reaction product 2z3-diaminophenazine (DAP; λ_{ex} 405 nm, λ_{em} 550 nm), using a plate reader Tecan Infinite F200 PRO. Control experiments were performed under identical conditions with the system depleted in enzymes or glucose, replacing any missing component with 10 mM PB 7.0 supplemented with 100 mM NaCl. Fluorescence data were normalized to the maximum fluorescence signal recorded during the experiment for accurate comparison and analysis.

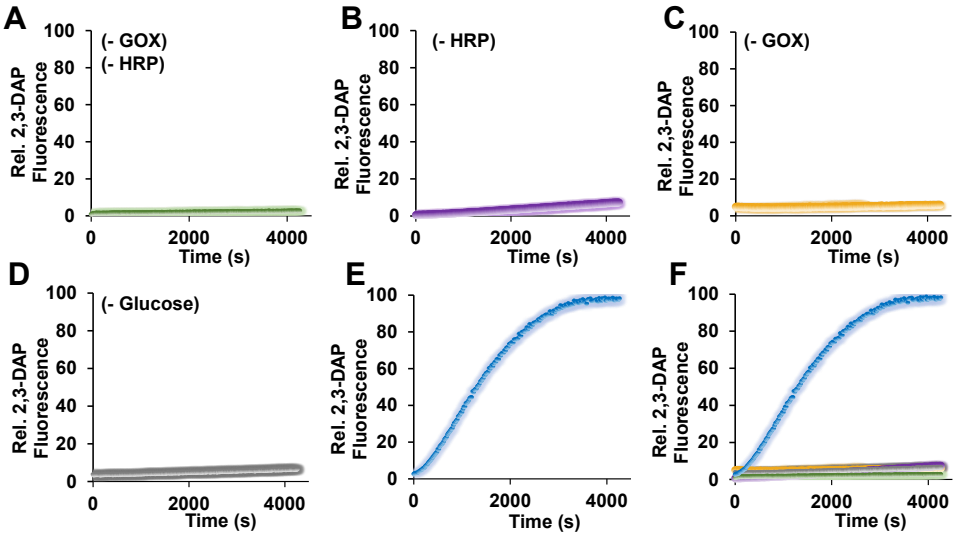

Figure 97. Enzymatic cascade reaction monitored by following the fluorescence signal of DAP. Plots show the fluorescence increase with time of substrates (A), GOX@C+ substrates (B), HRP@C + substrates (C), GOX@C + HRP@C + *o*PD (D), GOX@C + HRP@C + substrates (E) and the superposition of all of them (F). Shaded plots represent standard deviation.

3.3.7 Studies on doped coacervates

FRAP Measurements and Analysis. Coacervates encapsulating Cy5-BSA (100 µL, 5.1 µM BSA) were transferred to a µ-side 18 well glass bottom (Ibidi). FRAP experiments were performed with the FRAP interface available in Leica LAS X software. For imaging, samples were excited with a white light laser (WLL2; λ_{ex} 649 nm; λ_{em} 654-700 nm) and visualized with a HC PL APO CS2 93×/1.30 Gly objective. An initial image was acquired to define a region of interest (ROI), 1 µm × 1 µm, equivalent to approximately a quarter of the droplet. Then, three images of 256 × 125 µm were acquired before the ROI was bleached for 30 iterations of 649 nm (100% laser power). The recovery was monitored for 5 min after photobleaching by obtaining 180 image series (0.26% laser power). The intensities of the bleached ROI, reference area (a nearby coacervate that was not bleached), and the background were extracted from the images with Image-J. Data were normalized by removing the background intensity and dividing by the intensity of the reference area. A first-order exponential equation was fitted using Origin 2022 (OriginLab) from which the recovery half-life, and apparent diffusion coefficient D_{app} were calculated. The halftime of recovery ($\tau_{1/2}$) was calculated from equation 1, where τ is the fluorescence recovery time constant.[118]

$$\tau_{1/2} = \tau \cdot \ln(2) \qquad \text{Eq 1}$$

D_{app} was calculated following equation 2, an approximation reported in the literature[118] which assumes 2D diffusion, where ω is the radius of the bleached region.

$$D_{app} = 0.88\omega^2 / 4\tau_{1/2} \qquad \text{Eq 2}$$

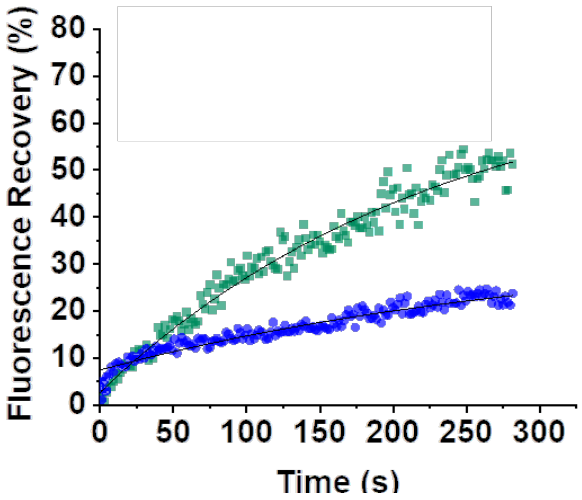

Figure 98. Fluorescence recovery after photobleaching (FRAP) curves fitted to an exponential growth model equation for C-EGCG (blue), and C-CAT (green).

Doping Effect over the Enzymatic Cascade Reaction. Coacervates encapsulating GOX or HRP were doped with different catechols following the above-described procedures. The EEs of both enzymes were found to be independent of the dopant (Figure 99). Coacervates encapsulating GOX (60 µl) and HRP (30 µL) were placed in a 96-well microplate (Nunc F96 MicroWell flat black from Thermo Scientific) to achieve final protein concentrations of 10 µg/mL and 5 µg/mL, respectively. Then, Then, *ortho*-phenylenediamine (oPD, 2 µL, 27.7 mM) and glucose (6 µL, 16.7 mM) were added stepwise to initiate the enzymatic cascade reaction. The reaction progression was followed by measuring the appearance of the fluorescence of the reaction product 2z3-diaminophenazine (DAP; λ_{ex} 405 nm, λ_{em} 550 nm), using a plate reader Tecan Infinite F200 PRO. Fluorescence data were normalized to the maximum fluorescence signal recorded during the experiment for accurate comparison and analysis.

To discard any artefact, a control experiment was conducted employing CAT doped and control coacervates in an enzymatic cascade reaction conducted following the above-described experiment. After reaching constant levels of fluorescence, coacervates were dissolved by adding 100 µL of CH_3OH containing urea as protein inhibitor. Fluorescence measurements were then conducted selecting optimal gain values. The relative differences between fluorescence levels before and after solution were then calculating by dividing the fluorescence from the doped sample by the control one. The obtained values demonstrated no differences between both relations, confirming the absence of quenching issues.

USC
UNIVERSIDADE DE SANTIAGO DE COMPOSTELA

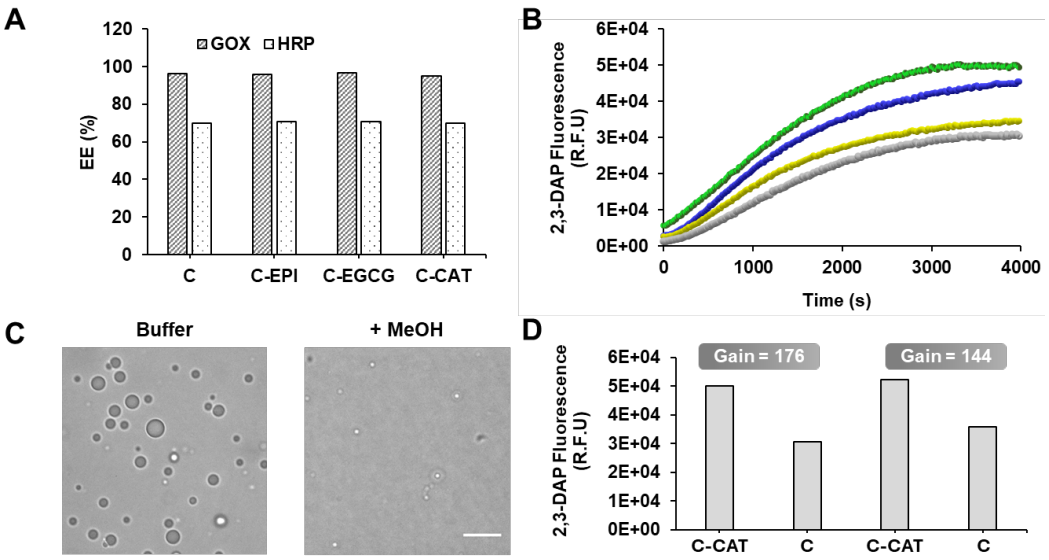

Figure 99. Protein studies with doped coacervates. Encapsulation efficiency (EE) for GOX and HRP in doped coacervates (A). Enzymatic production of 2,3-DAP using doped coacervates: undoped (gray); C-EPI (yellow); C-EGCG (blue) and C-CAT (green) (B). Brightfield microscopy images showing coacervate disintegration after the addition of MeOH (C). Fluorescence intensity measurements showing the 2,3-DAP signal after completion of the enzymatic cascade reaction before and after the addition of MeOH (D).

USC
UNIVERSIDADE DE SANTIAGO DE COMPOSTELA

4. RESULTS AND DISCUSSION

4.1 A HIERARCHICAL ASSEMBLY OF *IN SITU* PREPARED BORONATE-ESTER DENDRIMERS REGULATES THE SIZE OF DOXORUBICIN POLYMER THERAPEUTICS

4.1.1 Research Background

Cancer is the second leading cause of premature death worldwide and is expected to surpass heart disease at first position in the next few years.[154,155] Current strategies to treat cancer rely on surgery, chemotherapy, radiation, and some combinations of them. Chemotherapy uses cytotoxic agents to kill or block the growth of cancer cells. Nevertheless, despite its use is becoming standard in the clinic, conventional chemotherapeutic agents are plagued by drawbacks such as non-specific systemic distribution, water-solubility issues, or the development of multi-drug resistance.[156] As discussed in the first section of this thesis, DDS attempt to overcome those limitations by improving the delivery of the drug into the affected tissue. However, the chemotherapy efficacy of any DDS depends on the optimal selection of the carrier.[157,] Giving the already discussed importance of developing DDS able to interact with the tumoral environment, and the unique properties of DCvC to achieve molecular control over such interaction, our group has developed an advanced carrier based on a PEG-GATG copolymer functionalized with peripheral Wulff-type BAs.[158] This system efficiently binds drugs containing 1,2-diol groups under physiological conditions, while facilitating the controlled release of the drug below the pK_a of the BAs in the endosome-lysosome. Similar to approaches such as PISA,[159] the *in situ* conjugation of the drugs onto the dendritic surface via a fast-forming and strong boronate ester alters the hydrophilic-hydrophobic balance of the copolymer, resulting in its self-assembly into nanometric micelles.

As outlined in Section 1.2, several structural parameters must be considered to guarantee the efficacy of a given DDS. Among them, the size of the carrier is particularly important since it controls the PK and tumour retention.[160] However, the control over size remains elusive by current chemical technologies. In this context, our group has recently demonstrated how the hierarchical assembly of dendrimers can be programmed to engineer size-controlled PIC micelles (from 40 nm up to nearly 2 μm).[161] This unpublished study introduces a method to tune the size of PIC micelles employing a PEG-dendritic copolymer/dendrimer pair and an oppositely charged polyamino acid. Control over the size is achieved through the adjustment of micelle PEGylation, involving modulation of either the % PEG or the MW of PEG block. The formation of PIC aggregates has been correlated with the architecture and the self-assembly of the monomeric unit PIC (uPIC), the minimum neutral assembly formed from oppositely charged species in the early stages of the PIC growth. Since preparing PIC micelles in a single step with a precise core-corona structure and a wide range of diameters necessarily involves a hierarchical assembly of uPICs, a simple model, based on core-shell spherical particles, was developed to describe such an organized structure. This model, validated by static light scattering (SLS), discloses how the number of particles (*N*), the total surface area of particles (*S*), and the PEG density per particle (*D*) change with % PEG along the micelle series.

The present section of this thesis aims to bridge the last two technologies into a more advanced DDS. By taking advantage of the micelle PEGylation, it was possible to tune the size of micelles prepared by hierarchical assembly of boronate-ester dendrimers produced *in situ* from diol drugs. Doxorubicin (DOX), a frontline chemotherapeutic drug widely used for the treatment of

USC DE SANTIAGO DE COMPOSTELA

various cancers, lymphomas, and certain leukemias, was selected as test bank of this polymer therapeutic technology.

4.1.2 The PEGylation Degree Determines the Size of Boronate Based Micelles

The force which drives micelle formation is based on the amphiphilic character of a given structure. Once a CMC of these entities is reached in aqueous solution, they tend to self-assemble into micelles following a templated pattern: the hydrophilic sections are displayed through the exterior, attempting to minimize the interactions of the hydrophobic inner core within the aqueous solution. In the case of PIC micelles, this core is formed by the association of oppositely charged scaffolds in a stoichiometric charge ratio, letting the PEG chains to confine such interaction by their assembly along a hydrophilic external layer. Inspired by the principles of this assembly process, the above-described method was based on reducing PEGylation while maintaining a constant amount of charged units. Such reduction leaded the obtention of larger micelles, which accommodate a reduced number of PEG chains at the corona while incorporating increasing amount of nonPEGylated components within the core. Aimed by the effectivity of this method, herein the charged components will be substituted by the employment of *in situ* hydrophobized dendrimers. Although this methodology relies on a self-assemble process that cannot be explained by the uPIC theory, it confirms the founded PEGylation-template effect.

For developing such a technology, a PEG_{5k}-dendritic block copolymer (PEG[G3]-BA) and its nonPEGylated analog (3[G2]-BA), both from the GATG family and functionalized with 27 peripheral BAs, were employed. A PEGylation degree (% PEG) was defined as the percentage between PEG[G3]-BA and 3[G2]-BA. *Ortho*-aminomethylphenyl-BAs were selected due to their advantageous pK_a (approximately 6.5). Given that boronate ester formation is optimal at pH levels above the pK_a, these compounds will facilitate the formation of stable boronate bonds at physiological pH. Furthermore, they will enable the controlled dissociation of the ester bonds in acidic environments, thus providing both stability and responsiveness to pH changes. Among the large library of commercially available diols, CAT was selected as a model low molecular weight molecule with high-water solubility and strong association to BAs in aqueous solutions due to a favorable syn-periplanar diol orientation and an electron-donating character.

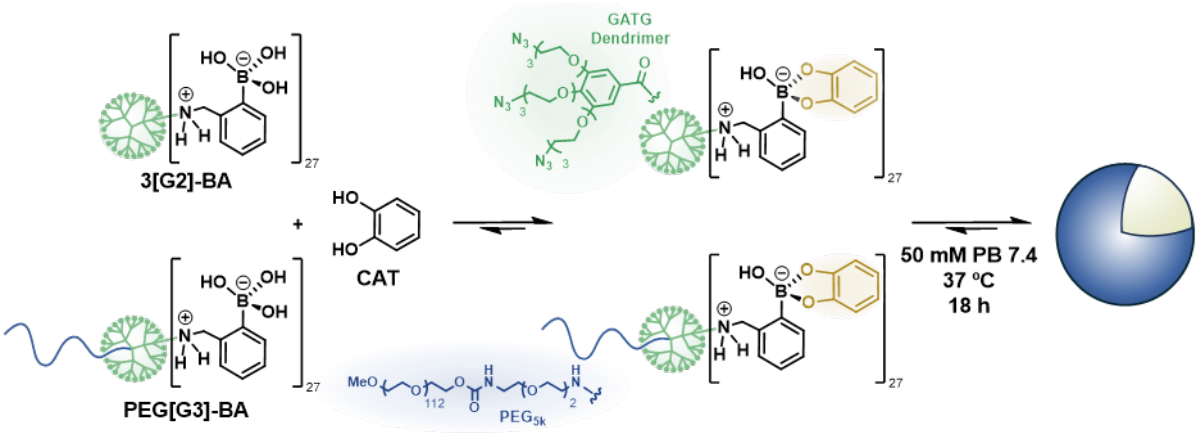

Figure 100. Schematic representation of the catechol-driven *in situ* hydrophobization and self-assembly of 3[G2]-BA and PEG[G3]-BA.

USC
UNIVERSIDADE DE SANTIAGO DE COMPOSTELA

Micelles with variable % PEG from PEG[G3]-BA/3[G2]-BA and CAT were prepared in 50 mM PB pH 7.4 by adding a mixture of dendritic components over a CAT solution accounting for 27 equiv (Figure 100).

The *in situ* incorporation of CAT units on the dendritic surface drives the dendrimer hydrophobization and self-assembly into micelles, with a size dictated by the employed % PEG (Figure 101). The size of the resulting structures was analysed by DLS measurements after 18 h of formation at 37 ºC, which revealed *R* increasing gradually from 16 to 535 nm on reducing the % PEG from 100 to 0.15%, with very low PDI (Figure 101, and 31-32). Micelles prepared at % PEG ≥ 0.4 were highly stable over time, as corroborated by DLS measurements performed 1 month after formation and storage at 4 ºC (Table 4, Figures 33-34). Interestingly, further reductions of % PEG below 0.15% caused micelle aggregation, highlighting the crucial role of the PEG chains at the corona, which not only serve as templates for micelle formation but are also essential for colloidal stability.

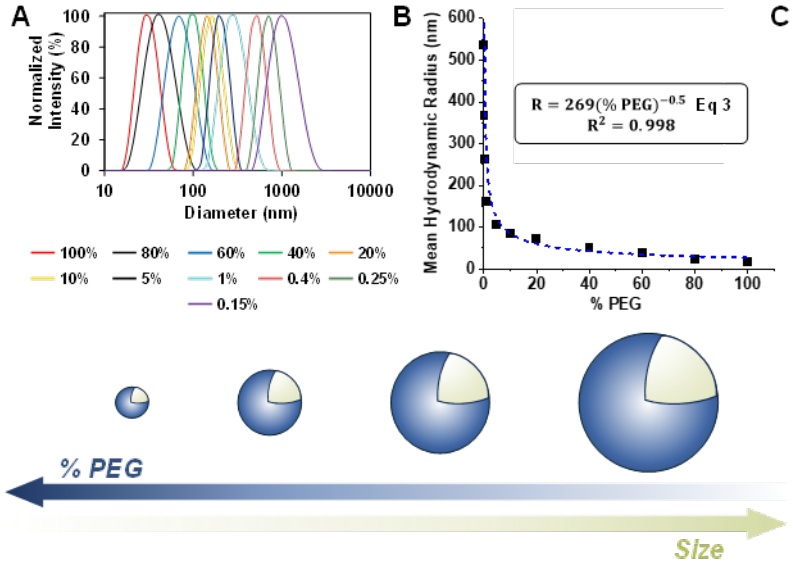

C

% PEG	Mean Hydrodinamic Radius (R, nm)	PDI
100	16 ± 1	0.10 ± 0.02
80	22 ± 1	0.12 ± 0.01
60	37 ± 1	0.08 ± 0.02
40	51 ± 1	0.02 ± 0.01
20	73 ± 1	0.02 ± 0.01
10	83 ± 1	0.04 ± 0.01
5	104 ± 2	0.03 ± 0.02
1	160 ± 4	0.16 ± 0.02
0.4	263 ± 3	0.02 ± 0.01
0.25	368 ± 6	0.10 ± 0.06
0.15	535 ± 17	0.16 ± 0.02

Figure 101. Impact of PEGylation on the size of CAT micelles. DLS size distribution of micelles prepared from PEG[G3]-BA/3[G2]-BA and CAT at different % PEG (A). (B). Variation of hydrodynamic radius (*R*) with % PEG; R^2 (R-squared) is the coefficient of determination (C). *R* and polydispersity index (PDI) of micelles.

The variation of *R* with % PEG is plotted in Figure 101B. The data points fit a power function (Eq 3):

$$R = 269\ (\%\ PEG)^{-0.5} \qquad \text{Eq 3}$$

Such an equation constitutes an extremely useful tool for the preparation of micelles with tailored diameter from a few nm up to the micron by simply selecting the % PEG, which variation along the whole series accounts for a factor of 667. Interestingly, the exponent -0.5 in Eq 3 indicates an inverse proportionality between % PEG and R^2 and hence, the surface area of the micelles. This relation confirms that the PEG chains effectively template the size of these micelles, corroborating the successful translation of the PIC-based methodology to these polyboronate micelles. As observed, while initial reductions of % PEG from 100 to 20% result in slight size increases (only 5-fold), further % PEG reductions lead to much larger sizes (up to 30-fold).

USC UNIVERSIDADE DE SANTIAGO DE COMPOSTELA

An important aspect to remark relies on the dynamic character of amphiphile activation. While static amphiphilic polymers are rapidly trapped into supramolecular aggregates in contact with aqueous solutions, the present process involves two simultaneous and interconnected equilibrium steps. First, BAs need to bond catechol to form the aggregating structures, and once a critical bonding point is reached the formed amphiphiles will be allowed to undergo self-assembly. As detailed in the description of the formation process, the CBA ratio was set to 1 along the series. To confirm the completeness of the boronate ester formation, the presence of unreacted BAs in the reaction medium was studied. This was addressed by performing fluorescence experiments with ARS, a catechol dye with extremely high affinity for BAs which exhibits a dramatic change in fluorescence intensity after boronate ester formation. Studies were performed by measuring the fluorescence of micelles with different PEGylation degrees (100, and 5%) after treatment with ARS (λ_{ex} 495 nm). Fluorescence values were compared with calibrations curves made independently from PEG[G3]-BA and 3[G2]-BA. Results confirmed complete functionalization of dendritic BAs as tested micelles afforded undistinguishable fluorescence as ARS (Figure 102). The absence of free BAs supports the concept of "micelle as nanoreactor" which argues that the pumping of H_2O molecules to the micelle external milieu acts as driving force for the boronate ester formation.

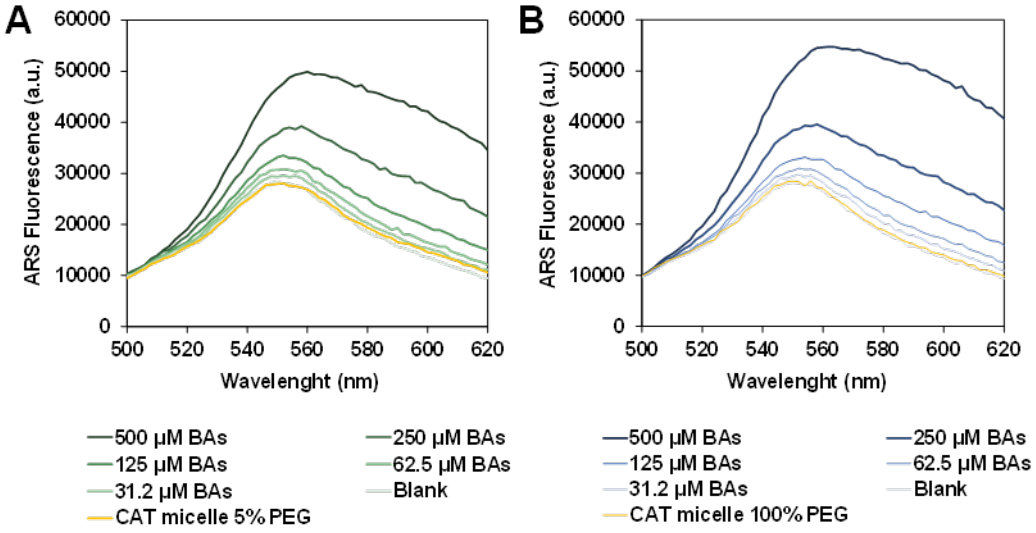

Figure 102. Quantification of free BAs by the ARS assay. Fluorescence measurements of free 3[G2]-BA (A) and PEG[G3]-BA (B) at different concentrations and CAT micelles prepared at 100 and 5 %PEG. Samples were excited at 495 nm and fluorescence was recorded from 500 to 620 nm.

Further characterization of CAT micelles was conducted to gather information about their morphology and internal structure. The morphology of the micelles was examined using STEM, which allows screening of aggregates across a broad range of diameters. Four micelles with different % PEG (100, 40, 5, and 0.4%) were analyzed, representing the entire series (Figure 101B). The resulting images, collected in Figure 103, show a good correlation with those sizes obtained from DLS measurements (Figure 103E). The core-corona structure of the micelles was determined by LSCM using a fluorescently labeled micelle prepared from FITC-PEG[G3]-BA (a version of the copolymer incorporating fluorescein isothiocyanate attached to the dendritic region) (Figure 103F). Overall, these results support the hypothesis that the size of dendritic polyboronate micelles can be regulated by simply adjusting the % PEG.

USC UNIVERSIDADE DE SANTIAGO DE COMPOSTELA

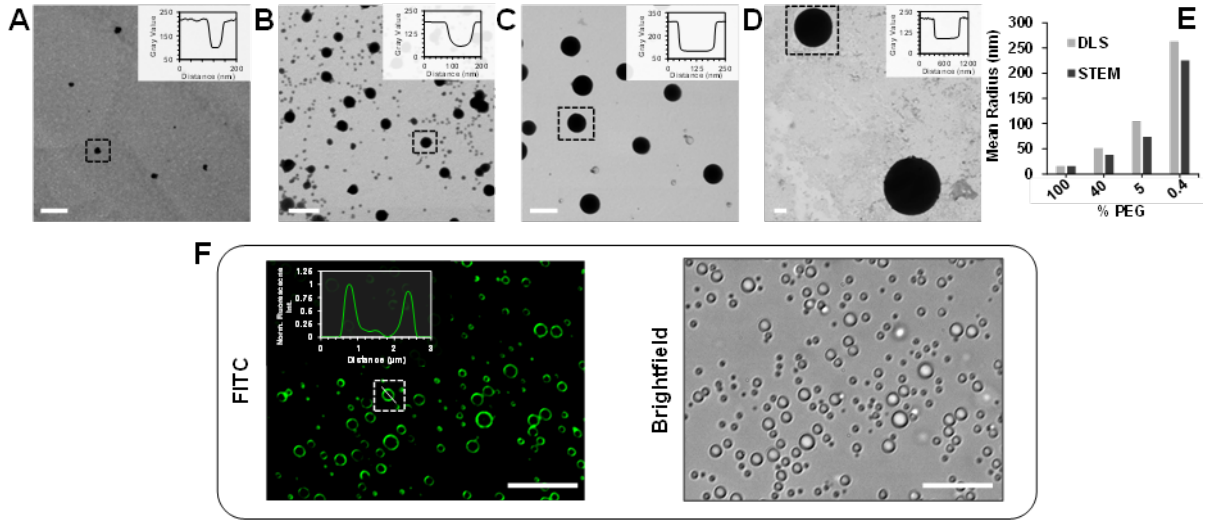

Figure 103. Characterization of CAT micelles. Top panel: STEM images of CAT micelles with representative % PEG: 100% (A), 40% (B), 5% (C), 0.4% (D). Comparison between the radii of the micelles obtained by DLS and STEM (E). LSCM images of fluorescently labeled micelles prepared from 0.25% FITC-PEG[G3]-BA (green). Scale bar 10 μm (F).

4.1.3 A Model of Spherical Micelles Describes the Hierarchical Assembly

To understand the hierarchical self-assembly of CAT micelles with tailored sizes, a model based on perfect spheres, analogous to that used for PIC micelles, was envisaged. This model, initially developed and validated by SLS for PIC micelles, aims to uncover how N, S, and D evolve across the micelle series as a function of % PEG.

Starting from the equation for the volume of a sphere (Eq 4) where r is the radius, a new equation was derived in which, N_i represents the number of micelles in the sample and V_i is defined as the total volume of micelles in the sample for any given % PEG (Eq 5). Assuming that: (a) the volume of the PEG corona is negligible compared to that of the micelle, and (b) the density of the core (and so, the total volume of micellar cores) is independent of the % PEG, Eq 6 was obtained to relate the relative number of micelles for two different % PEG (^{rel}N) with their respective radii.

$$V_{\text{sphere}} = \frac{4}{3}\,\pi\, r^3 \qquad \text{Eq 4}$$

$$V_{\text{i}} = N_{\text{i}}\,\frac{4}{3}\,\pi\, R_{\text{i}}^3 \qquad \text{Eq 5}$$

$$\left.\begin{aligned} V_{\text{i}} &= N_{\text{i}}\,\frac{4}{3}\,\pi\, R_{\text{i}}^3 \\ V_{\text{k}} &= N_{\text{k}}\,\frac{4}{3}\,\pi\, R_{\text{k}}^3 \end{aligned}\right\} V_{\text{i}} = V_{\text{k}} \rightarrow N_{\text{i}}\, R_{\text{i}}^3 = N_{\text{k}}\, R_{\text{k}}^3 \rightarrow {}^{\text{rel}}N = \frac{N_{\text{i}}}{N_{\text{k}}} = \left(\frac{R_{\text{k}}}{R_{\text{i}}}\right)^3 \qquad \text{Eq 6}$$

Then, the dependence between S and % PEG was addressed. Using the equation for the surface area of a sphere (Eq 7), S_{i} was defined as the total surface area of micelles in a sample for any % PEG (Eq 8). By examining the ratio between the total surface area of two micelles with different % PEG and considering Eq 6, Eq 9 was obtained to describe the relative total surface area of micelles (^{rel}S) for two % PEG as a function of their radii.

$$S_{\text{sphere}} = 4\,\pi\,r^2 \quad \text{Eq 7}$$

$$S_{\text{i}} = N_{\text{i}}\,4\,\pi\,R_{\text{i}}^2 \quad \text{Eq 8}$$

$$\left.\begin{aligned} S_{\text{i}} &= N_{\text{i}}\,4\,\pi\,R_{\text{i}}^2 \\ S_{\text{k}} &= N_{\text{k}}\,4\,\pi\,R_{\text{k}}^2 \end{aligned}\right\}$$

$$\frac{S_{\text{i}}}{S_{\text{k}}} = \frac{N_{\text{i}}}{N_{\text{k}}}\left(\frac{R_{\text{i}}}{R_{\text{k}}}\right)^2 = \left(\frac{R_{\text{k}}}{R_{\text{i}}}\right)^3\left(\frac{R_{\text{i}}}{R_{\text{k}}}\right)^2 = \frac{R_{\text{k}}}{R_{\text{i}}} \rightarrow {}^{\text{rel}}S = \frac{S_{\text{i}}}{S_{\text{k}}} = \frac{R_{\text{k}}}{R_{\text{i}}} \quad \text{Eq 9}$$

Finally, the evolution of D with % PEG was determined. For each % PEG, D_{i} is defined as the ratio between the number of moles of PEG[G3]-BA used in the preparation of the micelles (n_{i}, equal to the moles of PEG[G3]-BA) and S_{i}, the total surface area of micelles (Eq 8). From the ratio between the PEG density of two micelles with different % PEG and considering Eq 9, Eq. 11 was derived to describe the relative PEG density ($^{\text{rel}}D$) for two micelles with different % PEG as a function of their radii and moles of PEG.

$$D_{\text{i}} = \frac{n_{\text{i}}}{S_{\text{i}}} \quad \text{Eq 10}$$

$$\left.\begin{aligned} D_{\text{i}} &= \frac{n_{\text{i}}}{S_{\text{i}}} \\ D_{\text{k}} &= \frac{n_{\text{k}}}{S_{\text{k}}} \end{aligned}\right\} \; {}^{\text{rel}}D = \frac{D_{\text{i}}}{D_{\text{k}}} = \frac{n_{\text{i}}\,S_{\text{k}}}{n_{\text{k}}\,S_{\text{i}}} = \frac{n_{\text{i}}}{n_{\text{k}}}\frac{1}{{}^{\text{rel}}S} \rightarrow {}^{\text{rel}}D = \frac{n_{\text{i}}\,R_{\text{i}}}{n_{\text{k}}\,R_{\text{k}}} \quad \text{Eq 11}$$

An analysis of Eq 6, 9, and 11 using the R data for the micelles shown in Figure 101B predicts that decreasing % PEG (increasing R) along the series results in a drastic reduction of N (inversely proportional to the cube of the ratio of radii, Eq 6) and moderate reductions of S (inversely proportional to the radii ratio, Eq 9) and D (proportional to the ratio of radii × n , Eq 11). Figure 104 shows plots of estimated $^{\text{rel}}N$, $^{\text{rel}}S$, and $^{\text{rel}}D$ values normalized to the 0.15% PEG micelle versus % PEG. As expected, reducing % PEG from 100 to 0.15% results in a decay of approximately four orders of magnitude for $^{\text{rel}}N$, but only one order of magnitude for $^{\text{rel}}S$ and $^{\text{rel}}D$. Although increasing R increases the surface area of the individual micelles with the square of the radius (Eq 7), the inverse dependence of N on the cube of the radius (Eq 6) causes S to decrease overall with the radius (Eq 9). The effect of % PEG on D is shown in Figure 104C. While a % PEG as low as 0.15% can stabilize giant micelles, lower % PEG end up aggregating because such a low D value do not provide enough colloidal stability.

Attending to the dependence of $^{\text{rel}}N$, $^{\text{rel}}S$, and $^{\text{rel}}D$ with R (Eq 6, 9, and 11) and the experimental variation of R with % PEG (Eq 3), the observed decays of $^{\text{rel}}N$, $^{\text{rel}}S$ and $^{\text{rel}}D$ with % PEG were fitted to power functions with exponents 1.5, 0.5, and 0.5, respectively (Eq 12-14; Figure 104), with excellent coefficients of determination (R-squared). Eq 12-14 allow estimates of $^{\text{rel}}N$, $^{\text{rel}}S$, and $^{\text{rel}}D$ to be made for any micelle with a known % PEG. Interestingly, data points for the more PEGylated micelles did not fit well the power functions. Slightly larger $^{\text{rel}}N$ and $^{\text{rel}}S$, and smaller $^{\text{rel}}D$ than the fittings were obtained for the 80 and 100% PEG because of the somewhat larger sizes predicted for these micelles by Eq 3 (Figure 101B). Indeed, despite the excellent fit of R versus % PEG (Eq 3), slight variations between the experimental and estimated sizes for the smallest micelles translate into larger deviations for N, S and D. In addition, these variations

USC UNIVERSIDADE DE SANTIAGO DE COMPOSTELA

might be explained by the increase in surface area due to the surface roughness of these particles and the fact that the micelle size is not completely monodisperse.

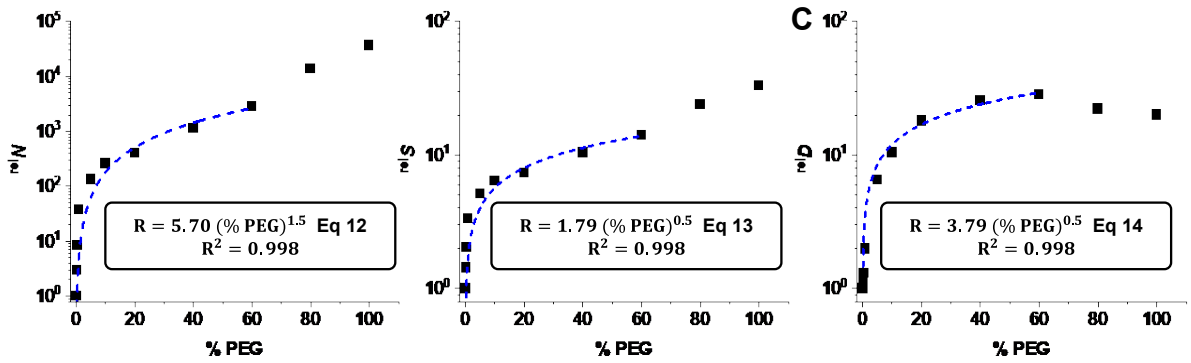

Figure 104. Plots and power function fits for CAT-Micelles of estimated ^{rel}N (A), ^{rel}S (B), and ^{rel}D (C) obtained using eq 4, 7, 9 and *R* data by DLS, normalized to the 0.15% PEG micelle versus % PEG. Gray line indicates the corresponding simulated for Eq 4, 7, and 9.

4.1.4 The PEGylation Degree Regulates the Size of a Doxorubicin Polymer Therapeutic

Previous sections have elucidated how the hierarchical assembly of *in situ* prepared boronate-ester dendrimers can drive the size regulation of CAT micelles, an assembly process driven by a tuning of the amphiphilic character of the dendritic scaffold. A more ambitious objective was to expand this technology for preparing a polymer therapeutic of a diol drug. With this aim, we have focused on DOX as therapeutic cargo actively participating in the self-assembly process. As detailed in Section 3.1.1, our group has recently developed a DDS capable of binding multiple diol-containing drugs, including DOX trapping via its 2-keto-1,3-diol functionality. This conjugation facilitates a self-assembly process similar to that previously described for CAT, resulting in the formation of nanometric micelles with high EE and DL. Due to its inherent high fluorescence, DOX represents an excellent probe to enable the study of both, the structural pharmacological properties of this novel DDS (EE, DL, release…). By combining size control with the pharmacological activity and intrinsic properties of DOX, in this part of the thesis a new technology to create a size-controlled and intelligent DDS is described.

Pursuing that goal, the already described dendritic scaffolds (PEG[G3]-BA and 3[G2]-BA) were employed. A multi-functionalization approach was adopted by introducing equimolar amounts of CAT and DOX. Given that CAT forms stronger boronate ester bonds than DOX in aqueous solution, a substoichiometric ratio of diols relative to free BAs (accounting for 80 % of the BAs on the dendritic components) was selected to prevent competitive displacement.

DOX micelles with variable % PEG were prepared by adding a mixture of the dendritic components in 50 mM Na_2HPO_4 over a DOX (1:1 molar ratio) solution in 50 mM NaH_2PO_4 (Figure 105). The pH of the micelles was 7.4.

USC UNIVERSIDADE DE SANTIAGO DE COMPOSTELA

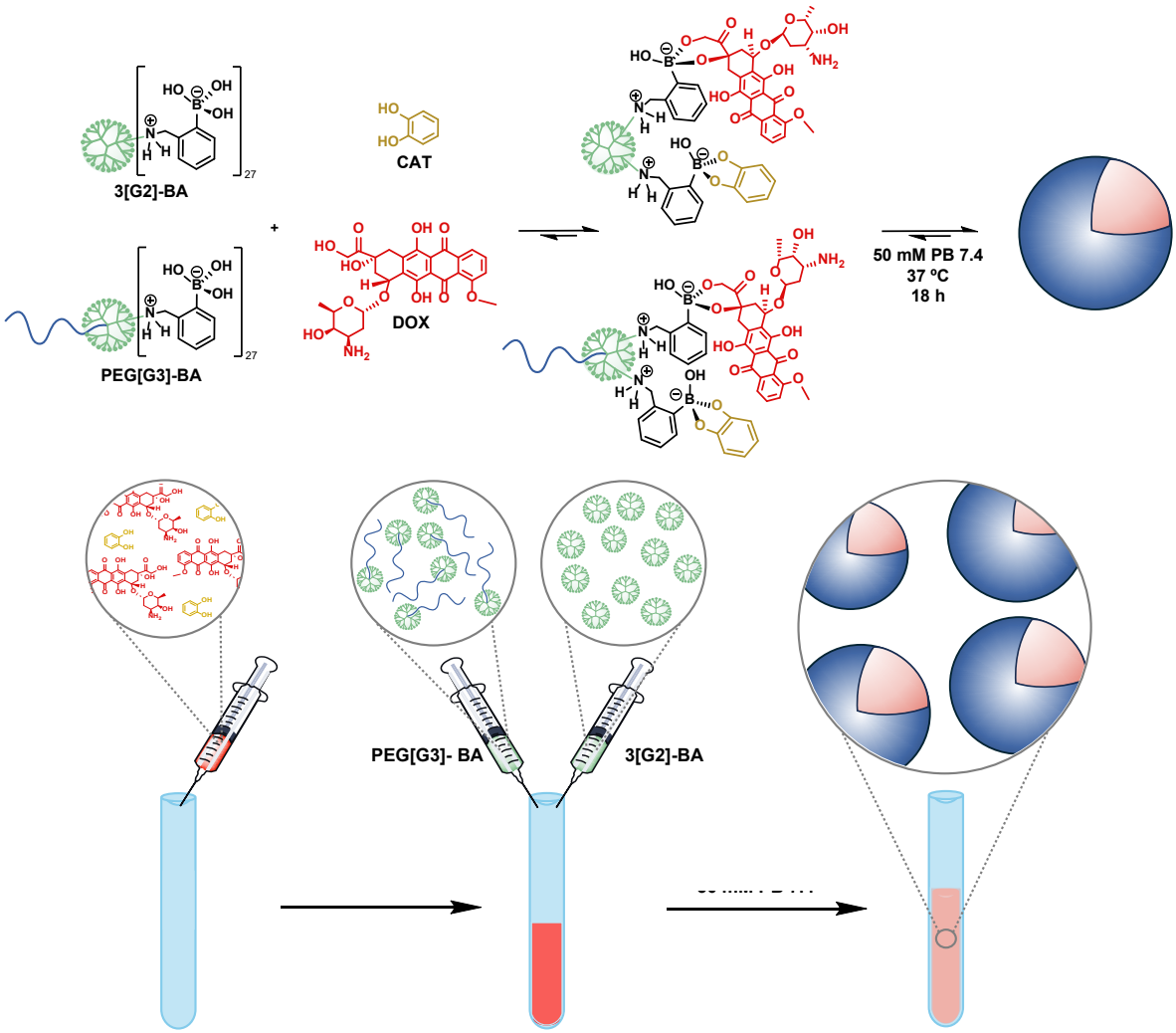

Figure 105. Schematic representation of the CAT/DOX-driven *in situ* hydrophobization and self-assembly of 3[G2]-BA and PEGH[G3]-BA.

The size of the resulting micelles was analysed by DLS measurements after 18 h of formation at 37 ºC, revealing *R* modulation from 16 to 350 nm on reducing the % PEG from 100 to 1%, with very low PDI (Figures 106 and 35-36). As seen for CAT, further reductions of % PEG led to micelle aggregation as D values below a certain limit do not provide enough colloidal stabillity. DOX micelles were highly stable over time, as corroborated by DLS measurements performed 1 month after formation and storage at 4 ºC (Table 5, Figures 37-38). Furthermore, giving the potential pharmacological application of these micelles, stability was also tested by maintaining the resulting micelles at 37 ºC in PBS for 24 h with no apparent size and PDI variation (Table 5, Figures 35-36). The micellar structure of the DOX assemblies was confirmed by LSCM (Figure 106D) images of the largest micelles (3, 2, and 1% PEG), which show cores coloured as red due to the fluorescence of the DOX molecules confined at the core of the micelles.

The plot represented in Figure 106B displays the variation of *R* with % PEG. As for PIC and CAT micelles, data points fit a power function:

$$R = 278\ (\%\ PEG)^{-0.5} \qquad \text{Eq 15}$$

USC UNIVERSIDADE DE SANTIAGO DE COMPOSTELA

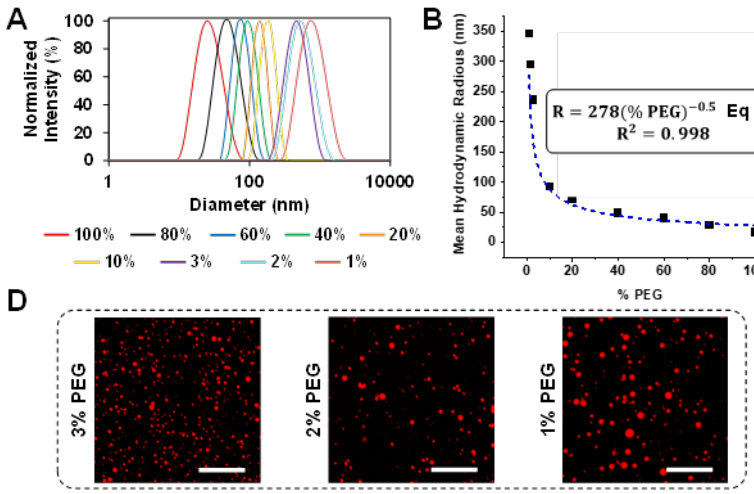

C

% PEG	Mean Hydrodinamic Radius (R, nm)	PDI
100	14 ± 1	0.16 ± 0.02
80	27 ± 1	0.22 ± 0.01
60	39 ± 1	0.06 ± 0.02
40	50 ± 1	0.05 ± 0.02
20	71 ± 1	0.02 ± 0.01
10	93 ± 9	0.03 ± 0.01
3	244 ± 9	0.14 ± 0.03
2	294 ± 5	0.12 ± 0.02
1	348 ± 12	0.16 ± 0.02

Figure 106. Impact of PEGylation on the size of DOX micelles. DLS size distribution of DOX micelles prepared from PEG[G3]-BA/3[G2]-BA, CAT, and DOX at different % PEG (A). Variation of *R* with % PEG; R^2 is the coefficient of determination (B). *R* and PDI of micelles (C). LSCM Images of DOX micelles prepared at different % PEG. Scale bar 10 μm (D).

Again, the exponent -0.5 in Eq 15 indicates an inverse proportionality between % PEG and R^2 and hence, the surface area of the micelles. This confirms not only that the PEG chains at the corona template the size of the micelles, but also proves the successful application of this technology to tune the size of DOX polyboronate micelles. As observed, while initial reductions of % PEG from 100 to 20% result in slight size increases (only 5-fold), further % PEG reductions lead to much larger sizes (up to 25-fold).

Application of the model of spherical micelles was to DOX micelles afforded identical trends as for CAT in how the number of particles (*N*), the total surface area of particles (*S*), and PEG density per particle (*D*), vary along the micelle series as a function of % PEG. Figure 107 shows plots of estimated ^{rel}N, ^{rel}S, and ^{rel}D values normalized to the 1% PEG micelle versus % PEG. Notably, fittings of these data points to power functions with exponents 1.5, 0.5, and 0.5, respectively (Eq 16-18; Figure 107), gave excellent coefficients of determination (R-squared). Overall, Eq 16-18 reveal as powerful tools to estimate values of ^{rel}N, ^{rel}S, and ^{rel}D for any boronate ester dendritic micelle with a known % PEG_{5k}, independently of the diol involved in the preparation.

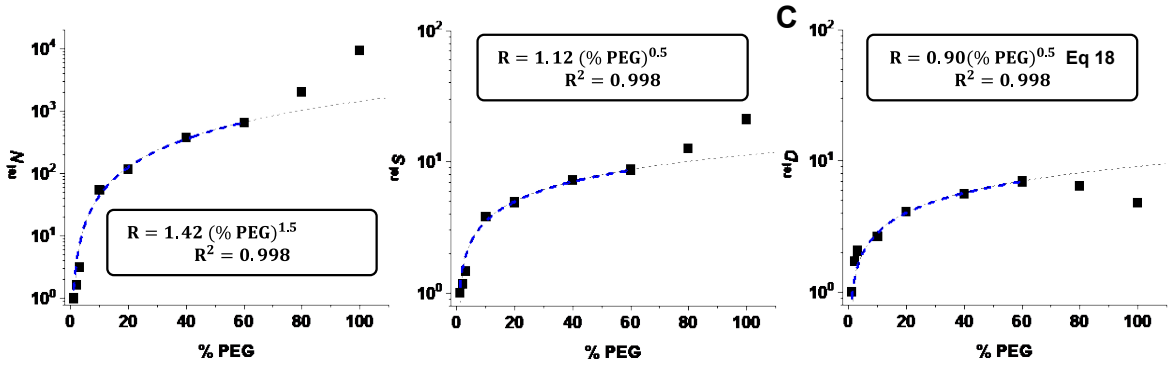

Figure 107. Plots and power function fits for DOX Micelles of estimated ^{rel}N (A), ^{rel}S (B), and ^{rel}D (C) obtained using eq 4, 7, 9 and *R* data by DLS, normalized to the 1% PEG micelle versus % PEG. Gray line indicates the corresponding simulated for Eq 4, 7, and 9.

USC UNIVERSIDADE DE SANTIAGO DE COMPOSTELA

4.1.5 DOX Micelles as Size-Tailored DDS

Given that the self-assembly process is governed by the *in situ* variation of the hydrophilic-hydrophobic balance of the dendritic components and considering the substantial differences in the physical properties of the micelles across the % PEG series, EE and DL were analyzed for all tested micelles (Table 3). A constant EE of 81% ±1% was revealed for all micelles, independently of the % PEG, which is consistent with an efficient covalent bonding of DOX via a boronate ester.

To analyze the impact of the size of the micelles on their application as DDS, three micelles with representative diameters were selected: 28 nm (100% PEG), 100 nm (40% PEG), and 582 nm (2% PEG).

% PEG has a drastic effect on the size and PEG density of DOX micelles and can significantly influence the kinetics of the DOX release. Release experiments were conducted to analyze the cumulative release of DOX under various conditions: (i) 50 mM PB, pH 7.4, 150 mM NaCl, representing physiological conditions, (ii) 50 mM PB, pH 6.8, 150 mM NaCl, simulating tumoral tissue, and (iii) 50 mM AcONa, pH 5.0, 150 mM NaCl, mimicking the pH conditions typically found within endosomal compartments. Results showed a tremendous impact of PEGylation/size on the drug release (Figure 108). Under physiological conditions, the release of DOX is favored for the 100% PEG micelles, with a 23% cumulative release after 4 days compared with 13% for 40% PEG, and an almost negligible release of 5% for 2% PEG (Figure 108B). Conversely, while the release from the 100% PEG micelle revealed quite insensitive to pH, with only a slight increase up to 28%, the larger and less PEGylated micelles release DOX faster under acidic conditions, with a cumulative release of 22% for the 40% PEG and 18% for the 2% PEG micelles at pH 6.8, which respectively increase up to 34% and 35% at pH 5.0 (Figure 108C, and D).

The observed inverse relationship between PEGylation and pH-triggered release has been interpreted as the combined result of size and PEG density on surface (both depending on % PEG). Thus, the slower release of DOX at neutral pH from the larger micelles (a size effect related to the long pathway from the internal core to the corona) is counterbalance at lower pH by a reduced PEG density at the corona, which exposes the boronate esters at the core to the hydrolytic external medium, thereby activating a selective pH-response. Thus, the pH-triggered release of drugs joins size and PEG density as an additional micelle property that can be tuned with % PEG. Considering that PK and biodistribution are size-dependent properties,[32] and the slightly acidic pH of solid tumors (extracellular pH in tumor 6.6–6.9),[162] the ability to simultaneously control the micellar size and drug release kinetics in response to acidic media proves extremely useful for the clinical application of DDS.

On the other hand, as discussed in the first section, PEGylation represents a trade-off between prolonged systemic circulation and efficient cellular delivery. While the stability and circulation time are enhanced for PEGylated nanoparticles, PEG shielding can limit their cellular entrance due to steric hindrance and decreased particle-membrane associations.

USC UNIVERSIDADE DE SANTIAGO DE COMPOSTELA

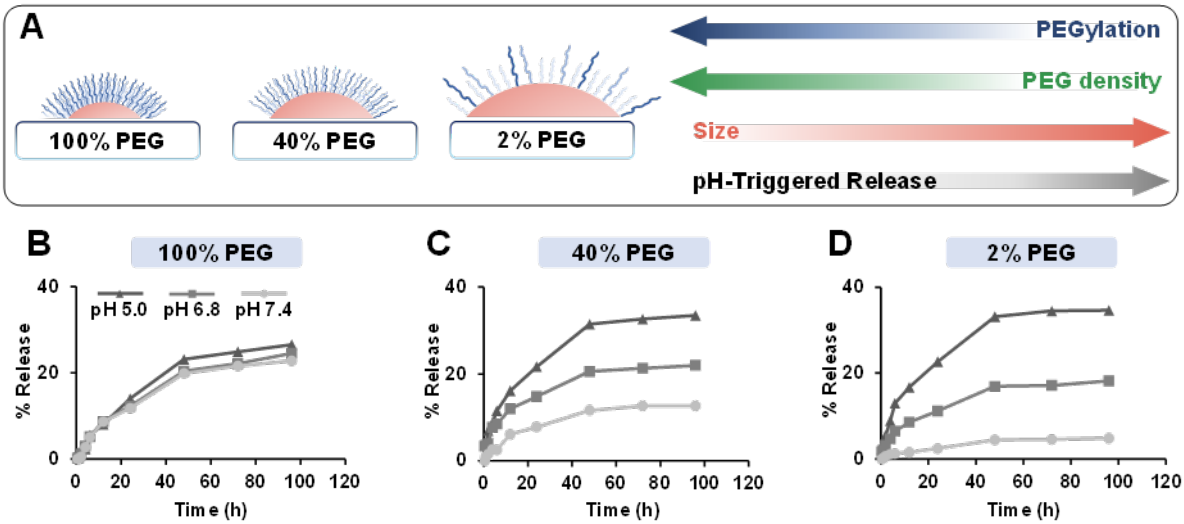

Figure 108. Influence of % PEG in the pH-dependent release of DOX from DOX micelles. Schematic representation of the observed effect (A). Cumulative release of DOX form 100% PEG DOX micelle (B); 40% PEG DOX micelle (C); and 2% PEG DOX micelle (D).

Due to the remarkable variation of size, PEG density on surface, and kinetics of drug release along the series of DOX micelles, additional experiments were performed to see whether these variations could impact the intracellular trafficking and cytotoxicity of DOX micelles. First, i*n vitro* experiments were conducted using F-98 cells (rat glioma) for comparing the time-dependent intracellular distribution of free DOX and three selected DOX micelles (100, 40, and 2% PEG). Flow cytometry measurements indicated no difference between free or micellar DOX, with all tested samples promoting DOX uptake (≈ 100%) in F-98 cells (Figure 109).

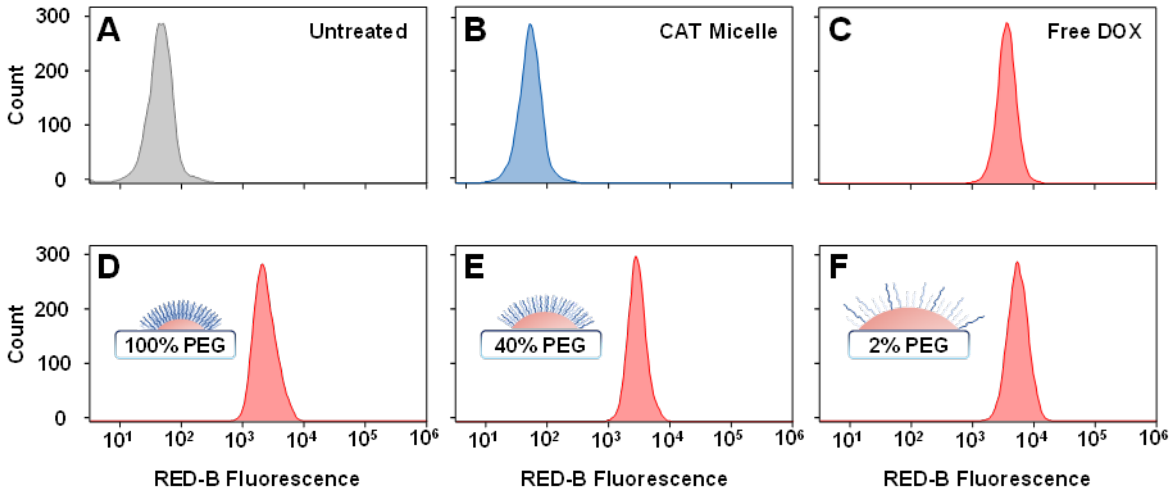

Figure 109. Uptake of DOX micelles by F-98 cells measured by flow cytometry. Histograms displaying number of cells (count) vs RED-B fluorescence intensity. Experiments performed with untreated cells (A), and cells after 5 h of incubation with CAT micelles (B), free DOX (C), and DOX micelles 100% PEG (D), 40% PEG (E), and 2% PEG (F).

However, significant differences were observed when analyzing the intracellular trafficking of these samples. Due to the small size and hydrophobic nature of DOX, it is likely internalized into cells via passive diffusion, followed by rapid nuclear accumulation. This accumulation is driven by the intercalation of DOX into DNA, inhibiting DNA replication and transcription, thereby inducing cellular mortality. Actually, after just 1 h of incubation, free DOX (red) was selectively detected in nuclei of F98 cells by LSCM, as determined by complete colocalization

with Hoechst (blue) (Figure 110). Conversely, DOX in micelles mostly colocalized at the same time with LysoTracker Green (green), a well-known endosome/lysosome marker, with a faint DOX fluorescence also detected within cytoplasmatic vacuoles. It was only after 1 h of additional incubation time that, in response to the environment of the endosome/ lysosome, localization of DOX was also observed in both the endosome/lysosome and nucleus for the micelles (Figure 110). This is interpreted as the result of a pH-triggered release of the drug followed by endosomal escape and migration to the cell nuclei. Interestingly, 2% PEG micelles were easily detected along the image series due to their large diameter, as confirmed by the variations in their endo/ lysosomal distribution when compared to the higher PEGylated micelles.

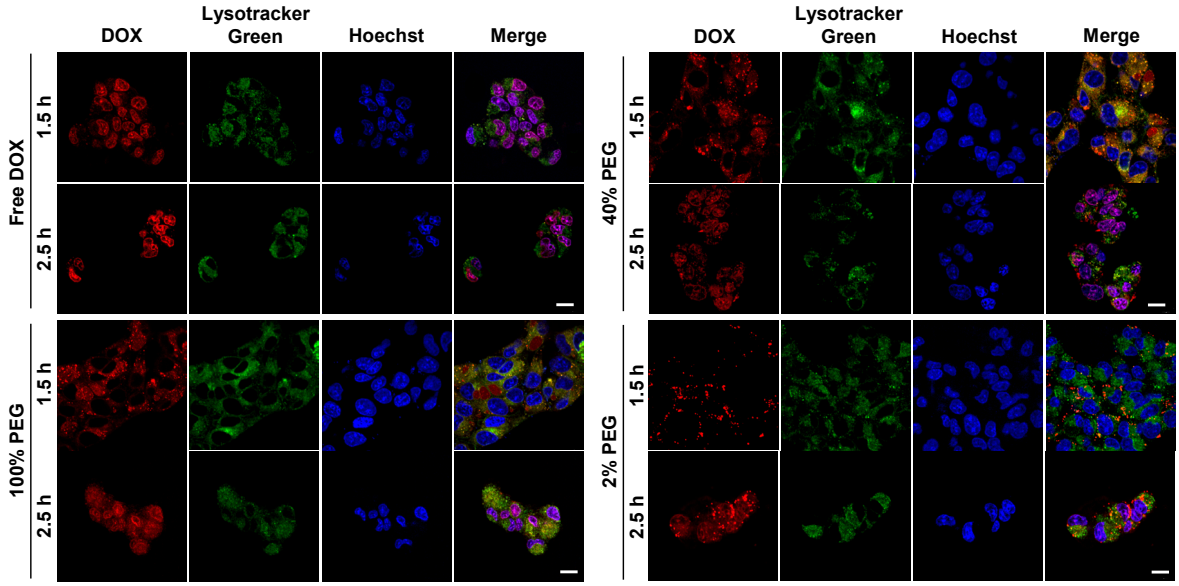

Figure 110. Intracellular trafficking of DOX micelles (100%, 40%, and 2% PEG) in F-98 cells assessed by LSCM. Acidic organelles were stained with LysoTracker Green (green), and nuclei were stained with Hoechst (blue). Images show colocalization of DOX (red) with LysoTracker Green for all-tested micelles, and with Hoechst for free DOX at short incubation times, confirming the successful internalization of DOX micelles by endocytosis. Longer incubation times reveal colocalization of DOX with Hoechst for all tested micelles, confirming endosomal escape and migration of DOX to the cell nuclei. Scale bar 10 μm.

Finally, the cytotoxicity of DOX micelles towards F-98 cells was tested by employing a colorimetric assay (CCK 8) after 24 and 48 h, using untreated cells as positive control. As shown in Figure 111A, no main differences in cytotoxicity were observed as a function of the % PEG. All tested micelles (100%, 40%, and 2% PEG) demonstrated similar cytotoxicity levels at 24 and 48 h. Additionally, cells were incubated with the dendritic components (3[G2]-BA and PEG[G3]-BA) at the same concentrations as in the micelle to confirm their nontoxic behavior (Figure 111B). Although displaying slightly lower cytotoxicity than free DOX, encapsulated DOX is expected to translate into improved PK and more efficient delivery to tumor sites. Several reports have described DDSs of DOX that, despite being less toxic compared to the free drug during *in vitro* assays, demonstrated substantially superior antitumor efficacy in animal models.[163] In this context, further research prioritizes *in vivo* experiments to comprehensively evaluate the therapeutic efficacy of our findings.

USC UNIVERSIDADE DE SANTIAGO DE COMPOSTELA

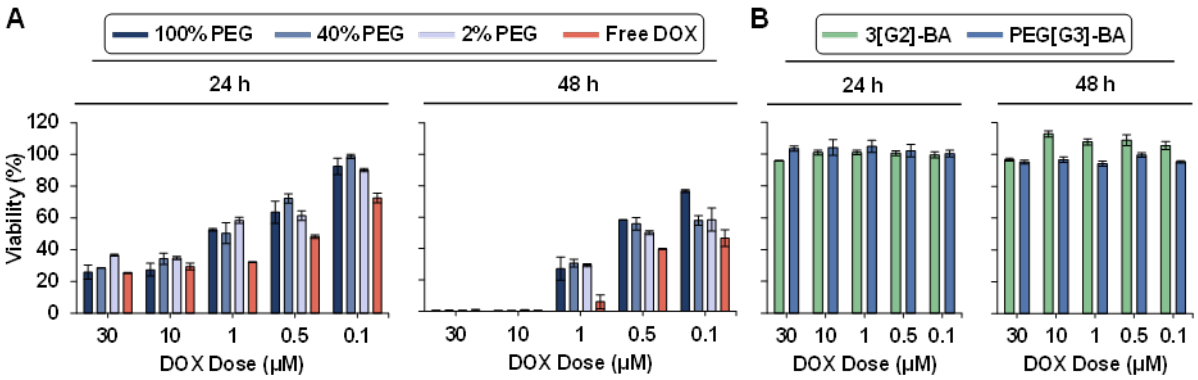

Figure 111. Cell viability (CCK-8; 24 and 48 h) of F-98 cells in the presence of DOX micelles and free DOX (A) or in presence of the dendritic components in representative amounts corresponding to those in the micelle doses (B).

USC
UNIVERSIDADE DE SANTIAGO DE COMPOSTELA

4.2 Dynamic Boronate Chemistry Accelerates the Screening of Polymeric Gene Delivery Vehicles *via In Situ* Complexation of Nucleic Acids

The results from this section have already been published as Bruno Delgado Gonzalez,[a] Roi Lopez-Blanco,[a] Samuel Parcero-Bouzas,[a] Natalia Barreiro-Piñeiro,[b] Lucas Garcia-Abuin,[a] and Eduardo Fernandez-Megia[a] Dynamic Covalent Boronate Chemistry Accelerates the Screening of Polymeric Gene Delivery Vectors via *In Situ* Complexation of Nucleic Acids. *J. Am. Chem. Soc.* **2024**, 146, 17211-17219. https://doi.org/10.1021/jacs.4c03384

[a] Centro Singular de Investigación en Química Biolóxica e Materiais Moleculares (CIQUS), Departamento de Química Orgánica, Universidade de Santiago de Compostela, Jenaro de la Fuente s/n, 15782 Santiago de Compostela, Spain

[b] Centro Singular de Investigación en Química Biolóxica e Materiais Moleculares (CIQUS), Departamento de Bioquímica e Bioloxía Molecular, Universidade de Santiago de Compostela, Jenaro de la Fuente s/n, 15782 Santiago de Compostela, Spain

4.2.1 Research Background

Gene therapy provides exciting new therapeutic opportunities beyond the reach of traditional treatments.[65,15] The key step in gene therapy is the efficient delivery of NAs to target cells and tissues, achieved through the use of viral and nonviral vectors.[164] In recent years, there has been a growing demand for nonviral alternatives[68,165,166] to overcome the limitations associated with viral vectors.[66] Among the reported candidates, polymeric structures are particularly noteworthy due to their exquisite structural tunability, which is crucial for developing gene delivery vectors capable of overcoming multiple biological barriers.

Recent advances in synthetic methodologies and click chemistry allow researchers to impart desired functions to polymeric gene carriers by assessing diverse monomer functionalities and polymer architectures.[167,168,67] Still, the path is not free of obstacles as material properties need to be engineered for each NA, including the nature of the charged groups, the polymer structure and molecular weight, and the surface charge of the polyelectrolyte complex (polyplex).[67] Also, the polycation chemical composition is usually tailored by introducing hydrophobic moieties and PEG chains to improve the biocompatibility, cargo protection, or transfection. In addition, certain parameters must be carefully balanced. The positive charges that allow the complexation of NAs, their cellular internalization and endosomal escape are also responsible for some cytotoxicity.[169] The same applies to PEGylation that usually affords a marked decrease in cellular internalization[170] and endosomal escape.[171] As a result, the identification of polymers that can replace viral vectors in clinical gene therapy has proven elusive.[67] The need to fine-tune several structural parameters represents a bottleneck of current screening processes, which has only been partially dampened by the advent of combinatorial approaches.[89,172,90,91,173,174] Therefore, there is an urgent demand for technologies to speed up the optimization of polymeric vectors by simultaneous adjustment of multiple variables.[175]

DCvC represents a promising pillar for such innovative technologies, owing to the dynamic character of the obtained structures. However, despite being largely exploited for the engineering of stimuli-responsive materials and the controlled release of drugs,[137, 141] DCvC has found scarce application in gene therapy.[176] Only a handful of dynamic covalent polymerizations and post-functionalizations of polymeric gene carriers have been described so far.[177,178,142] Even fewer examples have taken advantage of DCvC to prepare polymeric carriers in the presence of NAs to which they complex *in situ*.[179] These are limited to already introduced

seminal reports by Aida, Li and Yang, and Ulrich on cationic polydisulfides,[144,145] and polyhydrazones[146,147,180] with known ability to transfect oligonucleotides, but not pDNA. In addition, the potential of DCvC for the *in situ* optimization of polymeric gene vectors using dynamic covalent libraries has remained largely unexplored.[180]

Herein, we describe a highly adaptable gene delivery platform using a polymeric BA that is activated in the presence of pDNA by the addition of cationic catechols (Figure 113). The fast and strong boronate ester bonding affords cationic dynamic polyboronates able to complex pDNA *in situ* to afford polyplexes that, without further manipulation, efficiently transfect cells. The robustness of the strategy entitles the simultaneous screening of several structural parameters at will (PEGylation, surface charge, polycation chemical composition, hydrophilic/hydrophobic balance), enabling the adaptive optimization of lead polymeric vectors using dynamic covalent libraries.

4.2.2 A Highly Adaptable Gene Delivery Platform based on Cationic Polyboronate Vectors

BAs bind diols under aqueous conditions in a pH-reversible manner, recognized as an archetypal illustration of stimuli-responsive DCvC.[128,136] The optimal pH for boronate ester formation is above the pK_a of the BA, whereas they are hydrolyzed at lower pH. These properties, along with a low toxicity, have led to the widespread use of BAs in glycan sensing, supramolecular organizations, sugar- and pH-responsive materials.[128,136] To develop a polymeric BA gene delivery platform, *ortho*-aminomethylphenylboronic acid was selected because of a convenient pK_a ca. 6.5 (Figure 112).[129] In the presence of cationic catechols, polymeric BA were expected to afford cationic polyboronates with ability to condense NAs at physiological pH, while hydrolyzing upon cell internalization under the acidic conditions of the endosome. A dendritic scaffold and a pDNA were selected to test the feasibility of this strategy. Dendrimers are tree-like polymers with globular architecture that efficiently transfect NAs when incorporating cationic peripheral groups.[181] Their monodispersity makes them ideal candidates for evaluating new technologies and bioapplications.[182] The selection of a pDNA for *in situ* complexation was aimed to broaden the transfection scope of current cationic dynamic polymers, which are limited to oligonucleotides.[163-67] Thus, a dendrimer and a PEG_{5k}-dendritic block copolymer of the GATG,[152,183] family with 27 peripheral azides were selected for functionalization with terminal BA groups following a one-pot, three-step reductive amination (procedure described in Section 2.2.3) 3[G2]-BA and PEG[G3]-BA (Figure 113) were obtained in very good yields and characterized with convincing evidence by ^{1}H and ^{13}C NMR, IR, and MALDI-TOF MS (Figures 39-45). The completion of the functionalization was easily monitored by IR (disappearance of the intense signal of azide at ca. 2100 cm^{-1}) and ^{1}H NMR (disappearance of the characteristic signals of the methylene protons in α to the azide at ca. 3.40 ppm that shift to ca. 3.00 ppm, and appearance of a new aromatic signal corresponding to the proton in *ortho* to the BA at ca. 7.40 ppm).

Five parameters were selected for simultaneous screening as a stress test of this adaptable gene delivery platform (Figure 112): (i) The PEGylation degree (% PEG), the ratio between PEG[G3]-BA and 3[G2]-BA. (ii) The N/P ratio of ionizable nitrogen atoms in the polymer (equal to BA groups) to negatively charged phosphate groups in the NAs. (iii) CBA ratio. (iv) The polycation chemical composition among a selection of catechols functionalized with primary (A) and tertiary (T) amines, guanidine (G), ethylenediamine (D), and imidazole (I)

groups with recognized ability to condense and transfect NAs. While the A and T groups were taken as standard cationizable groups of widespread use in polymeric gene delivery endeavors, G, D and I were chosen for their reported superior endosomal escape ability.[184,185,186] Finally (v), the incorporation of catechols with hydrophobic moieties such as, a medium-chain fatty acid (octanoic acid, O), a fluorocarbon chain (perfluorobutanoic acid, P), and cholesterol (C) was assessed as a means to enhance the transfection efficiency by tuning the hydrophilic-hydrophobic balance.[67] Polyplexes from cationic polyboronates were referred to as:

% PEG - N/P – CBA X

where X refers to the nature of the added catechols. For example, 7.5-5-10G refers to a polyplex prepared from a 7.5:92.5 molar ratio between PEG[G3]-BA and 3[G2]-BA, with a N/P ratio of 5, and 10 guanidinylated catechols (G) per BA group.

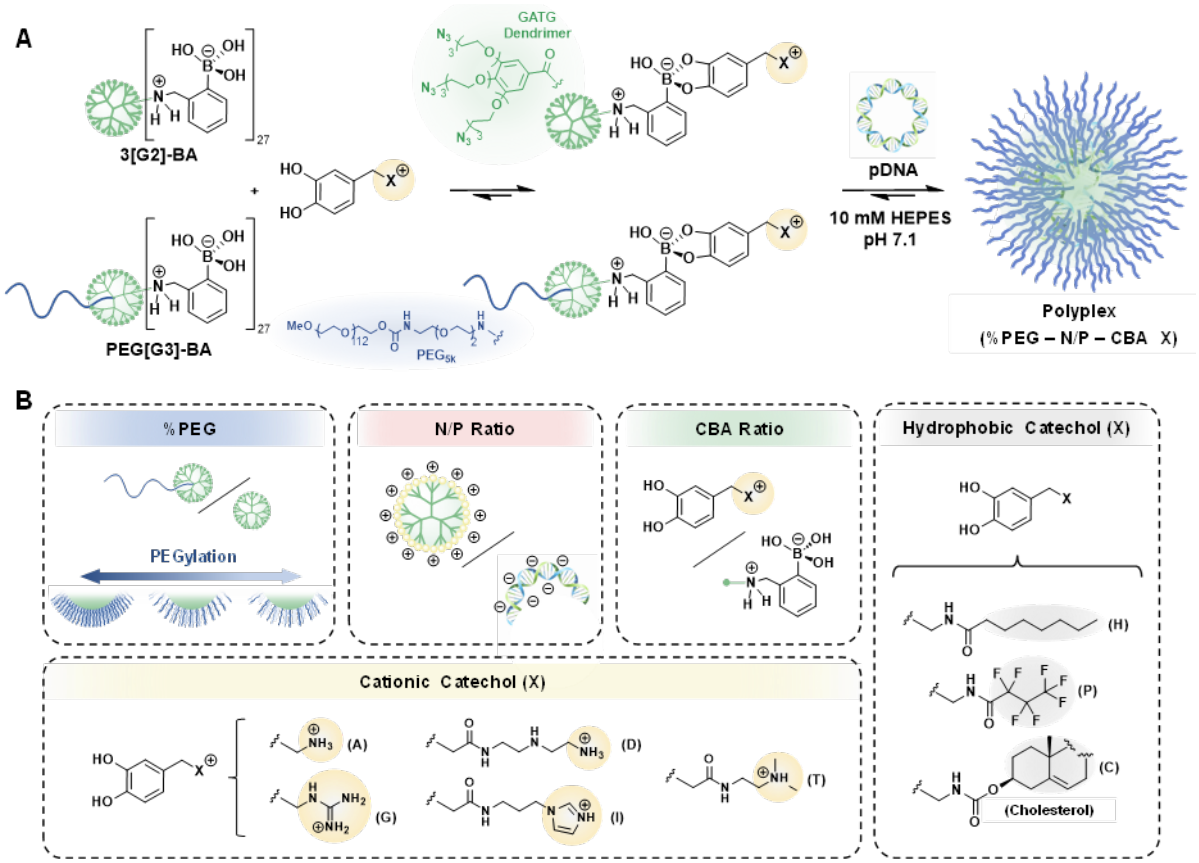

Figure 112. Schematic representation of the activation of polymeric BA vectors and *in situ* NAs complexation by the addition of cationic catechols (A). Parameters selected for simultaneous polyplex screening by dynamic covalent libraries: PEGylation degree (% PEG), N/P ratio, ratio between cationic catechols and BAs (CBA ratio), polycation chemical composition, and hydrophilic/hydrophobic balance (B).

4.2.3 Dynamic Covalent Libraries for Screening Polymeric Vectors

An initial assessment of the activation of PEG[G3]-BA/3[G2]-BA and *in situ* complexation of pDNA by the addition of cationic catechols was done by DLS with the polyplex 5-10-5G. A pDNA encoding the enhanced green fluorescent protein (EGFP) was used for these studies (pEGFP-N1). It was confirmed that neither the dendritic components nor the cationic catechol was independently capable of condensing pDNA in 10 mM HEPES, pH 7.1. Only the three

USC DE COMPOSTELA

component mixture rendered polyplexes with monodisperse size distributions and a mean diameter of about 140 nm, a suitable size for gene delivery applications (Figure 115A). The pH sensitivity of the polyplexes was confirmed by DLS (Figure 113). While monodisperse size distributions were observed at pH 7.1, the polyplexes disassembled into pDNA and the polymeric components at pH 5.0, evidencing the hydrolysis of the boronate esters. Degradation of the vector under the acidic conditions of the endosome is of relevance as it can contribute to the release and endosomal escape of pDNA, and limit cytotoxicity.

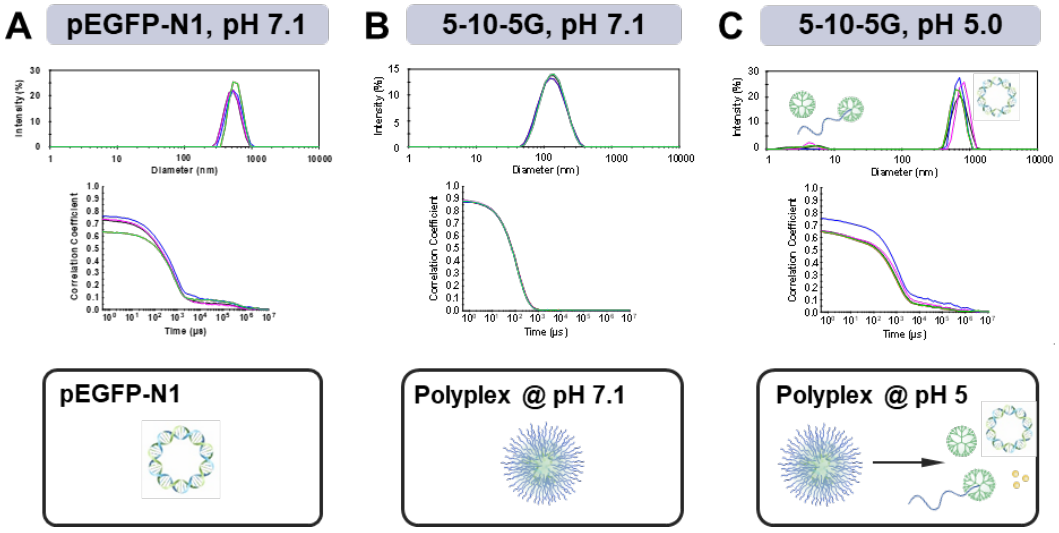

Figure 113. pH sensitivity of the polyplexes. DLS size distributions and correlation functions of pEGFP-N1 (10 ng/µL in 10 mM HEPES 7.1) (A), and the polyplex 5-10-5G (10 ng/µL of pEGFP-N1) in 10 mM HEPES 7.1 (B) and after acidification at pH 5.0 (0.1 M HCl, 300 rpm orbital stirring in an Eppendorf Thermomixer C for 18 h at 37 ºC (C).

Before proceeding with the screening of polymeric vectors, evidence of boronate ester formation was obtained by ^{1}H NMR titration of 3[G2]-BA with increasing concentrations of Cat-G (Figure 114). The progressive disappearance of the 3[G2]-BA signals centered at 7.36 (H_{1A}), 3.97 (H_{2A}), and 3.00 ppm (H_{3A}) was accompanied by the appearance of new peaks at 7.57 (H_{1E}), 4.24 (H_{2E}), and 3.16 (H_{3E}) ppm. In addition, new signals corresponding to Cat-G in the ester are also seen at 6.66-6.31 (aromatic), 3.16 (H_{2GE}), and 2.54 (H_{1GE}) ppm. Relative integration of the H_{1A} and H_{1E} protons afforded conversions of 54, 78, and 95% for the CBA ratios 1, 2, and 5, respectively. Accordingly, a CBA of 5 was set for initial polyplexing studies.

The effect of % PEG in the size of the polyplexes was also analyzed with the guanidinylated G-polyplexes of N/P 10 and CBA 5. While % PEG lower than 1% led to precipitation associated with a limited colloidal stability, values above 50% were discarded as leading to polydispersed polyplexes (Figure 75). As a result, the range of % PEG for screening was restricted to values between 1 and 25%.

USC
UNIVERSIDADE DE SANTIAGO DE COMPOSTELA

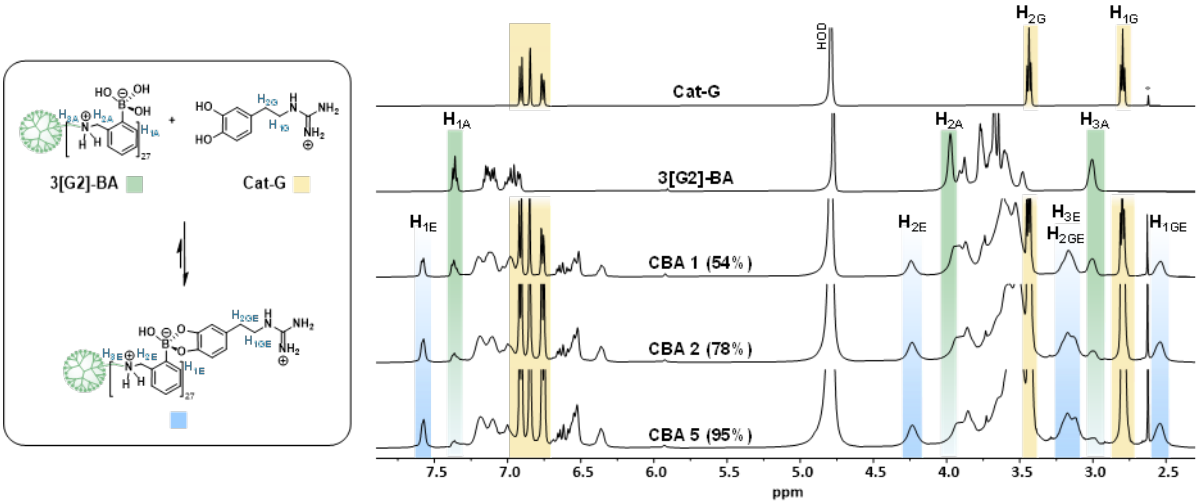

Figure 114. Determination of boronate ester formation by ^{1}H NMR (500 MHz). Titration of 3[G2]-BA with increasing concentrations of Cat-G: Cat-G (0.62 mM in D2O, pH 7.1) was sequentially added to 3[G2]-BA (0.6 mL, 0.76 mM in D2O, pH 7.1) in an NMR tube, accounting for a CBA of 1, 2, and 5.

Polyplexes were then produced by dynamic covalent libraries and evaluated for their size and polydispersity index (PDI), pDNA complexation (pEGFP-N1), and transfection efficiency *in vitro* (see Section 2.2). These experiments were conducted in HEK-293 cells for 72 h using LP 2000 and untreated cells as positive and negative controls, respectively. A first combinatorial library was designed to get general trends about the effect of % PEG (3 different values selected: 5, 12.5, 25%), the N/P ratio (3 ratios analyzed: 5, 10, 15), and the nature of the cationic group (G, A, D, and mixtures thereof) on the polyplex performance (Figure 115-116). In this library, which accounted for 33 polyplexes, the CBA ratio was set to 5. DLS data for these polyplexes is shown in Figure 115A and along Section 2.2.5 (size distributions and correlation functions in Figures 76-86, hydrodynamic sizes and PDI in Tables 11-15). A mean diameter of ca. 125-150 nm was observed for the G-polyplexes, independently of % PEG. Conversely, a size increase inversely proportional to % PEG was revealed for A- and D-polyplexes (up to 220 and 260 nm, respectively), probably associated with a lower pDNA complexing ability. No major effect of the N/P ratio on the size of the polyplexes was seen for any of the cationic catechols, independently of the % PEG. Partial substitution of catechol G with various proportions of A and/or D slightly increased the polyplex size, especially for D. Despite differences in size, a complete pDNA complexation was revealed for all polyplexes by gel retardation experiments on agarose gel (Figure 115B). A decreased packing efficiency of the ethylenediamine (D) group was also evident by ethidium bromide staining of the wells on agarose gel (accessibility of the dye to the polyplexed pDNA). The transfection efficiency of the polyplexes was analyzed by flow cytometry to quantify EGFP expression: percentage of EGFP positive cells and median fluorescence. Early experiments confirmed the necessity of the cationic catechol and dendrimers for efficient transfection (Figures 87-88). As seen in Figures 115C and 89, while some of the G-polyplexes showed transfection efficiencies higher than LP 2000, none of the A- or D-polyplexes produced any transfection, confirming a much lower performance. Similarly, the incorporation of catechols A and, particularly, D into the G-polyplexes drastically reduced transfection efficiency. Among the G-polyplexes, increased transfections were observed for the higher N/P ratios and lower % PEG. Doping one of the best performing G-polyplexes (5-10-5G) with either alternative T and I cationic catechols (Figure 90) or catechols O, P, and C to enhance the hydrophobic interactions with pDNA (Figure 115D) did not afford improved transfections.

USC DE SANTIAGO DE COMPOSTELA

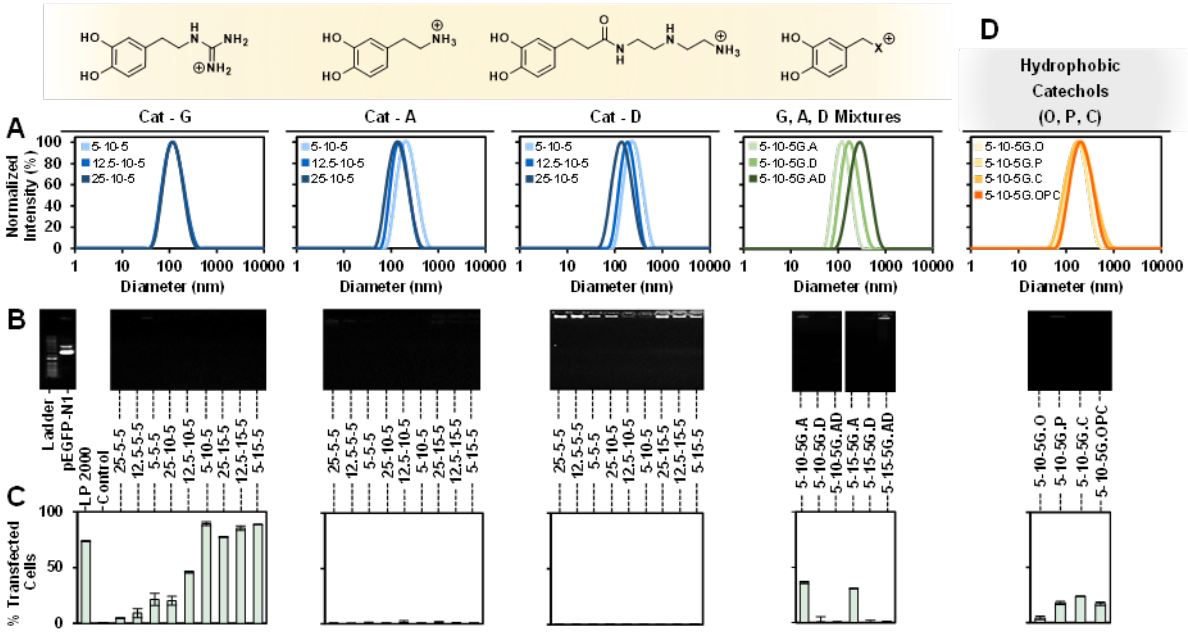

Figure 115. First screening of polymeric vectors. DLS size distribution of G-, A-, and D-polyplexes produced by dynamic covalent libraries (A). Evaluation of pDNA (pEGFP-N1) complexation by gel retardation experiments with ethidium bromide on agarose gel (B). Transfection efficiency (percentage of EGFP positive HEK-293 cells after 72 h) measured by flow cytometry (C). Doping the 5-10-5G polyplex with a 10% of hydrophobic catechols (O, P, C) reduces transfection (D).

4.2.4 Endocytosis-Endosomal Escape Dilemma of Cationic Polyboronates

While the influence of N/P on transfection efficiency was to be expected,[67] that of % PEG could not be unequivocally associated with an impaired endocytosis or endosomal escape, since PEGylation is known to dramatically damage both steps.[170,171] As the same picture applies to A, D, T, and I cationic catechols (low or nil transfection observed), we decided to confront this endocytosis vs endosomal escape issue by analyzing in detail the cell internalization and intracellular trafficking of some of these polyplexes using a Cy5 fluorescently labeled version of the pEGFP-N1 plasmid. Four polyplexes were selected for this study with varying % PEG and cationic catechol, namely 25-10-5G, 5-10-5G, 5-10-5A, and 5-10-5D. Flow cytometry data of HEK-293 cells treated for 5 h with these polyplexes revealed quantitative cell internalizations and similar fluorescence intensities (Figure 91). LSCM experiments performed at the same time showed for the four polyplexes a clean colocalization of Cy5 with LysoTracker Red, a well-known endosome-lysosome marker, confirming their internalization by an endocytic pathway (Figure 116A). In the absence of differences at the cell internalization step, the lower transfections for the highly PEGylated polyplexes, and those incorporating cationic catechols other than G, point to a deficient endosomal escape.

The physical properties of polyplexes determine their stability and performance. Given the dramatic influence of PEGylation on transfection, we decided to analyze the effect of % PEG on the morphology of the polyplexes using transmission electron microscopy (TEM). Polyplexes 1-10-5G, 5-10-5G, and 25-10-5G were selected. While TEM images for 1-10-5G showed highly compact condensates, larger % PEG resulted into particles with increasingly dense coronas (Figure 116B). Since an intimate contact between the cationic carrier and the endosomal membrane has been suggested as a requirement for efficient endosomal destabilization and NAs release into the cytosol,[171,187] such coronas might explain the poor

endosomal escape of highly PEGylated polyplexes. Another polyplex parameter intrinsically related to PEGylation is the surface charge. Despite positively charged polyplexes facilitate cellular uptake and endosomal escape, more neutral particles are often preferred to avoid interaction with negatively charged serum proteins.[67] Accordingly, the zeta potential of the above polyplexes was measured. As expected, a reduction from 49 to 11 mV was observed when increasing %P EG from 1 to 25% (Figure 116B), a charge shielding that offers great opportunities for fine-tuned gene therapy applications. Regarding the superior transfection efficiency of G-polyplexes, guanidinylated polymeric vectors have been recognized to outperform amine-derived analogs in terms of endosomal escape.[184,188,189] Pending more conclusive studies, the net positive charge, bidentate structure, and hydrogen bond ability of the guanidinium group[190] emerge as a successful cocktail for NAs complexation and transmembrane efficiency.[191]

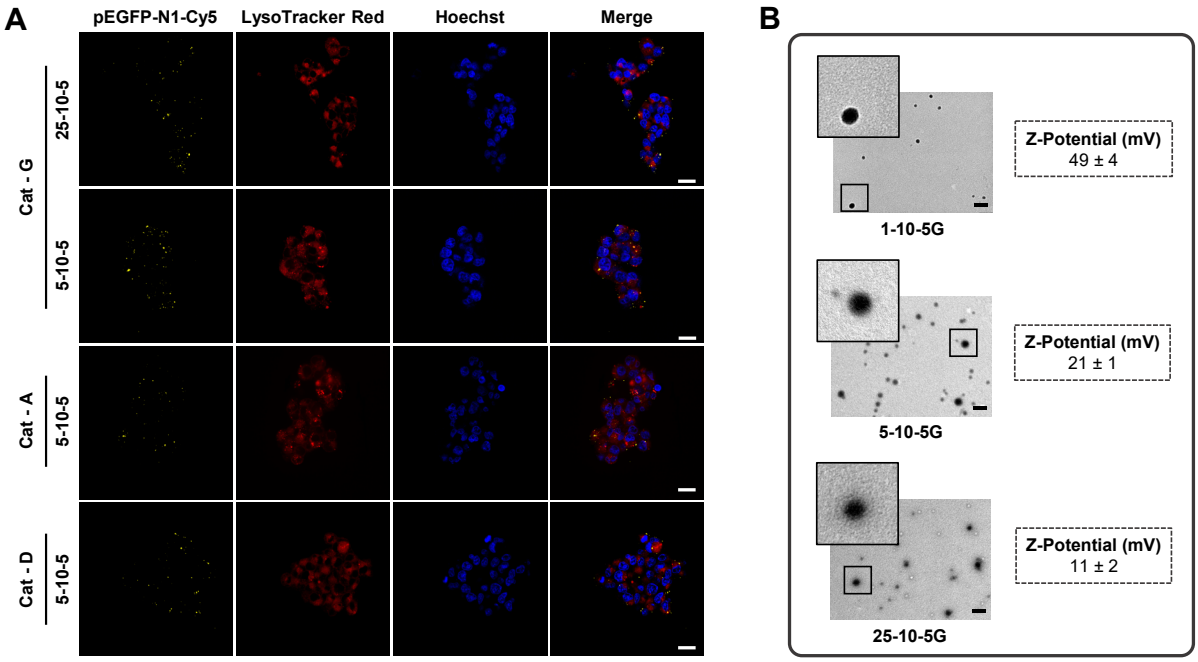

Figure 116. LSCM images of HEK-293 cells incubated for 5 h with 25-10-5G, 5-10-5G, 5-10-5A, and 5-10-5D polyplexes show colocalization of pEGFP-N1-Cy5 (yellow) with LysoTracker Red (red), confirming their successful internalization by endocytosis. Nuclei stained in blue (Hoechst). Scale bar 20 μm (A). TEM images and zeta potential of polyplexes with different % PEG. Scale bar 200 nm (B).

4.2.5 Optimizing Polymeric Vectors by Dynamic Covalent Libraries

The dynamic covalent library in Figure 115 illustrates that polymeric BAs can be activated by cationic catechols and complex pDNA *in situ* to afford polyplexes that efficiently transfect cells. The potential of DCvC to adaptively optimize cell transfection was also demonstrated, with the best results obtained with polyplexes made of G-catechol, with % PEG lower than 12.5 and high N/P ratios. With the aim of further optimizing G-polyplexes, a second combinatorial library was planned focusing on the screening of even lower % PEG (4 values selected: 1, 2.5, 5, and 7.5%). In this library the N/P ratio was kept as above (same 3 values analyzed: 5, 10, 15) while the CBA ratio was varied for the first time (3 values: 2, 5, 10). A total of 36 polyplexes were produced with a size close to 150 nm (see Section 2.2.5) and full pDNA complexation ability. Figure 117 shows their transfection efficiencies (EGFP expression by flow cytometry), and cytotoxicities (CCK-8 assay) in HEK-293 cells after 72 h. Transfection was highly

influenced by the N/P and CBA ratios. Up to 15 formulations showed transfection efficiencies similar to or larger than LP 2000, with the highest percentage of EGFP positive cells and median fluorescence values corresponding to N/P 10 and 15. Interestingly, the CBA ratio modulates the transfection within each N/P. Highest transfections were observed at CBA 10 for N/P 5, CBA 5 and 10 for N/P 10, and CBA 5 for N/P 15. So, a balance between both parameters is revealed, with higher CBA ratios increasing the transfection at low N/P ratios but compromising cell viability at higher N/P, especially for N/P 15. Of note, CBA 2 did not produce any transfection at all, an effect probably associated with a deficient dendrimer cationization (boronate formation, as shown in Figure 114) leading to nonfunctional carriers. As for % PEG, although differences in transfection within the 1-7.5% range are small, marginal increases are observed at lower % PEG, as already seen in Figure 115.

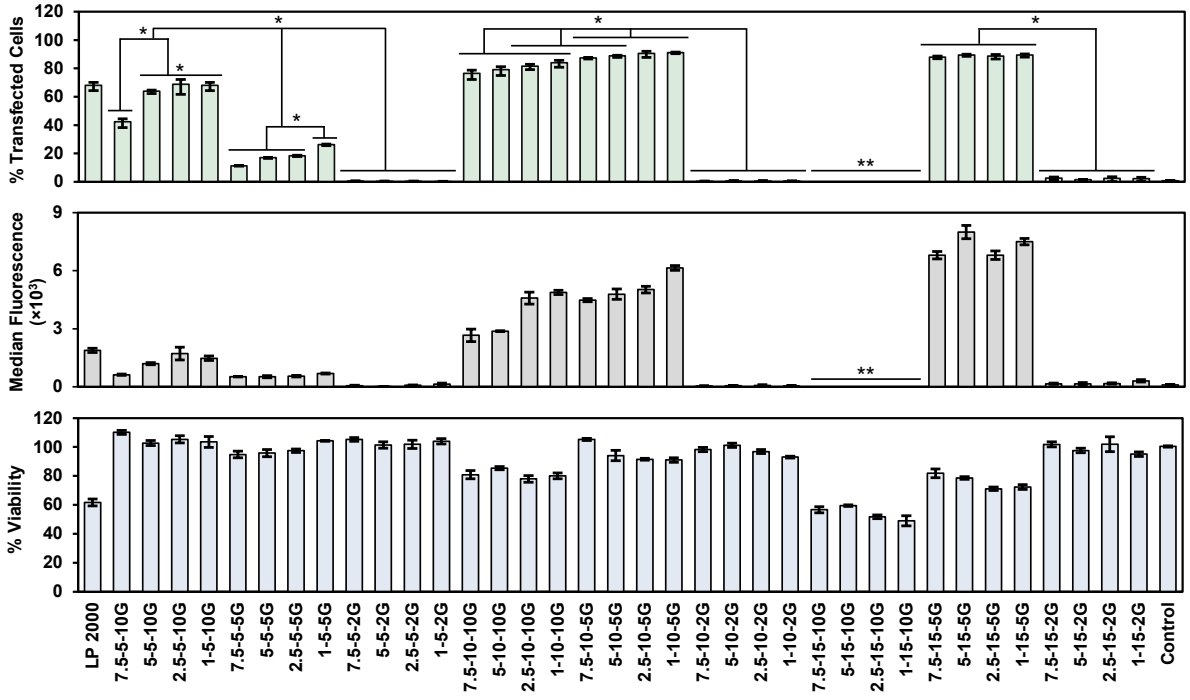

Figure 117. Transfection efficiencies (percentage of EGFP positive cells and median fluorescence by flow cytometry) and cell viability (CCK-8 assay) after 72 h in HEK-293 cells. (∗) indicates statistical difference (p<0.0001) analyzed by one-way ANOVA followed by a Tukey multiple comparisons test. (**) did not reach the required number of events by flow cytometry.

Among the optimized polyplexes, 1-10-5G and 1-15-5G were selected for further transfection studies, such as dose-dependence and efficiency in cell lines other than HEK-293. While 1-10-5G showed a drastic reduction of transfection at plasmid concentrations below 1 μg /well, 1-15-5G proved to be more insensitive to dilution, as further verified by fluorescence microscopy imaging (Figures 118A and 88). When these polyplexes optimized for HEK-293 were tested in cell lines such as COS-7, HepG2, and HeLa, transfection efficiencies similar to those of LP 2000 were obtained, particularly for 1-15-5G (Figure 118B).

USC
UNIVERSIDADE DE SANTIAGO DE COMPOSTELA

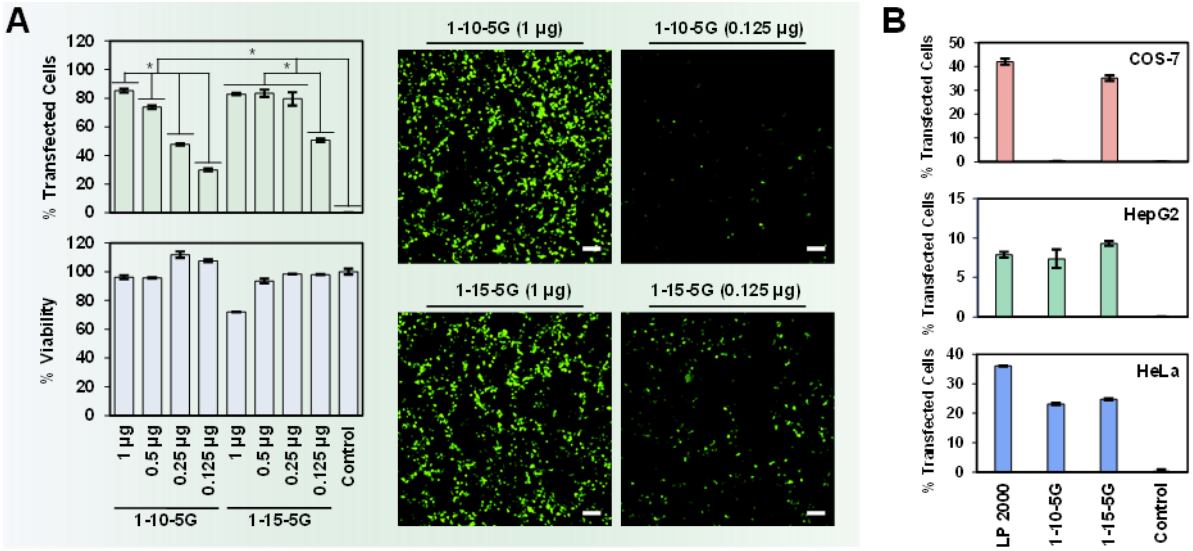

Figure 118. Dose-dependent transfection and cell viability of 1-10-5G and 1-15-5G polyplexes after 72 h in HEK-293 cells (left panel); fluorescence microscopy images of transfected cells after 72 h with different concentrations of both polyplexes. Scale bar 100 µm (right panel). (A). Transfection efficiency of 1-10-5G and 1-15-5G polyplexes after 48 h in COS-7, HepG2, and HeLa cells (B).

4.2.6 Protection Imparted by Cationic Polyboronate Vectors to pDNA

Since the practical application of *in vivo* gene therapy often requires genes to be injected directly into the bloodstream, the interaction of polymeric vectors with blood cells deserves special attention. Cationic polymers are known to electrostatically bind the membrane of erythrocytes, leading to reduced circulation half-lives and even embolism due to aggregation.[192,193] Consequently, the blood compatibility of cationic polyboronate vectors was assessed by studying their capacity to induce aggregation (optical microscopy) and damage the membrane (hemolysis by absorbance at 540 nm) of erythrocytes. Gratifyingly, when erythrocytes were incubated for 1 h at 37 ºC with increasing concentrations of 3[G2]-BA / PEG[G3]-BA and catechol G at a CBA ratio of 5, neither aggregation (Figure 119A) nor hemolysis (Figure 92) was detected even at the highest concentrations analyzed, stressing the blood compatibility of cationic polyboronate vectors.

Negatively charged proteoglycans and glycosaminoglycans abundant within serum-rich environments can displace NAs from polyplexes, compromising the success of gene therapy. This is of special relevance during cell internalization when polyplexes need to penetrate the ECM.[67,194] To assess the protection imparted by cationic polyboronate vectors to polyplexed pDNA against decomplexation by glycosaminoglycans, two of the optimized polyplexes, 1-10-5G and 1-15-5G, were incubated with increasing concentrations of highly charged polyanionic competitors (hyaluronic acid, heparin, dextran sulfate; 2 h, 37 ºC, PBS). The extent of protection was measured by monitoring the fluorescence increase of ethidium bromide permeating the polyplex and intercalating into accessible pDNA, relative to untreated polyplexes and naked pDNA (positive control). Results are summarized in Figure 119B as a function of the relative number of negative charges between the polyanionic competitors and phosphate groups in pDNA. While almost no fluorescence increase was seen for polyplexes in the absence of competitors (highly compacted pDNA), raising the concentration of polyanions resulted in a higher accessibility of ethidium bromide to pDNA, an effect more pronounced for 1-10-5G due to its lower N/P ratio. Not only do the levels of ethidium bromide accessibility compare well

with values reported in the literature,[70,195] but also gel electrophoresis revealed an absence of free pDNA for 1-15-5G treated with dextran sulfate at the end point of the study, confirming the robustness of the polyplexes. Finally, since pDNA is rapidly degraded in the presence of serum, the protection of NAs from endogenous nucleases is a critical requirement in gene therapy. The ability of cationic polyboronate vectors to protect pDNA towards endonucleases was confirmed by incubating polyplexes 1-10-5G and 1-15-5G with the enzyme DNase I (1 U/µg pEGFP-N1, 60 min, 37 ºC, 10 mM HEPES pH 7.1). The integrity of the polyplexed plasmid was confirmed by agarose gel electrophoresis whereas naked pDNA was completely degraded (Figure 119C).

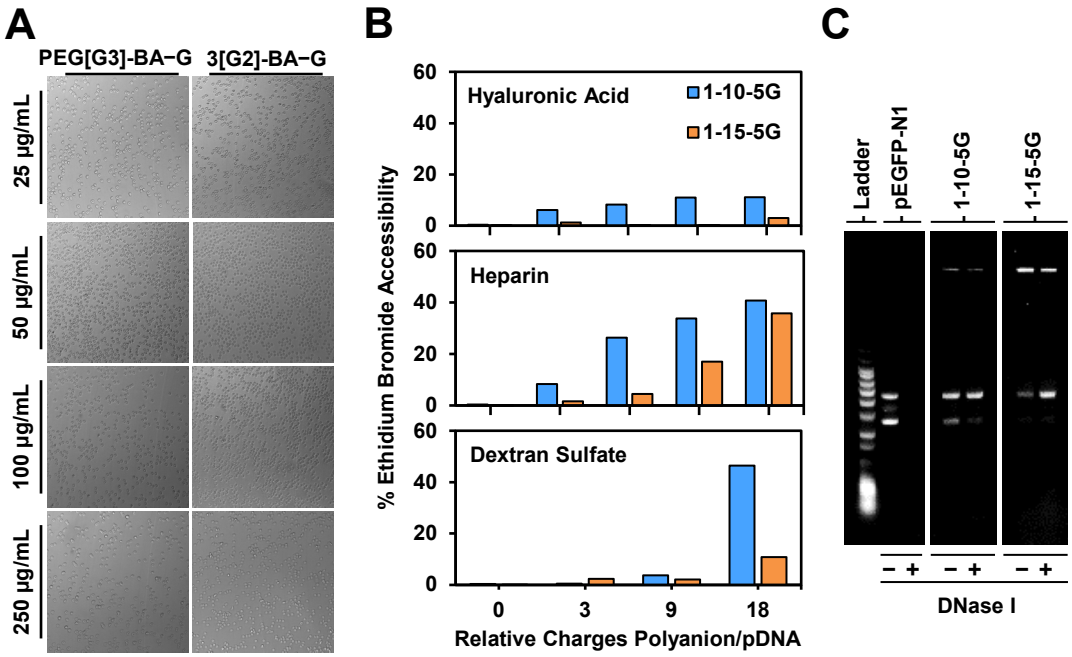

Figure 119. ***In vitro*** **experiments with optimized polyplexes. Erythrocyte aggregation test of cationic polyboronate vectors (optical microscopy). Erythrocytes (1% suspension in PBS) were incubated with increasing concentrations of 3[G2]-BA / PEG[G3]-BA and catechol G at a CBA ratio of 5 for 1 h at 37 °C. Scale bar 100 µm (A). Protection imparted by cationic polyboronate vectors to polyplexed pDNA against decomplexation by glycosaminoglycans (measured by ethidium bromide fluorescence; 18 relative charges polyanion/pDNA account for 138 µg/mL of hyaluronic acid, 55 µg/mL of heparin, and 43 µg/mL of dextran sulfate) (B) and degradation by endonucleases (agarose gel electrophoresis) (C).**

USC
UNIVERSIDADE DE SANTIAGO DE COMPOSTELA

4.3 Dynamic Covalent Boronate Chemistry for the *In Situ* Preparation, Stabilization, and Activity Optimization of Coacervate Artificial Cells

4.3.1 Research Background

Cells represent the basic structural and functional units of all forms of life. Over the last decades, theories explaining their evolution have given rise to the emerging field of bottom-up synthetic biology, which aims to create artificial cell models[196] that could be essential not only for understanding the origin of cellular life,[197] but also hold promising biotechnological applications.[198,199]Among the architectures commonly used as mimics of natural cells, CCs are particularly noteworthy.[200] These droplets, formed through liquid-liquid phase separation via the association of oppositely charged polyelectrolytes,[105] represent excellent mimics of the crowded cell interior and naturally occurring MLOs,[106] which play crucial roles in many vital functions.[107,201,202]

The phase separation processes that lead to coacervate formation are primarily governed by the concentrations of the individual components. Thus, any variation in their concentration, either due to expression or degradation processes, can effectively promote the formation or disintegration of the corresponding droplets. This concept has been extensively exploited in living cells, leading to regulatory processes based on changes in the molecular composition, [203] which ultimately affect the solubility of certain molecules.[204] Inspired by this regulation, many scientific efforts have focused on translating such behavior into controlled coacervation methods, primarily by modulating pH,[205] light irradiation,[113] fuel concentration,[206] or enzymatic processes.[207] However, although these novel technologies effectively achieve control over coacervation, they often fail to provide stabilization and structural diversity, which are essential for CCs function.[208,118]

In this context, DCvC constitutes a promising methodology for the development of adaptable and responsive networks. DCvC involves chemical reactions performed reversibly under equilibrium control.[209] However, although it has been largely employed in the design of stimuli-responsive materials,[210] its application for controlling the phase separation of polymeric scaffolds to build artificial cell models remains unexplored.

Here in, a highly adaptable method for inducing coacervation is described by using a polymeric BA that is activated by the simultaneous attachment of a cationic and an anionic catechol (Figure 120). The fast-forming and strong boronate ester bond in H_2O affords dynamic zwitterionic polyboronates able to rapidly phase-separate into single liquid droplets. The high adaptability of this strategy is also exploited for (i) a droplet stabilization through the hierarchical assembly of a PEGylated polymeric BA, and (ii) for modulating CCs properties, such as protein partitioning or internal dynamics, by tuning the ratio between cationic and an anionic catechols or by including catechol dopants following a dynamic covalent approach.

4.3.2 Formation of CCs Induced by the *In Situ* Phase Separation of Dynamic Zwitterionic Polyboronates

A dendrimer was employed as polymeric scaffold to test the feasibility of this strategy. Dendrimers are tree-like polymers with globular architecture. Their monodispersity makes them ideal candidates for evaluating new technologies and bioapplications. However, their use in the construction of coacervates remains unexplored. Thus, a dendrimer (3[G2]-BA) of the

GATG family, with 27 peripheral BAs, was chosen. Cat-G and 3,4-dihydroxyhydrocinnamic acid (Cat-CA) were selected as cationic and anionic catechols, respectively, for preparing dynamic zwitterionic polyboronates. The strong electrostatic interaction between guanidinium ions and carboxylates in aqueous media is expected to drive a phase separation of the obtained polyboronates to afford CCs.

The pH-dependent coupling between BAs and diols represents a typical example of stimuli-responsive DCvC. While the formation of boronate esters is favored at pH values above the pK_a of the BAs, they are hydrolyzed at lower pH. To employ BAs as initiators for inducing phase separation at physiological pH, *ortho*-aminomethylphenylboronic acid was selected due to its characteristic pK_a (*ca.* 6.5). Upon the simultaneous addition of the oppositely charged catechols, dendritic BAs resulted in zwitterionic polyboronates able to phase separate *in situ* into individual droplets with a mean diameter around 3 μm.

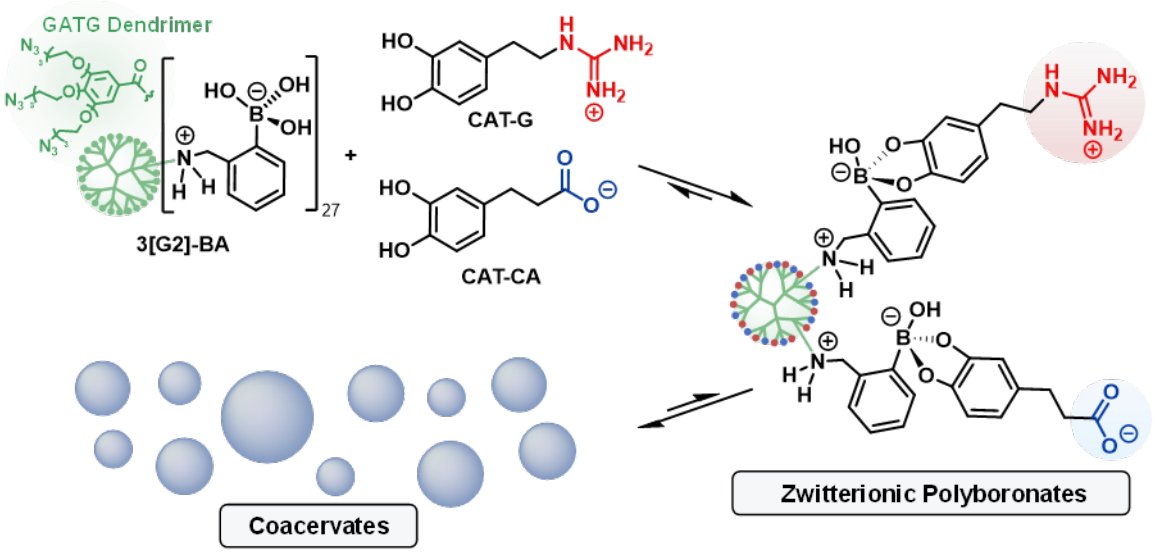

Figure 120. Schematic representation of the activation of polymeric BAs and *in situ* phase separation by the addition of oppositely charged catechols.

4.3.3 DCvC for the Stabilization of Polyboronate Coacervates

The use of coacervates as cell mimics has often been limited by their lack of a membrane to maintain their structural integrity. Nevertheless, studies over the past decade have demonstrated that the interfacial assembly of polymers, lipids, proteins, or other structures can prevent droplet coalescence without altering their permeability to small compounds and communication between droplet populations.[208] In this study, the interfacial stabilization of the polyboronate coacervates was achieved through the hierarchical assembly of PEG[G3]-BA, a PEG_{5k}-dendritic block copolymer also carrying 27 peripheral BAs, on the surface of the droplets 15 min after inducing coacervation (Figure 121A). Initial coacervation studies were conducted fixing a stoichiometric molar ratio between Cat-CA and Cat-G to avoid any effect of charge excess. The neutrality of the obtained droplets was demonstrated by ζ-potential measurements that showed values close to 0 mV (Figure 93). The core-corona structure of the stabilized coacervates was demonstrated by LSCM (Figure 121A), using a fluorescently labeled dendrimer (Cy5-3[G2]BA; red) and a fluorescently labeled version of the copolymer incorporating FITC (FITC-PEG[G3]-BA; green). Furthermore, the efficacy of the stabilization process was confirmed by comparing the temporal stability of the droplets. While the

nonstabilized droplets exhibited complete disintegration after 1 h, those incorporating PEG[G3]-BA on their surface remained stable for up to a week (Figure 94). The proposed stabilization mechanism is illustrated in Figure 121B. In summary, stabilization is hypothesized to occur in three steps. Initially, PEG[G3]-BA might be attracted to the droplet surface (1). Subsequently, functionalization of the dendritic region may occur on the droplet surface owing to the enhanced local concentration of catechols [211] (2). This would lead to an increased amphiphilic character of the copolymer, thereby facilitating its anchorage to the surface and thus, the stabilization of the droplet (3).

Then, experiments to elucidate the role of CBA ratio on the stabilization mechanism of the coacervates were conducted. Three distinct coacervates prepared with three different CBA (1, 2, and 3) were stabilized with FITC-PEG[G3]-BA (6 µM). A stoichiometric charge balance was maintained during these experiments. LSCM was performed 1 h post-coacervation for analyzing the fluorescence from FITC-PEG[G3]-BA. All particles displayed fluorescence peaks at the corona (Figure 121D), which corroborates the successful assembly of the copolymer onto the surface of the droplets irrespective of the CBA ratio employed during preparation. Still, significant differences were found regarding the fluorescence intensity profiles among the distinct droplets (Figure 121C, and D). Interestingly, a FITC fluorescence intensity inversely proportional to CBA was revealed. Highest fluorescence intensities were observed at CBA 1, with up to a 20-fold difference between the fluorescence at the corona and the core of the droplets. Conversely, when the CBA ratio was increased to 2, the peak fluorescence was reduced to one-third of that observed at a CBA 1 (8-fold difference with the core), while at CBA 3, this difference diminished to below 5-fold. The lowered intensity values observed when increasing the CBA were attributed to the ability of PEG[G3]-BA to react with the excess of catechol groups in solution, preventing its anchoring to the surfaces of the droplets.

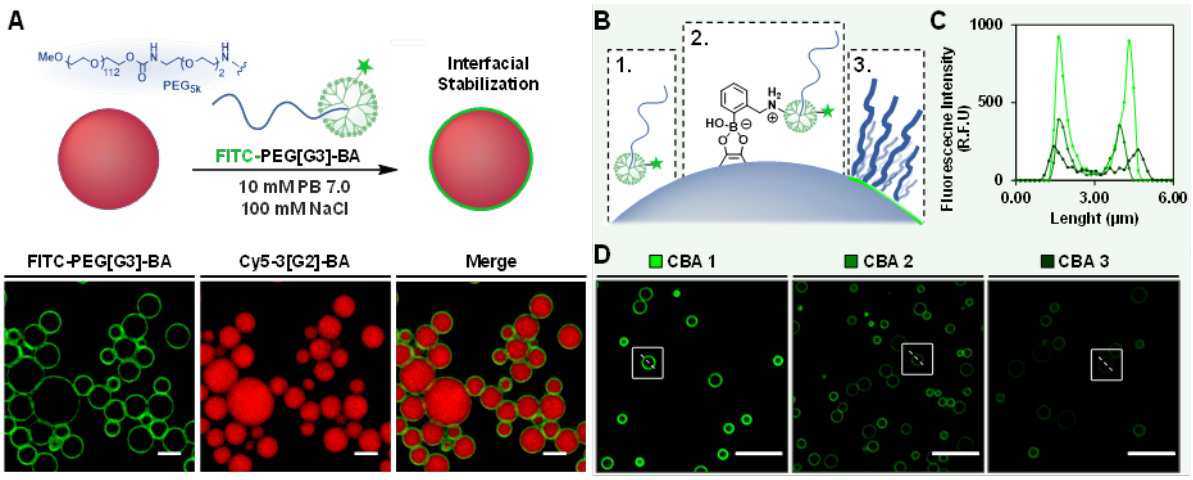

Figure 121. Schematic representation of the interfacial stabilization due to the hierarchical assembly of PEG[G3]-BA. LSCM images showing the fluorescence from FITC-PEG[G3]-BA (at the corona) and Cy5-3[G2]-BA (inner core of the droplets). Scale bar 10 µm (A). Schematic representation of the proposed stabilization mechanism (B). Fluorescence intensity profile of highlighted droplets and cross sections prepared with varying CBA (1, 2, and 3) (C). LSCM images showing the fluorescence from FITC-PEG[G3]-BA for coacervates prepared with varying CBA (1, 2, and 3) (left);). Scale bar 10 µm (D).

USC UNIVERSIDADE DE SANTIAGO DE COMPOSTELA

4.3.4 Life-Like Activity of Stabilized Polyboronate Coacervates: Protein Encapsulation and Chemical Communication

An essential characteristic of CCs is their capacity to promote macromolecular sequestration. This characteristic can be enhanced by modulating the affinity of the cargo for the inner core of the coacervates. For example, numerous studies depend on protein modifications to enhance entrapment within the droplets. Alternative approaches involve the use of an excess of charge during coacervate preparation, typically employing an excess of one polyelectrolyte. Here, the robustness of DCvC enabled an adaptation of this latter strategy to enhance protein partitioning within the coacervates by adjusting the molar ratio between Cat-CA and Cat-G. This allowed modulation of the inner environment of the droplets in a feasible manner without altering the polymeric scaffold. Three different Cat-CA/Cat-G ratios were studied (2:1, 1:1, and 1:2). Glucose oxidase GOX (160 kDa, pI 4.2) and HRP (60 kDa, pI 7.2), both fluorescently labeled with Cy5 were selected to assess the viability of this approach due to their largely different pI, and their complementarity in enzymatic cascade reactions. Interestingly, a direct relationship between the catechol charge ratio and EE was observed independently of the pI, with EE increasing for GOX (from 83 to 96 %) and HRP (from 52 to 71%) with the excess of Cat-G (Figure 122A), a phenomenon presumably attributable to the net positive charge, bidentate structure, and hydrogen bonding capability of the guanidinium group.[190] LSCM images were obtained to further corroborate the protein partitioning within the droplets using the optimized molar ratio of catechols (Figure 122A). Furthermore, protein exchange between different populations of coacervates was discarded by analyzing the mixture of coacervates encapsulating GOX and HRP fluorescently labelled with AF-488 (green) and Cy5 (blue), respectively (Figure 122B, t = 0 min).

Maintaining an active droplet-droplet communication after interfacial stabilization represents a challenge on synthetic biology. The archetypical example of enzymatic cascade reaction between GOX and HRP was selected to assess such a life–like behavior of stabilized polyboronate coacervates. Coacervates prepared with a CBA 1 and a 2:1 charge ratio were loaded with either GOx (GOx@C) or HRP (HRP@C). Chemical communication between droplets was qualitatively and quantitatively studied by employing glucose and amplex red or *ortho*-phenylenediamine (*o*PD) as substrates. Oxidation of glucose by GOX produces H_2O_2 as a byproduct. Effective communication would be confirmed by H_2O_2 transport between droplets and oxidation of amplex red or *o*PD to the fluorescently active products resorufin and 2,3-DAP.

For qualitative studies, LSCM experiments were conducted with amplex red and coacervates charged with fluorescently labeled versions of the proteins: AF488-GOx@C (green) and Cy5-HRP@C (blue) (Figure 122B). After the addition of substrates, the time-dependent production of resorufin (red) within the sample was monitored. As expected, resorufin fluorescence signal initially appeared in Cy5-HRP@C. After 10 min, while an intense fluorescence level was detected within these compartments, resorufin migration towards AF488-GOX@C was also observed (Figures 122B and 95-96). Then, quantitative analysis of the reaction progress was performed with *o*PD (GOx@C and HRP@C) by monitoring the progressive appearance of the fluorescence signal of 2,3-DAP (Figure 122C). Reaction profile shows a maximum 2,3-DAP relative fluorescence value reached 4000 s after the addition of the substrates. Control experiments showed no 2,3-DAP production in the absence of either any of the enzymes or glucose (Figures 97 and 122C). These findings validate the ability of PEG[G3]-BA to prevent protein migration between populations while allowing the diffusion of small molecules, thereby corroborating the life-like behavior of polyboronate coacervates.

USC
DE COMPOSTELA

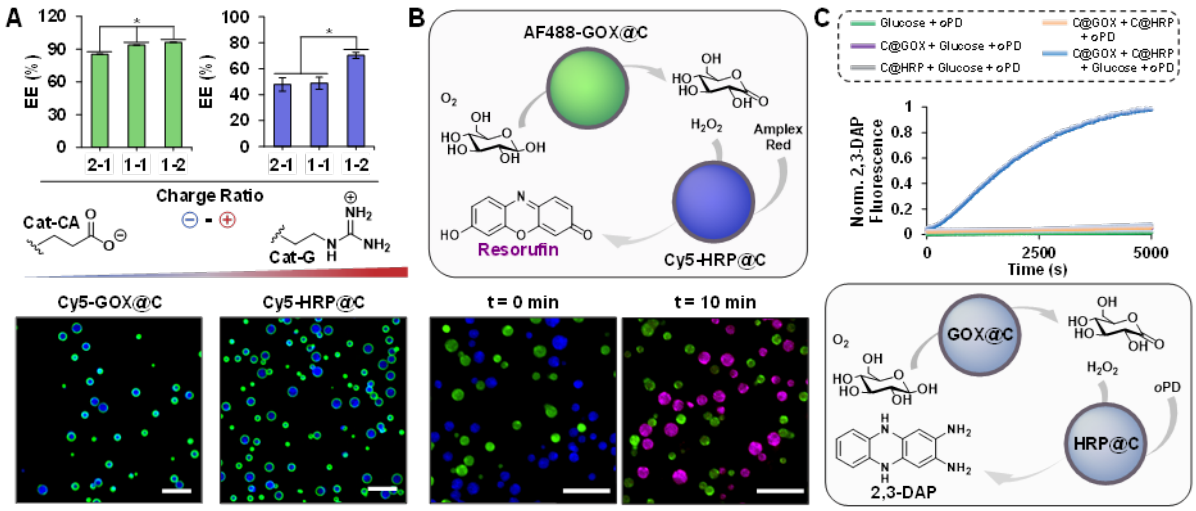

Figure 122. Protein uptake and chemical communication in coacervate populations. Quantification of protein uptake into droplets prepared with varying the molar ratios between Cat-CA and Cat-G. Data obtained through fluorescence measurements of the supernatants after centrifugation. (*) indicates statistical difference ($p < 0.05$) analyzed by one-way ANOVA, followed by a Tukey multiple comparisons test (top). LSCM images of Cy5-GOX@C and Cy5-HRP@C formed using a 2-to-1 excess of Cat-G and stabilized with FITC-PEG [G3]-BA (down). Scale bar 10 µm (A). Schematic representation and LSCM images of the GOX/HRP enzymatic production of resorufin from AF488@C-GOX and Cy5-HRP@C droplets, identified by AF-488 (green) or Cy5 (blue), respectively. Scale bar 10 µm (B). Schematic representation and enzymatic production of 2,3-DAP from GOX@C and HRP@C droplets measured by product fluorescence.

4.3.5 Optimizing Polyboronate Coacervates by the Introduction of Dopants

Recent reports have demonstrated that variations in the multivalency or charge density of polyelectrolytes undergoing phase separation can significantly affect the internal dynamics and ribozyme/enzyme activity within CCs.[117,118] In this context, DCvC emerge as a promising tool to tune the CCs composition and properties by incorporating different functional moieties along a polymeric backbone. To explore this approach, three commercially available natural catechols were selected as dopants to stress test this adaptable methodology: CAT, EGCG, and EPI (Figure 123). Effective phase separation into discrete droplets was observed for coacervates prepared with a 10 mol% of the three dopants (CBA 1, 2:1 charge ratio).

The impact of doping on the coacervates internal dynamics and on the interaction between coacervates with a protein cargo was examined employing FRAP experiments using Cy5-labeled bovine serum albumin (Cy5-BSA) as model payload (Figure 123A). While minimal internal mobility was observed for BSA within the undoped coacervates, the introduction of dopants significantly increased BSA-Cy5 diffusion, resulting in higher recovery values. Notably, a slight increase was observed for EPI (+5.4%), while a substantial increase in fluorescence recovery was observed for EGCG (+15%) and CAT-doped coacervates (+45%), representing a 6-fold enhancement for the latter. The enhanced recovery values obtained for EGCG and CAT allowed for the fitting of the FRAP recovery curves, thereby enabling the determination of the apparent diffusion coefficient (D_{app}) of BSA in stabilized droplets doped either with EGCG ($4.04 \cdot 10^{-4}$ µm²/s), and CAT ($5.44 \cdot 10^{-4}$ µm²/s) (Figure 98). Consequently, the gel-like structure of undoped coacervates, typical of guanidine-based CCs,[212] can be tuned by *in situ* modification of the zwitterionic polyboronates undergoing phase separation.

USC UNIVERSIDADE DE SANTIAGO DE COMPOSTELA

Enhanced protein mobility within CCs has been correlated with enhanced enzymatic activity.[118] Therefore, the influence of dopants on the *o*PD enzymatic transformation was further analyzed. Doped coacervates encapsulating GOX or HRP were prepared, showing indistinguishable EE for both enzymes (Figure 99). Enzymatic reaction profiles were recorded under identical conditions for all coacervates. Analysis of the reaction profiles between 500 and 1500 s after the addition of glucose revealed enhanced kinetics for doped droplets. Interestingly, the observed trends in reaction kinetics agree with that observed in the fluorescence recovery values, highlighting the importance of manipulating protein mobility on the activity of the final droplets. (Figure 123B).

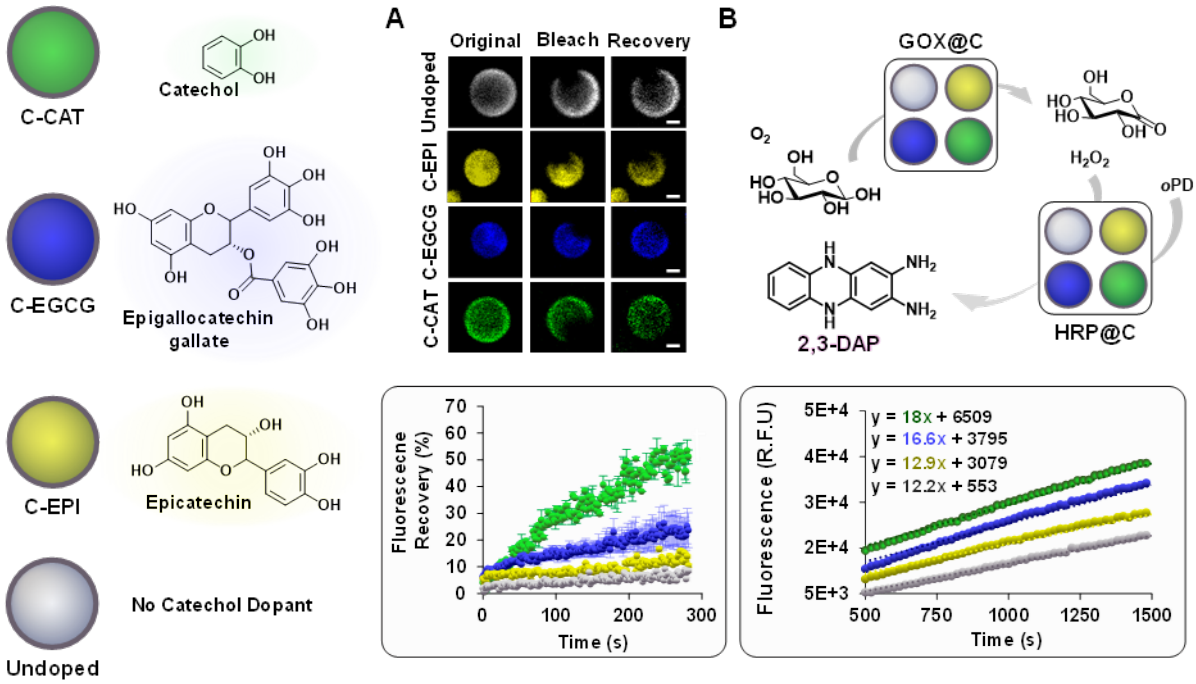

Figure 123. Studies on doped coacervates. Schematic representation of doped coacervates and dopants structures. Representative LSCM images indicating fluorescence recovery due to Cy5-BSA diffusion for each dopant. Scale bar 1 µm. Temporal Cy5-BSA fluorescence recovery: undoped (gray); C-EPI (yellow); C-EGCG (blue) and C-CAT (green) (A). Schematic representation and reaction profiles of the enzymatic cascade production of 2,3-DAP from *o*PD and glucose on doped coacervates monitored by product fluorescence: undoped (gray); C-EPI (yellow); C-EGCG (blue) and C-CAT (green).

USC UNIVERSIDADE DE SANTIAGO DE COMPOSTELA

5. CONCLUSIONS

- In the first part of this thesis, a novel DCvC technology for obtaining a size-tunable polymer therapeutic of DOX was developed. A successful hierarchical transfer of information from the assembly of PEG-dendritic copolymers to polyboronate micelles allowed the preparation of pH-responsive DOX loaded micelles as a DDS with tailored size and PEG density at the corona. This study sheds light on the impact these last parameters play in the pH-triggered drug release, intracellular trafficking, and cytotoxicity of the resulting micelles.

- A highly adaptable gene delivery platform is described in the second part of this thesis using a dendritic BA that is activated in the presence of pDNA by the addition of cationic catechols. The resulting cationic polyboronates can complex pDNA *in situ* leading to polyplexes that efficiently transfect cells. The robustness of this DCvC strategy entitles the simultaneous screening of several structural parameters at will (PEGylation, surface charge, polycation chemical composition, hydrophilic/hydrophobic balance), enabling the accelerated screening and adaptive optimization of lead polymeric vectors by means of dynamic covalent libraries. The strategy is envisaged to be easily adapted to polymeric gene delivery vectors with alternative architectures, and even nonviral peptide- and lipid-based carriers.

- Finally, the last part of the thesis illustrates the robustness of DCvC to construct coacervate-based artificial cell models exhibiting life-like behavior. This methodology, based on dendritic boronic acids, enables the production of coacervates from *in situ* prepared zwitterionic polyboronates and facilitated the stabilization of the droplets through the hierarchical assembly of a dendritic-linear block copolymer. The results also emphasize how the internal properties of the droplets can be modulated by the addition of catechol dopants, influencing the internal dynamics and enzymatic activity inside the coacervate.

USC
UNIVERSIDADE DE SANTIAGO DE COMPOSTELA

6. REFERENCES

(1) Riehemann, K.; Schneider, S. W.; Luger, T. A.; Godin, B.; Ferrari, M.; Fuchs, H. Nanomedicine - Challenge and Perspectives. *Angew. Chem., Int. Ed.* **2009**, *48* (5), 872–897.

(2) Krämer, J.; Kang, R.; Grimm, L. M.; De Cola, L.; Picchetti, P.; Biedermann, F. Molecular Probes, Chemosensors, and Nanosensors for Optical Detection of Biorelevant Molecules and Ions in Aqueous Media and Biofluids. *Chem. Rev.* **2022**, *122* (3), 3459–3636.

(3) Fusi, A. D.; Li, Y.; Llopis-Lorente, A.; Patiño, T.; van Hest, J. C. M.; Abdelmohsen, L. K. E. A. Achieving Control in Micro-/Nanomotor Mobility. *Angew. Chem., Int. Ed.* **2023**, *62* (5).

(4) Liu, Y.; Liu, B.; Nie, Z. Concurrent Self-Assembly of Amphiphiles into Nanoarchitectures with Increasing Complexity. *Nano Today* **2015**, *10* (3), 278–300.

(5) Sowerby, S. J.; Holm, N. G.; Petersen, G. B. Origins of Life: A Route to Nanotechnology. *BioSystems* **2001**, *61* (1), 69–78.

(6) Zhang, Z. G.; Li, Y. Polymerized Small-Molecule Acceptors for High-Performance All-Polymer Solar Cells. *Angew. Chem., Int. Ed.* **2021**, *60* (9), 4422–4433.

(7) Goujon, N.; Casado, N.; Patil, N.; Marcilla, R.; Mecerreyes, D. Organic Batteries Based on Just Redox Polymers: Abstract. *Prog. Polym. Sci.* **2021**, *122*, 101449.

(8) Becker, M. L.; Burdick, J. A. Introduction: Polymeric Biomaterials. *Chem. Rev.* **2021**, *121* (18), 10789–10791.

(9) Liechty, W. B.; Kryscio, D. R.; Slaughter, B. V.; Peppas, N. A. Polymers for Drug Delivery Systems. *Annu. Rev. Chem. Biomol. Eng.* **2010**, *1*, 149–173.

(10) Clothier, G. K. K.; Guimarães, T. R.; Thompson, S. W.; Rho, J. Y.; Perrier, S.; Moad, G.; Zetterlund, P. B. Multiblock Copolymer Synthesis via RAFT Emulsion Polymerization. *Chem. Soc. Rev.* **2023**, *52* (10), 3438–3469.

(11) Xu, J.; Hadjichristidis, N. Heteroatom-Containing Degradable Polymers by Ring-Opening Metathesis Polymerization. *Prog. Polym. Sci.* **2023**, *139*, 101656.

(12) Chakraborty, B.; Luscombe, C. K. Cross-Dehydrogenative Coupling Polymerization via C−H Activation for the Synthesis of Conjugated Polymers. *Angew. Chem., Int. Ed.* **2023**, *62* (21).

(13) Ruiz-Mirazo, K.; Briones, C.; De La Escosura, A. Prebiotic Systems Chemistry: New Perspectives for the Origins of Life. *Chem. Rev.* **2014**, *114* (1), 285–366.

(14) Anselmo, A. C.; Mitragotri, S. An Overview of Clinical and Commercial Impact of Drug Delivery Systems. *J. Control. Release* **2014**, *190*, 15–28.

(15) Vargason, A. M.; Anselmo, A. C.; Mitragotri, S. The Evolution of Commercial Drug Delivery Technologies. *Nat. Biomed. Eng.* **2021**, *5* (9), 951–967.

USC UNIVERSIDADE DE SANTIAGO DE COMPOSTELA

(16) Park, H.; Otte, A.; Park, K. Evolution of Drug Delivery Systems: From 1950 to 2020 and Beyond. *J. Control. Release* **2022**, *342*, 53–65.

(17) Yun, Y. H.; Lee, B. K.; Park, K. Controlled Drug Delivery: Historical Perspective for the next Generation. *J. Control. Release* **2015**, *219*, 2–7.

(18) Jingjing Gao, Jeffrey M Karp, Robert Langer, and N. J. The Future of Drug Delivery. *Chem. Mater.* **2023**, *35* (2), 359–363.

(19) Svenson, S.; Tomalia, D. A. Dendrimers in Biomedical Applications-Reflections on the Field. *Adv. Drug Deliv. Rev.* **2012**, *64*, 102–115.

(20) Allen, T. M.; Cullis, P. R. Liposomal Drug Delivery Systems: From Concept to Clinical Applications. *Adv. Drug Deliv. Rev.* **2013**, *65* (1), 36–48.

(21) Kataoka, K.; Harada, A.; Nagasaki, Y. Block Copolymer Micelles for Drug Delivery: Design, Characterization and Biological Significance. *Adv. Drug Deliv. Rev.* **2012**, *64*, 37–48.

(22) Moghimi, S. M.; Patel, H. M. Serum-Mediated Recognition of Liposomes by Phagocytic Cells of the Reticuloendothelial System - The Concept of Tissue Specificity. *Adv. Drug Deliv. Rev.* **1998**, *32* (1–2), 45–60.

(23) Tenzer, S.; Docter, D.; Kuharev, J.; Musyanovych, A.; Fetz, V.; Hecht, R.; Schlenk, F.; Fischer, D.; Kiouptsi, K.; Reinhardt, C.; Landfester, K.; Schild, H.; Maskos, M.; Knauer, S. K.; Stauber, R. H. Rapid Formation of Plasma Protein Corona Critically Affects Nanoparticle Pathophysiology. *Nat. Nanotechnol.* **2013**, *8* (10), 772–781.

(24) Kolate, A.; Baradia, D.; Patil, S.; Vhora, I.; Kore, G.; Misra, A. PEG - A Versatile Conjugating Ligand for Drugs and Drug Delivery Systems. *J. Control. Release* **2014**, *192*, 67–81.

(25) Parodi, A.; Quattrocchi, N.; Van De Ven, A. L.; Chiappini, C.; Evangelopoulos, M.; Martinez, J. O.; Brown, B. S.; Khaled, S. Z.; Yazdi, I. K.; Enzo, M. V.; Isenhart, L.; Ferrari, M.; Tasciotti, E. Synthetic Nanoparticles Functionalized with Biomimetic Leukocyte Membranes Possess Cell-like Functions. *Nat. Nanotechnol.* **2013**, *8* (1), 61–68.

(26) Anselmo, A. C.; Lynn Modery-Pawlowski, C.; Menegatti, S.; Kumar, S.; Vogus, D. R.; Tian, L. L.; Chen, M.; Squires, T. M.; Gupta, A. Sen; Mitragotri, S. Platelet-like Nanoparticles: Mimicking Shape, Flexibility, and Surface Biology of Platelets to Target Vascular Injuries. *ACS Nano* **2014**, *8* (11), 11243–11253.

(27) Shih, H. P.; Zhang, X.; Aronov, A. M. Drug Discovery Effectiveness from the Standpoint of Therapeutic Mechanisms and Indications. *Nat. Rev. Drug Discov.* **2018**, *17* (1), 19–33.

(28) Allard, E.; Passirani, C.; Benoit, J. P. Convection-Enhanced Delivery of Nanocarriers for the Treatment of Brain Tumors. *Biomaterials* **2009**, *30* (12), 2302–2318.

(29) Matsumura, Y.; Maeda, H. A New Concept for Macromolecular Therapeutics in Cancer Chemotherapy: Mechanism of Tumoritropic Accumulation of Proteins and the Antitumor Agent Smancs. *Cancer Res.* **1986**, *46* (8), 6387–6392.

USC UNIVERSIDADE DE SANTIAGO DE COMPOSTELA

(30) Zhao, Z.; Ukidve, A.; Kim, J.; Mitragotri, S. Targeting Strategies for Tissue-Specific Drug Delivery. *Cell* **2020**, *181* (1), 151–167.

(31) Mitchell, M. J.; Billingsley, M. M.; Haley, R. M.; Wechsler, M. E.; Peppas, N. A.; Langer, R. Engineering Precision Nanoparticles for Drug Delivery. *Nat. Rev. Drug Discov.* **2021**, *20* (2), 101–124.

(32) Blanco, E.; Shen, H.; Ferrari, M. Principles of Nanoparticle Design for Overcoming Biological Barriers to Drug Delivery. *Nat. Biotechnol.* **2015**, *33* (9), 941–951.

(33) Gentile, F.; Chiappini, C.; Fine, D.; Bhavane, R. C.; Peluccio, M. S.; Cheng, M. M. C.; Liu, X.; Ferrari, M.; Decuzzi, P. The Effect of Shape on the Margination Dynamics of Non-Neutrally Buoyant Particles in Two-Dimensional Shear Flows. *J. Biomech.* **2008**, *41* (10), 2312–2318.

(34) Geng, Y.; Dalhaimer, P.; Cai, S.; Tsai, R.; Tewari, M.; Minko, T.; Discher, D. E. Shape Effects of Filaments versus Spherical Particles in Flow and Drug Delivery. *Nat. Nanotechnol.* **2007**, *2* (4), 249–255.

(35) Parmar, K.; Patel, J.; Pathak, Y. Factors Affecting the Clearance and Biodistribution of Polymeric Nanoparticles. *Mol. Pharm.* **2008**, *5* (4), 505–515.

(36) Thurston, G.; McLean, J. W.; Rizen, M.; Baluk, P.; Haskell, A.; Murphy, T. J.; Hanahan, D.; McDonald, D. M. Cationic Liposomes Target Angiogenic Endothelial Cells in Tumors and Chronic Inflammation in Mice. *J. Clin. Invest.* **1998**, *101* (7), 1401–1413.

(37) Thakor, P.; Bhavana, V.; Sharma, R.; Srivastava, S.; Singh, S. B.; Mehra, N. K. Polymer–Drug Conjugates: Recent Advances and Future Perspectives. *Drug Discov. Today* **2020**, *25* (9), 1718–1726.

(38) Cycle, M.-C.; Jose, S.; Cinu, T. A.; Sebastian, R.; Shoja, M. H.; Aleykutty, N. A.; Durazzo, A.; Lucarini, M.; Santini, A.; Souto, E. B. Transferrin-Conjugated Docetaxel–PLGA Nanoparticles for Tumor Targeting: Influence on MCF-7 Cell Cycle. *Polymers (Basel).* **2019**, *11* (1905), 1–20.

(39) Urello, M. A.; Xiang, L.; Colombo, R.; Ma, A.; Joseph, A.; Boyd, J.; Peterson, N.; Gao, C.; Wu, H.; Christie, R. J. Metabolite-Based Modification of Poly(l-Lysine) for Improved Gene Delivery. *Biomacromolecules* **2020**, *21* (9), 3596–3607.

(40) Ekladious, I.; Colson, Y. L.; Grinstaff, M. W. Polymer–Drug Conjugate Therapeutics: Advances, Insights and Prospects. *Nat. Rev. Drug Discov.* **2019**, *18* (4), 273–294.

(41) Rideau, E.; Dimova, R.; Schwille, P.; Wurm, F. R.; Landfester, K. Liposomes and Polymersomes: A Comparative Review towards Cell Mimicking. *Chem. Soc. Rev.* **2018**, *47* (23), 8572–8610.

(42) Zelmer, C.; Zweifel, L. P.; Kapinos, L. E.; Craciun, I.; Güven, Z. P.; Palivan, C. G.; Lim, R. Y. H. Organelle-Specific Targeting of Polymersomes into the Cell Nucleus. *Proc. Natl. Acad. Sci. U. S. A.* **2020**, *117* (6), 2770–2778.

(43) Ainoa Guinart, Maria Korpidou, Daniel Doellerer, Gianni Pacella, Marc C. A. Stuart, Ionel Adrian Dinu, Giuseppe Portale, Cornelia Palivan, and B. L. F. Synthetic Molecular Motor Activates Drug Delivery from Polymersomes. *Proc. Natl. Acad. Sci.* **2023**, *120*, e2301279120.

USC

(44) Hwang, D.; Ramsey, J. D.; Kabanov, A. V. Polymeric Micelles for the Delivery of Poorly Soluble Drugs: From Nanoformulation to Clinical Approval. *Adv. Drug Deliv. Rev.* **2020**, *156*, 80–118.

(45) Newkome, G. R.; Yao, Z. Q.; Baker, G. R.; Gupta, V. K. Cascade Molecules: A New Approach to Micelles. *J. Org. Chem.* **1985**, *50* (11), 2003–2004.

(46) Tomalia, D. A.; Baker, H.; Dewald, J.; Hall, M.; Kallos, G.; Martin, S.; Roeck, J.; Ryder, J.; Smith, P. A New Class of Polymers: Starburst-Dendritic Macromolecules. *Polym. J.* **1985**, *17* (1), 117–132.

(47) Ren, M.; Li, Y.; Zhang, H.; Li, L.; He, P.; Ji, P.; Yang, S. An Oligopeptide/Aptamer-Conjugated Dendrimer-Based Nanocarrier for Dual-Targeting Delivery to Bone. *J. Mater. Chem. B* **2021**, *9* (12), 2831–2844.

(48) Chawla, M.; Kaushik, R. D.; Malik, M. K.; Pundir, V.; Singh, J.; Rehmaan, H. Development and Optimization of RofA-PAMAM Dendrimer Complex Materials for Sustained Drug Delivery. *Mater. Today Commun.* **2022**, *33* (June), 104881.

(49) Sousa-Herves, A.; Riguera, R.; Fernandez-Megia, E. PEG-Dendritic Block Copolymers for Biomedical Applications. *New J. Chem.* **2012**, *36* (2), 205–210.

(50) Sousa-Herves, A.; Novoa-Carballal, R.; Riguera, R.; Fernandez-Megia, E. GATG Dendrimers and PEGylated Block Copolymers: From Synthesis to Bioapplications. *AAPS J.* **2014**, *16* (5), 948–961.

(51) Serge J. Meunier, Quigquan Wu, Sho-Nong Wang, and R. R. Synthesis of Hyperbranched Glycodendrimers Incorporating α-Thiosialosides Based on a Gallic Acid Core. *Can. J. Chem.* **1997**, *75*, 1472–1482.

(52) Fernandez-Villamarin, M.; Sousa-Herves, A.; Porto, S.; Guldris, N.; Martínez-Costas, J.; Riguera, R.; Fernandez-Megia, E. A Dendrimer-Hydrophobic Interaction Synergy Improves the Stability of Polyion Complex Micelles. *Polym. Chem.* **2017**, *8* (16), 2528–2537.

(53) Zhong, H.; Chan, G.; Hu, Y.; Hu, H.; Ouyang, D. A Comprehensive Map of FDA-Approved Pharmaceutical Products. *Pharmaceutics* **2018**, *10* (4), 1–19.

(54) Wang, D.; Li, M.; Zhang, H.; Feng, C.; Wu, L.; Yan, L. A Novel Redox-Sensitive Drug Delivery System Based on Trimethyl-Locked Polycarbonate. *Biomacromolecules* **2023**, *24* (9), 4303–4315.

(55) Li, N.; Cai, H.; Jiang, L.; Hu, J.; Bains, A.; Hu, J.; Gong, Q.; Luo, K.; Gu, Z. Enzyme-Sensitive and Amphiphilic PEGylated Dendrimer-Paclitaxel Prodrug-Based Nanoparticles for Enhanced Stability and Anticancer Efficacy. *ACS Appl. Mater. Interfaces* **2017**, *9* (8), 6865–6877.

(56) Lee, E. S.; Gao, Z.; Bae, Y. H. Recent Progress in Tumor PH Targeting Nanotechnology. *J. Control. Release* **2008**, *132* (3), 164–170.

(57) Wang, Y.; Huang, D.; Wang, X.; Yang, F.; Shen, H.; Wu, D. Fabrication of Zwitterionic and PH-Responsive Polyacetal Dendrimers for Anticancer Drug Delivery. *Biomater. Sci.* **2019**, *7* (8), 3238–3248.

USC UNIVERSIDADE DE SANTIAGO DE COMPOSTELA

(58) Li, Y.; Chen, M.; Yao, B.; Lu, X.; Song, B.; Vasilatos, S. N.; Zhang, X.; Ren, X.; Yao, C.; Bian, W.; Sun, L. Dual PH/ROS-Responsive Nanoplatform with Deep Tumor Penetration and Self-Amplified Drug Release for Enhancing Tumor Chemotherapeutic Efficacy. *Small* **2020**, *16* (32), 1–14.

(59) Anguela, X. M.; High, K. A. Entering the Modern Era of Gene Therapy. *Annu. Rev. Med.* **2019**, *70*, 273–288.

(60) Bhatia, V.; Ateeq, B. Molecular Underpinnings Governing Genetic Complexity of ETS-Fusion-Negative Prostate Cancer. *Trends Mol. Med.* **2019**, *25* (11), 1024–1038.

(61) Lächelt, U.; Wagner, E. Nucleic Acid Therapeutics Using Polyplexes: A Journey of 50 Years (and Beyond). *Chem. Rev.* **2015**, *115* (19), 11043–11078.

(62) Kulkarni, J. A.; Witzigmann, D.; Thomson, S. B.; Chen, S.; Leavitt, B. R.; Cullis, P. R.; van der Meel, R. The Current Landscape of Nucleic Acid Therapeutics. *Nat. Nanotechnol.* **2021**, *16* (6), 630–643.

(63) Wang, D.; Tai, P. W. L.; Gao, G. Adeno-Associated Virus Vector as a Platform for Gene Therapy Delivery. *Nat. Rev. Drug Discov.* **2019**, *18* (5), 358–378.

(64) Bartlett, J. S.; Wilcher, R.; Samulski, R. J. Infectious Entry Pathway of Adeno-Associated Virus and Adeno-Associated Virus Vectors. *J. Virol.* **2000**, *74* (6), 2777–2785.

(65) Katherine A. High, M.D. and Maria G. Roncarolo, M. D. Gene Therapy. *N. Engl. J. Med.* **2019**, *381* (5), 455–464.

(66) Gene Therapy at the Crossroads. *Nat. Biotechnol.* **2022**, *40* (5), 621.

(67) Kumar, R.; Santa Chalarca, C. F.; Bockman, M. R.; Bruggen, C. Van; Grimme, C. J.; Dalal, R. J.; Hanson, M. G.; Hexum, J. K.; Reineke, T. M. Polymeric Delivery of Therapeutic Nucleic Acids. *Chem. Rev.* **2021**, *121* (18), 11527–11652.

(68) Sheridan, C. Why Gene Therapies Must Go Virus-Free. *Nat. Biotechnol.* **2023**, *41* (6), 737–739.

(69) Cedervall, T.; Lynch, I.; Lindman, S.; Berggård, T.; Thulin, E.; Nilsson, H.; Dawson, K. A.; Linse, S. Understanding the Nanoparticle-Protein Corona Using Methods to Quntify Exchange Rates and Affinities of Proteins for Nanoparticles. *Proc. Natl. Acad. Sci. U. S. A.* **2007**, *104* (7), 2050–2055.

(70) McLendon, P. M.; Buckwalter, D. J.; Davis, E. M.; Reineke, T. M. Interaction of Poly(Glycoamidoamine) DNA Delivery Vehicles with Cell-Surface Glycosaminoglycans Leads to Polyplex Internalization in a Manner Not Solely Dependent on Charge. *Mol. Pharm.* **2010**, *7* (5), 1757–1768.

(71) Suk, J. S.; Xu, Q.; Kim, N.; Hanes, J.; Ensign, L. M. PEGylation as a Strategy for Improving Nanoparticle-Based Drug and Gene Delivery. *Adv. Drug Deliv. Rev.* **2016**, *99*, 28–51.

(72) Fischer, D.; Li, Y.; Ahlemeyer, B.; Krieglstein, J.; Kissel, T. In Vitro Cytotoxicity Testing of Polycations: Influence of Polymer Structure on Cell Viability and Hemolysis. *Biomaterials* **2003**, *24* (7), 1121–1131.

(73) Monnery, B. D. Polycation-Mediated Transfection: Mechanisms of Internalization and Intracellular Trafficking. *Biomacromolecules* **2021**, *22* (10), 4060–4083.

(74) Huotari, J.; Helenius, A. Endosome Maturation. *EMBO J.* **2011**, *30* (17), 3481–3500.

(75) Jiang, Y.; Lu, Q.; Wang, Y.; Xu, E.; Ho, A.; Singh, P.; Wang, Y.; Jiang, Z.; Yang, F.; Tietjen, G. T.; Cresswell, P.; Saltzman, W. M. Quantitating Endosomal Escape of a Library of Polymers for MRNA Delivery. *Nano Lett.* **2020**, *20* (2), 1117–1123.

(76) Vermeulen, L. M. P.; De Smedt, S. C.; Remaut, K.; Braeckmans, K. The Proton Sponge Hypothesis: Fable or Fact? *Eur. J. Pharm. Biopharm.* **2018**, *129* (May), 184–190.

(77) Yun Hak Kim, Myoung-Eun Han, S.-O. O. The Molecular Mechanism for Nuclear Transport and Its Application. *Curr. Opin. Cell Biol.* **2017**, *50*, 77–85.

(78) Shi, J.; Schellinger, J. G.; Johnson, R. N.; Choi, J. L.; Chou, B.; Anghel, E. L.; Pun, S. H. Influence of Histidine Incorporation on Buffer Capacity and Gene Transfection Efficiency of HPMA-Co-Oligolysine Brush Polymers. *Biomacromolecules* **2013**, *14* (6), 1961–1970.

(79) Carlson, P. M.; Schellinger, J. G.; Pahang, J. A.; Johnson, R. N.; Pun, S. H. Comparative Study of Guanidine-Based and Lysine-Based Brush Copolymers for Plasmid Delivery. *Biomater. Sci.* **2013**, *1* (7), 736–744.

(80) Choi, J. L.; Tan, J. K. Y.; Sellers, D. L.; Wei, H.; Horner, P. J.; Pun, S. H. Guanidinylated Block Copolymers for Gene Transfer: A Comparison with Amine-Based Materials for Invitro and Invivo Gene Transfer Efficiency. *Biomaterials* **2015**, *54*, 87–96.

(81) Ahmed, S. T.; Leckband, D. E. Protein Adsorption on Grafted Zwitterionic Polymers Depends on Chain Density and Molecular Weight. *Adv. Funct. Mater.* **2020**, *30* (30), 1–10.

(82) Chang, Y.; Shu, S. H.; Shih, Y. J.; Chu, C. W.; Ruaan, R. C.; Chen, W. Y. Hemocompatible Mixed-Charge Copolymer Brushes of Pseudozwitterionic Surfaces Resistant to Nonspecific Plasma Protein Fouling. *Langmuir* **2010**, *26* (5), 3522–3530.

(83) Zhang, Z.; Chen, S.; Jiang, S. Dual-Functional Biomimetic Materials: Nonfouling Poly(Carboxybetaine) with Active Functional Groups for Protein Immobilization. *Biomacromolecules* **2006**, *7* (12), 3311–3315.

(84) Wu, P.; Luo, X.; Wu, H.; Zhang, Q.; Wang, K.; Sun, M.; Oupicky, D. Combined Hydrophobization of Polyethylenimine with Cholesterol and Perfluorobutyrate Improves SiRNA Delivery. *Bioconjug. Chem.* **2020**, *31* (3), 698–707.

(85) Sharma, D.; Singh, J. Synthesis and Characterization of Fatty Acid Grafted Chitosan Polymer and Their Nanomicelles for Nonviral Gene Delivery Applications. *Bioconjug. Chem.* **2017**, *28* (11), 2772–2783.

(86) Lv, J.; Wang, H.; Rong, G.; Cheng, Y. Fluorination Promotes the Cytosolic Delivery of Genes, Proteins, and Peptides. *Acc. Chem. Res.* **2022**, *55* (5), 722–733.

(87) Lynn, D. M.; Langer, R. Degradable Poly (-Amino Esters): Synthesis , Characterization , and Self-Assembly with Plasmid DNA. *J. Am. Chem. Soc.* **2000**, 10, 10761–10768.

USC UNIVERSIDADE DE SANTIAGO DE COMPOSTELA

(88) Lynn, D. M.; Anderson, D. G.; Putnam, D.; Langer, R. Accelerated Discovery of Synthetic Transfection Vectors: Parallel Synthesis and Screening of a Degradable Polymer Library. *J. Am. Chem. Soc.* **2001**, *123* (33), 8155–8156.

(89) Akinc, A.; Lynn, D. M.; Anderson, D. G.; Langer, R. Parallel Synthesis and Biophysical Characterization of a Degradable Polymer Library for Gene Delivery. *J. Am. Chem. Soc.* **2003**, *125* (18), 5316–5323.

(90) Liu, H.; Chang, H.; Lv, J.; Jiang, C.; Li, Z.; Wang, F.; Wang, H.; Wang, M.; Liu, C.; Wang, X.; Shao, N.; He, B.; Shen, W.; Zhang, Q.; Cheng, Y. Screening of Efficient SiRNA Carriers in a Library of Surface-Engineered Dendrimers. *Sci. Rep.* **2016**, *6*, 1–11.

(91) Kumar, R.; Le, N.; Tan, Z.; Brown, M. E.; Jiang, S.; Reineke, T. M. Efficient Polymer-Mediated Delivery of Gene-Editing Ribonucleoprotein Payloads through Combinatorial Design, Parallelized Experimentation, and Machine Learning. *ACS Nano* **2020**, *14* (12), 17626-17639.

(92) Buddingh', B. C.; Van Hest, J. C. M. Artificial Cells: Synthetic Compartments with Life-like Functionality and Adaptivity. *Acc. Chem. Res.* **2017**, *50* (4), 769–777.

(93) Miller, S. L.; William Schopf, J.; Lazcano, A. Oparin's "Origin of Life": Sixty Years Later. *J. Mol. Evol.* **1997**, *44* (4), 351–353.

(94) Mann, S. Nonliving Matter. *Acc. Chem. Res.* **2012**, *45* (12), 2131–2141.

(95) Murtas, G. Artificial Assembly of a Minimal Cell. *Mol. Biosyst.* **2009**, *5* (11), 1292–1297.

(96) Szostak, J. W.; Bartel, D. P.; Luisi, P. L. Szostak et Al. - 2001 - Synthesizing Life. *Nature* **2001**, *409*, 387–390.

(97) Mukwaya, V.; Mann, S.; Dou, H. Chemical Communication at the Synthetic Cell/Living Cell Interface. *Commun. Chem.* **2021**, *4* (1), 1–12.

(98) Lu, Y.; Allegri, G.; Huskens, J. Vesicle-Based Artificial Cells: Materials, Construction Methods and Applications. *Mater. horizons* **2022**, *9* (3), 892–907.

(99) Bangham, A. D.; Horne, R. W. Negative Staining of Phospholipids and Their Structural Modification by Surface-Active Agents as Observed in the Electron Microscope. *J. Mol. Biol.* **1964**, *8* (5), 660–668.

(100) Zhu, Y.; Cao, S.; Huo, M.; van Hest, J. C. M.; Che, H. Recent Advances in Permeable Polymersomes: Fabrication, Responsiveness, and Applications. *Chem. Sci.* **2023**, *14* (27), 7411–7437.

(101) Ellis, R. J. Macromolecular Crowding: Obvious but Underappreciated. *Trends Biochem. Sci.* **2001**, *26* (10), 597–604.

(102) Yu, I.; Mori, T.; Ando, T.; Harada, R.; Jung, J.; Sugita, Y.; Feig, M. Biomolecular Interactions Modulate Macromolecular Structure and Dynamics in Atomistic Model of a Bacterial Cytoplasm. *Elife* **2016**, *5*, 1–22.

USC UNIVERSIDADE DE SANTIAGO DE COMPOSTELA

(103) Skóra, T.; Vaghefikia, F.; Fitter, J.; Kondrat, S. Macromolecular Crowding: How Shape and Interactions Affect Diffusion. *J. Phys. Chem. B* **2020**, *124* (35), 7537–7543.

(104) Llopis-Lorente, A.; Schotman, M. J. G.; Humeniuk, H. V.; van Hest, J. C. M.; Dankers, P. Y. W.; Abdelmohsen, L. K. E. A. Artificial Cells with Viscoadaptive Behavior Based on Hydrogel-Loaded Giant Unilamellar Vesicles. *Chem. Sci.* **2023**, *15* (2), 629–638.

(105) Cook, A. B.; Novosedlik, S.; van Hest, J. C. M. Complex Coacervate Materials as Artificial Cells. *Accounts Mater. Res.* **2023**, *4* (3), 287–298.

(106) Yewdall, N. A.; André, A. A. M.; Lu, T.; Spruijt, E. Coacervates as Models of Membraneless Organelles. *Curr. Opin. Colloid Interface Sci.* **2021**, *52*, 101416.

(107) Banani, S. F.; Lee, H. O.; Hyman, A. A.; Rosen, M. K. Biomolecular Condensates: Organizers of Cellular Biochemistry. *Nat. Rev. Mol. Cell Biol.* **2017**, *18* (5), 285–298.

(108) Brangwynne, C. P.; Eckmann, C. R.; Courson, D. S.; Rybarska, A.; Hoege, C.; Gharakhani, J.; Jülicher, F.; Hyman, A. A. Germline P Granules Are Liquid Droplets That Localize by Controlled Dissolution/Condensation. *Science* **2009**, *324* (5935), 1729–1732.

(109) Chen, Y.; Yuan, M.; Zhang, Y.; Liu, S.; Yang, X.; Wang, K.; Liu, J. Construction of Coacervate-in-Coacervate Multi-Compartment Protocells for Spatial Organization of Enzymatic Reactions. *Chem. Sci.* **2020**, *11* (32), 8617–8625.

(110) Mountain, G. A.; Keating, C. D. Formation of Multiphase Complex Coacervates and Partitioning of Biomolecules within Them. *Biomacromolecules* **2020**, *21* (2), 630–640.

(111) Lu, T.; Spruijt, E. Multiphase Complex Coacervate Droplets. *J. Am. Chem. Soc.* **2020**, *142* (6), 2905–2914.

(112) Li, P.; Banjade, S.; Cheng, H. C.; Kim, S.; Chen, B.; Guo, L.; Llaguno, M.; Hollingsworth, J. V.; King, D. S.; Banani, S. F.; Russo, P. S.; Jiang, Q. X.; Nixon, B. T.; Rosen, M. K. Phase Transitions in the Assembly of Multivalent Signalling Proteins. *Nature* **2012**, *483* (7389), 336–340.

(113) Martin, N.; Tian, L.; Spencer, D.; Coutable-Pennarun, A.; Anderson, J. L. R.; Mann, S. Photoswitchable Phase Separation and Oligonucleotide Trafficking in DNA Coacervate Microdroplets. *Angew. Chemie* **2019**, *131* (41), 14736–14740.

(114) Nakashima, K. K.; Baaij, J. F.; Spruijt, E. Reversible Generation of Coacervate Droplets in an Enzymatic Network. *Soft Matter* **2018**, *14* (3), 361–367.

(115) Karoui, H.; Seck, M. J.; Martin, N. Self-Programmed Enzyme Phase Separation and Multiphase Coacervate Droplet Organization. *Chem. Sci.* **2021**, *12* (8), 2794–2802.

(116) Cakmak, F. P.; Choi, S.; Meyer, M. C. O.; Bevilacqua, P. C.; Keating, C. D. Prebiotically-Relevant Low Polyion Multivalency Can Improve Functionality of Membraneless Compartments. *Nat. Commun.* **2020**, *11* (1), 1–11.

(117) Iglesias-Artola, J. M.; Drobot, B.; Kar, M.; Fritsch, A. W.; Mutschler, H.; Dora Tang, T. Y.; Kreysing, M. Charge-Density Reduction Promotes Ribozyme Activity in RNA–Peptide Coacervates via RNA Fluidization and Magnesium Partitioning. *Nat. Chem.* **2022**, *14* (4), 407–416.

USC UNIVERSIDADE DE SANTIAGO DE COMPOSTELA

(118) Cook, A. B.; Gonzalez, B. D.; van Hest, J. C. M. Tuning of Cationic Polymer Functionality in Complex Coacervate Artificial Cells for Optimized Enzyme Activity. *Biomacromolecules* **2024**, *25* (1), 425–435.

(119) Dora Tang, T. Y.; Rohaida Che Hak, C.; Thompson, A. J.; Kuimova, M. K.; Williams, D. S.; Perriman, A. W.; Mann, S. Fatty Acid Membrane Assembly on Coacervate Microdroplets as a Step towards a Hybrid Protocell Model. *Nat. Chem.* **2014**, *6* (6), 527–533.

(120) Dewey, D. C.; Strulson, C. A.; Cacace, D. N.; Bevilacqua, P. C.; Keating, C. D. Bioreactor Droplets from Liposome-Stabilized All-Aqueous Emulsions. *Nat. Commun.* **2014**, *5*, 1–9.

(121) Mason, A. F.; Buddingh, B. C.; Williams, D. S.; Van Hest, J. C. M. Hierarchical Self-Assembly of a Copolymer-Stabilized Coacervate Protocell. *J. Am. Chem. Soc.* **2017**, *139* (48), 17309–17312.

(122) Jobdeedamrong, A.; Cao, S.; Harley, I.; Crespy, D.; Landfester, K.; Caire da Silva, L. Assembly of Biomimetic Microreactors Using Caged-Coacervate Droplets. *Nanoscale* **2022**, *15* (6), 2561–2566.

(123) Jiang, L.; Zeng, Y.; Li, H.; Lin, Z.; Liu, H.; Richardson, J. J.; Gao, Z.; Wu, D.; Liu, L.; Caruso, F.; Zhou, J. Peptide-Based Coacervate Protocells with Cytoprotective Metal-Phenolic Network Membranes. *J. Am. Chem. Soc.* **2023**, *145* (44), 24108–24115.

(124) Prof. Elias James Corey. The Logic of Chemical Synthesis : Multistep Synthesis of Complex Carbogenic Molecules. *Angew. Chem., Int. Ed. English* **1991**, *30* (5), 455–612.

(125) Jin, Y.; Wang, Q.; Taynton, P.; Zhang, W. Dynamic Covalent Chemistry Approaches toward Macrocycles, Molecular Cages, and Polymers. *Acc. Chem. Res.* **2014**, *47* (5), 1575–1586.

(126) Black, S. P.; Sanders, J. K. M.; Stefankiewicz, A. R. Disulfide Exchange: Exposing Supramolecular Reactivity through Dynamic Covalent Chemistry. *Chem. Soc. Rev.* **2014**, *43* (6), 1861–1872.

(127) Kölmel, D. K.; Kool, E. T. Oximes and Hydrazones in Bioconjugation: Mechanism and Catalysis. *Chem. Rev.* **2017**, *117* (15), 10358–10376.

(128) Brooks, W. L. A.; Sumerlin, B. S. Synthesis and Applications of Boronic Acid-Containing Polymers: From Materials to Medicine. *Chem. Rev.* **2016**, *116* (3), 1375–1397.

(129) Sun, X.; Chapin, B. M.; Metola, P.; Collins, B.; Wang, B.; James, T. D.; Anslyn, E. V. The Mechanisms of Boronate Ester Formation and Fluorescent Turn-on in Ortho-Aminomethylphenylboronic Acids. *Nat. Chem.* **2019**, *11* (9), 768–778.

(130) Tihal, R. D. P. and C. A. Mechanism of Boron Acid/Polyol Complex Formation. Comments on the Trigonal/Tetrahedral Interconversion on Boron. *Polyhedron* **1996**, *15* (19), 3411–3416.

USC
UNIVERSIDADE DE SANTIAGO DE COMPOSTELA

(131) Wiskur, S. L.; Lavigne, J. J.; Ait-Haddou, H.; Lynch, V.; Chiu, Y. H.; Canary, J. W.; Anslyn, E. V. PKa Values and Geometries of Secondary and Tertiary Amines Complexed to Boronic Acids - Implications for Sensor Design. *Org. Lett.* **2001**, *3* (9), 1311–1314.

(132) Sun, X.; James, T. D.; Anslyn, E. V. Arresting "Loose Bolt" Internal Conversion from -B(OH)2 Groups Is the Mechanism for Emission Turn-On in Ortho-Aminomethylphenylboronic Acid-Based Saccharide Sensors. *J. Am. Chem. Soc.* **2018**, *140* (6), 2348–2354.

(133) Valenzuela, S. A.; Howard, J. R.; Park, H. M.; Darbha, S.; Anslyn, E. V. 11B NMR Spectroscopy: Structural Analysis of the Acidity and Reactivity of Phenyl Boronic Acid-Diol Condensations. *J. Org. Chem.* **2022**, *87* (22), 15071–15076.

(134) Zhu, L.; Shabbir, S. H.; Gray, M.; Lynch, V. M.; Sorey, S.; Anslyn, E. V. A Structural Investigation of the N-B Interaction in an o-(N,N-Dialkylaminomethyl)Arylboronate System. *J. Am. Chem. Soc.* **2006**, *128* (4), 1222–1232.

(135) Collins, B. E.; Sorey, S.; Hargrove, A. E.; Shabbir, S. H.; Lynch, V. M.; Anslyn, E. V. Probing Intramolecular B-N Interactions in Ortho-Aminomethyl Arylboronic Acids. *J. Org. Chem.* **2009**, *74* (11), 4055–4060.

(136) Stubelius, A.; Lee, S.; Almutairi, A. The Chemistry of Boronic Acids in Nanomaterials for Drug Delivery. *Acc. Chem. Res.* **2019**, *52* (11), 3108–3119.

(137) Ulrich, S. Growing Prospects of Dynamic Covalent Chemistry in Delivery Applications. *Acc. Chem. Res.* **2019**, *52* (2), 510–519.

(138) Liu, B.; Wu, R.; Gong, S.; Xiao, H.; Thayumanavan, S. In Situ Formation of Polymeric Nanoassemblies Using an Efficient Reversible Click Reaction. *Angew. Chem., Int. Ed.* **2020**, *59* (35), 15135–15140.

(139) Wang, R.; Yin, C.; Liu, C.; Sun, Y.; Xiao, P.; Li, J.; Yang, S.; Wu, W.; Jiang, X. Phenylboronic Acid Modification Augments the Lysosome Escape and Antitumor Efficacy of a Cylindrical Polymer Brush-Based Prodrug. *J. Am. Chem. Soc.* **2021**, *143* (49), 20927–20938.

(140) Wang, K.; Xiao, X.; Liu, Y.; Zong, Q.; Tu, Y.; Yuan, Y. Self-Immolative Polyprodrug-Based Tumor-Specific Cascade Amplificated Drug Release Nanosystem for Orchestrated Synergistic Cancer Therapy. *Biomaterials* **2022**, *289*, 121803.

(141) Xu, J.; Li, Z.; Fan, Q.; Lv, J.; Li, Y.; Cheng, Y. Dynamic Polymer Amphiphiles for Efficient Intracellular and In Vivo Protein Delivery. *Adv. Mater.* **2021**, *33* (52), 1–11.

(142) Priegue, J. M.; Crisan, D. N.; Martínez-Costas, J.; Granja, J. R.; Fernandez-Trillo, F.; Montenegro, J. In Situ Functionalized Polymers for siRNA Delivery. *Angew. Chem., Int. Ed.* **2016**, *55* (26), 7492–7495.

(143) Priegue, J. M.; Lostalé-Seijo, I.; Crisan, D.; Granja, J. R.; Fernández-Trillo, F.; Montenegro, J. Different-Length Hydrazone Activated Polymers for Plasmid DNA Condensation and Cellular Transfection. *Biomacromolecules* **2018**, *19* (7), 2638–2649.

USC UNIVERSIDADE DE SANTIAGO DE COMPOSTELA

(144) Hashim, P. K.; Okuro, K.; Sasaki, S.; Hoashi, Y.; Aida, T. Reductively Cleavable Nanocaplets for SiRNA Delivery by Template-Assisted Oxidative Polymerization. *J. Am. Chem. Soc.* **2015**, *137* (50), 15608–15611.

(145) Zhou, J.; Sun, L.; Wang, L.; Liu, Y.; Li, J.; Li, J.; Li, J.; Yang, H. Self-Assembled and Size-Controllable Oligonucleotide Nanospheres for Effective Antisense Gene Delivery through an Endocytosis-Independent Pathway. *Angew. Chem., Int. Ed.* **2019**, *58* (16), 5236–5240.

(146) Bartolami, E.; Bessin, Y.; Gervais, V.; Dumy, P.; Ulrich, S. Dynamic Expression of DNA Complexation with Self-assembled Biomolecular Clusters. *Angew. Chemie* **2015**, *127* (35), 10321–10325.

(147) Laroui, N.; Coste, M.; Su, D.; Ali, L. M. A.; Bessin, Y.; Barboiu, M.; Gary-Bobo, M.; Bettache, N.; Ulrich, S. Cell-Selective SiRNA Delivery Using Glycosylated Dynamic Covalent Polymers Self-Assembled In Situ by RNA Templating. *Angew. Chem., Int. Ed.* **2021**, *60* (11), 5783–5787.

(148) Yu, S.; Chen, W.; Liu, G.; Flores, B.; DeWolf, E. L.; Fan, B.; Xiang, Y.; Webber, M. J. Glucose-Driven Droplet Formation in Complexes of a Supramolecular Peptide and Therapeutic Protein. *J. Am. Chem. Soc.* **2023**, *146*, 7498-7505.

(149) Delgado Gonzalez, B.; Lopez-Blanco, R.; Parcero-Bouzas, S.; Barreiro-Piñeiro, N.; Garcia-Abuin, L.; Fernandez-Megia, E. Dynamic Covalent Boronate Chemistry Accelerates the Screening of Polymeric Gene Delivery Vectors via In Situ Complexation of Nucleic Acids. *J. Am. Chem. Soc.* **2024**, *146*, 17211-17219

(150) Zhao, A. Y.; Brooks, A. F.; Raffel, D. M.; Stauff, J.; Arteaga, J.; Scott, P. J. H.; Shao, X. Fully Automated Radiosynthesis of [11C]Guanidines for Cardiac PET Imaging. *ACS Med. Chem. Lett.* **2020**, *11* (11), 2325–2330.

(151) Amato, A.; Migneco, L. M.; Martinelli, A.; Pietrelli, L.; Piozzi, A.; Francolini, I. Antimicrobial Activity of Catechol Functionalized-Chitosan versus Staphylococcus Epidermidis. *Carbohydr. Polym.* **2018**, *179*, 273–281.

(152) Fernandez-Villamarin, M.; Sousa-Herves, A.; Correa, J.; Munoz, E. M.; Taboada, P.; Riguera, R.; Fernandez-Megia, E. The Effect of PEGylation on Multivalent Binding: A Surface Plasmon Resonance and Isothermal Titration Calorimetry Study with Structurally Diverse PEG-Dendritic GATG Copolymers. *ChemNanoMat* **2016**, *2* (5), 437–446.

(153) Amaral, S. P.; Tawara, M. H.; Fernandez-Villamarin, M.; Borrajo, E.; Martínez-Costas, J.; Vidal, A.; Riguera, R.; Fernandez-Megia, E. Tuning the Size of Nanoassembles: A Hierarchical Transfer of Information from Dendrimers to Polyion Complexes. *Angew. Chem., Int. Ed.* **2018**, *57* (19), 5273–5277.

(154) Lin, L.; Li, Z.; Yan, L.; Liu, Y.; Yang, H.; Li, H. Global, Regional, and National Cancer Incidence and Death for 29 Cancer Groups in 2019 and Trends Analysis of the Global Cancer Burden, 1990–2019. *J. Hematol. Oncol.* **2021**, *14* (1), 1–24.

(155) Soerjomataram, I.; Bray, F. Planning for Tomorrow: Global Cancer Incidence and the Role of Prevention 2020–2070. *Nat. Rev. Clin. Oncol.* **2021**, *18* (10), 663–672.

USC UNIVERSIDADE DE SANTIAGO DE COMPOSTELA

(156) Costanzo, V.; Ratre, Y. K.; Andretta, E.; Acharya, R.; Bhaskar, L. V. K. S.; Verma, H. K. A Comprehensive Review of Cancer Drug–Induced Cardiotoxicity in Blood Cancer Patients: Current Perspectives and Therapeutic Strategies. *Curr. Treat. Options in Oncol.* **2024***, 25,* 465–495.

(157) Cheng, Z.; Li, M.; Dey, R.; Chen, Y. Nanomaterials for Cancer Therapy: Current Progress and Perspectives. *J. Hematol. Oncol.* **2021**, *14* (1), 1–27.

(158) Al-Ni'mat, M. A.; Parcero-Bouzas, S.; Amaral, S. P.; Fernandez-Megia, E. Self-Assembled Dendritic Boronate Micelles as a Promising Delivery Strategy for Gemcitabine. *ChemRxiv* **2021**, 1–20.

(159) D'Agosto, F.; Rieger, J.; Lansalot, M. RAFT-Mediated Polymerization-Induced Self-Assembly. *Angew. Chem., Int. Ed.* **2020**, *59* (22), 8368–8392.

(160) Wang, J.; Mao, W.; Lock, L. L.; Tang, J.; Sui, M.; Sun, W.; Cui, H.; Xu, D.; Shen, Y. The Role of Micelle Size in Tumor Accumulation. *ACS Nano* **2015**, *9* (7), 7195–7206.

(161) Lopez-Blanco, R.; Rodrigo Magana, J.; Esquena-Moret, J.; Fernandez-Megia, E. From Nanometric to Giant Polyion Complex Micelles via Hierarchical Assembly of a PEG-Dendritic Copolymer/Dendrimer Pair. *Manuscript in preparation*.

(162) Webb, B. A.; Chimenti, M.; Jacobson, M. P.; Barber, D. L. Dysregulated PH: A Perfect Storm for Cancer Progression. *Nat. Rev. Cancer* **2011**, *11* (9), 671–677.

(163) Andrew MacKay, J.; Chen, M.; McDaniel, J. R.; Liu, W.; Simnick, A. J.; Chilkoti, A. Self-Assembling Chimeric Polypeptide-Doxorubicin Conjugate Nanoparticles That Abolish Tumours after a Single Injection. *Nat. Mater.* **2009**, *8* (12), 993–999.

(164) Bulcha, J. T.; Wang, Y.; Ma, H.; Tai, P. W. L.; Gao, G. Viral Vector Platforms within the Gene Therapy Landscape. *Signal Transduct. Target. Ther.* **2021**, *6*, 53.

(165) Lostalé-Seijo, I.; Montenegro, J. Synthetic Materials at the Forefront of Gene Delivery. *Nat. Rev. Chem.* **2018**, *2* (10), 258–277.

(166) Carvalho, M. R.; Carvalho, C. R.; Maia, F. R.; Caballero, D.; Kundu, S. C.; Reis, R. L.; Oliveira, J. M. Peptide-Modified Dendrimer Nanoparticles for Targeted Therapy of Colorectal Cancer. *Adv. Ther.* **2019**, *2* (11), 1900132.

(167) He, D.; Wagner, E. Defined Polymeric Materials for Gene Delivery. *Macromol. Biosci.* **2015**, *15* (5), 600–612.

(168) Salameh, J. W.; Zhou, L.; Ward, S. M.; Santa Chalarca, C. F.; Emrick, T.; Figueiredo, M. L. Polymer-Mediated Gene Therapy: Recent Advances and Merging of Delivery Techniques. *Wiley Interdiscip. Rev. Nanomedicine Nanobiotechnology* **2020**, *12* (2), 1–23.

(169) Parhamifar, L.; Andersen, H.; Wu, L.; Hall, A.; Hudzech, D.; Moghimi, S. M. Polycation-Mediated Integrated Cell Death Processes. *Advances in Genetics* **2014**, 88, 353-398.

(170) Ogris, M.; Steinlein, P.; Carotta, S.; Brunner, S.; Wagner, E. DNA/Polyethylenimine Transfection Particles: Influence of Ligands, Polymer Size, and PEGylation on Internalization and Gene Expression. *AAPS PharmSci* **2001**, *3* (3), 21.

USC UNIVERSIDADE DE SANTIAGO DE COMPOSTELA

(171) Degors, I. M. S.; Wang, C.; Rehman, Z. U.; Zuhorn, I. S. Carriers Break Barriers in Drug Delivery: Endocytosis and Endosomal Escape of Gene Delivery Vectors. *Acc. Chem. Res.* **2019**, *52* (7), 1750–1760.

(172) Jordan J. Green, Robert Langer, and Anderson, D. G. A Combinatorial Polymer Library Approach Yields Insight into Nonviral Gene Delivery. *Acc. Chem. Res.* **2008**, *41* (6), 749–759.

(173) Zhang, D.; Atochina-Vasserman, E. N.; Maurya, D. S.; Huang, N.; Xiao, Q.; Ona, N.; Liu, M.; Shahnawaz, H.; Ni, H.; Kim, K.; Billingsley, M. M.; Pochan, D. J.; Mitchell, M. J.; Weissman, D.; Percec, V. One-Component Multifunctional Sequence-Defined Ionizable Amphiphilic Janus Dendrimer Delivery Systems for MRNA. *J. Am. Chem. Soc.* **2021**, *143* (31), 12315–12327.

(174) Zhang, D.; Atochina-Vasserman, E. N.; Lu, J.; Maurya, D. S.; Xiao, Q.; Liu, M.; Adamson, J.; Ona, N.; Reagan, E. K.; Ni, H.; Weissman, D.; Percec, V. The Unexpected Importance of the Primary Structure of the Hydrophobic Part of One-Component Ionizable Amphiphilic Janus Dendrimers in Targeted MRNA Delivery Activity. *J. Am. Chem. Soc.* **2022**, *144* (11), 4746–4753.

(175) Freitag, F.; Wagner, E. Optimizing Synthetic Nucleic Acid and Protein Nanocarriers: The Chemical Evolution Approach. *Adv. Drug Deliv. Rev.* **2021**, *168*, 30–54.

(176) Su, D.; Coste, M.; Diaconu, A.; Barboiu, M.; Ulrich, S. Cationic Dynamic Covalent Polymers for Gene Transfection. *J. Mater. Chem. B* **2020**, *8* (41), 9385–9403.

(177) Oupický, D.; Parker, A. L.; Seymour, L. W. Laterally Stabilized Complexes of DNA with Linear Reducible Polycations: Strategy for Triggered Intracellular Activation of DNA Delivery Vectors. *J. Am. Chem. Soc.* **2002**, *124* (1), 8–9.

(178) Catana, R.; Barboiu, M.; Moleavin, I.; Clima, L.; Rotaru, A.; Ursu, E. L.; Pinteala, M. Dynamic Constitutional Frameworks for DNA Biomimetic Recognition. *Chem. Commun.* **2015**, *51* (11), 2021–2024.

(179) García Coll, J.; Ulrich, S. Nucleic-Acid-Templated Synthesis of Smart Polymer Vectors for Gene Delivery. *ChemBioChem* **2023**, *24* (19), e202300333 .

(180) Su, D. D.; Ali, L. M. A.; Coste, M.; Laroui, N.; Bessin, Y.; Barboiu, M.; Bettache, N.; Ulrich, S. Structure-Activity Relationships in Nucleic-Acid-Templated Vectors Based on Peptidic Dynamic Covalent Polymers. *Chem. - A Eur. J.* **2023**, *29* (7), e202202921.

(181) Yang, J.; Zhang, Q.; Chang, H.; Cheng, Y. Surface-Engineered Dendrimers in Gene Delivery. *Chem. Rev.* **2015**, *115* (11), 5274–5300.

(182) Li, L.; Deng, Y.; Zeng, Y.; Yan, B.; Deng, Y.; Zheng, Z.; Li, S.; Yang, Y.; Hao, J.; Xiao, X.; Wang, X. The Application Advances of Dendrimers in Biomedical Field. *View* **2023**, *4* (6), 1–17.

(183) Amaral, S. P.; Tawara, M. H.; Fernandez-Villamarin, M.; Borrajo, E.; Martínez-Costas, J.; Vidal, A.; Riguera, R.; Fernandez-Megia, E. Tuning the Size of Nanoassembles: A Hierarchical Transfer of Information from Dendrimers to Polyion Complexes. *Angew. Chem., Int. Ed.* **2018**, *57* (19), 5273–5277.

USC UNIVERSIDADE DE SANTIAGO DE COMPOSTELA

(184) Hashimoto, T.; Kawazu, T.; Nagasaki, T.; Murakami, A.; Yamaoka, T. Quantitative Comparison between Poly(L-Arginine) and Poly(L-Lysine) at Each Step of Polyplex-Based Gene Transfection Using a Microinjection Technique. *Sci. Technol. Adv. Mater.* **2012**, *13*, No. 015009.

(185) Miyata, K.; Oba, M.; Nakanishi, M.; Fukushima, S.; Yamasaki, Y.; Koyama, H.; Nishiyama, N.; Kataoka, K. Polyplexes from Poly(Aspartamide) Bearing 1,2-Diaminoethane Side Chains Induce PH-Selective, Endosomal Membrane Destabilization with Amplified Transfection and Negligible Cytotoxicity. *J. Am. Chem. Soc.* **2008**, *130* (48), 16287–16294.

(186) He, J.; Xu, S.; James Mixson, A. The Multifaceted Histidine-Based Carriers for Nucleic Acid Delivery: Advances and Challenges. *Pharmaceutics* **2020**, *12* (8), 1–31.

(187) Bus, T.; Traeger, A.; Schubert, U. S. The Great Escape: How Cationic Polyplexes Overcome the Endosomal Barrier. *J. Mater. Chem. B* **2018**, *6* (43), 6904–6918.

(188) Najjar, K.; Erazo-Oliveras, A.; Mosior, J. W.; Whitlock, M. J.; Rostane, I.; Cinclair, J. M.; Pellois, J. P. Unlocking Endosomal Entrapment with Supercharged Arginine-Rich Peptides. *Bioconjug. Chem.* **2017**, *28* (12), 2932–2941.

(189) Richter, F.; Martin, L.; Leer, K.; Moek, E.; Hausig, F.; Brendel, J. C.; Brendel, J. C.; Traeger, A.; Traeger, A. Tuning of Endosomal Escape and Gene Expression by Functional Groups, Molecular Weight and Transfection Medium: A Structure-Activity Relationship Study. *J. Mater. Chem. B* **2020**, *8* (23), 5026–5041.

(190) Wexselblatt, E.; Esko, J. D.; Tor, Y. On Guanidinium and Cellular Uptake. *J. Org. Chem.* **2014**, *79* (15), 6766–6774.

(191) Zhou, Y.; Han, S.; Liang, Z.; Zhao, M.; Liu, G.; Wu, J. Progress in Arginine-Based Gene Delivery Systems. *J. Mater. Chem. B* **2020**, *8* (26), 5564–5577.

(192) Ogris, M.; Brunner, S.; Schüller, S.; Kircheis, R.; Wagner, E. PEGylated DNA/Transferrin-PEI Complexes: Reduced Interaction with Blood Components, Extended Circulation in Blood and Potential for Systemic Gene Delivery. *Gene Ther.* **1999**, *6* (4), 595–605.

(193) Chollet, P.; Favrot, M. C.; Hurbin, A.; Coll, J. L. Side-Effects of a Systemic Injection of Linear Polyethylenimine-DNA Complexes. *J. Gene Med.* **2002**, *4* (1), 84–91.

(194) Ruponen, M.; Rönkkö, S.; Honkakoski, P.; Pelkonen, J.; Tammi, M.; Urtti, A. Extracellular Glycosaminoglycans Modify Cellular Trafficking of Lipoplexes and Polyplexes. *J. Biol. Chem.* **2001**, *276* (36), 33875–33880.

(195) Floyd, T. G.; Song, J. I.; Hapeshi, A.; Laroque, S.; Hartlieb, M.; Perrier, S. Bottlebrush Copolymers for Gene Delivery: Influence of Architecture, Charge Density, and Backbone Length on Transfection Efficiency. *J. Mater. Chem. B* **2022**, 3696–3704.

(196) Hirschi, S.; Ward, T. R.; Meier, W. P.; Muller, D. J.; Fotiadis, D. Synthetic Biology: Bottom-Up Assembly of Molecular Systems. *Chem. Rev.* **2022**, *122* (21), 16294–16328.

(197) Powell, K. How Biologists Are Creating Life-like Cells from Scratch. *Nature* **2018**, *563* (7730), 172–175.

USC UNIVERSIDADE DE SANTIAGO DE COMPOSTELA

(198) Chen, S.; Chen, X.; Su, H.; Guo, M.; Liu, H. Advances in Synthetic-Biology-Based Whole-Cell Biosensors: Principles, Genetic Modules, and Applications in Food Safety. *Int. J. Mol. Sci.* **2023**, *24* (9), 7989.

(199) Piunti, C.; Cimetta, E. Microfluidic Approaches for Producing Lipid-Based Nanoparticles for Drug Delivery Applications. *Biophys. Rev.* **2023**, *4*, 031304.

(200) Lin, Z.; Beneyton, T.; Baret, J. C.; Martin, N. Coacervate Droplets for Synthetic Cells. *Small Methods* **2023**, *2300496*, 1–26.

(201) Chen, X.; Wu, X.; Wu, H.; Zhang, M. Phase Separation at the Synapse. *Nat. Neurosci.* **2020**, *23* (3), 301–310.

(202) Yoshizawa, T.; Nozawa, R. S.; Jia, T. Z.; Saio, T.; Mori, E. Biological Phase Separation: Cell Biology Meets Biophysics. *Biophys. Rev.* **2020**, *12* (2), 519–539.

(203) Su, Q.; Mehta, S.; Zhang, J. Liquid-Liquid Phase Separation: Orchestrating Cell Signaling through Time and Space. *Mol. Cell* **2021**, *81* (20), 4137–4146.

(204) Tsang, B.; Pritišanac, I.; Scherer, S. W.; Moses, A. M.; Forman-Kay, J. D. Phase Separation as a Missing Mechanism for Interpretation of Disease Mutations. *Cell* **2020**, *183* (7), 1742–1756.

(205) Douliez, J. P.; Martin, N.; Gaillard, C.; Beneyton, T.; Baret, J. C.; Mann, S.; Beven, L. Catanionic Coacervate Droplets as a Surfactant-Based Membrane-Free Protocell Model. *Angew. Chem., Int. Ed.* **2017**, *56* (44), 13689–13693.

(206) Späth, F.; Donau, C.; Bergmann, A. M.; Kränzlein, M.; Synatschke, C. V.; Rieger, B.; Boekhoven, J. Molecular Design of Chemically Fueled Peptide-Polyelectrolyte Coacervate-Based Assemblies. *J. Am. Chem. Soc.* **2021**, *143* (12), 4782–4789.

(207) Van Haren, M. H. I.; Nakashima, K. K.; Spruijt, E. Coacervate-Based Protocells: Integration of Life-like Properties in a Droplet. *J. Syst. Chem.* **2020**, *8*, 107–120.

(208) Gao, N.; Mann, S. Membranized Coacervate Microdroplets: From Versatile Protocell Models to Cytomimetic Materials. *Acc. Chem. Res.* **2023**, *56* (3), 297–307.

(209) Rowan, S. J.; Cantrill, S. J.; Cousins, G. R. L.; Sanders, J. K. M.; Stoddart, J. F. Dynamic Covalent Chemistry. *Angew. Chem., Int. Ed.* **2002**, *41*, 898−952

(210) Cougnon, F. B. L.; Stefankiewicz, A. R.; Ulrich, S. Dynamic Covalent Synthesis. *Chem. Sci.* **2023**, *15* (3), 879–895.

(211) Li, M.; Mirshafian, R.; Wang, J.; Mohanram, H.; Ahn, K. A.; Hosseinzadeh, S.; Pervushin, K. V.; Waite, J. H.; Yu, J. Compliant Clients: Catechols Exhibit Enhanced Solubility and Stability in Diverse Complex Coacervates. *Biomacromolecules* **2023**, *24* (9), 4190–4198.

(212) Fisher, R. S.; Elbaum-Garfinkle, S. Tunable Multiphase Dynamics of Arginine and Lysine Liquid Condensates. *Nat. Commun.* **2020**, *11* (1).

USC UNIVERSIDADE DE SANTIAGO DE COMPOSTELA

7. APPENDICES

7.1 List of Figures

Figure 1 Schematic representation of applications of polymers in diverse areas and fields.

Figure 2 Evolution of drug delivery systems through the introduction of FDA-approved drug products from the Spansule® oral controlled release formulation to the lipid nanoparticle formulations for COVID-19 vaccine delivery.

Figure 3 Schematic representation of the differences between tumoral and healthy tissues, and the EPR effect.

Figure 4 Schematic representation of the active transport of a DDS through the incorporation of different ligands.

Figure 5 Schematic representation of the distribution of nanoparticles based on their architecture

Figure 6 Schematic representation of a polymer-drug conjugate.

Figure 7 Schematic representation of a polymersome.

Figure 8 Schematic representation of a polymeric micelle.

Figure 9 Schematic representation of diverse polymeric and dendritic structures.

Figure 10 Diagram illustrating the primary biomedical applications of GATG family dendrimers developed by our research group.

Figure 11 Schematic representation of polymeric micelles able to response towards variations in redox conditions, tumor overexpressed enzymes, and pH.

Figure 12 Schematic illustration of the endogenous pathways through which various nucleic acid payloads are processed.

Figure 13 Schematic representation of the degradation of gene delivery carriers.

Figure 14 Schematic representation of the transfection process from polyplex uptake till protein expression.

Figure 15 Combinatorial approaches for the screening of gene delivery vectors.

Figure 16 Diverse soft micro-compartmentalized assemblages used for synthetic cell modeling.

Figure 17 Molecular model of a bacterial cytoplasm.

Figure 18 Schematic representation of segregative and associative phase separation processes.

Figure 19 Multi-compartmentalized coacervates.

Figure 20 Controlled coacervation technologies.

Figure 21 Membranized coacervate microdroplets based on molecular/macromolecular interfacial self-assembly.

Figure 22 Schematic representation of the three steps involved in disulfide exchange mechanism.

Figure 23 Schematic representation of the formation of hydrazones.

USC UNIVERSIDADE DE SANTIAGO DE COMPOSTELA

Figure 24 Schematic representation of the equilibriums of BAs in aqueous solution.

Figure 25 Studies performed by Liu *et al.* based on the drug conjugation induced self-assembly.

Figure 26 DCvC for DOX delivery.

Figure 27 Dynamic polymer supra-amphiphilies for intracellular protein delivery described by Chen and coworkers.

Figure 28 Reported works by Montenegro and coworkers.

Figure 29 Reported works by the groups of Aida and Yang on cationic poly(disulfides).

Figure 30 Molecular structure of the BA modified peptide amphiphile and schematic representation of its assemble into spherical aggregates.

Figure 31 DLS histograms and correlation functions of CAT micelles with different % PEG recorded at 37 ºC immediately after formation.

Figure 32 DLS histograms and correlation functions of CAT micelles with different % PEG recorded at 37 ºC immediately after formation.

Figure 33 DLS histograms and correlation functions of CAT micelles with different % PEG recorded immediately after formation (37 ºC), and after 1 month of storage at 4 ºC (25 ºC).

Figure 34 DLS histograms and correlation functions of CAT micelles with different % PEG recorded immediately after formation (37 ºC), and after 1 month of storage at 4 ºC (25 ºC).

Figure 35 DLS histograms and correlation functions of DOX micelles with different % PEG recorded immediately after formation (37 ºC), after dialysis (37 ºC), and after 24 h at 37 ºC (37 ºC).

Figure 36 DLS histograms and correlation functions of DOX micelles with different % PEG recorded immediately after formation (37 ºC), after dialysis (37 ºC), and after 24 h at 37 ºC (37 ºC).

Figure 37 DLS histograms and correlation functions of DOX micelles with different % PEG recorded immediately after formation (37 ºC), and after 1 month of storage at 4 ºC (25 ºC).

Figure 38 DLS histograms and correlation functions of DOX micelles with different % PEG recorded immediately after formation (37 ºC), and after 1 month of storage at 4 ºC (25 ºC).

Figure 39 ^{1}H NMR spectrum (D_2O, 500 MHz) of PEG[G3]-BA.

Figure 40 ^{13}C NMR spectrum (D_2O, 125 MHz) of PEG[G3]-BA.

Figure 41 IR spectrum of PEG[G3]-BA.

Figure 42 MALDI-TOF MS of PEG[G3]-BA.

Figure 43 ^{1}H NMR spectrum (CD_3OD, 500 MHz) of 3[G2]-BA

Figure 44 ^{13}C NMR spectrum (CD_3OD, 125 MHz) of 3[G2]-BA.

Figure 45 IR spectrum of 3[G2]-BA.

Figure 46 ^{1}H NMR spectrum (DMSO-d_6, 500 MHz) of Protected Cat-D.

USC UNIVERSIDADE DE SANTIAGO DE COMPOSTELA

Figure 47 ^{13}C NMR spectrum (CD_3CN, 125 MHz) of Protected Cat-D.

Figure 48 IR spectrum of Protected Cat-D.

Figure 49 ^{1}H NMR spectrum (CD_3OD, 500 MHz) of Cat-D.

Figure 50 ^{13}C NMR spectrum (CD_3OD, 125 MHz) of Cat-D.

Figure 51 IR spectrum of Cat-D

Figure 52 ^{1}H NMR spectrum ($CDCl_3$, 500 MHz) of Protected Cat-T.

Figure 53 ^{13}C NMR spectrum ($CDCl_3$, 125 MHz) of Protected Cat-T.

Figure 54 IR spectrum of Protected Cat-T.

Figure 55 ^{1}H NMR spectrum (CD_3OD, 500 MHz) of Cat-T.

Figure 56 ^{13}C NMR spectrum (CD_3OD, 125 MHz) of Cat-T.

Figure 57 IR spectrum of Cat-T

Figure 58 ^{1}H NMR spectrum ($CDCl_3$, 500 MHz) of Protected Cat-I.

Figure 59 ^{13}C NMR spectrum ($CDCl_3$, 125 MHz) of Protected Cat-I.

Figure 60 IR spectrum of Protected Cat-I

Figure 61 ^{1}H NMR spectrum (CD_3OD, 500 MHz) of Cat-I.

Figure 62 ^{13}C NMR spectrum (CD_3OD, 125 MHz) of Cat-I.

Figure 63 IR spectrum of Cat-I.

Figure 64 ^{1}H NMR spectrum ($CDCl_3$, 500 MHz) of Cat-O.

Figure 65 ^{13}C NMR spectrum ($CDCl_3$, 125 MHz) of Cat-O.

Figure 66 IR spectrum of Cat-O.

Figure 67 ^{1}H NMR spectrum (CD_3OD, 300 MHz) of Cat-P.

Figure 68 ^{13}C NMR spectrum (CD_3OD, 125 MHz) of Cat-P.

Figure 69 ^{13}C NMR spectrum (CD_3OD, 125 MHz, ^{19}F decoupled, ^{1}H coupled) of Cat-P

Figure 70 ^{19}F NMR spectrum (CD_3OD, 282 MHz, ^{13}C decoupling) of Cat-P.

Figure 71 IR spectrum of Cat-P.

Figure 72 ^{1}H NMR spectrum ($CDCl_3$, 500 MHz) of Cat-C.

Figure 73 ^{13}C NMR spectrum ($CDCl_3$, 125 MHz) of Cat-C

Figure 74 IR spectrum of Cat-C.

Figure 75 DLS histograms and correlation functions of polyplexes prepared with Cat-G at different % PEG.

Figure 76 DLS histograms and correlation functions of polyplexes prepared with Cat-G at different N/P and CBA ratios.

USC UNIVERSIDADE DE SANTIAGO DE COMPOSTELA

Figure 77 DLS histograms and correlation functions of polyplexes prepared with Cat-G at different N/P and CBA ratios.
Figure 78 DLS histograms and correlation functions of polyplexes prepared with Cat-G at different N/P and CBA ratios.
Figure 79 DLS histograms and correlation functions of polyplexes prepared with Cat-G at different N/P and CBA ratios.
Figure 80 DLS histograms and correlation functions of polyplexes prepared with Cat-A at different N/P.
Figure 81 DLS histograms and correlation functions of polyplexes prepared with Cat-D at different N/P.
Figure 82 DLS histograms and correlation functions of polyplexes prepared with a mixture of Cat-G (75 %) and Cat-A (25 %) at different N/P.
Figure 83 DLS histograms and correlation functions of polyplexes prepared with a mixture of Cat-G (75 %) and Cat-D (25 %) at different N/P.
Figure 84 DLS histograms and correlation functions of polyplexes prepared with a mixture of Cat-G (50 %), Cat-A (25 %), and Cat-D (25 %) at different N/P.
Figure 85 DLS histograms and correlation functions of polyplexes prepared with mixtures of 75% Cat-G and 25% Cat-T, 75% Cat-G and 25% Cat-I, and 50% Cat-G, 25% Cat-T, and 25% Cat-I.
Figure 86 DLS histograms and correlation functions of G polyplexes dopped with 10 mol% Cat-O, 10 mol% Cat-P, 10 mol% Cat-C, and 3.33 mol% each of Cat-O, Cat-P, and Cat-C.
Figure 87 Gating for analyzing in vitro transfection efficiency by flow cytometry.
Figure 88 Gating for analyzing in vitro transfection efficiency by flow cytometry.
Figure 89 Median EGFP fluorescence of HEK-293 cells transfected for 72 h with G-, A-, and D-polyplexes of different % PEG and N/P ratios (CBA 5) measured by flow cytometry.
Figure 90 Polyplex 5-10-5G dopped with Cat-T and Cat-I.
Figure 91 Histograms displaying number of cells vs Cy5 fluorescence intensity showing the region selected as Cy5 positive cells.
Figure 92 Percentage of hemoglobin released upon incubation of erythrocytes (3% w/v in PBS) with increasing concentrations of PEG[G3]-BA or 3[G2]-BA and Cat-G at a CBA ratio of 5, for 1 h at 37 °C.
Figure 93 Characterization of coacervates prepared at CBA = 1, and stoichiometric ratio of charges.
Figure 94 Stabilization of coacervates with PEG-[G3]-BA.
Figure 95 Enzymatic Cascade Reaction by LSCM.
Figure 96 Enzymatic cascade control experiments by LSCM.
Figure 97 Enzymatic cascade reaction monitored by following the fluorescence signal from 2,3-DAP.
Figure 98 Fluorescence recovery after photobleaching (FRAP) curves fitted to an exponential growth model equation.
Figure 99 Protein studies with doped coacervates.

USC DE COMPOSTELA

Figure 100 Schematic representation of the catechol-driven *in situ* hydrophobization and self-assembly of 3[G2]-BA and PEG[G3]-BA.
Figure 101 Impact of PEGylation on the size of CAT-Micelles
Figure 102 Quantification of free BAs by the ARS assay.
Figure 103 Characterization of CAT-Micelles.
Figure 104 Plots and power function fits for CAT-Micelles of estimated ^{rel}N, ^{rel}S, and ^{rel}D.
Figure 105 Schematic representation of the CAT/DOX-driven *in situ* hydrophobization and self-assembly of 3[G2]-BA and PEG[G3]-BA.
Figure 106 Impact of PEGylation on the size of DOX micelles.
Figure 107 Plots and power function fits for DOX micelles of estimated ^{rel}N, ^{rel}S, and ^{rel}D.
Figure 108 Influence of % PEG in the pH-dependent release of DOX from DOX micelles.
Figure 109 Flow Cytometry
Figure 110 Intracellular trafficking of DOX micelles (100%, 40%, and 2% PEG) in F-98 cells assessed by LSCM.
Figure 111 Cell viability (CCK-8; 24 and 48 h) of F-98 cells in the presence of DOX micelles, free DOX, and components.
Figure 112 Schematic representation of the activation of polymeric boronic acid vectors and *in situ* nucleic acid complexation by the addition of cationic catechols, and parameters selected for simultaneous polyplex screening by dynamic covalent libraries.
Figure 113 pH sensitivity of the polyplexes.
Figure 114 Determination of boronate ester formation by ^{1}H NMR (500 MHz).
Figure 115 First screening of polymeric vectors
Figure 116 Transfection efficiencies (percentage of EGFP positive cells and median fluorescence by flow cytometry) and cell viability (CCK-8 assay) after 72 h in HEK-293 cells.
Figure 117 Dose–dependent transfection and cell viability of 1-10-5G and 1-15-5G polyplexes after 72 h in HEK-293 cells and after 48 h in COS-7, HepG2, and HeLa cells.
Figure 118 Erythrocyte aggregation test of cationic polyboronate vectors,
Figure 119 *In vitro* experiments with optimized polyplexes.
Figure 120 Schematic representation of the activation of polymeric boronic acids and *in situ* phase separation by the addition of oppositely charged catechols.
Figure 121 Schematic representation of the interfacial stabilization due to the hierarchical assembly of PEG[G3]-BA.
Figure 122 Protein uptake and chemical communication in coacervate populations.
Figure 123 Studies on doped coacervates.

USC UNIVERSIDADE DE SANTIAGO DE COMPOSTELA

7.2 List of Tables

Table 1 Volume (µL) of PEG[G3]-BA and 3[G2]-BA solutions used in the preparation of CAT micelles with different % PEG, and corresponding values of micelle concentration.

Table 2 Volume (µL) of PEG[G3]-BA and 3[G2]-BA solutions used in the preparation of DOX micelles with different % PEG.

Table 3 EEs, DLs, and calculated values of DOX, and micelle concentration of DOX micelles prepared with different % PEG.

Table 4 Mean hydrodynamic radius (*R*, nm) and PDI (in brackets) of CAT micelles obtained after 18 h of formation at 37 ºC, and after storage for 1 month at 4 ºC.

Table 5 Mean hydrodynamic radius (*R*, nm) and PDI (in brackets) of DOX micelles obtained immediately after 18 h of formation at 37 ºC, after dialysis, after 24 h at 37 ºC, and after storage for 1 month at 4 ºC.

Table 6 Concentration (mg/mL) of solutions of PEG[G3]-BA and 3[G2]-BA used in the preparation of polyplexes with N/P 5, 10, and 15.

Table 7 Concentration (mg/mL) of Cat-G solutions used in the preparation of polyplexes with N/P 5, 10, and 15.

Table 8 Concentration (mg/mL) of solutions of catechols A, D, T, and I used in the preparation of polyplexes with CBA 5.

Table 9 Concentration (mg/mL) of solutions of catechols O, P, and C used in the preparation of G polyplexes with N/P 10 and CBA 5.

Table 10 Volume (µL) of PEG[G3]-BA and 3[G2]-BA solutions used in the preparation of polyplexes with different % PEG.

Table 11 Mean hydrodynamic diameter (nm) and PDI of Cat-G polyplexes.

Table 12 Mean hydrodynamic diameter (nm) and PDI of Cat-A polyplexes.

Table 13 Mean hydrodynamic diameter (nm) and PDI of Cat-D polyplexes.

Table 14 Mean hydrodynamic diameter (nm) and PDI of mixed polyplexes.

Table 15 Mean hydrodynamic diameter (nm) and PDI of polyplexes dopped with catechols O, P, and C.

Table 16 Concentration (mg/mL) of solutions of Cat-G, and Cat-CA used in the preparation of coacervates at different CBA.

Table 17 Concentration (mg/mL) of solutions of EPI, EGCG and CAT used in the preparation of coacervates at CBA 1.

Table 18 Volume (µL) of Cat-G and Cat-CA solutions used for coacervate preparation.

USC UNIVERSIDADE DE SANTIAGO DE COMPOSTELA

7.3 List of Publications

Dynamic Covalent Boronate Chemistry Accelerates the Screening of Polymeric Gene Delivery Vectors via *In Situ* Complexation of Nucleic Acids

***Journal of the American Chemical Society*,** volume 146, pages 17211-17219, 2024

DOI: https://doi.org/10.1021/jacs.4c03384

Specific Contribution to the Publication

Conceptualization, methodology, and research. Participation in the design of the methodology and contextualization. Execution of the experimental part: synthesis and characterization of components, planning of experiments, preparation and characterization of vectors, and biological experiments. Analysis of obtained data and participation in decision-making. Preparation of the first manuscript. Creation of figures for the final version.

Quality Metrics

The journal in which the second part of this thesis (Sections 2.2, and 3.2) was published has the following quality indicators: an impact factor of 14.4 (2023 Journal Citation Reports), a CiteScore of 24.4 (2023 calculated by Scopus), and a total number of citations in 2023: 568,265. Additionally, it is ranked in the first quartile (Q1) in Chemistry (interdisciplinary).

Journal Authorization

The article has been published in the "Open Access" modality of the American Chemical Society (CC-BY 4.0 License); therefore, the author has permission to include it in his doctoral thesis.

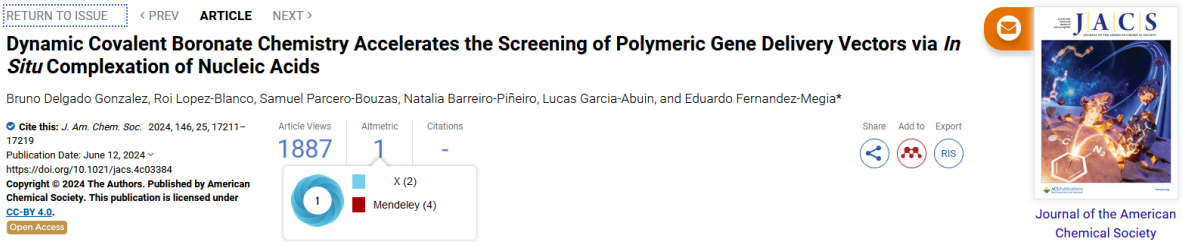

7.4 RIGHTS AND PERMISSIONS

Figure 2.

Order Summary

Licensee:	Bruno Delgado Gonzalez
Order Date:	Jul 2, 2024
Order Number:	5820811403761
Publication:	Journal of Controlled Release
Title:	Evolution of drug delivery systems: From 1950 to 2020 and beyond
Type of Use:	reuse in a thesis/dissertation
Order Ref:	22JCRPK2
Order Total:	0.00 EUR

View or print complete details of your order and the publisher's terms and conditions.

Sincerely,

Copyright Clearance Center

Figure 5.

Order Summary

Licensee:	Bruno Delgado Gonzalez
Order Date:	Jul 2, 2024
Order Number:	5820831340927
Publication:	Nature Reviews Drug Discovery
Title:	Engineering precision nanoparticles for drug delivery
Type of Use:	Thesis/Dissertation
Order Ref:	21NRDDLR5
Order Total:	0.00 EUR

View or print complete details of your order and the publisher's terms and conditions.

Sincerely,

Copyright Clearance Center

Figure 12.

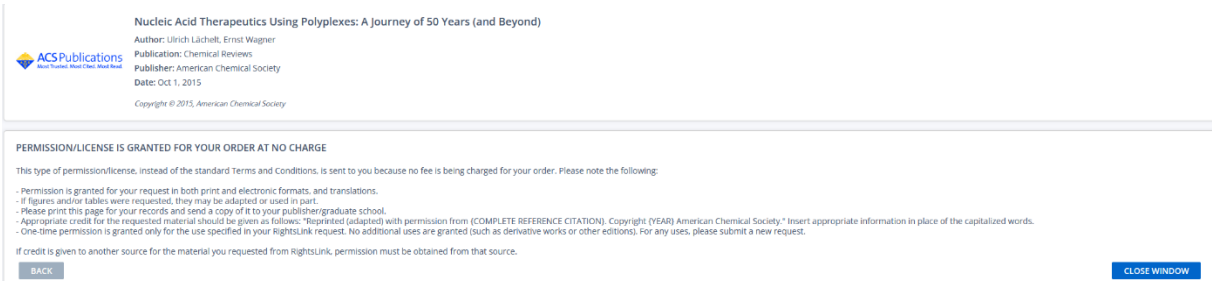

USC UNIVERSIDADE DE SANTIAGO DE COMPOSTELA

Figure 15A.

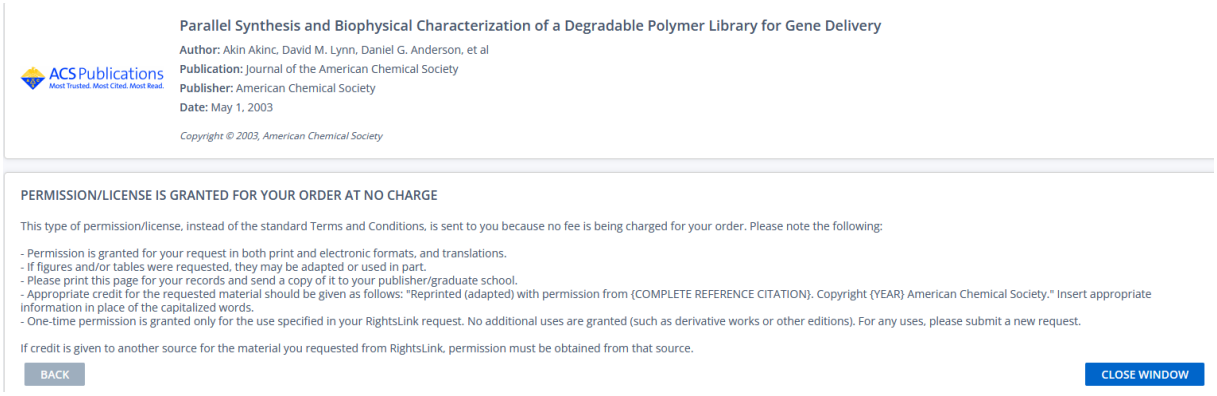

Parallel Synthesis and Biophysical Characterization of a Degradable Polymer Library for Gene Delivery

Author: Akin Akinc, David M. Lynn, Daniel G. Anderson, et al
Publication: Journal of the American Chemical Society
Publisher: American Chemical Society
Date: May 1, 2003

Copyright © 2003, American Chemical Society

PERMISSION/LICENSE IS GRANTED FOR YOUR ORDER AT NO CHARGE

This type of permission/license, instead of the standard Terms and Conditions, is sent to you because no fee is being charged for your order. Please note the following:

- Permission is granted for your request in both print and electronic formats, and translations.
- If figures and/or tables were requested, they may be adapted or used in part.
- Please print this page for your records and send a copy of it to your publisher/graduate school.
- Appropriate credit for the requested material should be given as follows: "Reprinted (adapted) with permission from {COMPLETE REFERENCE CITATION}. Copyright {YEAR} American Chemical Society." Insert appropriate information in place of the capitalized words.
- One-time permission is granted only for the use specified in your RightsLink request. No additional uses are granted (such as derivative works or other editions). For any uses, please submit a new request.

If credit is given to another source for the material you requested from RightsLink, permission must be obtained from that source.

BACK CLOSE WINDOW

Figure 15B.

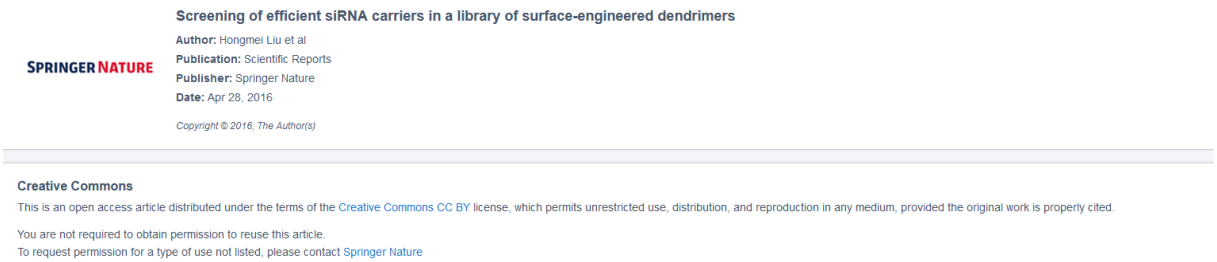

Screening of efficient siRNA carriers in a library of surface-engineered dendrimers

Author: Hongmei Liu et al
Publication: Scientific Reports
Publisher: Springer Nature
Date: Apr 28, 2016

Copyright © 2016, The Author(s)

Creative Commons

This is an open access article distributed under the terms of the Creative Commons CC BY license, which permits unrestricted use, distribution, and reproduction in any medium, provided the original work is properly cited.

You are not required to obtain permission to reuse this article.
To request permission for a type of use not listed, please contact Springer Nature

Figure 15C.

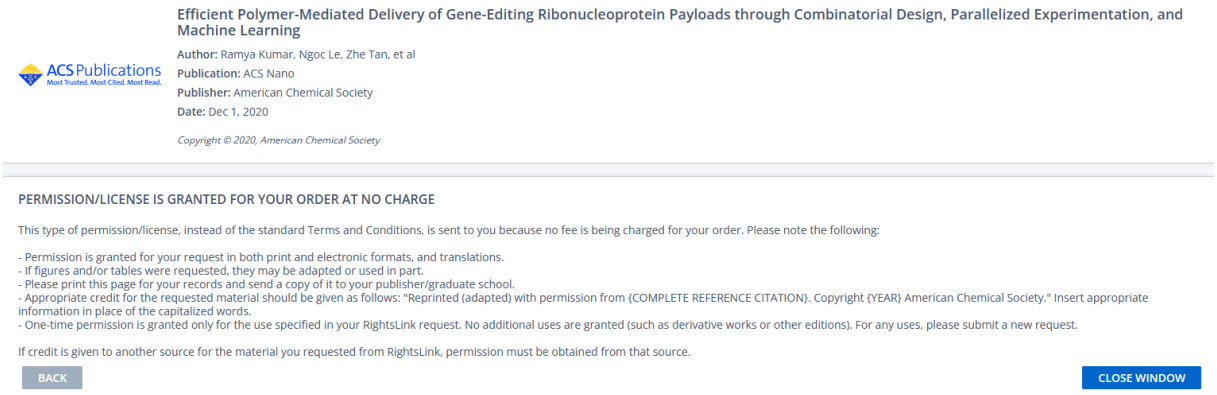

Efficient Polymer-Mediated Delivery of Gene-Editing Ribonucleoprotein Payloads through Combinatorial Design, Parallelized Experimentation, and Machine Learning

Author: Ramya Kumar, Ngoc Le, Zhe Tan, et al
Publication: ACS Nano
Publisher: American Chemical Society
Date: Dec 1, 2020

Copyright © 2020, American Chemical Society

PERMISSION/LICENSE IS GRANTED FOR YOUR ORDER AT NO CHARGE

This type of permission/license, instead of the standard Terms and Conditions, is sent to you because no fee is being charged for your order. Please note the following:

- Permission is granted for your request in both print and electronic formats, and translations.
- If figures and/or tables were requested, they may be adapted or used in part.
- Please print this page for your records and send a copy of it to your publisher/graduate school.
- Appropriate credit for the requested material should be given as follows: "Reprinted (adapted) with permission from {COMPLETE REFERENCE CITATION}. Copyright {YEAR} American Chemical Society." Insert appropriate information in place of the capitalized words.
- One-time permission is granted only for the use specified in your RightsLink request. No additional uses are granted (such as derivative works or other editions). For any uses, please submit a new request.

If credit is given to another source for the material you requested from RightsLink, permission must be obtained from that source.

BACK CLOSE WINDOW

Figure 16.

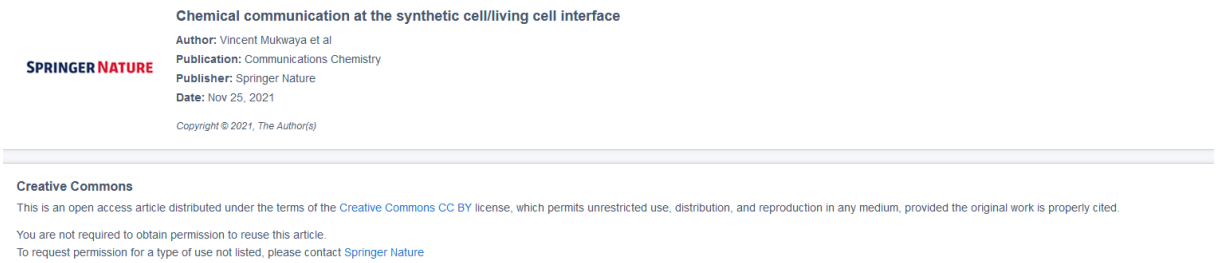

Chemical communication at the synthetic cell/living cell interface

Author: Vincent Mukwaya et al
Publication: Communications Chemistry
Publisher: Springer Nature
Date: Nov 25, 2021

Copyright © 2021, The Author(s)

Creative Commons

This is an open access article distributed under the terms of the Creative Commons CC BY license, which permits unrestricted use, distribution, and reproduction in any medium, provided the original work is properly cited.

You are not required to obtain permission to reuse this article.
To request permission for a type of use not listed, please contact Springer Nature

USC UNIVERSIDADE DE SANTIAGO DE COMPOSTELA

Figure 17.

Copyright

© 2016, Yu et al.

This article is distributed under the terms of the Creative Commons Attribution License, which permits unrestricted use and redistribution provided that the original author and source are credited.

Figure 18.

RETURN TO ISSUE | < PREV **ARTICLE** NEXT >

Complex Coacervate Materials as Artificial Cells

Alexander B. Cook, Sebastian Novosedlik, and Jan C. M. van Hest*

Cite this: *Acc. Mater. Res.* 2023, 4, 3, 287−298
Publication Date: February 13, 2023
https://doi.org/10.1021/accountsmr.2c00239
Copyright © 2023 The Authors. Co-published by ShanghaiTech University and American Chemical Society. This publication is licensed under CC-BY 4.0.
Open Access

Article Views 7253 | Altmetric 8 | Citations 5
LEARN ABOUT THESE METRICS

Share Add to Export RIS

Accounts of Materials Research

PDF (10 MB) Catálogo Iacobus

SUBJECTS: Genetics, Liquids, Membranes, Peptides and proteins, Polymers

Figure 19A.

Open Access Article
BY-NC This Open Access Article is licensed under a Creative Commons Attribution-Non Commercial 3.0 Unported Licence

DOI: 10.1039/D0SC03849K (Edge Article) *Chem. Sci.*, 2020, **11**, 8617-8625

Construction of coacervate-in-coacervate multi-compartment protocells for spatial organization of enzymatic reactions†

Yufeng Chen , Min Yuan , Yanwen Zhang , Songyang Liu , Xiaohai Yang , Kemin Wang * and Jianbo Liu *

State Key Laboratory of Chemo/Biosensing and Chemometrics, College of Chemistry and Chemical Engineering, Key Laboratory for Bio-Nanotechnology and Molecular Engineering of Hunan Province, Hunan University, Changsha 410082, P. R. China. E-mail: liujianbo@hnu.edu.cn; kmwang@hnu.edu.cn

Figure 19B.

RETURN TO ISSUE | < PREV **ARTICLE** NEXT >

Multiphase Complex Coacervate Droplets

Tiemei Lu and Evan Spruijt*

Cite this: *J. Am. Chem. Soc.* 2020, 142, 6, 2905−2914
Publication Date: January 20, 2020
https://doi.org/10.1021/jacs.9b11468
Copyright © 2020 American Chemical Society. This publication is licensed under CC-BY-NC-ND.
Open Access

Article Views 24398 | Altmetric 23 | Citations 208
LEARN ABOUT THESE METRICS

Share Add to Export RIS

Journal of the American Chemical Society

PDF (9 MB) Catálogo Iacobus SI Supporting Info (2) »

SUBJECTS: Fluorescence, Liquids, Molecules, Polymers, Salts

USC UNIVERSIDADE DE SANTIAGO DE COMPOSTELA

Figure 20A.

Order Summary

Licensee:	Bruno Delgado Gonzalez
Order Date:	Jul 2, 2024
Order Number:	5820851187587
Publication:	Angewandte Chemie International Edition
Title:	Photoswitchable Phase Separation and Oligonucleotide Trafficking in DNA Coacervate Microdroplets
Type of Use:	Dissertation/Thesis
Order Ref:	19ACIEMN20A
Order Total:	0.00 EUR

View or print complete details of your order and the publisher's terms and conditions.

Sincerely,

Copyright Clearance Center

Figure 20B.

Order Summary

Licensee:	Bruno Delgado Gonzalez
Order Date:	Jul 2, 2024
Order Number:	5820860039004
Publication:	Advanced Materials
Title:	Peptide-Based Coacervate-Core Vesicles with Semipermeable Membranes
Type of Use:	Dissertation/Thesis
Order Ref:	22ADVMATST20B
Order Total:	0.00 EUR

View or print complete details of your order and the publisher's terms and conditions.

Sincerely,

Copyright Clearance Center

Figure 20C.

Reversible generation of coacervate droplets in an enzymatic network

K. K. Nakashima, J. F. Baaij and E. Spruijt, *Soft Matter*, 2018, **14**, 361 **DOI:** 10.1039/C7SM01897E

This article is licensed under a Creative Commons Attribution-NonCommercial 3.0 Unported Licence. You can use material from this article in other publications, without requesting further permission from the RSC, provided that the correct acknowledgement is given and it is not used for commercial purposes.

Figure 20D.

Self-programmed enzyme phase separation and multiphase coacervate droplet organization

H. Karoui, M. J. Seck and N. Martin, *Chem. Sci.*, 2021, **12**, 2794 **DOI:** 10.1039/D0SC06418A

This article is licensed under a Creative Commons Attribution 3.0 Unported Licence. You can use material from this article in other publications without requesting further permissions from the RSC, provided that the correct acknowledgement is given.

Figure 21.

Membranized Coacervate Microdroplets: from Versatile Protocell Models to Cytomimetic Materials

Ning Gao and Stephen Mann*

Cite this: *Acc. Chem. Res.* 2023, 56, 3, 297–307
Publication Date: January 10, 2023
https://doi.org/10.1021/acs.accounts.2c00696
Copyright © 2023 The Authors. Published by American Chemical Society. This publication is licensed under CC-BY 4.0.
Open Access

Article Views 8967 | Altmetric 5 | Citations 8
LEARN ABOUT THESE METRICS

Share | Add to | Export RIS

Accounts of Chemical Research

PDF (11 MB)

Figure 25

Order Summary

Licensee:	Bruno Delgado Gonzalez
Order Date:	Jul 2, 2024
Order Number:	5820861459686
Publication:	Angewandte Chemie International Edition
Title:	In Situ Formation of Polymeric Nanoassemblies Using an Efficient Reversible Click Reaction
Type of Use:	Dissertation/Thesis
Order Ref:	20ACIETN25
Order Total:	0.00 EUR

View or print complete details of your order and the publisher's terms and conditions.

Sincerely,

Copyright Clearance Center

USC UNIVERSIDADE DE SANTIAGO DE COMPOSTELA

Figure 26A.

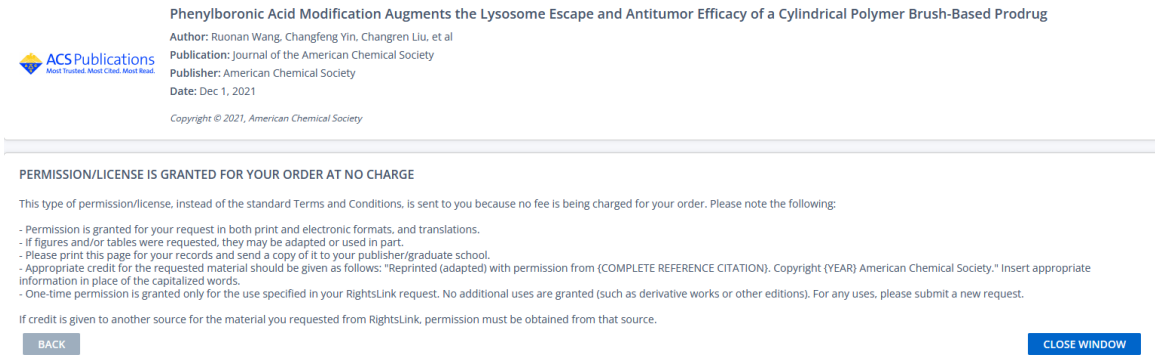

Phenylboronic Acid Modification Augments the Lysosome Escape and Antitumor Efficacy of a Cylindrical Polymer Brush-Based Prodrug

Author: Ruonan Wang, Changfeng Yin, Changren Liu, et al
Publication: Journal of the American Chemical Society
Publisher: American Chemical Society
Date: Dec 1, 2021

Copyright © 2021, American Chemical Society

PERMISSION/LICENSE IS GRANTED FOR YOUR ORDER AT NO CHARGE

This type of permission/license, instead of the standard Terms and Conditions, is sent to you because no fee is being charged for your order. Please note the following:

- Permission is granted for your request in both print and electronic formats, and translations.
- If figures and/or tables were requested, they may be adapted or used in part.
- Please print this page for your records and send a copy of it to your publisher/graduate school.
- Appropriate credit for the requested material should be given as follows: "Reprinted (adapted) with permission from {COMPLETE REFERENCE CITATION}. Copyright {YEAR} American Chemical Society." Insert appropriate information in place of the capitalized words.
- One-time permission is granted only for the use specified in your RightsLink request. No additional uses are granted (such as derivative works or other editions). For any uses, please submit a new request.

If credit is given to another source for the material you requested from RightsLink, permission must be obtained from that source.

BACK CLOSE WINDOW

Figure 26B.

Order Summary

Licensee:	Bruno Delgado Gonzalez
Order Date:	Jul 2, 2024
Order Number:	5820870183286
Publication:	Biomaterials
Title:	Self-immolative polyprodrug-based tumor-specific cascade amplificated drug release nanosystem for orchestrated synergistic cancer therapy
Type of Use:	reuse in a thesis/dissertation
Order Ref:	22BIOMATERIALSYN26B
Order Total:	0.00 EUR

View or print complete details of your order and the publisher's terms and conditions.

Sincerely,

Copyright Clearance Center

Figure 27.

Order Summary

Licensee:	Bruno Delgado Gonzalez
Order Date:	Jul 2, 2024
Order Number:	5820880379310
Publication:	Advanced Materials
Title:	Dynamic Polymer Amphiphiles for Efficient Intracellular and In Vivo Protein Delivery
Type of Use:	Dissertation/Thesis
Order Ref:	21ADVMATCG27
Order Total:	0.00 EUR

View or print complete details of your order and the publisher's terms and conditions.

Sincerely,

Copyright Clearance Center

USC UNIVERSIDADE DE SANTIAGO DE COMPOSTELA

Figure 28A.

Order Summary

Licensee:	Bruno Delgado Gonzalez
Order Date:	Jul 2, 2024
Order Number:	5820881110363
Publication:	Angewandte Chemie International Edition
Title:	In Situ Functionalized Polymers for siRNA Delivery
Type of Use:	Dissertation/Thesis
Order Ref:	16ACIEMO28A
Order Total:	0.00 EUR

View or print complete details of your order and the publisher's terms and conditions.

Sincerely,

Copyright Clearance Center

Figure 28B.

RETURN TO ISSUE | < PREV **ARTICLE** NEXT >

Different-Length Hydrazone Activated Polymers for Plasmid DNA Condensation and Cellular Transfection

Juan M. Priegue, Irene Lostalé-Seijo, Daniel Crisan, Juan R. Granja, Francisco Fernández-Trillo*, and Javier Montenegro*

Cite this: *Biomacromolecules* 2018, 19, 7, 2638−2649
Publication Date: April 13, 2018
https://doi.org/10.1021/acs.biomac.8b00252
Copyright © 2018 American Chemical Society. This publication is licensed under CC-BY.
Open Access

Article Views	Altmetric	Citations
3081	8	29

LEARN ABOUT THESE METRICS

Share Add to Export RIS

Biomacromolecules

PDF (9 MB) Catálogo Iacobus SI Supporting Info (1) »

SUBJECTS: Aldehydes, Fluorescence, Gene delivery, Genetics, Polymers

Figure 29A.

Reductively Cleavable Nanocaplets for siRNA Delivery by Template-Assisted Oxidative Polymerization

Author: P. K. Hashim, Kou Okuro, Shigekazu Sasaki, et al
Publication: Journal of the American Chemical Society
Publisher: American Chemical Society
Date: Dec 1, 2015

Copyright © 2015, American Chemical Society

PERMISSION/LICENSE IS GRANTED FOR YOUR ORDER AT NO CHARGE

This type of permission/license, instead of the standard Terms and Conditions, is sent to you because no fee is being charged for your order. Please note the following:

- Permission is granted for your request in both print and electronic formats, and translations.
- If figures and/or tables were requested, they may be adapted or used in part.
- Please print this page for your records and send a copy of it to your publisher/graduate school.
- Appropriate credit for the requested material should be given as follows: "Reprinted (adapted) with permission from (COMPLETE REFERENCE CITATION). Copyright (YEAR) American Chemical Society." Insert appropriate information in place of the capitalized words.
- One-time permission is granted only for the use specified in your RightsLink request. No additional uses are granted (such as derivative works or other editions). For any uses, please submit a new request.

If credit is given to another source for the material you requested from RightsLink, permission must be obtained from that source.

BACK CLOSE WINDOW

USC UNIVERSIDADE DE SANTIAGO DE COMPOSTELA

Figure 29B.

Order Summary

Licensee:	Bruno Delgado Gonzalez
Order Date:	Jul 2, 2024
Order Number:	5820890116864
Publication:	Angewandte Chemie International Edition
Title:	Self-Assembled and Size-Controllable Oligonucleotide Nanospheres for Effective Antisense Gene Delivery through an Endocytosis-Independent Pathway
Type of Use:	Dissertation/Thesis
Order Ref:	19ACIEYG29B
Order Total:	0.00 EUR

View or print complete details of your order and the publisher's terms and conditions.

Sincerely,

Copyright Clearance Center

Figure 30

ACS Publications
Most Trusted. Most Cited. Most Read.

Glucose-Driven Droplet Formation in Complexes of a Supramolecular Peptide and Therapeutic Protein

Author: Sihan Yu, Weike Chen, Guoqiang Liu, et al
Publication: Journal of the American Chemical Society
Publisher: American Chemical Society
Date: Mar 1, 2024

Copyright © 2024, American Chemical Society

PERMISSION/LICENSE IS GRANTED FOR YOUR ORDER AT NO CHARGE

This type of permission/license, instead of the standard Terms and Conditions, is sent to you because no fee is being charged for your order. Please note the following:

- Permission is granted for your request in both print and electronic formats, and translations.
- If figures and/or tables were requested, they may be adapted or used in part.
- Please print this page for your records and send a copy of it to your publisher/graduate school.
- Appropriate credit for the requested material should be given as follows: "Reprinted (adapted) with permission from {COMPLETE REFERENCE CITATION}. Copyright {YEAR} American Chemical Society." Insert appropriate information in place of the capitalized words.
- One-time permission is granted only for the use specified in your RightsLink request. No additional uses are granted (such as derivative works or other editions). For any uses, please submit a new request.

If credit is given to another source for the material you requested from RightsLink, permission must be obtained from that source.

BACK CLOSE WINDOW

Other images, tables, and figures

All other images, tables, and figures not included in the preceding section have been created individually by the student for this thesis. Figures 1, 3, 4, 6, 7, 11, 13, and 14 were created with BioRender.com using an Academic Subscription.

USC UNIVERSIDADE DE SANTIAGO DE COMPOSTELA

The discovery of new structure-activity relationships represents a promising avenue for designing innovative materials and understanding the principles governing biological processes. Nevertheless, advances in this field have been limited by current methodologies used in the preparation of polymeric structures. In this context, dynamic covalent chemistry emerges as a valuable tool for developing highly adaptable materials. This thesis aims to bridge these two concepts. By employing a dendrimer and a dendritic block copolymer as bricks, and the fast-forming and strong boronate bond as cement, a novel technology has been developed for constructing bioactive materials with implications in drug delivery, gene therapy, and the fabrication of artificial cells.